

1 **Exclusive  $\pi^-$  Electroproduction off the Neutron in**  
2 **Deuterium in the Resonance Region**

3 Ye Tian, Ralf. W. Gothe

4 *University of South Carolina*  
5 *712 Main Street, Columbia, South Carolina, 29201*

# Abstract

6

7 This analysis note focuses on extracting the exclusive  $\gamma^*n(p) \rightarrow p\pi^-(p)$  reaction cross  
8 section from deuterium data. The existing  $\gamma^*n \rightarrow p\pi^-$  event generator is modified to include  
9 the spectator (proton) information based on the CD-Bonn potential [20] to simulate the real  
10 data process. With this method, the exclusive quasi-free process is isolated successfully as  
11 demonstrated by the comparison of the spectator momentum distribution of the simulation  
12 with the missing momentum distribution of the data, and the kinematical final-state-interaction  
13 contribution factor  $R_{FSI}$  is extracted directly from the data according to the ratio between the  
14 exclusive quasi-free and full cross sections. The results of this analysis note are new the exclusive  
15 and quasi-free cross sections off neutrons bound in deuterium. Furthermore, the corresponding  
16 structure functions are extracted from those cross sections as well. The experiment was done  
17 in Hall B at the Thomas Jefferson National Laboratory (JLab) by using the CEBAF Large  
18 Acceptance Spectrometer (CLAS) detector, the “e1e” run data off a liquid deuterium target  
19 will provide these final results with a kinematic coverage for the hadronic invariant mass ( $W$ )  
20 up to 1.825 GeV and in the momentum transfer ( $Q^2$ ) range of 0.4 – 1.0 GeV/c<sup>2</sup>.

# Contents

21

22	<b>1</b>	<b>Single-Pion Electroproduction off the Moving Neutron</b>	<b>1</b>
23	1.1	Data Status . . . . .	1
24	1.2	Kinematics . . . . .	2
25	1.3	The Fermi Motion . . . . .	3
26	1.4	Off-shell Effects . . . . .	4
27	1.5	The Final State Interaction (FSI) . . . . .	5
28	1.6	Boosting of the Kinematic Variables . . . . .	5
29	1.7	Formalism . . . . .	7
30	<b>2</b>	<b>Data Analysis</b>	<b>10</b>
31	2.1	Data Processing . . . . .	10
32	2.2	Quality Check . . . . .	11
33	2.3	Electron Identification . . . . .	11
34	2.3.1	Minimum Momentum Cut . . . . .	12
35	2.3.2	$\theta_{CC}$ versus Segment Cut . . . . .	12
36	2.3.3	The Cut on Number of Photo-electrons . . . . .	13
37	2.3.4	Sampling Fraction Cut . . . . .	14
38	2.4	Pion Identification . . . . .	14
39	2.4.1	Pion $\Delta T$ Cut . . . . .	15
40	2.5	Proton Identification . . . . .	16
41	2.5.1	Proton $\Delta T$ Cut . . . . .	17
42	2.6	Timing Correction . . . . .	17
43	2.7	Kinematic Corrections . . . . .	18
44	2.7.1	Electron Momentum Correction . . . . .	18
45	2.7.2	Proton Energy Loss Correction . . . . .	20
46	2.8	Electron Fiducial Cuts . . . . .	28
47	2.8.1	EC Coordinate $U$ , $V$ , and $W$ Fiducial Cut . . . . .	28
48	2.8.2	$\phi_e$ versus $\theta_e$ Cut . . . . .	28
49	2.8.3	The Electron Polar Angle ( $\theta$ ) versus Momentum ( $p$ ) Cut . . . . .	29
50	2.9	Pion Fiducial Cuts . . . . .	32
51	2.9.1	The Pion $\phi$ versus $\theta$ Cut . . . . .	32
52	2.9.2	The Pion Polar Angle ( $\theta$ ) versus Momentum ( $p$ ) Cut . . . . .	33
53	2.10	Proton Fiducial Cuts . . . . .	35
54	2.10.1	The Proton $\phi$ versus $\theta$ Cut . . . . .	35
55	2.10.2	The Proton Polar Angle ( $\theta$ ) versus Momentum ( $p$ ) Cut . . . . .	35
56	2.11	Event Selection . . . . .	38
57	2.11.1	Exclusive Events Selection . . . . .	38
58	2.11.2	Quasi-free Exclusive Events Selection . . . . .	38

59	<b>3 Simulation</b>	<b>41</b>
60	3.1 Event Generator . . . . .	41
61	3.2 GSIM . . . . .	41
62	3.3 GPP . . . . .	43
63	3.4 RECSIS . . . . .	45
64	<b>4 Corrections and Normalization</b>	<b>46</b>
65	4.1 Kinematic Binning . . . . .	46
66	4.2 Bin Centering Corrections . . . . .	47
67	4.3 Luminosity . . . . .	48
68	4.4 Empty-Target Background Subtraction . . . . .	49
69	4.5 Acceptance Corrections . . . . .	50
70	4.6 Radiative Corrections . . . . .	51
71	4.7 Background Subtraction . . . . .	51
72	4.8 Inclusive Cross Section . . . . .	52
73	<b>5 Results</b>	<b>55</b>
74	5.1 Cross Sections . . . . .	55
75	5.1.1 The Exclusive Cross Section . . . . .	55
76	5.1.2 The Exclusive Quasi-free Cross Section . . . . .	55
77	5.2 Kinematically Defined Quasi-Free Contribution . . . . .	61
78	5.3 Structure Functions . . . . .	65
79	5.4 Legendre Polynomials Expansion . . . . .	66
80	5.5 Systematic Uncertainty . . . . .	66
81	5.5.1 Electron ID cuts . . . . .	67
82	5.5.2 $\pi^-$ ID cuts . . . . .	67
83	5.5.3 Proton ID cuts . . . . .	68
84	5.5.4 Event Selection . . . . .	69
85	5.5.5 Boost . . . . .	71
86	5.5.6 Deuteron Potential . . . . .	72
87	5.5.7 Bin Centering Correction . . . . .	73
88	5.5.8 Radiative Correction . . . . .	73
89	5.5.9 Normalization . . . . .	73
90	5.5.10 Summary . . . . .	74
91	5.5.11 Error Propagation . . . . .	75
92	<b>6 Summary and Conclusions</b>	<b>76</b>
93	<b>Appendices</b>	<b>80</b>
94	<b>Appendix A Parameter Tables</b>	<b>80</b>
95	<b>Appendices</b>	<b>86</b>
96	<b>Appendix B Differential Cross Sections</b>	<b>86</b>
97	<b>Appendices</b>	<b>111</b>



# 98 List of Figures

99	1.1	The resonance process of single-pion electroproduction off a neutron in deu-	
100		terium. The initial proton in the deuteron is treated as the spectator, named as	
101		$P_s$ . . . . .	2
102	1.2	(a)The momentum distribution of initial neutron in the exclusive $\gamma^*n(p) \rightarrow$	
103		$p\pi^-(p)$ process, which is moving in the deuteron in the lab frame, and (b) with	
104		log scale. . . . .	4
105	1.3	(Color online) The comparison of $W$ distributions. Black line presents $W_f$ , blue	
106		line shows $W_i$ calculated by setting $n^\mu = (-\vec{p}_s, E_n)$ ( $E_n$ with Eq. (1.15)). The	
107		other colors present the $W_i$ distribution by setting $n_\mu$ to $(-\vec{p}_s, m_n)$ (cyan), $(0, m_n)$	
108		(magenta), $(-\vec{p}_s, m_n + 2\frac{k_n^2}{2m_n} + 2\text{MeV})$ (blue), $(-\vec{p}_s, m_n + \frac{k_n^2}{2m_n} + 1\text{MeV})$ (orange),	
109		and $(-\vec{p}_s, m_n - \frac{k_n^2}{2m_n} - 1\text{MeV})$ (green). . . . .	5
110	1.4	Kinematic sketch as in the text for the three leading terms in $\gamma^* + D \rightarrow \pi^- + p + p$	
111		process (a) quasi-free, (b) pp re-scattering, and (c) $p\pi^-$ re-scattering. Diagrams	
112		(b) and (c) are two main sources of kinematical final state interactions. . . . .	6
113	1.5	Kinematics of $\pi^-$ electroproduction off a moving neutron. The leptonic neutron	
114		rest frame plane is formed by $e^\mu$ and $e^{\mu'}$ , where $k, E, k',$ and $E'$ are corresponding	
115		momentum and energy of the incoming and outgoing electrons. $q^\mu$ is the virtual	
116		photon four momentum and $\nu$ is the transferred energy. The hadronic CM frame	
117		plane is determined by final particles $p$ and $\pi$ , here $\theta_p^*$ and $\theta_\pi^*$ are their polar	
118		angles and $\phi_\pi^*$ the azimuthal angle of $\pi^-$ . . . . .	6
119	1.6	The $X$ and $Y$ projections of the $\hat{z}_{nrest}$ in the CM frame are plotted against each	
120		other for exclusive quasi-free events. . . . .	7
121	1.7	The $X$ and $Y$ projections of the $\hat{z}_{nrest}$ in the CM frame are plotted against each	
122		other for final-state-interaction dominated events. . . . .	8
123	2.1	(a) shows the exclusive number of events normalized to the live-time corrected	
124		charge for each file, and (b) shows it versus the scaled run number. Here the red	
125		curve shows Gaussian fit function, and two blue lines show the $3\sigma$ upper/lower	
126		cut limits. . . . .	11
127	2.2	Schematic diagram for the $\theta_{CC}$ reconstruction. . . . .	12
128	2.3	(a) Example $\theta_{CC}$ distribution of the 8th CC segment in sector 2, where the blue	
129		curve shows the Gaussian fit function, and the fitting parameters $\mu$ and $\sigma$ are	
130		shown in the statistic box. (b) The $\theta_{CC}$ versus segment number in sector 2 is	
131		plotted, where $\mu, \mu + 3\sigma,$ and $\mu - 4\sigma$ are marked as black stars and fit by a	
132		second degree polynomial functions, which are shown as blue curves. . . . .	13
133	2.4	Example $N_{phe} \times 10$ distributions of left and right PMTs in the CC 10th segment	
134		of sector 2 plotted separately and fit by the Poisson function Eq. (2.5) marked	
135		as red curve. . . . .	14

136	2.5	(a) An example of an $E_{total}/p$ distribution is fit with a Gaussian function (blue line). (b) $E_{total}/p$ versus $p$ distribution, where the black lines show the upper/lower $E_{total}/p$ cut limits. (c) $E_{total}/p$ versus $p$ distribution after all experimental data event selections. (d) $E_{total}/p$ versus $p$ distribution after all simulation event selections. . . . .	15
141	2.6	(a) Pion $\Delta T$ distribution with fitted Gaussian function (red curve) at $0.4 \text{ GeV}/c < p_\pi < 0.6 \text{ GeV}/c$ for sector 3. (b) Pion $\Delta T$ versus $p_\pi$ distribution with upper/lower $\Delta T$ cut limits for sector 3. . . . .	16
144	2.7	(a) The pion $\Delta T$ distribution in counter 40 of sector 3 shows two peaks at $0.1 \text{ ns}$ and $3.9 \text{ ns}$ (side band peaks), which are fit by two Gaussian functions (red curves) to get the shift parameters. (b) The same $\Delta T$ distribution with $\Delta T$ shift correction. . . . .	18
148	2.8	The pion $\Delta T$ versus $p_\pi$ distribution with upper/lower $\Delta T$ cut limits from counter 40 to 48 of sector 3. . . . .	19
150	2.9	The pion $\Delta T$ versus $p_\pi$ distribution with upper/lower $\Delta T$ cut limits from counter 40 to 48 of sector 3 after the $\Delta T$ shift correction. . . . .	20
152	2.10	(a) Proton $\Delta T$ distribution with Gaussian fit function (red curve) at $0.4 \text{ GeV}/c < p_\pi < 0.6 \text{ GeV}/c$ for sector 3. (b) Proton $\Delta T$ versus $p_{proton}$ distribution with upper/lower $\Delta T$ cut limits for sector 3. . . . .	21
155	2.11	The proton $\Delta T$ versus $p_\pi$ distribution with upper/lower $\Delta T$ cut limits from counter 40 to 48 of sector 3. . . . .	22
157	2.12	The proton $\Delta T$ versus $p_\pi$ distribution with upper/lower $\Delta T$ cut limits for counter 40 to 48 of sector 3 after the $\Delta T$ shift correction. . . . .	22
159	2.13	The $\Delta T$ versus momentum distribution without any $\Delta T$ correction for positive particles in the events that the good electron is the first particle. The corresponding proton selection $\Delta T$ cuts are shown as the tow solid black lines. . . . .	23
162	2.14	The $\Delta T$ versus momentum distribution with the $\Delta T$ corrections (Table A.3 in Appendix A of the notes ) for positive particles in the events that the good electron is the first particle. The corresponding proton selection $\Delta T$ cuts are shown as the tow solid black lines . . . . .	23
166	2.15	The $\Delta T$ versus momentum distribution without any $\Delta T$ correction for negative particles in the events that the good electron is the first particle. The corresponding pion selection $\Delta T$ cuts are shown as the tow solid black lines. . . . .	24
169	2.16	The $\Delta T$ versus momentum distribution with the $\Delta T$ corrections (Table A.3 in Appendix A of the notes ) for negative particles in the events that the good electron is the first particle. The corresponding pion selection $\Delta T$ cuts are shown as the tow solid black lines . . . . .	24
173	2.17	The differences between generated and reconstructed protons are presented by the black distributions for different $p_p$ at $\theta_p = 15^\circ$ . The blue lines indicate the Gaussian fits. . . . .	25
176	2.18	The ratio between Gaussian fit peak positions (in Fig. 2.17) and corresponding reconstructed momentum values, $\delta p/p$ , plotted against the reconstructed proton momentum ( $p$ ) is presented by the black circles, and the blue lines show the corresponding fit functions. . . . .	25
180	2.19	Fit parameters of $\delta p/p$ versus ( $p$ ) distributions plotted against the reconstructed proton $\theta$ is presented by the black points, and the blue lines show the corresponding fit functions. Here par[0], par[1], and par[2] correspond to the fit parameters in Eq. (2.18). . . . .	26

184	2.20	The example missing mass squared distributions of the spectator without any kinematic corrections (black line), with only electron momentum corrections (blue line), and with both electron momentum and proton energy loss corrections (red line) are plotted for sector 4, where the fit parameters in the statistics legend box correspond to the red-line Gaussian function fit. . . . .	26
185			
186			
187			
188			
189	2.21	The $\mu_{mism_{spector}}^2$ versus detector sectors without any kinematic corrections (black squares), with only electron momentum corrections (red triangles), and with both electron momentum and proton energy loss corrections (blue dots). . . . .	27
190			
191			
192	2.22	The $U$ , $V$ , and $W$ coordinate distributions in the electromagnetic calorimeter. The green area represents the selected events after the cuts. . . . .	28
193			
194	2.23	The $V$ coordinate distribution in the electromagnetic calorimeter. Red lines represent the hole cut limits. . . . .	29
195			
196	2.24	$\theta_e$ versus $\phi_e$ distributions of electrons are plotted for six sectors for experiment (left) and simulation (right) reconstructed data each side by side within the $0.8 \text{ GeV} <  \vec{p}_e  < 1.0 \text{ GeV}$ momentum interval. The blue lines show the fiducial cut boundaries for electrons. . . . .	30
197			
198			
199			
200	2.25	Example $\phi_e$ distributions of electrons in sector 4 for data with $0.8 \text{ GeV} <  \vec{p}_e  < 1.0 \text{ GeV}$ before (blue) and after (green) fiducial cuts. . . . .	30
201			
202	2.26	$\theta_e$ versus $p$ distributions of electrons in all six sectors are compared for experiment (left) and simulation (right) reconstructed data simultaneously each side by side. The top and bottom black lines show the $\theta_e$ cut boundaries, and the middle paired black lines show removed regions, which are reflected in Fig. 2.24 by the low event-rate bands. . . . .	31
203			
204			
205			
206			
207	2.27	(a) Typical example $\phi$ distribution of pions from the $0.2 \text{ GeV} <  \vec{p}_{\pi^-}  < 0.4 \text{ GeV}$ and $28^\circ < \theta_{\pi^-} < 30^\circ$ intervals in sector 1, which are fit by the function (Eq. (2.22)) shown by the red line, where the corresponding fit parameters $P_4$ , $P_5$ , and $P_6$ are heights of the corresponding plateau regions of the trapezoid function and $P_0$ , $P_1$ , $P_2$ , and $P_3$ are corresponding $\phi$ values of the inflection points. (b) Example $\phi$ versus $\theta$ distribution for pions in sector 1 within the same momentum interval. Corresponding fit parameters $P_0$ and $P_1$ of each $\theta$ bin are marked as stars and fit by the function (Eq. (2.23)) shown by the black line. . . . .	32
208			
209			
210			
211			
212			
213			
214			
215	2.28	Example $\phi$ versus $\theta$ distributions of pions after event selection in sector 1 for $0.2 \text{ GeV} < p_{\pi^-} < 1.2 \text{ GeV}$ within $0.2 \text{ GeV}$ increasing steps, and the fiducial cuts (blue lines) are plotted here for sector 1. . . . .	33
216			
217			
218	2.29	$\phi$ versus $\theta$ distributions of pions in different $p_{\pi^-}$ bins after event selection are plotted for sector 1 for experiment (left) and simulation (right) reconstructed data each side by side. The black lines represent the fiducial-cut boundaries. . . . .	34
219			
220			
221	2.30	$\theta$ versus $p$ distributions of pions in six sectors are compared for experiment (left) and simulation (right) reconstructed data each side by side. The middle paired black lines show the removed regions, which are reflected in Fig. 2.29 by the vertical low event-rate bands, and the bottom black lines represent $\theta > \theta_{min}^{\pi^-}$ cuts. . . . .	34
222			
223			
224			
225	2.31	(a) Typical example for a $\phi$ distribution of protons from the $0.2 \text{ GeV} <  \vec{p}_{proton}  < 0.4 \text{ GeV}$ and $28^\circ < \theta_{proton} < 30^\circ$ intervals in sector 1, which is fit by the function Eq. (2.22) and plotted as the red line. The corresponding fit parameters $P_4$ , $P_5$ , and $P_6$ are heights of the corresponding plateau regions of the trapezoid function, and $P_0$ , $P_1$ , $P_2$ , and $P_3$ are the corresponding $\phi$ values of the inflection points. (b) The $\phi$ versus $\theta$ distribution of protons for sector 1 within the same momentum interval. Corresponding fit parameters $P_0$ and $P_1$ of each $\theta$ bin are marked as stars, fit by the function Eq. (2.23), and shown by the black lines. . . . .	35
226			
227			
228			
229			
230			
231			
232			

233	2.32	Example $\phi$ versus $\theta$ distributions for protons in sector 1 for $0.2 \text{ GeV} < p_{\text{proton}} < 1.8 \text{ GeV}$ within $0.2 \text{ GeV}$ increasing steps and the fiducial cuts (blue lines) for sector 1. . . . .	36
234			
235			
236	2.33	$\phi$ versus $\theta$ distributions of protons plotted for six sectors for experimental experiment (left) and simulation (right) reconstructed data each side by side. The blue lines represent fiducial-cut boundaries. . . . .	36
237			
238			
239	2.34	$\theta$ versus $p$ distributions of protons in all six sectors are compared for experimental (left) and simulation (right) reconstructed data each side by side. The middle paired black lines show the removed regions, which are reflected in Fig. 2.33 by the vertical low event-rate bands. . . . .	37
240			
241			
242			
243	2.35	The $M_s^2$ distribution with the two cut limits represented by the red lines illustrates the exclusive event selection process. . . . .	38
244			
245	2.36	(Color online) The $ \vec{p}_s $ distribution of experimental data (black line) and simulation (blue line) where “green” and “red” filled areas represent the integral of the blue distribution from $0 \text{ MeV}$ to $200 \text{ MeV}$ and above $200 \text{ MeV}$ , respectively. . . . .	39
246			
247			
248	2.37	(a)(Color online) The black line represents the missing momentum distribution ( $ \vec{p}_s $ ) of the unmeasured proton from experimental data. Based on the CD-Bonn potential [20], the Monte Carlo simulated scaled proton momentum distribution leads to the red line and the detector-smearred simulated scaled distribution to the blue line.(b) The zoomed plot of (a) to investigates this comparison clearly. . . . .	40
249			
250			
251			
252			
253	2.38	momentum resolution . . . . .	40
254			
255	3.1	Flowchart showing the main steps of the detector and reaction simulation process. $\gamma^*n(p) \rightarrow p\pi^-(p)$ events are generated by a realistic event generator, passed through GSIM [1] and GPP [2], and cooked by RECSIS [3]. . . . .	42
256			
257	3.2	(a) $W$ distributions of exclusive quasi-free events of experimental data (black) and the corresponding simulated distribution for the MAID98 (blue), MAID2000 (magenta), MAID2003 (green), and MAID2007 (red) versions. (b) $Q^2$ distributions for the experimental events and the corresponding simulated events of (a). . . . .	42
258			
259			
260			
261			
262	3.3	Event start time ( $t_0$ ) distributions of the exclusive quasi-free events for experimental data (left) and simulation with smearing factor $f=0.9$ (right) are fit by Gaussian functions (red curves). The corresponding fit parameters are listed in the statistic boxes, respectively. . . . .	43
263			
264			
265			
266	3.4	The $\sigma$ of $t_0$ versus $f$ from the simulation events are fit by a linear function (blue), and the red line corresponds to the the $\sigma$ of $t_0$ from the measured exclusive quasi-free events. The $f$ value corresponding to the cross point is used to smear the simulated detector SC resolution. . . . .	44
267			
268			
269			
270	3.5	The fitted $\sigma$ values of $M_s^2$ distributions depending on different $a = b = c$ values are plotted as black points. These are fit by a linear function (blue). The red horizontal line represents the fitted $\sigma$ values of $M_s^2$ distributions from the experimental reconstructed events. The value of $a = b = c$ corresponding to the cross point is used to smear the simulated detector DC resolution. . . . .	44
271			
272			
273			
274			
275	3.6	The $M_s^2$ distributions of the exclusive quasi-free events for experimental data (left) and simulation with smearing factors $f = 0.9$ and $a = b = c = 2.5$ (right) are fit by Gaussian functions (red). The corresponding fit parameters are shown in their statistics legend boxes. . . . .	45
276			
277			
278			
279	4.1	$W$ and $Q^2$ binning for the $\pi^-$ electroproduction events, where vertical and horizontal lines are shown as the lower and upper corresponding bin limits. . . . .	47
280			

281	4.2	Example $\cos \theta^*$ and $\phi^*$ binning for the $\pi^-$ electroproduction events in $1.2 \text{ GeV} < W < 1.225 \text{ GeV}$ and $0.4 \text{ GeV}^2 < Q^2 < 0.6 \text{ GeV}^2$ bin, where vertical and horizontal lines show the lower and the upper bin limits. . . . .	48
282			
283			
284	4.3	Bin centering corrections $R_{BC}$ as a function of $\cos \theta^*$ and $\phi^*$ in the $W = 1.2125 \text{ GeV}$ and $Q^2 = 0.5 \text{ GeV}^2$ bin. . . . .	49
285			
286	4.4	(a) Measured electron vertex ( $Z_e$ ) distributions for full target events (black) and scaled empty target events (red). (b) The black distribution is kept the same as (a), and the vertex distribution for scaled empty target events is shifted to ( $Z_e - 1.5 \text{ mm}$ ) (red). . . . .	50
287			
288			
289			
290	4.5	$Z_e$ distributions for full- $LD_2$ -target (black) and scaled empty-target events (red) are plotted together in one canvas and compared with these of the empty target subtracted full $LD_2$ target events sector by sector. . . . .	50
291			
292			
293	4.6	$M_s^2$ distributions for measured (black) and simulated $\gamma^*n(p) \rightarrow p\pi^-(p)$ (blue), as well as simulated $\gamma^*p \rightarrow p\pi^-\pi^+$ events are plotted with the $M_s^2$ cut limits. . .	52
294			
295	4.7	$M_s^2$ distributions for measured (black) and simulated $\gamma^*n(p) \rightarrow p\pi^-(p)$ (red) events are plotted with the $M_s^2$ cut limits for $W = 1.2125 \text{ GeV}$ , $Q^2 = 0.5 \text{ GeV}^2$ , and $\cos \theta^* = -0.3$ in $\phi_{\pi^-}^* = 100^\circ, 140^\circ, 180^\circ, 220^\circ, 260^\circ,$ and $300^\circ$ bins individually. . .	53
296			
297			
298	4.8	$W$ dependent normalized yield distributions in the $eD \rightarrow e'X$ process are presented for data with black stars and for Osipenko's world-data parameterization with magenta stars in individual $Q^2$ bins from $0.4 \text{ GeV}^2$ to $1.7 \text{ GeV}^2$ in steps of $\Delta Q^2 = 0.1 \text{ GeV}^2$ . . . . .	54
299			
300			
301			
302	5.1	Exclusive (black points) and quasi-free (green squares) cross sections in $\mu\text{b}/\text{sr}$ are represented for $W = 1.2125 \text{ GeV}$ and $Q^2 = 0.5 \text{ GeV}^2$ . . . . .	56
303			
304	5.2	Exclusive (black points) and quasi-free (green squares) cross sections in $\mu\text{b}/\text{sr}$ are represented for $W = 1.2125 \text{ GeV}$ and $Q^2 = 0.7 \text{ GeV}^2$ . . . . .	57
305			
306	5.3	Exclusive (black points) and quasi-free (green squares) cross sections in $\mu\text{b}/\text{sr}$ are represented for $W = 1.2125 \text{ GeV}$ and $Q^2 = 0.9 \text{ GeV}^2$ . . . . .	58
307			
308	5.4	Exclusive (black points) and quasi-free (green squares) cross sections in $\mu\text{b}/\text{sr}$ are represented for $W = 1.4875 \text{ GeV}$ and $Q^2 = 0.5 \text{ GeV}^2$ . . . . .	59
309			
310	5.5	Exclusive (black points) and quasi-free (green squares) cross sections in $\mu\text{b}/\text{sr}$ are represented for $W = 1.6625 \text{ GeV}$ and $Q^2 = 0.5 \text{ GeV}^2$ . . . . .	60
311			
312	5.6	The ratios of $R_{FSI}(W_i, Q^2, \cos \theta_{\pi^-}^*, \phi_{\pi^-}^*)$ over $R_{FSI}(W_i, Q^2, \cos \theta_{\pi^-}^*)$ are represented by Blue points for different $\phi_{\pi^-}^*$ at $1.2 \text{ GeV} < W < 1.225 \text{ GeV}$ and $0.6 \text{ GeV}^2 < Q^2 < 0.8 \text{ GeV}^2$ . The individual plot shows the ratios for different $\cos \theta_{\pi^-}^*$ bins. The three lines from bottom to top correspond to 0.95, 1, and 1.05, respectively. . . . .	62
313			
314			
315			
316			
317	5.7	$R_{FSI}$ versus $\theta_{\pi^-}^*$ distribution example for individual $W_f$ bins, which are increasing by $0.025 \text{ GeV}$ in the range of $1.1 \text{ GeV} < W < 1.725 \text{ GeV}$ for $0.4 \text{ GeV}^2 < Q^2 < 0.6 \text{ GeV}^2$ . . . . .	63
318			
319			
320	5.8	$R_{FSI}$ versus $\theta_{\pi^-}^*$ distributions example for individual $W_f$ bins, which are increasing by $0.025 \text{ GeV}$ in the range of $1.1 \text{ GeV} < W < 1.725 \text{ GeV}$ for $0.6 \text{ GeV}^2 < Q^2 < 0.8 \text{ GeV}^2$ . . . . .	63
321			
322			
323	5.9	$R_{FSI}$ versus $\theta_{\pi^-}^*$ distributions example for individual $W_f$ bins, which are increasing by $0.025 \text{ GeV}$ in the range of $1.125 \text{ GeV} < W < 1.6 \text{ GeV}$ for $0.8 \text{ GeV}^2 < Q^2 < 1.0 \text{ GeV}^2$ . . . . .	64
324			
325			

326	5.10	Example of the $\cos\theta_{\pi^-}^*$ dependent structure functions $\sigma_T + \epsilon\sigma_L$ (top row), $\sigma_{TT}$ (middle row), and $\sigma_{TL}$ (bottom row) for $W = 1.2125$ GeV at $Q^2 = 0.5$ GeV <sup>2</sup> (left column), $Q^2 = 0.7$ GeV <sup>2</sup> (middle column), and $Q^2 = 0.9$ GeV <sup>2</sup> (right column) that are extracted for the exclusive (black points) and quasi-free (green squares) cross sections and compared with the predictions of the SAID (magenta points) and MAID2000 (blue points) models. The solid black bars represent the corresponding systematic uncertainties. The Legendre polynomial expansions are fitted to the corresponding structure function data for $\pi^-$ angular momenta up to $l = 1$ by dash lines, and up to $l = 2$ by solid lines. . . . .	65
327			
328			
329			
330			
331			
332			
333			
334			
335	5.11	The $\Delta T$ distribution of pions in six sectors. The black, blue, and red lines represent the $4\sigma$ , $3\sigma$ , and $2\sigma$ cut boundaries, respectively. . . . .	68
336			
337	5.12	The $\Delta T$ distribution of protons in six sectors. The black, blue, and red lines represent the $4\sigma$ , $3\sigma$ , and $2\sigma$ cut boundaries, respectively. . . . .	69
338			
339	5.13	(Color online) The $\phi_p$ versus $\theta_p$ distributions for six sectors without proton fiducial cuts. The magenta, blue, and black lines represent loose, chosen, and tight proton fiducial cuts, respectively. . . . .	70
340			
341			
342	5.14	(Color online) The spectator missing mass squared $M_s^2$ distributions for data (black curve) and simulation (blue curve). The black, red, and blue vertical lines represent loose, chosen, and tight $M_s^2$ cuts, respectively. . . . .	70
343			
344			
345	5.15	(Color online) The spectator missing momentum $ \vec{P}_s $ distributions for data (black curve) and simulation (blue curve). The black, red, and blue vertical lines represent loose, chosen, and tight $ \vec{P}_s $ cuts, respectively. . . . .	71
346			
347			
348	5.16	The normalized cumulative “spectator” proton momentum distributions from different deuteron potentials. The black, blue, and red points represent the CD-Bonn, Paris, and Hulthen potentials, respectively. . . . .	72
349			
350			
351	5.17	The $\phi_{\pi^-}^*$ dependence of the exclusive cross sections with and without radiative correction are marked as red points and black squares, respectively for an example at $W = 1.2125$ GeV and $Q^2 = 0.7$ GeV <sup>2</sup> . The individual plots correspond to different $\cos\theta_{\pi^-}^*$ bins. . . . .	74
352			
353			
354			
355	B.1	Exclusive (black points) and quasi-free (green squares) cross sections in $\mu\text{b}/\text{sr}$ are represented for $W = 1.1125$ GeV and $Q^2 = 0.5$ GeV <sup>2</sup> . . . . .	86
356			
357	B.2	Exclusive (black points) and quasi-free (green squares) cross sections in $\mu\text{b}/\text{sr}$ are represented for $W = 1.1125$ GeV and $Q^2 = 0.7$ GeV <sup>2</sup> . . . . .	87
358			
359	B.3	Exclusive (black points) and quasi-free (green squares) cross sections in $\mu\text{b}/\text{sr}$ are represented for $W = 1.1375$ GeV and $Q^2 = 0.5$ GeV <sup>2</sup> . . . . .	88
360			
361	B.4	Exclusive (black points) and quasi-free (green squares) cross sections in $\mu\text{b}/\text{sr}$ are represented for $W = 1.1375$ GeV and $Q^2 = 0.7$ GeV <sup>2</sup> . . . . .	89
362			
363	B.5	Exclusive (black points) and quasi-free (green squares) cross sections in $\mu\text{b}/\text{sr}$ are represented for $W = 1.1375$ GeV and $Q^2 = 0.9$ GeV <sup>2</sup> . . . . .	89
364			
365	B.6	Exclusive (black points) and quasi-free (green squares) cross sections in $\mu\text{b}/\text{sr}$ are represented for $W = 1.1625$ GeV and $Q^2 = 0.5$ GeV <sup>2</sup> . . . . .	90
366			
367	B.7	Exclusive (black points) and quasi-free (green squares) cross sections in $\mu\text{b}/\text{sr}$ are represented for $W = 1.1625$ GeV and $Q^2 = 0.7$ GeV <sup>2</sup> . . . . .	90
368			
369	B.8	Exclusive (black points) and quasi-free (green squares) cross sections in $\mu\text{b}/\text{sr}$ are represented for $W = 1.1625$ GeV and $Q^2 = 0.9$ GeV <sup>2</sup> . . . . .	91
370			
371	B.9	Exclusive (black points) and quasi-free (green squares) cross sections in $\mu\text{b}/\text{sr}$ are represented for $W = 1.1875$ GeV and $Q^2 = 0.5$ GeV <sup>2</sup> . . . . .	91
372			
373	B.10	Exclusive (black points) and quasi-free (green squares) cross sections in $\mu\text{b}/\text{sr}$ are represented for $W = 1.1875$ GeV and $Q^2 = 0.7$ GeV <sup>2</sup> . . . . .	92
374			







475	B.61 Exclusive (black points) and quasi-free (green squares) cross sections in $\mu\text{b}/\text{sr}$	
476	are represented for $W = 1.6125$ GeV and $Q^2 = 0.7$ GeV <sup>2</sup> . . . . .	117
477	B.62 Exclusive (black points) and quasi-free (green squares) cross sections in $\mu\text{b}/\text{sr}$	
478	are represented for $W = 1.6375$ GeV and $Q^2 = 0.5$ GeV <sup>2</sup> . . . . .	118
479	B.63 Exclusive (black points) and quasi-free (green squares) cross sections in $\mu\text{b}/\text{sr}$	
480	are represented for $W = 1.6375$ GeV and $Q^2 = 0.7$ GeV <sup>2</sup> . . . . .	118
481	B.64 Exclusive (black points) and quasi-free (green squares) cross sections in $\mu\text{b}/\text{sr}$	
482	are represented for $W = 1.6625$ GeV and $Q^2 = 0.5$ GeV <sup>2</sup> . . . . .	119
483	B.65 Exclusive (black points) and quasi-free (green squares) cross sections in $\mu\text{b}/\text{sr}$	
484	are represented for $W = 1.6625$ GeV and $Q^2 = 0.7$ GeV <sup>2</sup> . . . . .	119
485	B.66 Exclusive (black points) and quasi-free (green squares) cross sections in $\mu\text{b}/\text{sr}$	
486	are represented for $W = 1.6875$ GeV and $Q^2 = 0.5$ GeV <sup>2</sup> . . . . .	120
487	B.67 Exclusive (black points) and quasi-free (green squares) cross sections in $\mu\text{b}/\text{sr}$	
488	are represented for $W = 1.6875$ GeV and $Q^2 = 0.7$ GeV <sup>2</sup> . . . . .	120
489	B.68 Exclusive (black points) and quasi-free (green squares) cross sections in $\mu\text{b}/\text{sr}$	
490	are represented for $W = 1.7125$ GeV and $Q^2 = 0.5$ GeV <sup>2</sup> . . . . .	121
491	B.69 Exclusive (black points) and quasi-free (green squares) cross sections in $\mu\text{b}/\text{sr}$	
492	are represented for $W = 1.7125$ GeV and $Q^2 = 0.7$ GeV <sup>2</sup> . . . . .	121
493	B.70 Exclusive (black points) and quasi-free (green squares) cross sections in $\mu\text{b}/\text{sr}$	
494	are represented for $W = 1.7375$ GeV and $Q^2 = 0.5$ GeV <sup>2</sup> . . . . .	122
495	B.71 Exclusive (black points) and quasi-free (green squares) cross sections in $\mu\text{b}/\text{sr}$	
496	are represented for $W = 1.7375$ GeV and $Q^2 = 0.7$ GeV <sup>2</sup> . . . . .	122
497	B.72 Exclusive (black points) and quasi-free (green squares) cross sections in $\mu\text{b}/\text{sr}$	
498	are represented for $W = 1.7625$ GeV and $Q^2 = 0.5$ GeV <sup>2</sup> . . . . .	123
499	B.73 Exclusive (black points) and quasi-free (green squares) cross sections in $\mu\text{b}/\text{sr}$	
500	are represented for $W = 1.7875$ GeV and $Q^2 = 0.5$ GeV <sup>2</sup> . . . . .	123
501	B.74 Exclusive (black points) and quasi-free (green squares) cross sections in $\mu\text{b}/\text{sr}$	
502	are represented for $W = 1.8125$ GeV and $Q^2 = 0.5$ GeV <sup>2</sup> . . . . .	124

# Chapter 1

## Single-Pion Electroproduction off the Moving Neutron

Single-pion electroproduction has been the main process in the study of the  $N - N^*$  transition form factors of the lower mass nucleon resonances such as  $P_{33}(1232)$ ,  $P_{11}1440$ ,  $D_{13}(1520)$ ,  $S_{11}(1535)$ ,  $S_{11}(1650)$ ,  $F_{15}(1680)$ , and  $D_{33}(1700)$ . A moving neutron in a deuteron target is not the same as a free neutron at rest, we need to deal with the motion, off-shell effects, and final state interactions, which will be introduced in the following sections.

### 1.1 Data Status

Table 1.1: Summary of the single pion electroproduction off bound neutron in the deuterium target with  $R_{\pi^-/\pi^+} = \frac{d\sigma(\gamma\nu+n\rightarrow\pi^-+p)}{d\sigma(\gamma\nu+p\rightarrow\pi^++n)} = \frac{\text{Rate}(e+d\rightarrow e+\pi^-+p(p))}{\text{Rate}(e+d\rightarrow e+\pi^++n(n))}$ .

Reaction	Observable	$W$ value GeV	$Q^2$ value GeV <sup>2</sup>	Lab/experiment
$en(p) \rightarrow e' \pi^- p(p)$ $ep(n) \rightarrow e' \pi^+ n(n)$	$R_{\pi^-/\pi^+}$	2.15, 3.11	1.2, 4.0	Cornell/WSL [13]
$en(p) \rightarrow e' \pi^- p(p)$ $ep(n) \rightarrow e' \pi^+ n(n)$	$d\sigma/d\Omega_\pi$	2.15, 2.65	1.2, 2.0	Cornell/WSL [14]
$en(p) \rightarrow e' \pi^- p(p)$ $ep(n) \rightarrow e' \pi^+ n(n)$	$R_{\pi^-/\pi^+}$	1.28-1.71	0.5	NINA [34]
$en(p) \rightarrow e' \pi^- p(p)$ $ep(n) \rightarrow e' \pi^+ n(n)$	$R_{\pi^-/\pi^+}$	1.3-1.7	1.0	NINA [28]
$ep(n) \rightarrow e' \pi^+ n(n)$ $en(p) \rightarrow e' \pi^- p(p)$	$R_{\pi^+/\pi^-}$	1.16, 1.232	0.0856, 0.0656	ALS [23]
$en(p) \rightarrow e' p\pi^-(p)$	$\sigma_L, \sigma_T$	1.15, 1.6	0.4	JLab-HallA [22]
$en(p) \rightarrow e' p\pi^-(p)$	$\sigma_L, \sigma_T$	1.95, 2.45	0.6, 1.0, 1.6, 2.45	JLab-HallC [24]

The low-lying excited states of the proton have been studied in greater detail [15], there is still very little data available on neutron excitations. Because of the inherent difficulty in obtaining a free neutron target, a deuterium target is the best alternative. From the SAID database [4], the  $\pi^-$  electroproductions off neutrons in the deuterium are listed in the Tab. 1.1, in which, the ratio  $R_{\pi^-/\pi^+}$  was directly measured for most available data. Even though the differential cross sections were measured directly, they are only available for single or couple  $Q^2$  values and in parts of the whole resonance range. We need to accumulate sufficient and precise

519 data for the neutron, not only to study the isospin dependent structure of the nucleon and its  
 520 excitations, but also to aid the development of QCD based calculations and models.

521 The six simplest pion electroproduction reactions off the free proton, bound proton, and  
 522 bound neutron targets are summarized as

$$\gamma^* + p \rightarrow \pi^0 + p, \quad (1.1)$$

$$\gamma^* + p \rightarrow \pi^+ + n, \quad (1.2)$$

$$\gamma^* + D(p) \rightarrow \pi^+ + n + n_s, \quad (1.3)$$

$$\gamma^* + D(p) \rightarrow \pi^0 + p + n_s, \quad (1.4)$$

$$\gamma^* + D(n) \rightarrow \pi^- + p + p_s, \text{ and} \quad (1.5)$$

$$\gamma^* + D(n) \rightarrow \pi^0 + n + p_s. \quad (1.6)$$

528 All the listed single-pion reactions under the same experimental conditions are included in the  
 529 “ele” run, which took data with the CLAS detector at JLab from December 14th, 2002 to  
 530 January 24th, 2003. The combined analysis of processes Eq. (1.1)- (1.6) will provide the best  
 531 possible experimental information about the final state interactions and the off shell effects of  
 532 the bound nucleon, which are crucial to extract the free neutron information. In this analy-  
 533 sis note, the process Eq. (1.5) is analyzed, which includes both resonance and non-resonance  
 534 process, to extract corresponding cross sections off the neutron in the deuterium target in the  
 535 resonance region. The resonance process of interest Eq. (1.5) is shown in Fig. 1.1, where the  
 536 electron emits a virtual photon ( $\gamma^*$ ) exciting the neutron to one of its excitations ( $N^*$ ), then the  
 537 resonance decays to a  $\pi^-$  and a proton ( $p$ ). The initial proton in the deuteron is treated as a  
 538 spectator ( $P_s$ ), which will be discussed in Chapter 2 that discusses how to isolate the quasi-free  
 process.

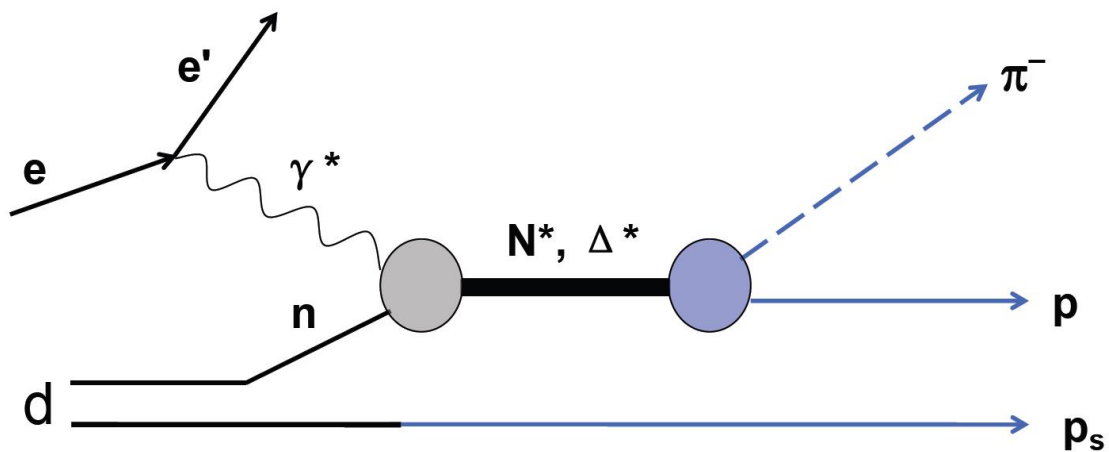


Figure 1.1: The resonance process of single-pion electroproduction off a neutron in deuterium. The initial proton in the deuteron is treated as the spectator, named as  $P_s$ .

539

## 540 1.2 Kinematics

541 Before we introduce the kinematics of the scattering from a bound neutron in a deuteron, we  
 542 first consider the case of scattering from a free neutron that is at rest in the lab frame, then  
 543 the chosen variables  $W_i$  and  $Q^2$  are defined as:

$$W_i^{rest} = \sqrt{(q^\mu + n^\mu)^2} = \sqrt{(p^\mu + (\pi^-)^\mu)^2} = W_f^{rest}, \quad (1.7)$$

$$(Q^{rest})^2 = -(q^\mu)^2 = (e^\mu - e^{\mu'})^2, \quad (1.8)$$

545 where  $q^\mu$  presents the four momentum of the virtual photon.  $W_i^{rest}$  and  $(Q^{rest})^2$  correspond  
 546 to the invariant mass of the photon-nucleon system and the four-momentum transfer of the  
 547 virtual photon for this scattering respectively, which are determined in the leptonic interaction  
 548 plane that is shown in Fig. 1.5 with the gray color. In addition, we also need to determine  
 549 two body final state  $p^\mu$  and  $(\pi^-)^\mu$ . In general, two final particles need to be described by  
 550  $4 \times 2 = 8$  components of their four vector momentum. Indeed, with the knowledge that they  
 551 are all on mass shell, it gives two restrictions ( $E_j^2 - k_j^2 = m_j^2; j = 1, 2$ ). Furthermore, the  
 552 energy momentum conservation laws impose four additional constraints for four momentum  
 553 components of the final particles. So we only need two kinematics variables to determine the  
 554 hadronic two body final state. Eventually, we end up with four variables to represent the  
 555  $\gamma^* n(p) \rightarrow p\pi^-(p)$  cross section.

556 For the kinematics of the process Eq. (1.5) that is the scattering from a bound neutron in a  
 557 deuteron, we have to consider the influence on the final cross sections of Fermi motion, off-shell  
 558 effects, and the final state interaction, which are introduced next.

### 559 1.3 The Fermi Motion

560 In the process Eq. (1.5), where the initial neutron is moving around “quasi-freely” in the  
 561 deuteron in the lab frame. By measuring all final particles  $e'$ ,  $p$ , and  $\pi^-$  exclusively, energy  
 562 and momentum conservation imply that the sums of the four-momenta before and after the  
 563 reaction are identical:

$$\begin{aligned} q^\mu + D^\mu &= (\pi^-)^\mu + p^\mu + p_s^\mu, \\ q^\mu + p_i^\mu + n^\mu &= (\pi^-)^\mu + p^\mu + p_s^\mu, \end{aligned} \quad (1.9)$$

564 where  $D^\mu$  is the four-momentum of deuteron that is at rest in the lab frame,  $D^\mu = (0, m_D)$ .  
 565  $n^\mu$  and  $p_i^\mu$  correspond to the four-momentum of the neutron and the proton, respectively, that  
 566 are moving and loosely bound in the deuteron in that frame. The outgoing missing proton  $p_s^\mu$ ,  
 567 which is not directly measured, is reconstructed from the Eq. (1.9) by

$$p_s^\mu = q^\mu + D^\mu - (\pi^-)^\mu - p^\mu, \quad (1.10)$$

568 and the momentum of this proton is calculated by

$$\vec{p}_s = \vec{q} - \vec{\pi}^- - \vec{p}. \quad (1.11)$$

569 Ignoring the off-shell effects at this moment, we focus on the motion first. In the quasi-free  
 570 process of the reaction Eq. (1.5), where the initial proton is treated as a “spectator” that is  
 571 totally unaffected by the interaction, thus  $p_i^\mu = p_s^\mu$  in Eq. (1.9) (ignoring the off-shell effects).  
 572 Then we can rewrite the Eq. (1.9) by

$$q^\mu + n^\mu = (\pi^-)^\mu + p^\mu, \quad (1.12)$$

573 and the initial neutron momentum is reconstructed by

$$\vec{n} = \vec{\pi}^- + \vec{p} - \vec{q}. \quad (1.13)$$

574 For the quasi-free process, by comparing Eq. 1.11 with Eq. 1.13, we get

$$\vec{p}_s = \vec{p}_i = -\vec{n}. \quad (1.14)$$

575 In contrast to the free neutron case, the neutron is now moving around with the Fermi momen-  
576 tum, which is reconstructed from Eq. (1.13) and graphed in Fig. 1.2a and 1.2b. This motion  
577 causes changes in the kinematics compared to scattering off a neutron at rest in the lab frame.  
578 Thus, in order to define the proper electron scattering plane, we first boost  $e^\mu$ ,  $(e')^\mu$ ,  $p^\mu$ , and  
579  $(\pi^-)^\mu$  from the lab frame into the neutron rest frame with the boost vector calculated from  
580  $n^\mu$  (Eq. (1.12)). In this frame, the variables  $W_i$ ,  $W_f$  and  $Q^2$  are calculated from Eq. (1.7) and  
581 Eq. (1.8), as well as the electron scattering plane is defined. Then  $W_f$  and  $Q^2$  are selected  
582 to represent the scattering cross sections off the moving neutron in the deuteron. So for this  
583 work, the final reported cross sections are not influenced by the Fermi momentum of the initial  
neutron in the deuteron.



Figure 1.2: (a) The momentum distribution of initial neutron in the exclusive  $\gamma^*n(p) \rightarrow p\pi^-(p)$  process, which is moving in the deuteron in the lab frame, and (b) with log scale.

584

## 585 1.4 Off-shell Effects

586 As mentioned previously, the bound neutron is also off-shell beside moving around in the  
587 deuteron. Even in the quasi-free process (isolating the quasi-free process is discussed in the  
588 Chapter 2),  $p_i^\mu$  is not equal to  $p_s^\mu$  due to the fact that the initial proton  $p_i$  is off-shell and outgoing  
589 “spectator” proton  $p_s$  is on-shell in the reaction Eq. (1.5). However the relation  $\vec{p}_i = \vec{p}_s = -\vec{n}$   
590 is not influence by the off-shell effects in the quasi-free process. So we can reconstruct the  
591 off-shell neutron four momentum by  $n^\mu = (-\vec{p}_s, M_n)$  and  $E_n = \sqrt{(-\vec{p}_s)^2 + (M_n)^2}$ . So it is  
592 better to choose  $W_f$ , which is well defined and measured directly from  $p$  and  $\pi^-$ , rather than  
593  $W_i$ , to present the final cross section. In the “spectator” situation, in order to conserve energy  
594 and momentum in the scattering process, we have set

$$M_n = m_n - 2\frac{k_n^2}{2m_n} - 2\text{MeV}, \quad (1.15)$$

595 reestablishing  $W_i = W_f$ . This can be seen in Fig. 1.3, where  $W_f$  is calculated by Eq. (1.7)  
596 and radiative corrected  $W_i$  is calculated by setting  $E_n$  with Eq. (1.15), which are presented by  
597 the black and red lines separately, and their peaks match each other. For other possible  $M_n$   
598 settings, we get shifted or smeared  $W_i$  distributions (radiative corrected) compared to  $W_f$ . The  
599 boost vector (from the lab frame to the CM frame) is calculated using the different  $W_i$  and  $W_f$ ,  
600 then the influence of those different boosts on the final cross section can be quantified. The  
601 result shows that these effects on the final cross sections are marginal and are accounted for as  
602 a source of systematic uncertainties described in Chapter 5.

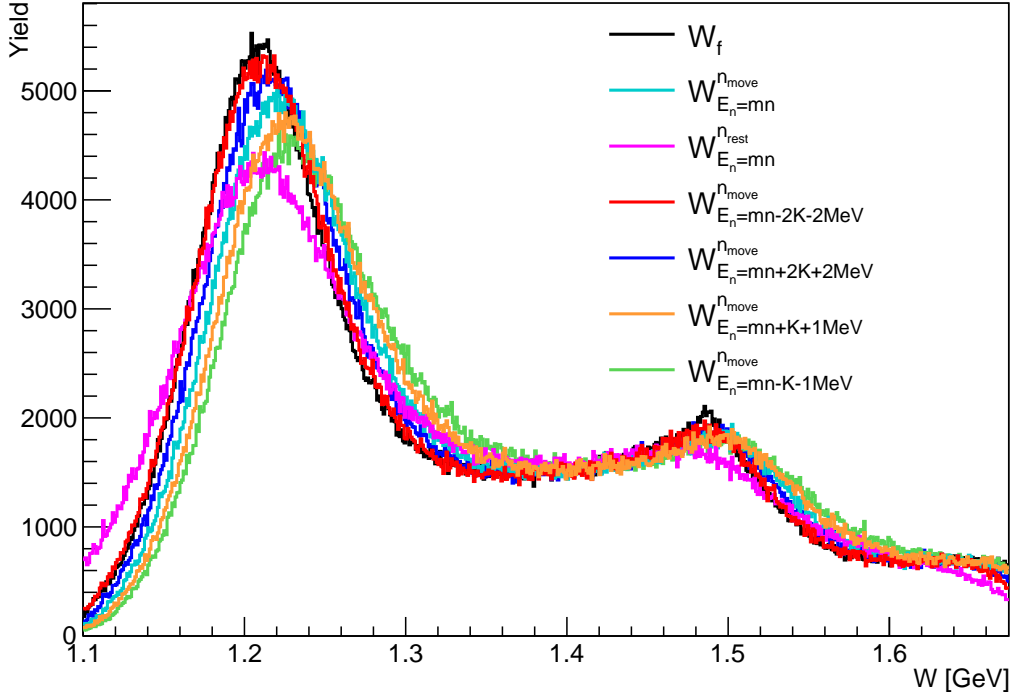


Figure 1.3: (Color online) The comparison of  $W$  distributions. Black line presents  $W_f$ , blue line shows  $W_i$  calculated by setting  $n^\mu = (-\vec{p}_s, E_n)$  ( $E_n$  with Eq. (1.15)). The other colors present the  $W_i$  distribution by setting  $n_\mu$  to  $(-\vec{p}_s, m_n)$  (cyan),  $(0, m_n)$  (magenta),  $(-\vec{p}_s, m_n + 2\frac{k_n^2}{2m_n} + 2\text{MeV})$  (blue),  $(-\vec{p}_s, m_n + \frac{k_n^2}{2m_n} + 1\text{MeV})$  (orange), and  $(-\vec{p}_s, m_n - \frac{k_n^2}{2m_n} - 1\text{MeV})$  (green).

## 1.5 The Final State Interaction (FSI)

The reaction process of interest here Eq. (1.5) is also depicted in Fig. 1.4 (a). For small missing momenta,  $|\vec{p}_s| < 200$  MeV, the quasi-free process is dominant (see Chapter 2). However in this process, it is possible to have final state interactions, such as  $pp$  re-scattering and  $p\pi$  re-scattering, also shown in Fig. 1.4 (b) and (c), respectively. It corresponds to the situation in which the outgoing proton or  $\pi^-$  interacts with the spectator proton ( $P_s$ ). Thus, the four momenta of the final state particles are changed due to these final state interactions. After isolating the quasi-free process, the kinematically defined FSI contribution factor  $R_{FSI}$  will be extracted from the data itself, and the details will be discussed in the Chapter 5. It is also possible to have other kinds of FSI in the pion production process off the deuteron, such as  $\pi^0 + n_s \rightarrow \pi^- + p$  and  $\pi^- + p_s \rightarrow \pi^0 + n$ , which can increase or decrease the final state  $\pi^-p$  production. If we want to quantify contribution of this kind of FSI from the data itself, a combined analysis of pion electroproduction off the free proton, the bound proton, and the bound neutron in the “e1e” run is needed. In this analysis note, this kind of final state interactions are not quantified.

## 1.6 Boosting of the Kinematic Variables

In order to get the correct variables to present the final cross sections of  $\pi^-$  electroproduction off the neutron in the deuterium target, we boost first all particles’ four momenta from the lab frame (deuterium at rest) into the neutron at rest frame with the boost vector  $\vec{\beta}_1 = -\vec{n}/E_n$ , where  $\vec{n}$  and  $E_n$  are calculated from  $n^\mu$  (Eq. (1.12)). Then the invariant mass  $W_f$  and the

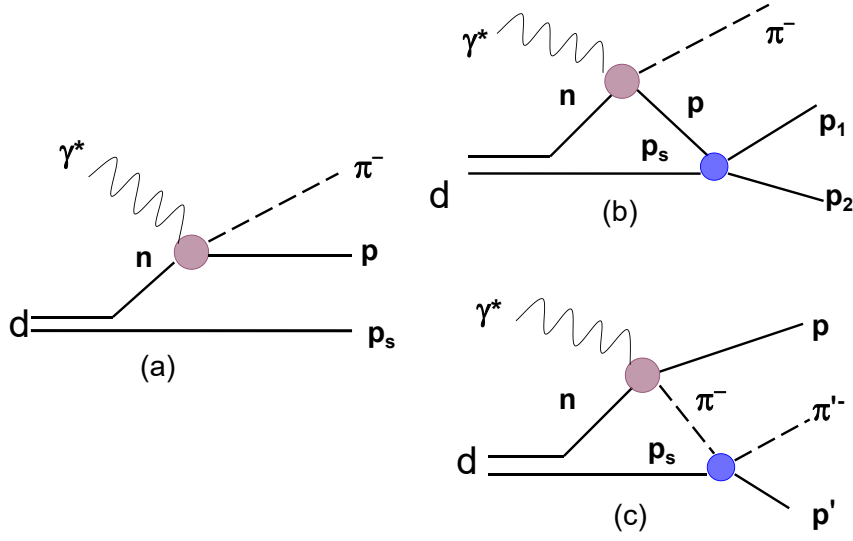


Figure 1.4: Kinematic sketch as in the text for the three leading terms in  $\gamma^* + D \rightarrow \pi^- + p + p$  process (a) quasi-free, (b) pp re-scattering, and (c)  $p\pi^-$  re-scattering. Diagrams (b) and (c) are two main sources of kinematical final state interactions.

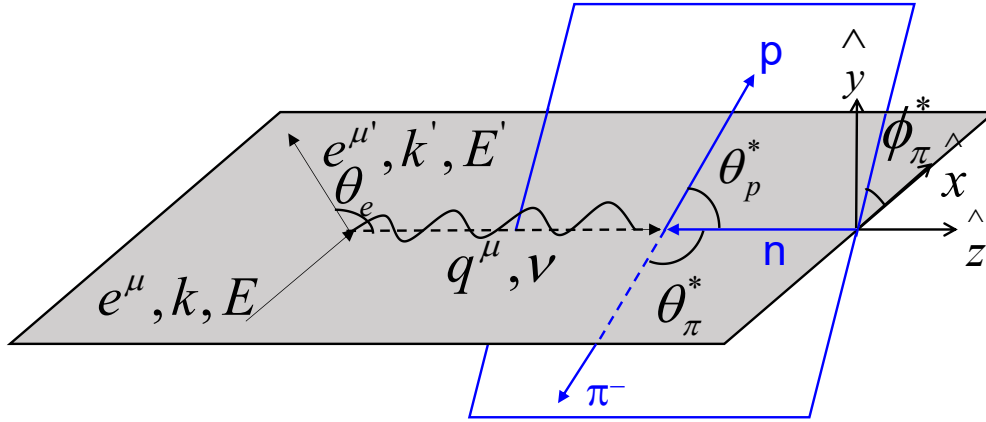


Figure 1.5: Kinematics of  $\pi^-$  electroproduction off a moving neutron. The leptonic neutron rest frame plane is formed by  $e^\mu$  and  $e^{\mu'}$ , where  $k$ ,  $E$ ,  $k'$ , and  $E'$  are corresponding momentum and energy of the incoming and outgoing electrons.  $q^\mu$  is the virtual photon four momentum and  $\nu$  is the transferred energy. The hadronic CM frame plane is determined by final particles  $p$  and  $\pi$ , here  $\theta_p^*$  and  $\theta_\pi^*$  are their polar angles and  $\phi_\pi^*$  the azimuthal angle of  $\pi^-$ .

623 momentum transfer  $Q^2$  are calculated by the Eq. (1.7) and (1.8) in this frame. In addition, by  
 624 setting the coordinates in this frame,  $\hat{z}_{nrest}$  parallel to the virtual photon direction and  $\hat{y}_{nrest}$   
 625 perpendicular to the electron scattering plane, we ensure that  $\hat{x}_{nrest}$  is staying in the electron  
 626 scattering plane and is set to be  $\hat{x}$  direction in the final coordinate system. Secondly, we directly  
 627 boost all particles' four momenta from the lab frame into the CM frame with the boost vector

628  $\vec{\beta}_2 = -(\vec{p} + \vec{\pi}^-)/(E_p + E_{\pi^-})$ , then set the  $\hat{z}_{CM}$  parallel to the virtual photon direction in this  
629 frame. Since the  $\hat{z}_{nrest}$  is not as well defined due to off-shell effects, it is better to set the final  
630  $\hat{z}$  parallel to  $\hat{z}_{CM}$ . The  $X$  and  $Y$  projections of the  $\hat{z}_{nrest}$  in the CM frame are plotted against  
631 each other for final-state-interaction dominated events and quasi-free events, which are shown  
632 in Fig. 1.7 and 1.6, respectively. It turns out that the spread of these distributions around  
633 zero correspond to the angle difference between  $\hat{z}_{nrest}$  and  $\hat{z}_{CM}$ , which are  $5.4^\circ$  for final-state-  
634 interaction dominated events in the exclusive process and  $< 1^\circ$  for quasi-free events. Although  
635 the final-state-interaction dominated events show significant spread, this coordinate choice is  
636 the best way to present the quasi-free results for the bound neutron data. The  $\cos\theta_{\pi^-}^*$  and  $\phi_{\pi^-}^*$   
637 are calculated ultimately in the CM frame. In summary, the coordinates are set by:

$$\hat{z} = \frac{\vec{q}^*}{|\vec{q}^*|}, \quad \text{with respect to the CM frame} \quad (1.16)$$

$\hat{x}$  is in the  $\vec{k}, \vec{k}'$  plane of the n rest frame and perpendicular to  $\hat{z}$ , and  
 $\hat{y} = \hat{z} \times \hat{x}$ ,

which are shown in Fig. 1.5.

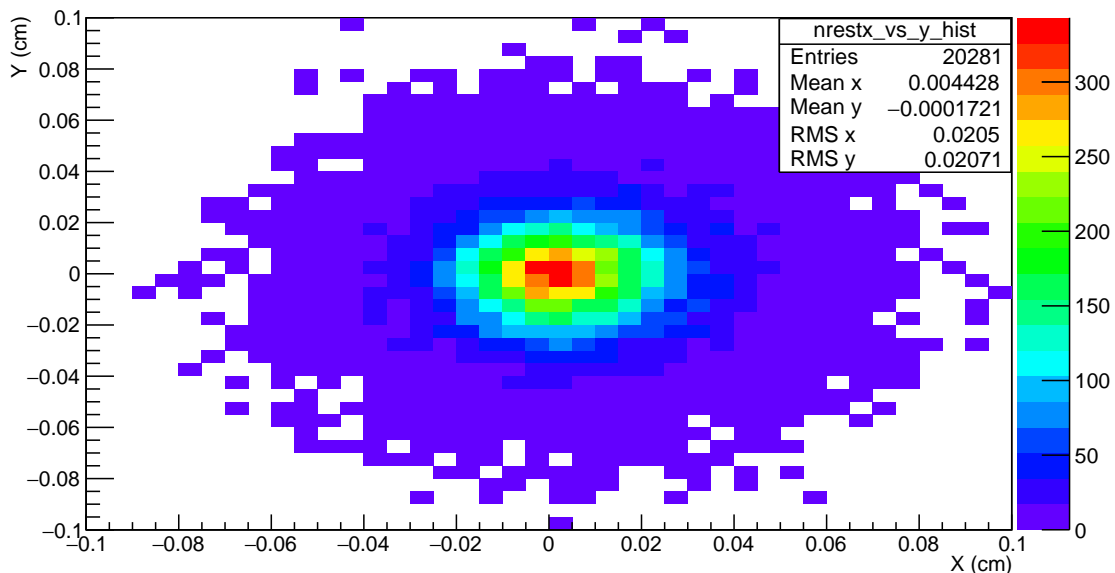


Figure 1.6: The  $X$  and  $Y$  projections of the  $\hat{z}_{nrest}$  in the CM frame are plotted against each other for exclusive quasi-free events.

638

## 639 1.7 Formalism

640 The cross section for the exclusive  $\gamma^*n \rightarrow p\pi^-$  reaction with unpolarized electron beam and  
641 unpolarized free neutron target is given by

$$\frac{d^5\sigma}{dE' d\Omega_{\pi^-}^* d\Omega_{e'}} = \Gamma_v(E', \Omega_{e'}) \frac{d\sigma}{d\Omega_{\pi^-}^*}. \quad (1.17)$$

642 Where the virtual photon flux that depends on the matrix elements of the leptonic interaction  
643 is calculated by

$$\Gamma_v(E', \Omega_{e'}) = \frac{\alpha}{2\pi^2} \frac{E'}{E} \frac{K_\gamma}{(1-\epsilon)Q^2}. \quad (1.18)$$



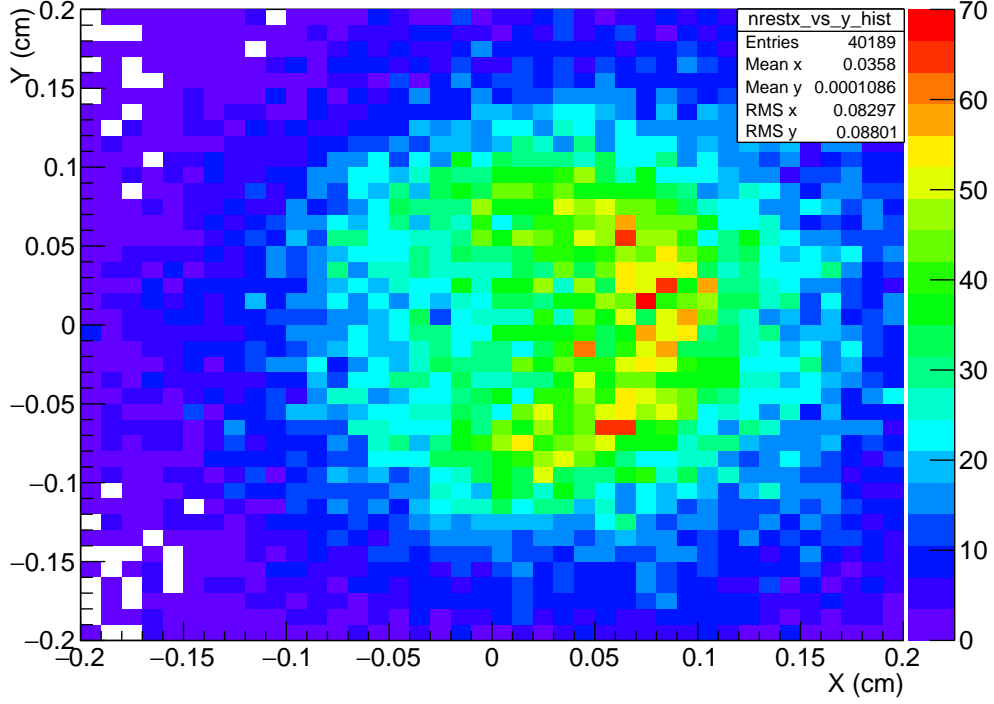


Figure 1.7: The  $X$  and  $Y$  projections of the  $\hat{z}_{nrest}$  in the CM frame are plotted against each other for final-state-interaction dominated events.

644 Here  $\alpha = 1/137$  represents the electromagnetic coupling constant,  $\epsilon$  corresponds to the trans-  
 645 verse polarization of the virtual photon,

$$\epsilon = \left( 1 + 2 \left( \frac{|\vec{q}|^2}{Q^2} \right) \tan^2 \frac{\theta_e}{2} \right)^{-1}, \quad (1.19)$$

646 and the photon equivalent energy is calculated by

$$K_\gamma = \frac{W^2 - M_n^2}{2M_n}. \quad (1.20)$$

647 In these equations “\*” denotes that the variable is calculated in the CM frame, all others are  
 648 in the neutron at rest frame. Moreover,  $E$  is the initial coming electron energy,  $E'$  and  $\theta_e$  are  
 649 outgoing electron energy and scattering angle.  $\Omega_{e'}$  and  $\Omega_{\pi^-}$  correspond to the solid angles of  
 650 outgoing electron and  $\pi^-$ . If we want to represent the cross sections in  $W$  and  $Q^2$  bins, the  
 651 Jacobian factor needs to be applied for the variables transformation  $(E', \Omega_{e'}) \rightarrow (W, Q^2)$

$$\frac{d^4\sigma}{dW dQ^2 d\Omega_{\pi^-}^*} = \frac{1}{J(W, Q^2)} \frac{d^4\sigma}{dE' d\Omega_{\pi^-}^* d\Omega_{e'}} = \frac{\Gamma_v(E_{e'}, \Omega_{e'})}{J(W, Q^2)} \frac{d\sigma}{d\Omega_{\pi^-}^*} = \Gamma_v(W, Q^2) \frac{d\sigma}{d\Omega_{\pi^-}^*}. \quad (1.21)$$

652 The invariant mass  $W$  and virtual photon momentum transferred  $Q^2$  are calculated by the  
 653 following equations:

$$W = \sqrt{Q^2 + M_n^2 + 2M_n(E - E')}, \quad (1.22)$$

$$Q^2 \simeq 4EE' \sin^2 \frac{\theta_e}{2} = 2EE' (1 - \cos \theta_e). \quad (1.23)$$

655 The Jacobian factor is defined by

$$\begin{aligned}
J(W, Q^2) &= \left| \frac{\partial W}{\partial E'} \frac{\partial W}{\partial \Omega_{e'}} \right| = \frac{1}{2\pi} \left| \frac{\partial W}{\partial E'} \frac{\partial W}{\partial \cos \theta_{e'}} \right| \\
&= \frac{1}{2\pi} \left| \frac{-E(1-\cos \theta_{e'}) - M_n}{W} \frac{EE'}{W} \right| \\
&= \frac{2E^2 E' (1 - \cos \theta_{e'}) + 2M_n EE'}{W} - \frac{2E^2 E' (1 - \cos \theta_{e'})}{W} \\
&= \frac{M_n EE'}{\pi W}
\end{aligned} \tag{1.24}$$

656 From Eq. (1.21) and (1.24) we can calculate the virtual photon flux, which depends on  
657  $(W, Q^2)$  by

$$\begin{aligned}
\Gamma_v(W, Q^2) &= \frac{\Gamma_v(E', \Omega_{e'})}{J(W, Q^2)} = \frac{\pi W}{EE' M_n} \left( \frac{\alpha}{2\pi^2} \frac{E'}{E} \frac{K_\gamma}{(1-\epsilon) Q^2} \right) \\
&= \frac{\alpha}{4\pi} \frac{1}{E^2 M_n^2} \frac{W(W^2 - M_n^2)}{(1-\epsilon) Q^2}.
\end{aligned} \tag{1.25}$$

658 Since  $Q^2 = -q^\mu q_\mu = |\vec{q}|^2 - \nu^2$  and  $Q^2 \simeq 4EE' \sin^2 \frac{\theta_e}{2}$ ,  $\epsilon$  also can be simplified as

$$\epsilon = \left( 1 + 2 \left( 1 + \frac{\nu^2}{Q^2} \right) \tan^2 \frac{\theta_e}{2} \right)^{-1} \simeq \left( 1 + 2 \frac{Q^2 + \nu^2}{4EE' - Q^2} \right)^{-1} \tag{1.26}$$

659 The hadronic differential cross section is calculated from the four fold differential cross section  
660 (Eq.(1.27)), which is extracted finally from the experimental yield.

$$\frac{d^4 \sigma}{dW dQ^2 d\Omega_{\pi^-}^*} = \Gamma_v(W, Q^2) \frac{d\sigma}{d\Omega_{\pi^-}^*}. \tag{1.27}$$

$$\frac{d\sigma}{d\Omega_{\pi^-}^*} = \frac{1}{\Gamma_v(W, Q^2)} \frac{d^4 \sigma}{dW dQ^2 d\Omega_{\pi^-}^*}. \tag{1.28}$$

661 For the exclusive  $\gamma^* n(p) \rightarrow p \pi^-(p)$  reaction, we use the same equations to extract the  
662 hadronic differential cross section by ignoring the off-shell effects when calculating the virtual  
663 photon flux. From now on,  $W$  represents  $W_f$ , along with  $Q^2$  that are calculated in the neutron  
664 rest frame.  $\cos \theta_{\pi^-}^*$  and  $\phi_{\pi^-}^*$  are calculated from the CM frame of  $p$  and  $\pi^-$  system.

# Chapter 2

## Data Analysis

In this analysis, the deuterium target data from the “e1e” run is analyzed. The data processing, particle identification, corrections, fiducial cuts, and event selection will be addressed in the following sections.

### 2.1 Data Processing

The data taken in CLAS is grouped into runs. Here a run is related to a continuous data taking period. An experiment operator usually ends a run once it reaches a certain size of the data or when something goes wrong during the data taking process. Furthermore, a run data set is split further into reasonable pieces (called run files) by DAQ automatically (typically 2GB for the “e1e” run), which is due to the filesystem limitation. The “e1e” run period of the liquid deuterium ( $LD_2$ ) target is subdivided into 94 run and 1985 run files related to the electron beam condition, from which we want to carry out the analysis. Besides these, there are 4 empty target run files, which are taking data without  $LD_2$ . The information of the empty target runs is needed to carry out the background subtraction process, details of which are introduced in the Chapter 4.

The raw data files are “cooked” with the CLAS reconstruction and analysis program (RECSIS) to extract information about the detector response and convert the raw detector data into momenta, vertices, times, and particle information, i.e. charge and particle ID. In more detail, the “RECSIS” program is in charge of the following tasks:

- geometrical matching of each DC track to the corresponding hits in the other detectors (i.e. CC, SC, and EC),
- identifying the trigger particle (i.e. electron),
- calculating time information (i.e. trigger time, particle times),
- identifying other particles corresponding to their tracks (i.e.  $p$ ,  $\pi^-$ ), and
- building an event and writing it to the output file (BOS files).

Basically, we choose and optimize which banks need to be saved in the BOS files to record outgoing particle information by setting the “tcl” file [5]. Here, in this analysis note, we use the EVNT, DCPB, CCPB, SCPB, and ECPB BOS bank information [6] to carry out the data analysis. Usually, the processed data is converted in different formats including these BOS banks. In this analysis, the output file with “ntuple” format is used because of its ROOT friendly structure.

## 697 2.2 Quality Check

698 In order to reduce the influence of unstable run conditions (due to beam, target, detector, etc.),  
 699 it is better to check the run quality first. For the  $LD_2$  target run period, we have 1985 run files  
 700 that need to be checked. The live time is the total time when the DAQ is actually recording  
 701 events. We plot the ratio of exclusive events to the live-time corrected charge (measured in the  
 702 Faraday cup) in Fig. 2.1a, then fit it by the Gaussian function, which is shown in red, to get  
 703 the corresponding fit parameters  $\mu$  and  $\sigma$ . Then the  $\mu - 3\sigma < ratio < \mu + 3\sigma$  cuts shown as  
 704 two blue lines in Fig. 2.1a are applied to all files, and only the selected “golden” files between  
 705 the two blue lines in Fig. 2.1b are used for the following data analysis, which are also listed in  
 706 the reference [7].

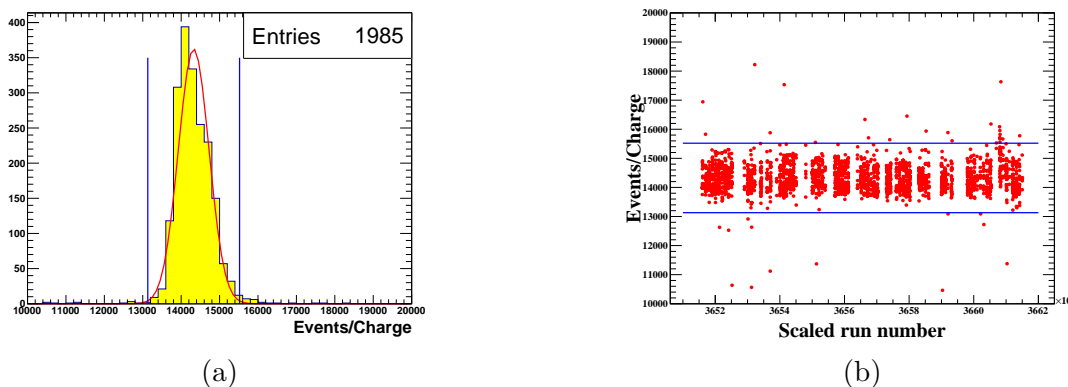


Figure 2.1: (a) shows the exclusive number of events normalized to the live-time corrected charge for each file, and (b) shows it versus the scaled run number. Here the red curve shows Gaussian fit function, and two blue lines show the  $3\sigma$  upper/lower cut limits.

## 707 2.3 Electron Identification

708 The EVNT bank IDs (electron ID: 11, proton ID: 2212, and  $\pi^-$  ID: -211), which mark particles  
 709 based on their basic information and some initial cuts performed during the “cooking” process,  
 710 are on the cross section level not reliable enough to be used for particle identification. Thus  
 711 we need to build effective cuts, which can be applied on candidate particles to finalize their  
 712 particle identity. Here the purpose of cutting on electron candidates is to reduce electronic  
 713 noise, accidental events, and the negative pion contamination as much as possible without  
 714 losing good electron candidates. We define an electron candidate by satisfying the following  
 715 requirements

- 716 • First negatively charged track: electron detection triggers the DAQ system to record data  
 717 from all the sub-detectors of CLAS.
- 718 •  $(DC_{stat}, EC_{stat}, SC_{stat}, \text{ and } CC_{stat})$  bits  $> 0$  [6]: electron should geometrically match each  
 719 DC track to the corresponding hits in the other detectors.
- 720 •  $stat$  bit  $> 0$  [6]: the trajectory of a electron passes the time-based tracking.

721 The purpose and details of each electron identification cut will be discussed below.

### 2.3.1 Minimum Momentum Cut

The forward EC is one of the main trigger components in electroproduction experiments with CLAS. A threshold can be set to require a minimum energy for the trigger. A study of the inclusive cross section at various beam energies with CLAS [19] results in a low momentum cut  $p_{min}$  depending on the calorimeter low total threshold (in millivolt) of the trigger discriminator. In that study the safe electron  $p_{min}$  is obtained from

$$p_{min}(\text{in MeV}) = 214 + 2.47 \times EC_{threshold}(\text{in mV}), \quad (2.1)$$

where, for the “e1e” run, the  $EC_{threshold} = 100$  mV and  $p_{min} = 461$  MeV. So  $p_{electron} > 461$  MeV cut is applied on electron candidates at first.

### 2.3.2 $\theta_{CC}$ versus Segment Cut

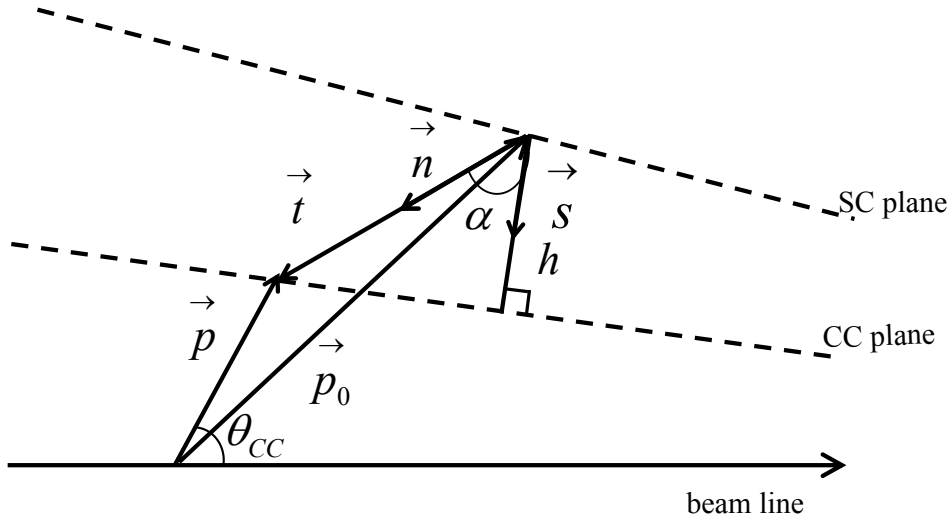


Figure 2.2: Schematic diagram for the  $\theta_{CC}$  reconstruction. Here  $\vec{p}_0$  is the intersection of the track with the SC plane (read from DCPB bank  $(x_{sc}, y_{sc}, z_{sc})$ ),  $\vec{n}$  is the normalized direction of the track from the SC plane (read from DCPB bank  $(cx_{sc}, cy_{sc}, cz_{sc})$ ), and  $\vec{p}$  is the unbent track to the CC plane.

The requirement of the negative DC track with the corresponding signal in the CC is not good enough to select real electron candidates. Therefore, the  $\theta_{CC}$  cut is applied to help. Since the torus magnetic field bends the electrons toward the beam line and CC segments are placed radially according to the CLAS polar angle, it is convenient to use  $\theta_{CC}$  (see Fig. 2.2) rather than the  $\theta$  angle at the vertex. There should be an one to one correspondence between  $\theta_{CC}$  and CC segment number for real electron tracks, while background and accidental noise should not show such correlation. Basically, we can calculate  $\theta_{CC}$  in Fig. 2.2 from

$$\theta_{CC} = \arccos\left(\frac{|\vec{p}_z|}{|\vec{p}|}\right). \quad (2.2)$$

Here the CC plane equation is  $Ax + By + Cz + D = 0$ , with  $A = -0.000784$ ,  $B = 0$ ,  $C = -0.00168$ ,  $D = 1$ , and  $\vec{S} = (A, B, C)$  (see CLAS note [30]). In Fig. 2.2, we can calculate  $\vec{P} = \vec{P}_0 + t\vec{n}$ , where  $t = \frac{h}{\cos \alpha}$ , and  $\cos \alpha = \frac{(\vec{n} \cdot \vec{S})}{|\vec{S}|}$ . Then the  $\theta_{CC}$  distribution of each CC segment is fit by a Gaussian distribution (see Fig. 2.3a), and the corresponding fitting parameters  $\mu$  and

742  $\sigma$  are obtained. Then  $\mu$ ,  $\mu + 3\sigma$ , and  $\mu - 4\sigma$  are plotted in Fig. 2.3b as black stars, which are  
 743 fit by a second degree polynomial functions. The cuts:

$$\theta_{CC\mu} - 4\sigma < \theta_{CC} < \theta_{CC\mu} + 3\sigma, \quad (2.3)$$

744 accounting for the distribution not being completely symmetric around the mean, are applied  
 to both experimental data and simulation.

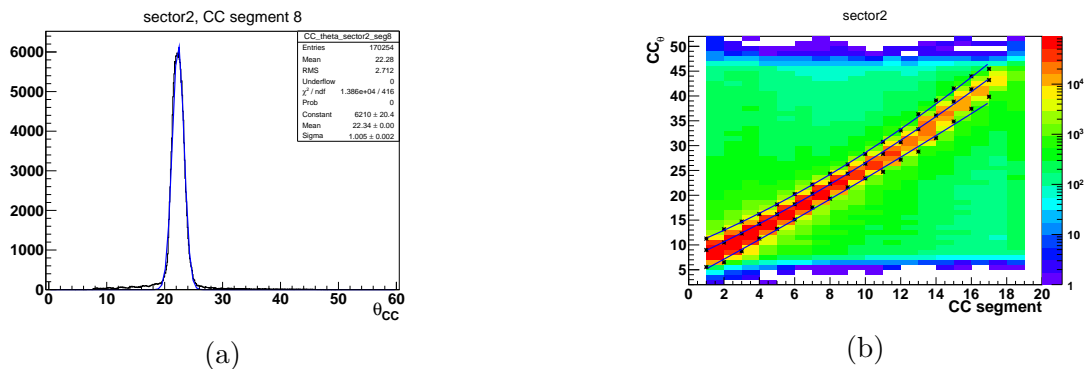


Figure 2.3: (a) Example  $\theta_{CC}$  distribution of the 8th CC segment in sector 2, where the blue curve shows the Gaussian fit function, and the fitting parameters  $\mu$  and  $\sigma$  are shown in the statistic box. (b) The  $\theta_{CC}$  versus segment number in sector 2 is plotted, where  $\mu$ ,  $\mu + 3\sigma$ , and  $\mu - 4\sigma$  are marked as black stars and fit by a second degree polynomial functions, which are shown as blue curves.

745

### 746 2.3.3 The Cut on Number of Photo-electrons

747 The Cherenkov detector is designed to separate negative pions from electrons. In the CC, the  
 748 momentum threshold for electrons and pions are  $\sim 9$  MeV/c and  $\sim 2.5$  GeV/c, respectively.  
 749 The CC's ADC signal is converted to a number of photo-electrons ( $N_{phe}$ ) and multiplied by  
 750 10 ( $N_{phe} \times 10$  caused by the reconstruction code). In order to better eliminate negative pions  
 751 and background noise, a  $N_{phe} \times 10 > 30$  cut is applied on electron candidates. For example,  
 752 in Fig. 2.4, the green area under the Poisson fit function (from Eq. (2.5) marked as red curve)  
 753 corresponds to safe electron candidates, and the small peak at  $N_{phe} \times 10 \sim 20$  contains not only  
 754 background and negative pions, but also good electron candidates with low CC efficiency hits.  
 755 With the extrapolation of the fitted Poisson function we can quantify those lost candidates by  
 756 the calculated red area, which can be recovered by applying the correction factor ( $N_{phe_{correct}}$ )  
 757 as a weight for each accepted event. The weight factor  $N_{phe_{correct}}$  is calculated by

$$N_{phe_{correct}} = \frac{\text{green area}}{\text{red area} + \text{green area}} = \frac{\int_0^{450} f(x) dx}{\int_0^{30} f(x) dx + \int_0^{450} f(x) dx}, \quad (2.4)$$

758 where  $f(x)$  is the fitted Poisson function (see red curves Fig. 2.4) defined as

$$f(x) = p_0 \frac{p_1^{\left(\frac{x}{p_2}\right)} e^{-p_1}}{\Gamma\left(\frac{x}{p_2} + 1\right)}, \quad (2.5)$$

759 where  $p_0$ ,  $p_1$ , and  $p_2$  are free fit parameters. Then the green and red area are calculated by  
 760 integrating the fitted Poisson function (Eq. 2.4). The correction factor is calculated from the  
 761  $N_{phe} \times 10$  distribution of left/right PMT in each CC segment per sector. After applying the  
 762  $N_{phe} \times 10 > 30$  cut, the weight of events is set to be  $N_{phe_{correct}}$  rather than 1, and the final  
 763 cross sections are calculated from those weighted events.

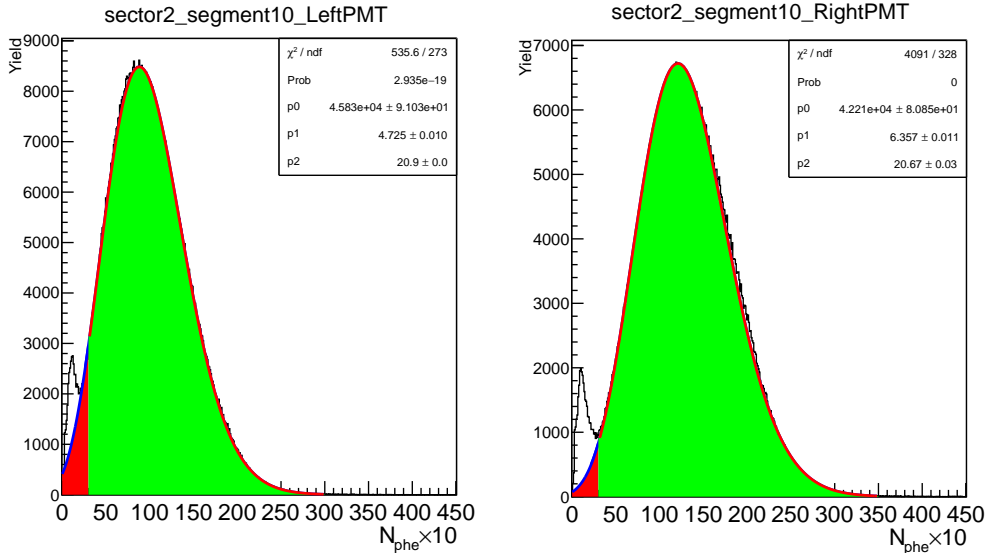


Figure 2.4: Example  $N_{phe} \times 10$  distributions of left and right PMTs in the CC 10th segment of sector 2 plotted separately and fit by the Poisson function Eq. (2.5) marked as red curve.

### 2.3.4 Sampling Fraction Cut

764

765 When high momentum pions exceed the Cherenkov radiation threshold, the separation of elec-  
766 trons and negative pions becomes impossible by the CC. Thus the EC is used for separating  
767 the electrons from the fast moving pions. Pions and electrons have different mechanisms of  
768 primary energy deposition in the EC. Electrons deposit their energy mainly by bremsstrahlung  
769 and pair production and subsequent showering reactions. This energy deposition mechanism is  
770 momentum dependent. Meanwhile, pions lose most of their energy due to the ionization, which  
771 is here practically independent of their momentum. Actually, the incident charged particles  
772 can interact with the lead atoms of the EC detector when they are moving through, so the EC  
773 can only measure a fraction of their energy. The fraction is called a sample fraction (SF)  $\frac{E_{total}}{p}$ ,  
774 which is the ratio of the total energy deposited in the EC to the momentum. For  $e^-/\pi^-$  separa-  
775 tion, all electron candidates are divided into eight momentum ( $p$ ) bins, and in each of them,  
776 the  $\frac{E_{total}}{p}$  is plotted and fit with Gaussian function (see Fig. 2.5a). Then the corresponding fit  
777 parameters  $\mu$ ,  $\mu + 3\sigma$ , and  $\mu - 3\sigma$  are plotted on Fig. 2.5b as black stars, which are fit by a  
778 third degree polynomial functions. The cuts,

$$\left(\frac{E_{total}}{p_e}\right)_\mu - 3\sigma < \frac{E_{total}}{p_e} < \left(\frac{E_{total}}{p_e}\right)_\mu + 3\sigma, \quad (2.6)$$

779 are applied to the data. An example  $E_{total}/p$  distribution of the survival data is shown in  
780 Fig. 2.5c. Since the sampling-fraction distributions of simulated reconstructed events are shifted  
781 compared to the data, modified cuts are built by the same method as for the data and applied  
782 to the simulated reconstructed events. An example distribution from the simulated events that  
783 survive the cut is given in Fig. 2.5d.

## 2.4 Pion Identification

784

785 Similar to the electrons, pions are affected by the geometrical and efficiency effects of different  
786 sub-detectors of CLAS. A pion candidate should satisfy initial requirements as follow:

- 787 • coincidence with one and only one good electron,

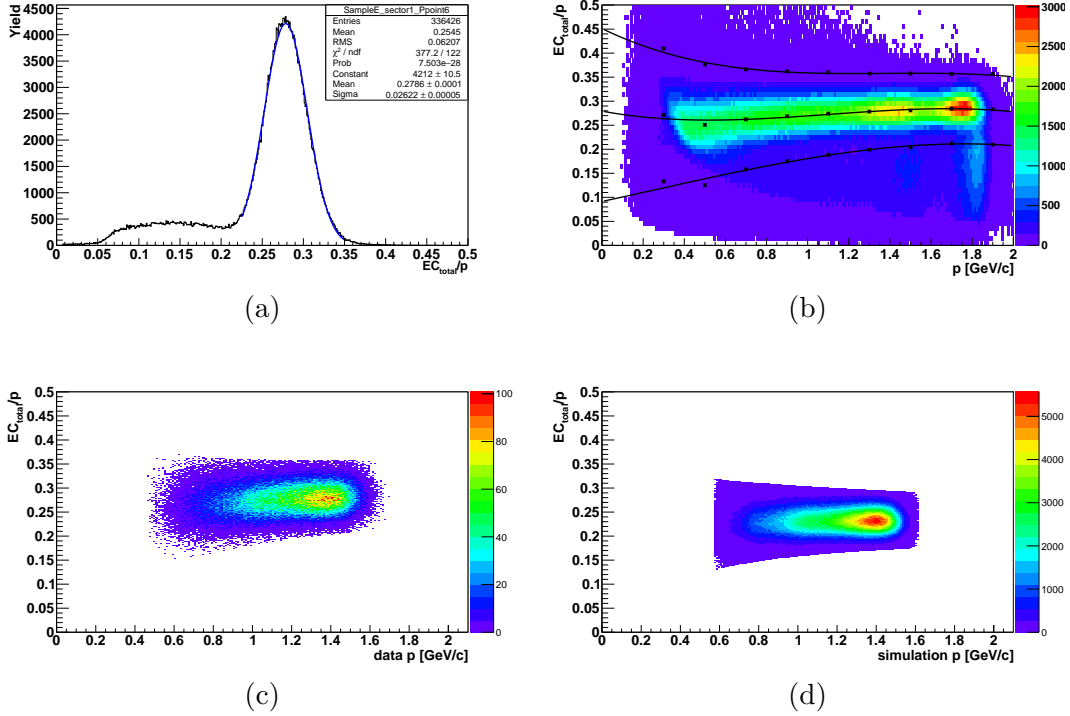


Figure 2.5: (a) An example of an  $E_{total}/p$  distribution is fit with a Gaussian function (blue line). (b)  $E_{total}/p$  versus  $p$  distribution, where the black lines show the upper/lower  $E_{total}/p$  cut limits. (c)  $E_{total}/p$  versus  $p$  distribution after all experimental data event selections. (d)  $E_{total}/p$  versus  $p$  distribution after all simulation event selections.

- 788 • not the first negatively charged track,
- 789 •  $(DC_{stat}, SC_{stat})$  bits  $> 0$  [6]: the pion candidates must have signal from DC and SC, and
- 790 •  $stat$  bit  $> 0$  [6]: like for the electron, the trajectory of a pion should pass the time-based
- 791 tracking.

## 792 2.4.1 Pion $\Delta T$ Cut

793 The time difference  $\Delta T_i$  between the time calculated by the speed and track length of the  
 794 pion candidates and the actual measured SC time  $t_i^{sc}$  should peak at zero for pions. This time  
 795 difference is given by

$$\Delta T_i = \frac{l_i^{sc}}{\beta_i c} - t_i^{sc} + t_0 \sim 0, \quad (2.7)$$

796 where  $\beta_i = \frac{v_i}{c}$  is the speed of the pion candidate calculated from the momentum and the  
 797 assumed mass  $m_i$  of the pion by

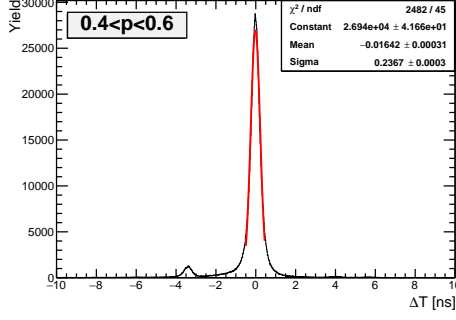
$$\beta_i = \sqrt{\frac{p_i^2}{m_i^2 c^2 + p_i^2}}, \quad (2.8)$$

798 and  $t_0$  is the start time of each reconstructed event

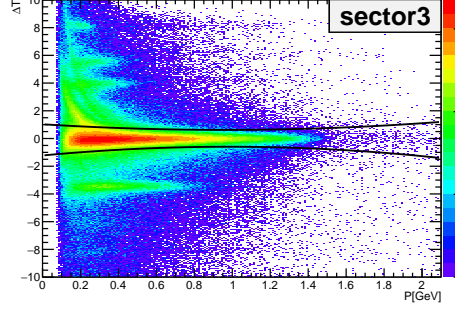
$$t_0 = t_e^{sc} - \frac{l_e^{sc}}{c}. \quad (2.9)$$

799 Here  $t_e^{sc}$  is the electron time measured from SC,  $l_e^{sc}$  is the path length of the electron track from  
 800 the vertex to the SC hit, and  $c$  is the speed of light. Then  $t_0$  is used as the reference time for  
 801 all remaining tracks in that event.





(a)



(b)

Figure 2.6: (a) Pion  $\Delta T$  distribution with fitted Gaussian function (red curve) at  $0.4 \text{ GeV}/c < p_\pi < 0.6 \text{ GeV}/c$  for sector 3. (b) Pion  $\Delta T$  versus  $p_\pi$  distribution with upper/lower  $\Delta T$  cut limits for sector 3.

802 The calculated  $\Delta T_i$  for each pion candidate is plotted in different momentum bins for each  
 803 sector, as seen in the example in Fig. 2.6a for the  $0.4 \text{ GeV}/c < p_\pi < 0.6 \text{ GeV}/c$  bin in sector 3,  
 804 and then fit by a Gaussian function to get the parameters  $\mu$  and  $\sigma$  of the peak. After applying  
 805 the same method for all covered momentum bins, we get two fitted polynomial curves for  $\mu - 3\sigma$   
 806 and  $\mu + 3\sigma$ , which are shown in Fig. 2.6b as an example. Next the cuts,

$$(\Delta T_{\pi^-})_\mu - 3\sigma < \Delta T_{\pi^-} < (\Delta T_{\pi^-})_\mu + 3\sigma, \quad (2.10)$$

807 will be applied on the initial pion candidates for each detector sector individually.

## 808 2.5 Proton Identification

809 Similar to the pions, a proton candidate should satisfy initial requirements as follows:

- 810 • coincidence with one and only one good electron,
- 811 • not the first positively charged track,
- 812 •  $(DC_{stat}, SC_{stat}) \text{ bits} > 0$  [6]: the proton candidates must have signals from both the DC and  
 813 the SC, and
- 814 •  $stat \text{ bit} > 0$  [6]: like the electron, the trajectory of a proton should pass the time-based  
 815 tracking.

## 2.5.1 Proton $\Delta T$ Cut

For the proton  $\Delta T$  calculation, the Eq. (2.7) and (2.8) are used by substituting  $i$  for proton candidates. Then, in a similar way as for pions, proton  $\Delta T$  upper/lower cut limits are carried out from the  $\Delta T$  fit method in individual proton momentum bins by

$$(\Delta T_{proton})_{\mu} - 3\sigma < \Delta T_{proton} < (\Delta T_{proton})_{\mu} + 3\sigma, \quad (2.11)$$

and an example is shown in Fig. 2.10a and Fig. 2.10b.

## 2.6 Timing Correction

If we only apply the above  $\Delta T_{pion}$  cuts, we will lose some good pion candidates that are shown in side band peaks seen in Fig. 2.6b, due to improper time reconstruction. For example, the side bands located at -4, 4, 6 and 8 ns (Fig. 2.6b) could be attributed to the misaligned TOF paddles, that have been assigned to the wrong RF bunch. In order to include these side band events, we plot the  $\Delta T$  distribution for each counter in the SC system per sector to check the side band problem. Figure 2.7a shows an example of a side band peaking at  $-3.90$  ns and the main zero peak shifted to  $-0.05$  ns as well as the Gaussian functions fitted for both peaks to get the corresponding fitting parameters  $\mu_1$  and  $\mu_2$ . Then two shifts,

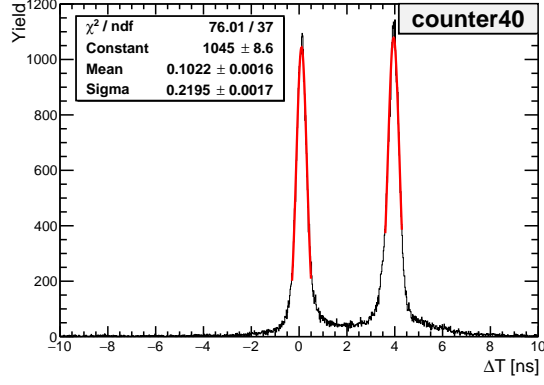
$$\Delta T = \Delta T - \mu_1(-3.90 \text{ ns}), \text{ for } \Delta T < -2 \text{ ns and} \quad (2.12)$$

$$\Delta T = \Delta T - \mu_2(-0.05 \text{ ns}), \text{ for } \Delta T > -2 \text{ ns,} \quad (2.13)$$

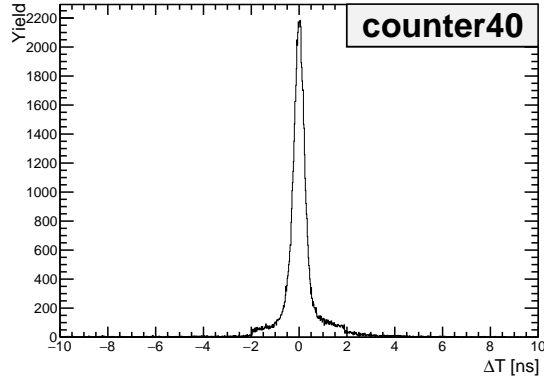
are applied to correct for the improper time reconstruction. After the correction, Fig. 2.7b shows the results. The  $\Delta T$  shift of each counter per sector are listed in Tab. A.3 and Tab. A.4 of the Appendix A. Since the last 18 scintillation paddles of the SC system are paired into 9 logical counters, it is more likely to have  $\Delta T$  side bands in the last 9 logical counters per sector, as seen in the examples of the  $\Delta T$  distribution without and with  $\Delta T$  shifts for counters from 40 to 48 in sector 3 in Fig. 2.8 and Fig. 2.9 individually. Since improper time reconstruction is independent of particle type,  $\Delta T$  shift correction parameters for protons are the same as pions.

The example plots, which show that the  $\Delta T$  shift correction parameters for pions also work well for protons, are presented in Fig. 2.11 and 2.12, which are  $\Delta T$  versus  $p_{proton}$  distributions without and with a  $\Delta T$  shift (same as pions). Since protons are bent outward from the beam line, it is easy to use proton's  $\Delta T$  distribution to test the higher counter number problem. Here, Figure 2.11 shows the counter 48 has collected unreasonable amount of events for unknown reason. We therefore removed all events from the counters 48 in all sectors for both experimental and simulation data (see Fig. 2.9 and Fig. 2.12) and from counter 17 in sector 5.

In summary, the proton  $\Delta T$  versus momentum distributions for all 6 sectors with/without  $\Delta T$  corrections are shown in Fig. 2.14 and Fig. 2.13. The pion  $\Delta T$  versus momentum distributions for all 6 sectors with/without  $\Delta T$  corrections are shown in Fig. 2.16 and Fig. 2.15. On those plots, the corresponding determined  $\Delta T$  cuts Eq. (2.10) and Eq. (2.11) are shown as black lines. Finally, those  $\Delta T$  cuts have been applied to the  $\Delta T$  corrected experimental data and also have been applied to simulation events directly without any  $\Delta T$  corrections. Even if there are some smearing effects for those  $\Delta T$  side bands (which are not obvious from the above  $\Delta T$  plots Fig. 2.14 and Fig. 2.16), the systematic uncertainties study already take care of those effects by varying the  $\Delta T$  cut with  $\Delta T_{\mu} \pm 4\sigma$  and  $\Delta T_{\mu} \pm 2\sigma$  (see section 5.52 and 5.53).



(a)



(b)

Figure 2.7: (a) The pion  $\Delta T$  distribution in counter 40 of sector 3 shows two peaks at 0.1 ns and 3.9 ns (side band peaks), which are fit by two Gaussian functions (red curves) to get the shift parameters. (b) The same  $\Delta T$  distribution with  $\Delta T$  shift correction.

## 2.7 Kinematic Corrections

855

856 Due to our incomplete knowledge of the actual CLAS detector geometry and magnetic field  
 857 distribution, which is not reproduced precisely in the simulation process, a momentum cor-  
 858 rection needs to be carried out for experimental data only. From reference [32] it is known  
 859 that momentum corrections are essential only for high-energetic particles. For the “e1e” run  
 860 (with beam energy 2.039 GeV), the expected momentum corrections for hadrons are signifi-  
 861 cantly less than for electrons and can be neglected. In addition, relativistic charged particles  
 862 other than electrons lose a measurable part of their energy by traveling through the target and  
 863 detector materials due to ionization. Hence, the reconstructed momentum is lower than the  
 864 initial momentum of these particles right at the vertex of the reaction. This effect has much  
 865 more influence on the heavy charged particles, which are the low energy protons in the  $\pi^-p$   
 866 channel, and can lead to mis-determination of kinematic quantities such as missing mass and  
 867 missing momentum. This effect is also reproduced in the simulation process also. Therefore,  
 868 the energy loss correction needs to be applied to the reconstructed proton momentum for both  
 869 experimental reconstructed data and simulation events.

### 2.7.1 Electron Momentum Correction

870

871 For the electron momentum correction, we used elastic events from the “e1e” run with a proton  
 872 target. As described in reference [32], the electron momentum correction method includes two

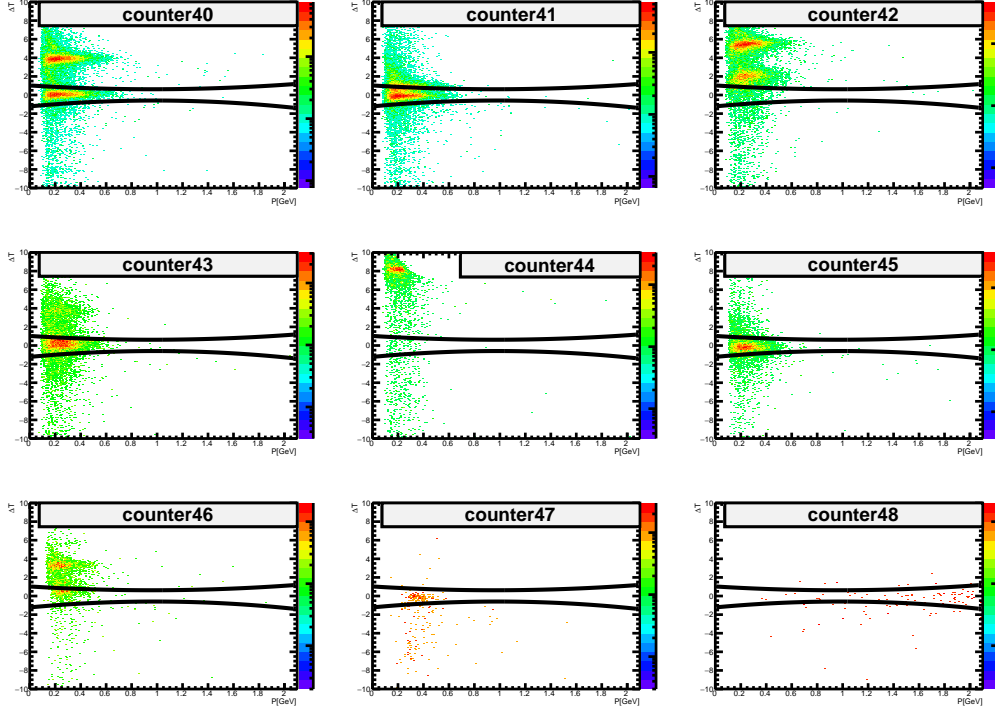


Figure 2.8: The pion  $\Delta T$  versus  $p_\pi$  distribution with upper/lower  $\Delta T$  cut limits from counter 40 to 48 of sector 3.

873 parts, electron polar angle and momentum magnitude corrections, which are both developed for  
 874 each sector individually. The angle corrections were separated from the momentum corrections  
 875 by using the constraints provided by the elastic  $ep \rightarrow ep$  scattering kinematics. The correspond-  
 876 ing correction procedures are followed by CLAS-Note 2003-012 [33] and the e1e dataset elastic  
 877 peak positions are shown for six CLAS sectors before and after electron momentum correction  
 878 in Fig. 2.12 of the CLAS-Note 2018 [22]. For e1e dataset the electron polar angle correction  
 879 functions are listed as:

$$\theta_{calculate} = \theta_e - \delta\theta_e, \quad (2.14)$$

880 here,  $\delta\theta_e$  is the difference between the calculated ( $\theta_{calculate}$ ) and measured polar angles ( $\theta_e$ ) of  
 881 electron, which was analyzed for all  $\phi_e$  and  $\theta_e$  angles.

$$\begin{aligned} \delta\theta_e &= A(\theta_e, sector) + B(\theta_e, sector) * \phi_e + C(\theta_e, sector) * \phi_e^2, \\ A(\theta_e, sector) &= \alpha_{sector}^A + \beta_{sector}^A * \theta_e + \gamma_{sector}^A * \theta_e^2 + \xi_{sector}^A * \theta_e^3, \\ B(\theta_e, sector) &= \alpha_{sector}^B + \beta_{sector}^B * \theta_e + \gamma_{sector}^B * \theta_e^2 + \xi_{sector}^B * \theta_e^3 + \eta_{sector}^B * \theta_e^4 + \kappa^B * \theta_e^5 \\ &\quad + \varepsilon^B * \theta_e^6, \end{aligned} \quad (2.15)$$

$$\begin{aligned} C(\theta_e, sector) &= \alpha_{sector}^C + \beta_{sector}^C * \theta_e + \gamma_{sector}^C * \sin\left(\frac{\xi_{sector}^C}{\theta_e} + \eta_{sector}^C\right), \\ C(\theta_e, sector2) &= \alpha_{sector}^C + \beta_{sector}^C * \theta_e + \gamma_{sector}^C * \theta_e^2 + \xi_{sector}^C * \theta_e^3 + \eta_{sector}^C * \theta_e^4 + \kappa^C * \theta_e^5, \end{aligned}$$

882 where  $\alpha_{sector}^A$ ,  $\beta_{sector}^A$ ,  $\gamma_{sector}^A$ ,  $\xi_{sector}^B$ ,  $\eta_{sector}^B$ ,  $\kappa^C$ , and  $\varepsilon^B$  are the parameters of orders term of  $\phi_e$   
 883 and  $\theta_e$  and the indices  $A(\theta_e, sector)$ ,  $B(\theta_e, sector)$ ,  $C(\theta_e, sector)$  are related to the power of  $\phi_e$ .  
 884 All parameters above are different for CLAS six sectors, which are listed in the Tab. A.8 of the  
 885 Appendix A.

886 Furthermore, the electron momentum correction functions are shown as:

$$p_{calculate} = p_e * \delta p_e, \quad (2.16)$$

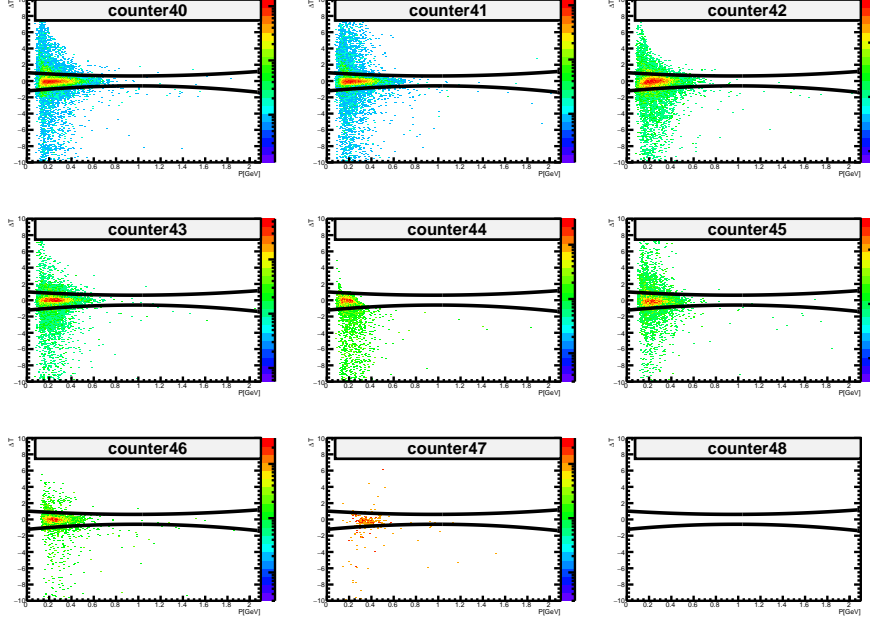


Figure 2.9: The pion  $\Delta T$  versus  $p_\pi$  distribution with upper/lower  $\Delta T$  cut limits from counter 40 to 48 of sector 3 after the  $\Delta T$  shift correction.

887 Here, the correction function  $\delta p_e$  is a scale factor, which depends on the specific sector, can be  
 888 represented as a function of  $\theta_e$  and  $\phi_e$  as follows.

$$\begin{aligned}
 \delta p_e &= A'(\theta_e, \text{sector}) + B'(\theta_e, \text{sector}) * \phi_e + C'(\theta_e, \text{sector}) * \phi_e^2 (\text{sector} 1, 2, 3, 4, \text{ and } 6), \\
 \delta p_e &= A'(\theta_e, \text{sector} 5) + B'(\theta_e, \text{sector} 5) * \phi_e + C'(\theta_e, \text{sector} 5) * \phi_e^2 \\
 &\quad + D'(\theta_e, \text{sector} 5) * \phi_e^3 + E'(\theta_e, \text{sector} 5) * \phi_e^4, \\
 A'(\theta_e, \text{sector}) &= \alpha_{\text{sector}}^{A'} + \beta_{\text{sector}}^{A'} * \theta_e + \gamma_{\text{sector}}^{A'} * \theta_e^2 + \xi_{\text{sector}}^{A'} * \theta_e^3 + \eta_{\text{sector}}^{A'} * \theta_e^4 + \kappa^{A'} * \theta_e^5, \\
 B'(\theta_e, \text{sector}) &= \alpha_{\text{sector}}^{B'} + \beta_{\text{sector}}^{B'} * \theta_e + \gamma_{\text{sector}}^{B'} * \theta_e^2 + \xi_{\text{sector}}^{B'} * \theta_e^3 + \eta_{\text{sector}}^{B'} * \theta_e^4 + \kappa^{B'} * \theta_e^5, \\
 C'(\theta_e, \text{sector}) &= \alpha_{\text{sector}}^{C'} + \beta_{\text{sector}}^{C'} * \theta_e + \gamma_{\text{sector}}^{C'} * \theta_e^2 + \xi_{\text{sector}}^{C'} * \theta_e^3 + \eta_{\text{sector}}^{C'} * \theta_e^4 + \kappa^{C'} * \theta_e^5,
 \end{aligned} \tag{2.17}$$

889 where  $\alpha_{\text{sector}}^{A'}$ ,  $\beta_{\text{sector}}^{A'}$ ,  $\gamma_{\text{sector}}^{A'}$ ,  $\xi_{\text{sector}}^{A'}$ ,  $\eta_{\text{sector}}^{A'}$  and  $\kappa^{A'}$  are the parameters of orders term of  $\phi_e$  and  $\theta_e$   
 890 and the indices  $A'(\theta_e, \text{sector})$ ,  $B'(\theta_e, \text{sector})$ ,  $C'(\theta_e, \text{sector})$ ,  $D'(\theta_e, \text{sector} 5)$  and  $E'(\theta_e, \text{sector} 5)$   
 891 are related to the power of  $\phi_e$ . All parameters above are listed in the Tab. A.9 of the Appendix  
 892 A.

893 An example missing mass squared distribution for the “spectator” proton is shown in  
 894 Fig. 2.20. The comparison between the black (no correction) and blue (with electron mo-  
 895 mentum correction) lines shows that the electron momentum correction shifts the missing mass  
 896 peak towards its expected value. But it is not enough, we have to carry out the proton energy  
 897 loss correction, which is introduced next.

## 898 2.7.2 Proton Energy Loss Correction

899 Original generated protons with momenta from 0 to 2 GeV and uniform polar and azimuthal  
 900 angles are passed through the GSIM and RECSIS reconstruction processes with all detector  
 901 materials switched on. The momentum differences between generated and reconstructed pro-  
 902 tons ( $\delta p$ ) are shown in Fig. 2.17, where as the ratio between the Gaussian fit peak position  
 903 (in Fig. 2.17) and the corresponding reconstructed momentum value as a function of the re-  
 904 constructed proton momentum is plotted in Fig. 2.18. By fitting the black circles in Fig. 2.18,

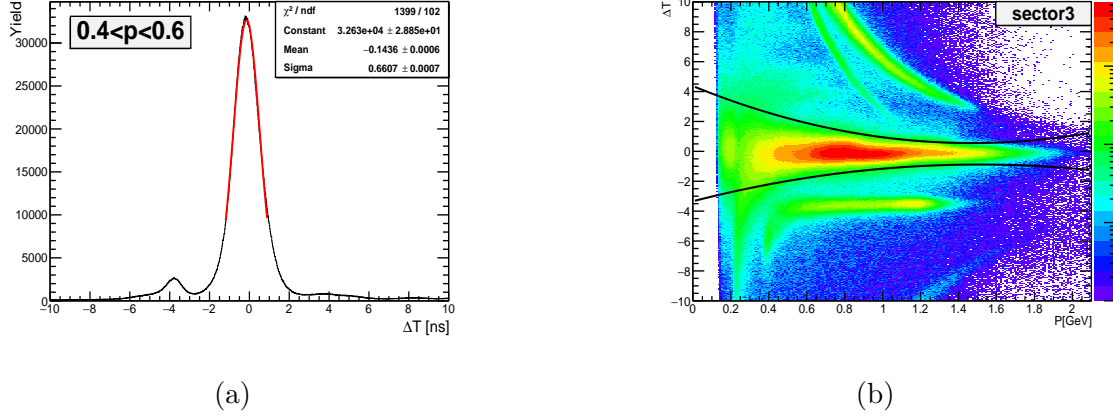


Figure 2.10: (a) Proton  $\Delta T$  distribution with Gaussian fit function (red curve) at  $0.4 \text{ GeV}/c < p_\pi < 0.6 \text{ GeV}/c$  for sector 3. (b) Proton  $\Delta T$  versus  $p_{proton}$  distribution with upper/lower  $\Delta T$  cut limits for sector 3.

905 the dependence of the momentum correction factor on the reconstructed momentum can be  
 906 identified clearly. Furthermore, the dependence of these fit parameters on corresponding  $\theta_p$  is  
 907 also shown in Fig. 2.19. Finally, the energy loss correction factor ( $\delta p$ ) is given by

$$\delta p = par[0] + par[1]p + par[2]/p, \quad (2.18)$$

908 where  $par[0]$ ,  $par[1]$ , and  $par[2]$  are the fit parameters that depend on  $\theta_p$ . They are defined by

$$\begin{aligned} par[0] &= c_0 + c_1\theta_p - c_2, \\ par[1] &= c_3 - c_4\theta_p + c_5(\theta_p)^2, \\ par[2] &= c_6 - c_7\theta_p + c_8(\theta_p)^2, \end{aligned} \quad (2.19)$$

909 where the parameters  $c_i$  ( $i = 0, 1, 2, 3, 4, 5, 6, 7, 8$ ) are listed in Tab. A.5 of the Appendix A.  
 910 After electron momentum and proton energy loss corrections, the Gaussian-fitted missing mass  
 911 squared distributions of spectator proton ( $(q^\mu + D^\mu - (\pi^-)^\mu - p^\mu)^2$ ) without any kinematic  
 912 correction, with only electron momentum correction, and with both corrections are plotted for  
 913 each sector to check the quality of kinematic corrections, and typical examples are shown in  
 914 Fig. 2.20. Then the corresponding fitted Gaussian means are obtained from these distributions  
 915 to calculate  $\mu_{mism_{spector}}^2 = \mu^2$ . Figure 2.21 shows that the values of  $\mu_{mism_{spector}}^2$  with both electron  
 916 and proton momentum corrections are closer to  $0.88 \text{ GeV}^2$  (squared proton rest mass value)  
 917 for all sectors.

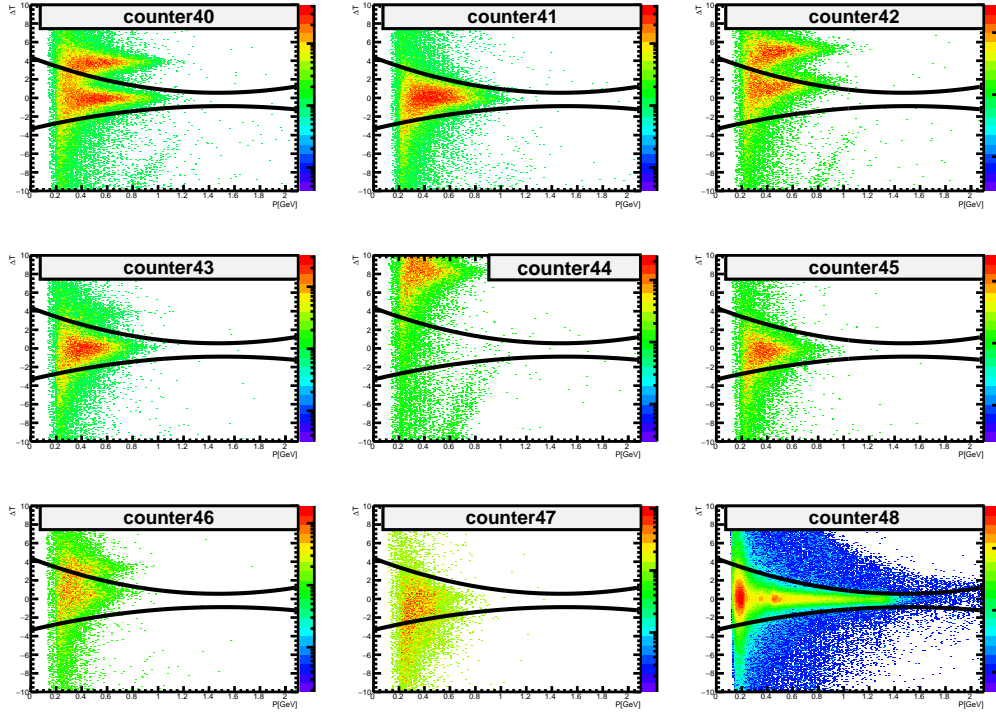


Figure 2.11: The proton  $\Delta T$  versus  $p_\pi$  distribution with upper/lower  $\Delta T$  cut limits from counter 40 to 48 of sector 3.

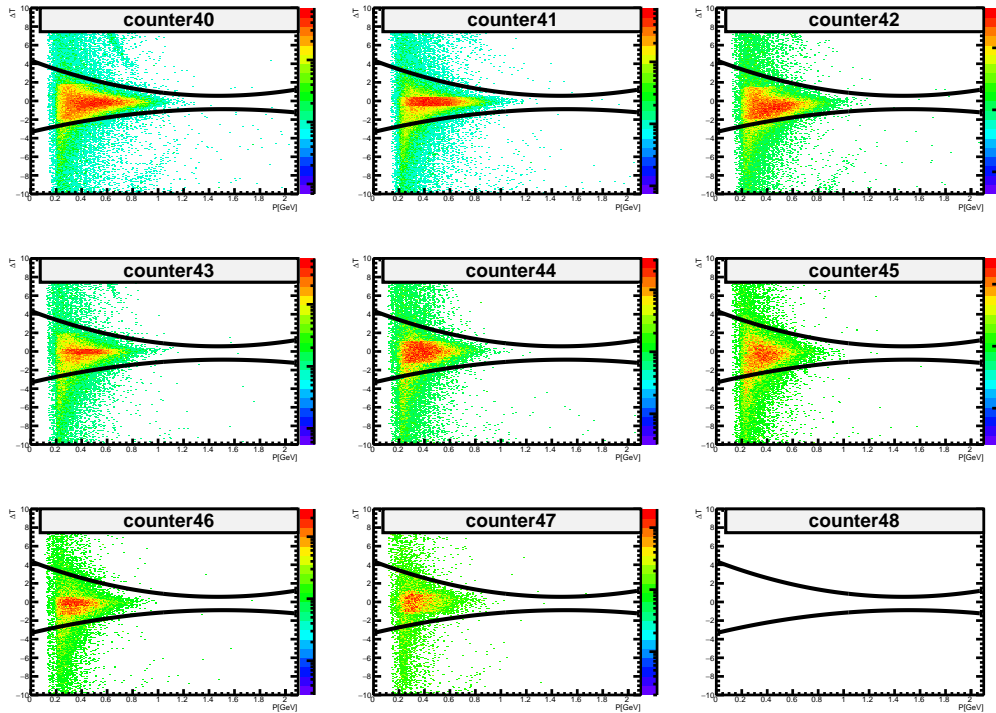


Figure 2.12: The proton  $\Delta T$  versus  $p_\pi$  distribution with upper/lower  $\Delta T$  cut limits for counter 40 to 48 of sector 3 after the  $\Delta T$  shift correction.



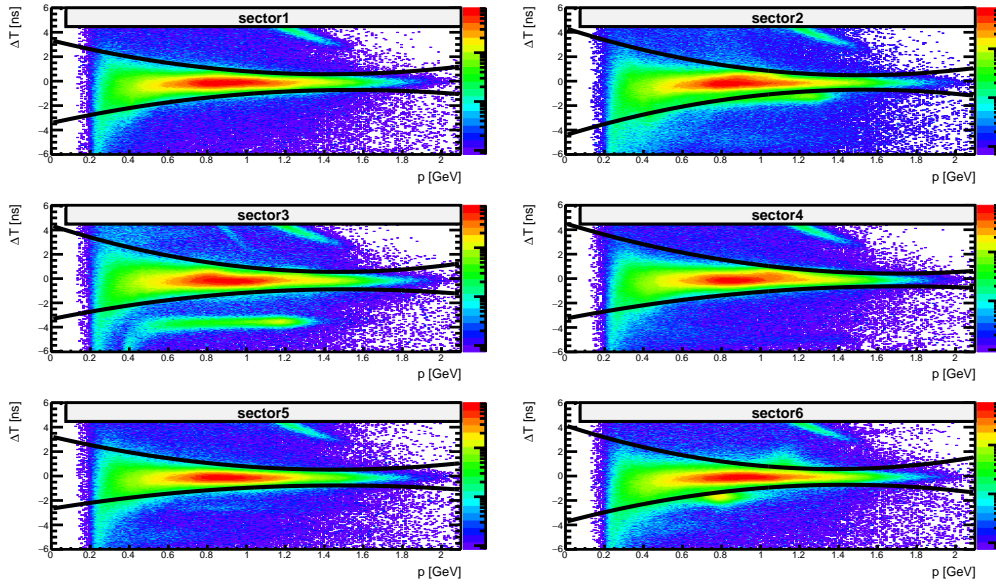


Figure 2.13: The  $\Delta T$  versus momentum distribution without any  $\Delta T$  correction for positive particles in the events that the good electron is the first particle. The corresponding proton selection  $\Delta T$  cuts are shown as the two solid black lines.

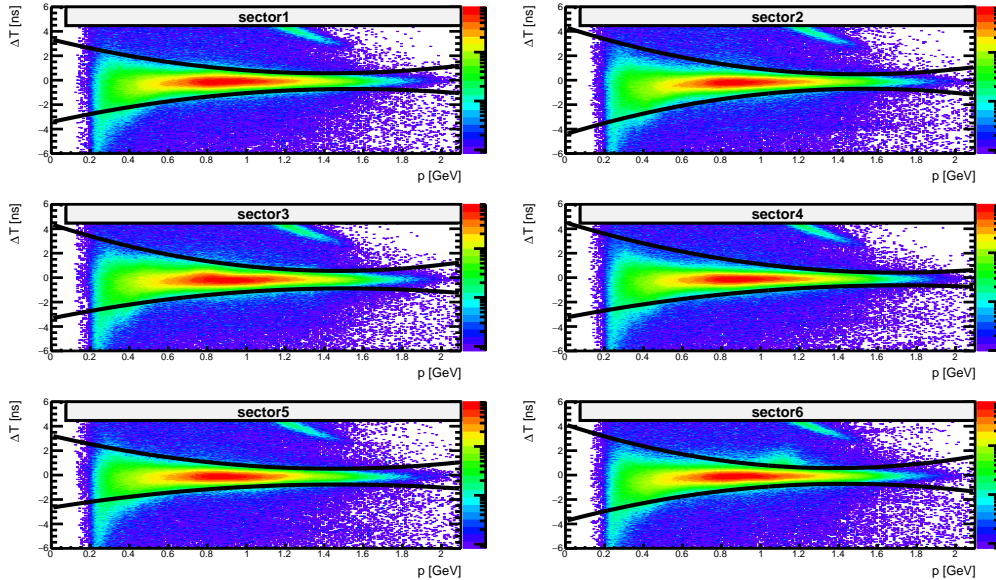


Figure 2.14: The  $\Delta T$  versus momentum distribution with the  $\Delta T$  corrections (Table A.3 in Appendix A of the notes ) for positive particles in the events that the good electron is the first particle. The corresponding proton selection  $\Delta T$  cuts are shown as the two solid black lines.



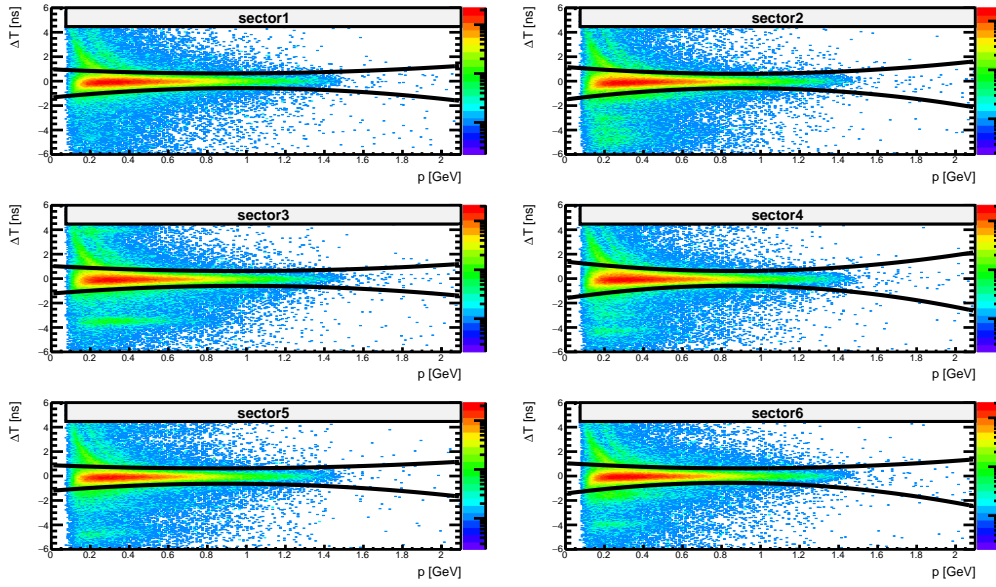


Figure 2.15: The  $\Delta T$  versus momentum distribution without any  $\Delta T$  correction for negative particles in the events that the good electron is the first particle. The corresponding pion selection  $\Delta T$  cuts are shown as the tow solid black lines.

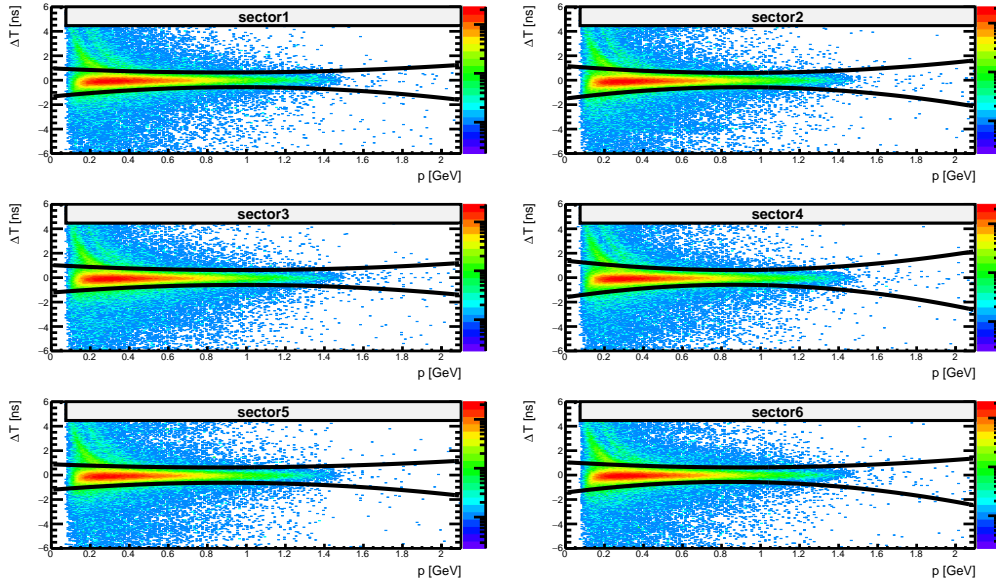


Figure 2.16: The  $\Delta T$  versus momentum distribution with the  $\Delta T$  corrections (Table A.3 in Appendix A of the notes ) for negative particles in the events that the good electron is the first particle. The corresponding pion selection  $\Delta T$  cuts are shown as the tow solid black lines

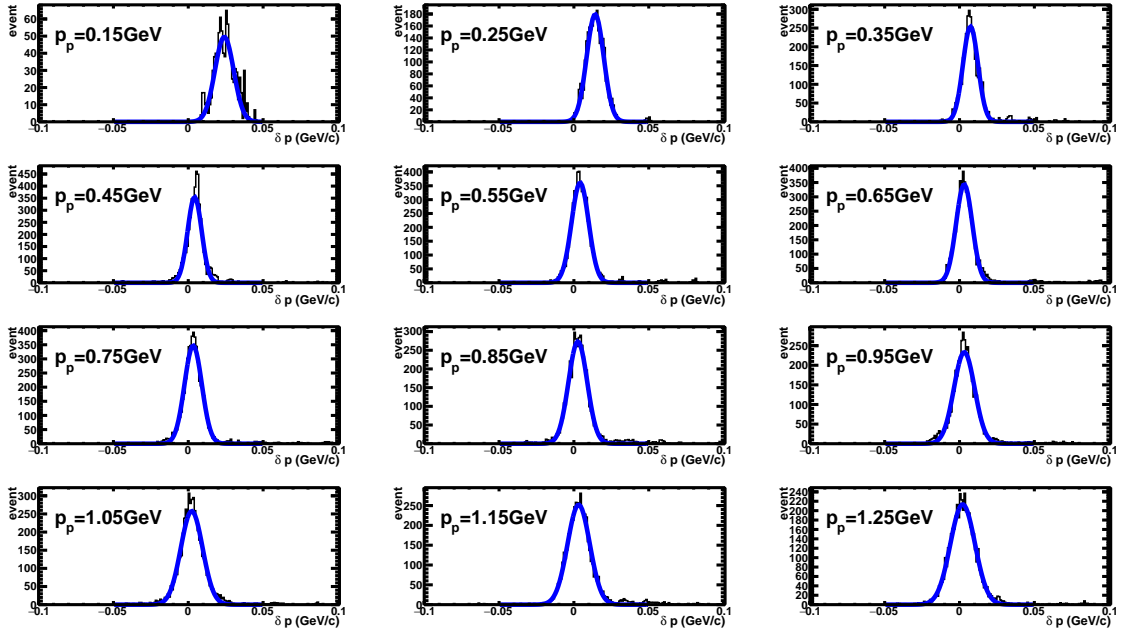


Figure 2.17: The differences between generated and reconstructed protons are presented by the black distributions for different  $p_p$  at  $\theta_p = 15^\circ$ . The blue lines indicate the Gaussian fits.

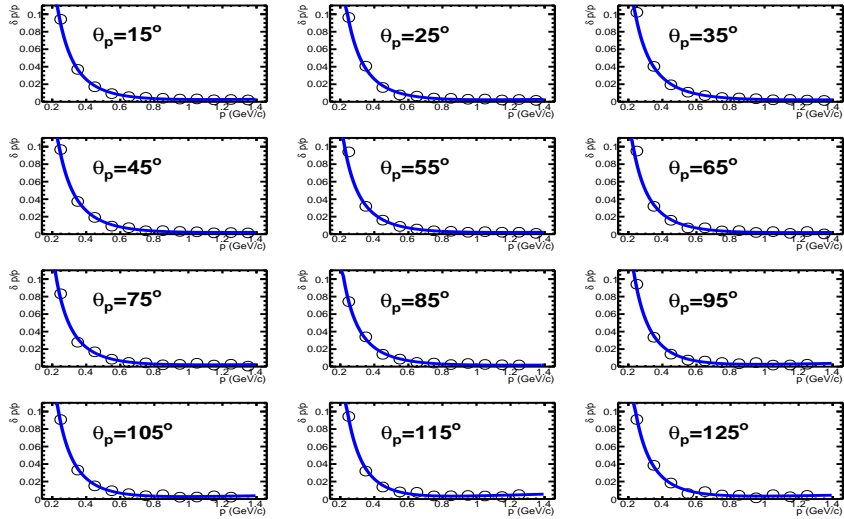


Figure 2.18: The ratio between Gaussian fit peak positions (in Fig. 2.17) and corresponding reconstructed momentum values,  $\delta p/p$ , plotted against the reconstructed proton momentum ( $p$ ) is presented by the black circles, and the blue lines show the corresponding fit functions.

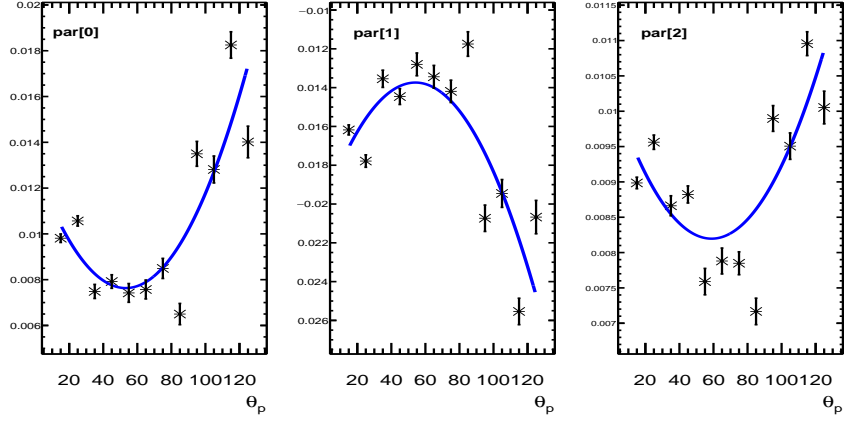


Figure 2.19: Fit parameters of  $\delta p/p$  versus  $(p)$  distributions plotted against the reconstructed proton  $\theta$  is presented by the black points, and the blue lines show the corresponding fit functions. Here `par[0]`, `par[1]`, and `par[2]` correspond to the fit parameters in Eq. (2.18).

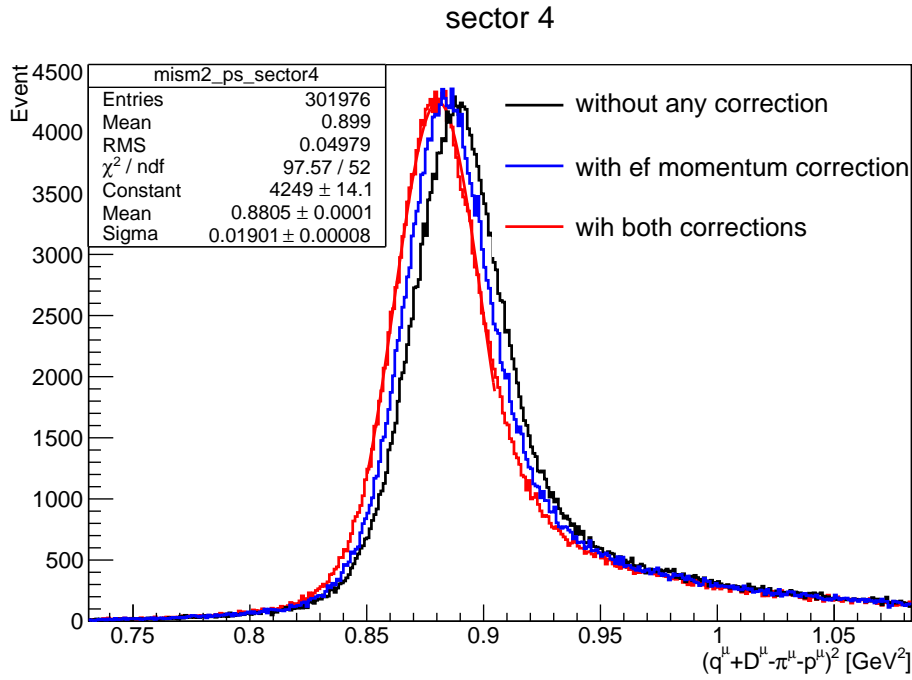


Figure 2.20: The example missing mass squared distributions of the spectator without any kinematic corrections (black line), with only electron momentum corrections (blue line), and with both electron momentum and proton energy loss corrections (red line) are plotted for sector 4, where the fit parameters in the statistics legend box correspond to the red-line Gaussian function fit.

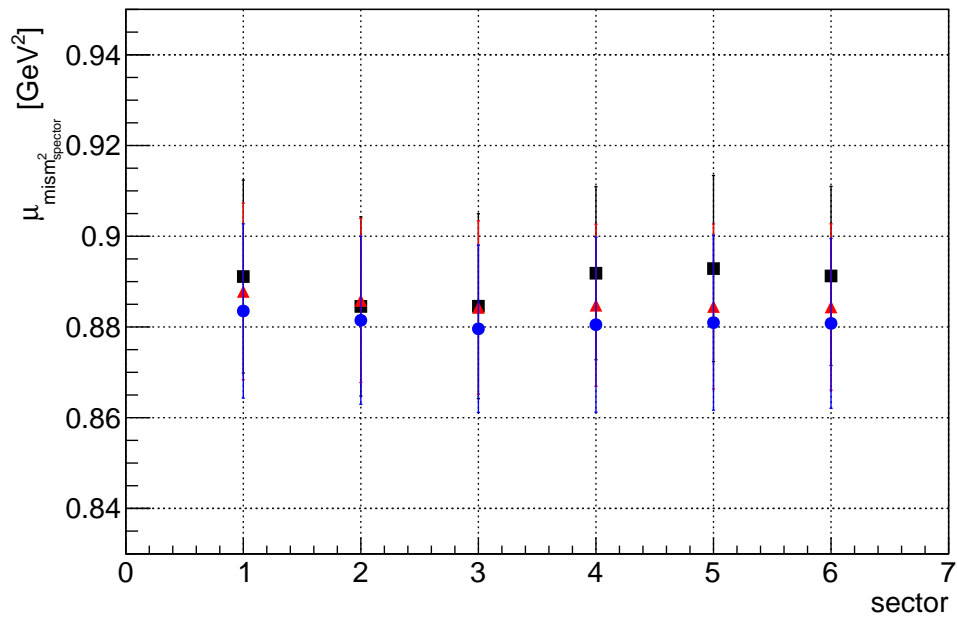


Figure 2.21: The  $\mu_{mism_{spector}}^2$  versus detector sectors without any kinematic corrections (black squares), with only electron momentum corrections (red triangles), and with both electron momentum and proton energy loss corrections (blue dots).

## 2.8 Electron Fiducial Cuts

The purpose of the fiducial cuts is to select maximally covered phase space regions with stable detector efficiencies, which are reproduced well in simulation. Due to the complex and different properties of the CLAS sub-detectors, the following fiducial cuts are introduced and applied to both experiment and simulation reconstructed data.

### 2.8.1 EC Coordinate $U$ , $V$ , and $W$ Fiducial Cut

When an electron hits the forward EC, it is expected to deposit energy proportional to its momentum. However, there is a chance that the shower produced by the electron will not be fully deposited in the calorimeter due to hitting it on the edge of the calorimeter. To avoid this kind of effect, we first cut out the edge of the  $U$ ,  $V$  and  $W$  coordinate planes of EC. The cut limits  $40 \text{ cm} < U < 400 \text{ cm}$ ,  $V < 370 \text{ cm}$ , and  $W < 405 \text{ cm}$  are illustrated in Fig. 2.22. There is a chance that the condition of the EC is changed for some particular region. In order to avoid that, we check  $U$ ,  $V$ , and  $W$  distributions for each sector. Additionally it turned out that there is a hole in the  $V$  distribution of sector 3 (see Fig. 2.23). The hole is cut out by demanding  $V < 305 \text{ cm}$  and  $V > 321 \text{ cm}$ . And all those cuts are applied on both experimental and reconstructed simulated data.

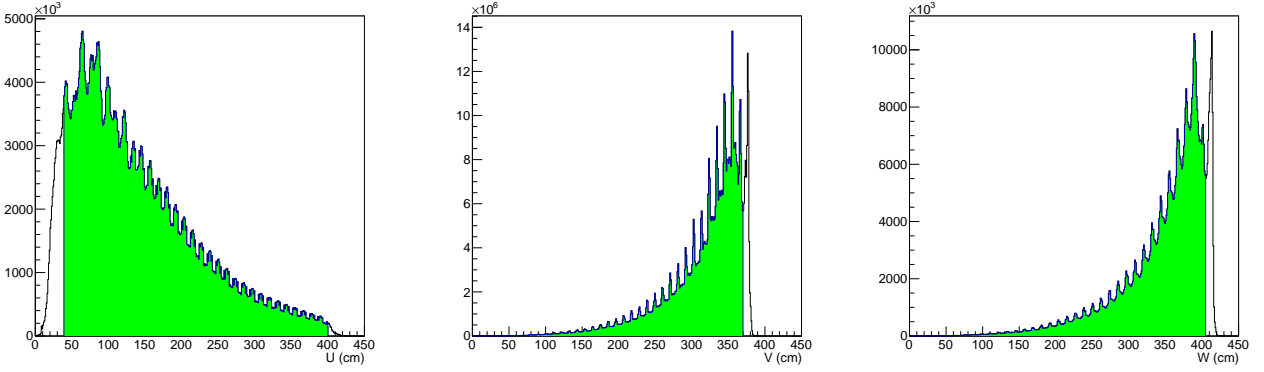


Figure 2.22: The  $U$ ,  $V$ , and  $W$  coordinate distributions in the electromagnetic calorimeter. The green area represents the selected events after the cuts.

### 2.8.2 $\phi_e$ versus $\theta_e$ Cut

Since the fiducial cut in the  $\phi_e$  versus  $\theta_e$  plane depends on the momentum of electrons ( $p_e$ ), we plot the  $\phi_e$  distribution for each  $\theta_e$  and  $p_e$  interval per sector, which is expected to be a flat distribution (see green regions in Fig. 2.25) because the cross section is  $\phi_e$  independent. The empirical shape of this kind of fiducial cut is carried out in [21] for the “e1e” run and is formulated as

$$\Delta\phi_e = 37.14 \sin((\theta_e - \theta_{min}) \frac{\pi}{180^\circ})^{p_1 + \frac{p_2}{\theta_e} + \frac{1500.0}{\theta_e^2}}, \quad (2.20)$$

where  $\Delta\phi_e$  represents the portion of the azimuthal angle  $\phi_e$  accepted by the electron fiducial cut for all possible corresponding kinematic variables  $\theta_e$  and  $p_e$ . Here  $\theta_{min}$  is the acceptable minimum polar angle  $\theta_e$ , which is calculated by

$$\theta_{min} = 12.0 + \frac{17.0}{p_e + 0.14}. \quad (2.21)$$

Furthermore,  $p_1 = 0.705 + 1.1p_e$  and  $p_2 = -63.1 + 30.0p_e$  are two momentum related parameters. Finally, the accepted regions are  $\theta_{min} < \theta_e < 50^\circ$  and  $(sector - 1)60^\circ - \Delta\phi_e < \phi_e^{sector} <$

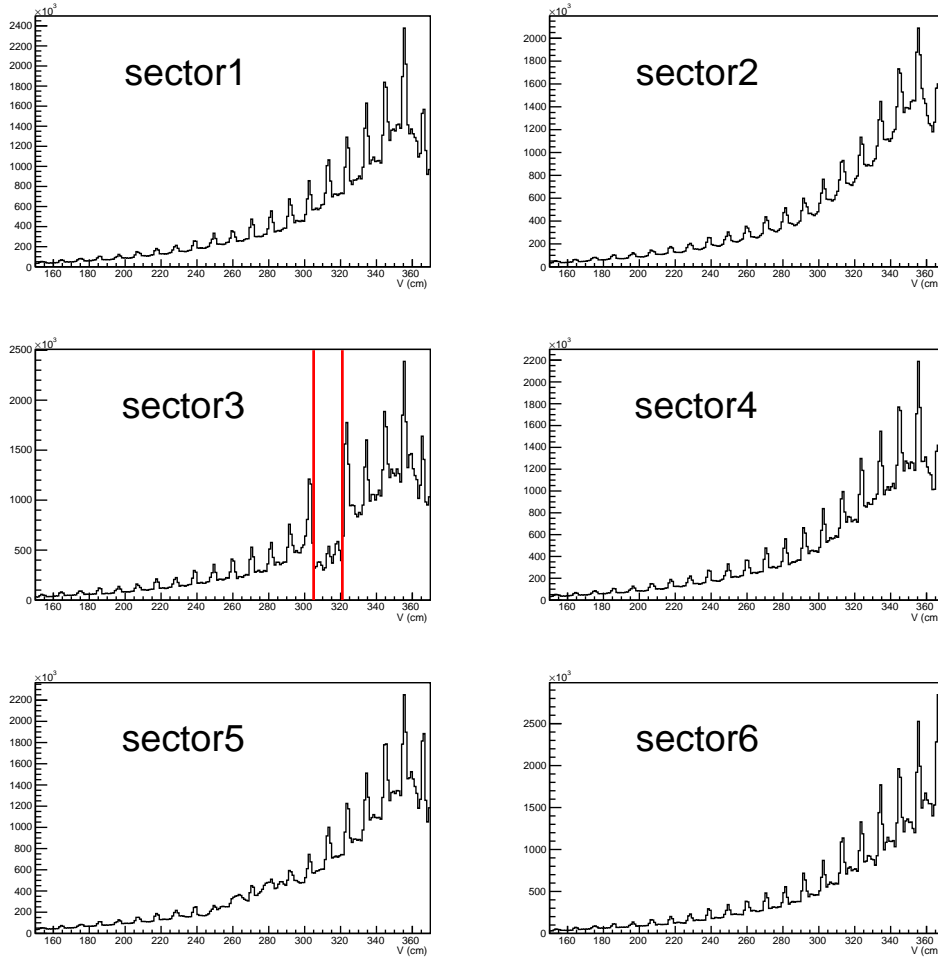


Figure 2.23: The  $V$  coordinate distribution in the electromagnetic calorimeter. Red lines represent the hole cut limits.

945  $(sector - 1)60^\circ + \Delta\phi_e$ , which are the same for experiment and simulation reconstructed data  
 946 and are shown inside the blue lines of Fig. 2.24 for examples.

### 947 **2.8.3 The Electron Polar Angle ( $\theta$ ) versus Momentum ( $p$ ) Cut**

948 As seen in Fig. 2.24, there are low efficiency regions (mainly caused by the dead wires of DC and  
 949 bad counters of SC) in the sectors 2, 3, and 5, which should be removed by the “cooking” process  
 950 and correctly translated to the simulation. However, this is not always the case, sometimes the  
 951 simulation reconstructed events are not reproducing those low efficiency regions, and this will  
 952 cause problems in calculating the correct acceptance of the detector. So, we remove detector  
 953 low efficiency regions based on the  $\theta$  versus  $p$  distribution for each final particle in each sector  
 954 separately. In Fig. 2.26, the middle black paired lines show boundaries of the removed regions  
 955 in each sector for electrons, which are applied simultaneously to experiment and simulation  
 956 reconstructed data.

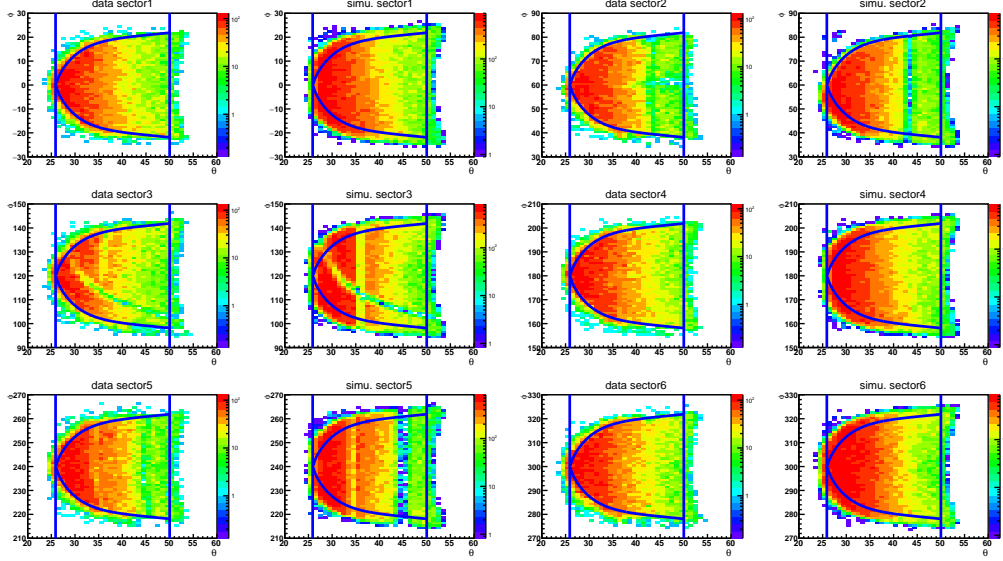


Figure 2.24:  $\theta_e$  versus  $\phi_e$  distributions of electrons are plotted for six sectors for experiment (left) and simulation (right) reconstructed data each side by side within the  $0.8 \text{ GeV} < |\vec{p}_e| < 1.0 \text{ GeV}$  momentum interval. The blue lines show the fiducial cut boundaries for electrons.

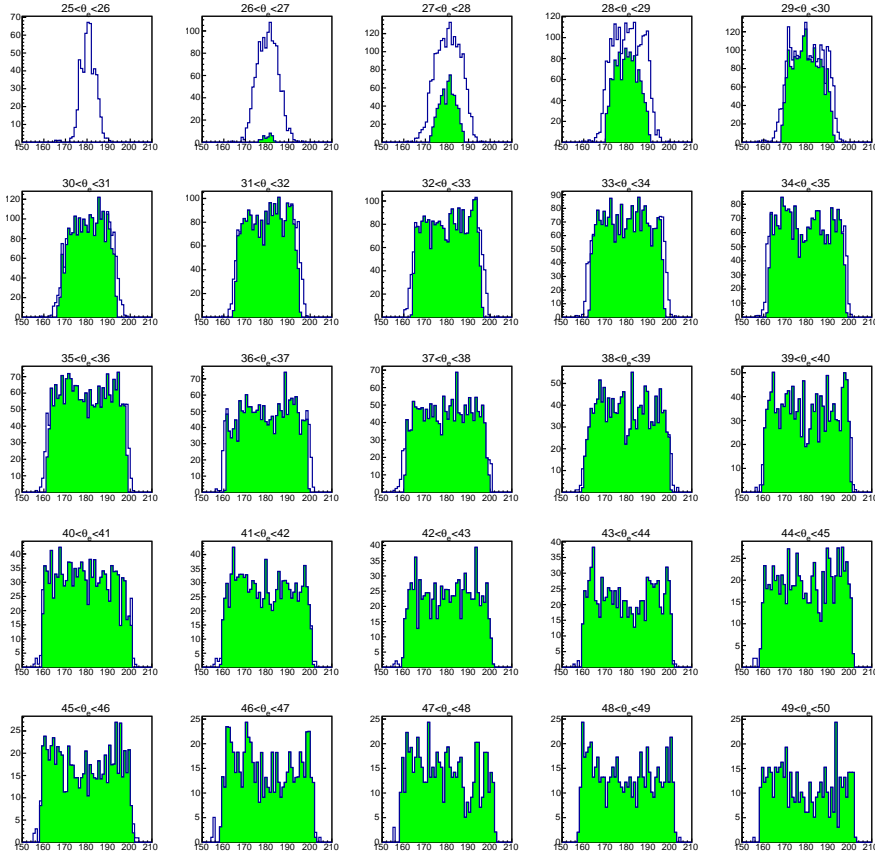


Figure 2.25: Example  $\phi_e$  distributions of electrons in sector 4 for data with  $0.8 \text{ GeV} < |\vec{p}_e| < 1.0 \text{ GeV}$  before (blue) and after (green) fiducial cuts.

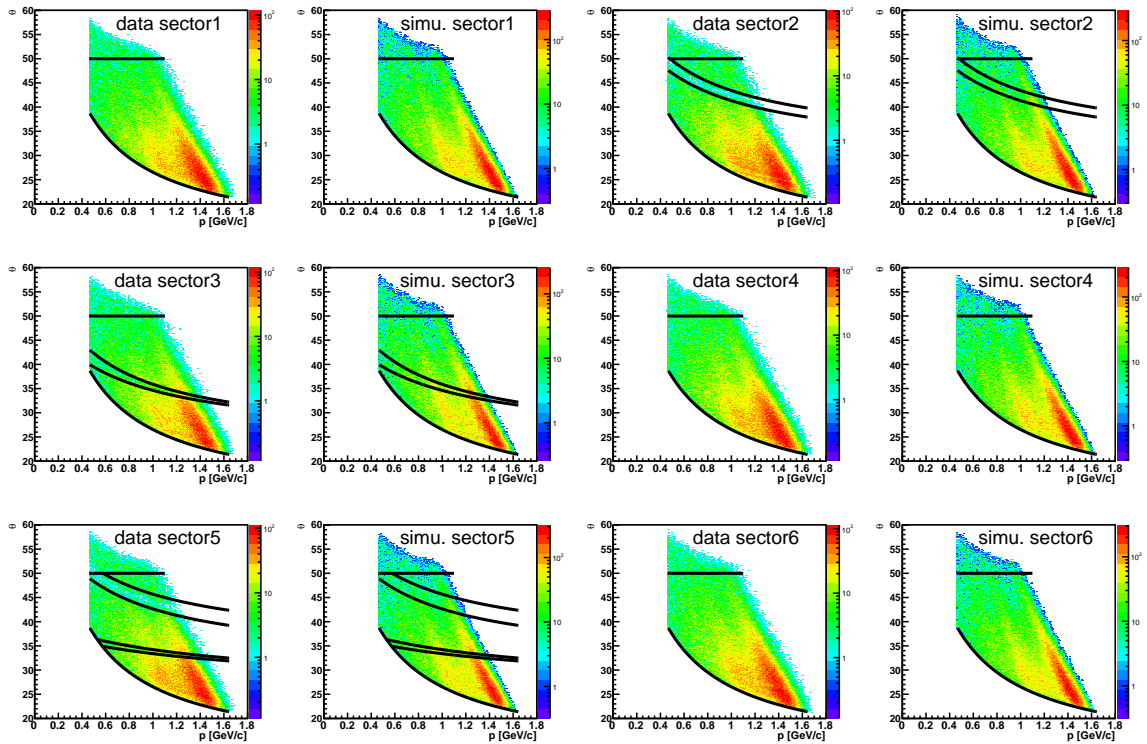


Figure 2.26:  $\theta_e$  versus  $p$  distributions of electrons in all six sectors are compared for experiment (left) and simulation (right) reconstructed data simultaneously each side by side. The top and bottom black lines show the  $\theta_e$  cut boundaries, and the middle paired black lines show removed regions, which are reflected in Fig. 2.24 by the low event-rate bands.



## 957 2.9 Pion Fiducial Cuts

958 The purpose of pion fiducial cuts is very similar to that of electron fiducial cuts. Since we do  
 959 not fully understand some of the low efficiency regions of the sub-detectors, we cannot fully  
 960 incorporate these effects in the simulation procedure. The solution is to cut out those regions  
 961 exactly in the same way for both experiment and simulation reconstructed data. The following  
 fiducial cuts are carried out for pions.

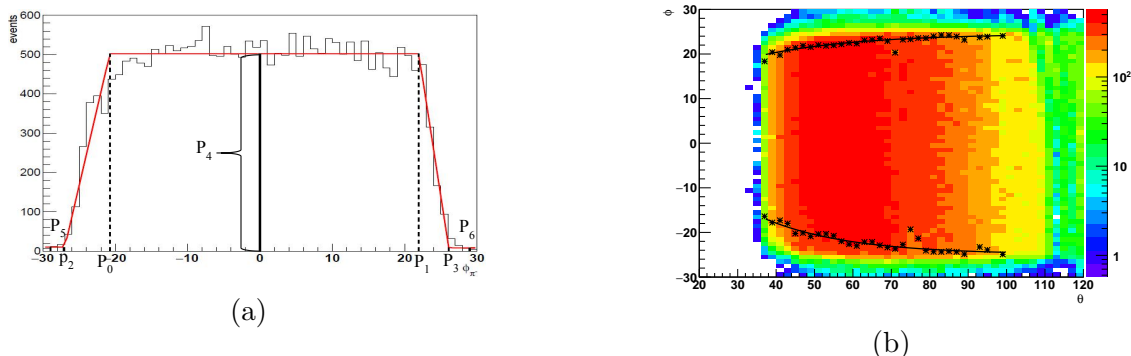


Figure 2.27: (a) Typical example  $\phi$  distribution of pions from the  $0.2 \text{ GeV} < |\vec{p}_{\pi^-}| < 0.4 \text{ GeV}$  and  $28^\circ < \theta_{\pi^-} < 30^\circ$  intervals in sector 1, which are fit by the function (Eq. (2.22)) shown by the red line, where the corresponding fit parameters  $P_4$ ,  $P_5$ , and  $P_6$  are heights of the corresponding plateau regions of the trapezoid function and  $P_0$ ,  $P_1$ ,  $P_2$ , and  $P_3$  are corresponding  $\phi$  values of the inflection points. (b) Example  $\phi$  versus  $\theta$  distribution for pions in sector 1 within the same momentum interval. Corresponding fit parameters  $P_0$  and  $P_1$  of each  $\theta$  bin are marked as stars and fit by the function (Eq. (2.23)) shown by the back line.

962

### 963 2.9.1 The Pion $\phi$ versus $\theta$ Cut

964 For pions, we also need to cut out the boundary regions of the detector. We initially plot their  
 965  $\phi$  versus  $\theta$  distributions in different  $p_{\pi^-}$  momentum bins in each sector as seen in the examples  
 966 in Fig. 2.28. Then we project these distributions on to the  $\phi$  axis for each  $\theta$  bin, as shown in  
 967 Fig. 2.27a. The data is fit by a “trapezoid + constant background” function (red curve), which  
 968 is defined [29] by

$$f = \begin{cases} P_5 & , \phi < P_2, \\ (P_4 - P_5) \frac{\phi - P_2}{P_0 - P_2} + P_5 & , P_2 \leq \phi < P_0, \\ P_4 & , P_0 \leq \phi \leq P_1, \\ (P_4 - P_6) \frac{\phi - P_3}{P_1 - P_3} + P_6 & , P_1 < \phi \leq P_3, \text{ and} \\ P_6 & , \phi > P_3, \end{cases} \quad (2.22)$$

969 where all parameters are shown in Fig. 2.27a, and the plateau region of the trapezoid between  
 970 parameters  $P_0$  and  $P_1$  is accepted by the fiducial cut. Every sector with each momentum and  
 971  $\theta$  bin has its own plateau  $\phi$  region, and the corresponding fit parameters  $P_0$  and  $P_1$  are plotted  
 972 as boundaries of the  $\theta$  versus  $\phi$  distribution (see Fig. 2.27b) and fit by modified exponential  
 973 functions

$$\begin{aligned} \phi_{\pi^-}^{max} &= C_{0max}(1 - e^{-C_1(\theta+C_2)}) + (\text{sector} - 1) * 60, \text{ and} \\ \phi_{\pi^-}^{min} &= C_{0min}(1 + e^{-C_1(\theta+C_2)}) + (\text{sector} - 1) * 60, \end{aligned} \quad (2.23)$$

974 where  $C_1$  is a constant fit parameter, however  $C_{0max}$ ,  $C_{0min}$ , and  $C_2$  are  $\pi^-$  momentum ( $p_{\pi^-}$ )  
 975 dependent parameters. In each  $\Delta p_{\pi^-} = 0.2 \text{ GeV}$  interval, the corresponding  $C_{0max}$ ,  $C_{0min}$ , and

976  $C_2$  are obtained, then the  $C_{0max}$ ,  $C_{0min}$ , and  $C_2$  versus  $p_{\pi^-}$  plots are created and fit by

$$C_{0max;0min;2}(p_{\pi^-}) = par[0] + par[1]P_{\pi^-} + \frac{par[2]}{p_{\pi^-}}, \quad (2.24)$$

977 where the corresponding fit parameters  $par[0]$ ,  $par[1]$ , and  $par[2]$ , along with  $C_1$ , are all listed  
 978 in Tab. A.6 of the Appendix A.  $\phi_{\pi^-}^{max}$  and  $\phi_{\pi^-}^{min}$  for sector 1 are plotted as two blue curves on the  
 $\phi$  versus  $\theta$  distributions in different  $p_{\pi^-}$  intervals, which are shown in Fig. 2.28. Finally, in order

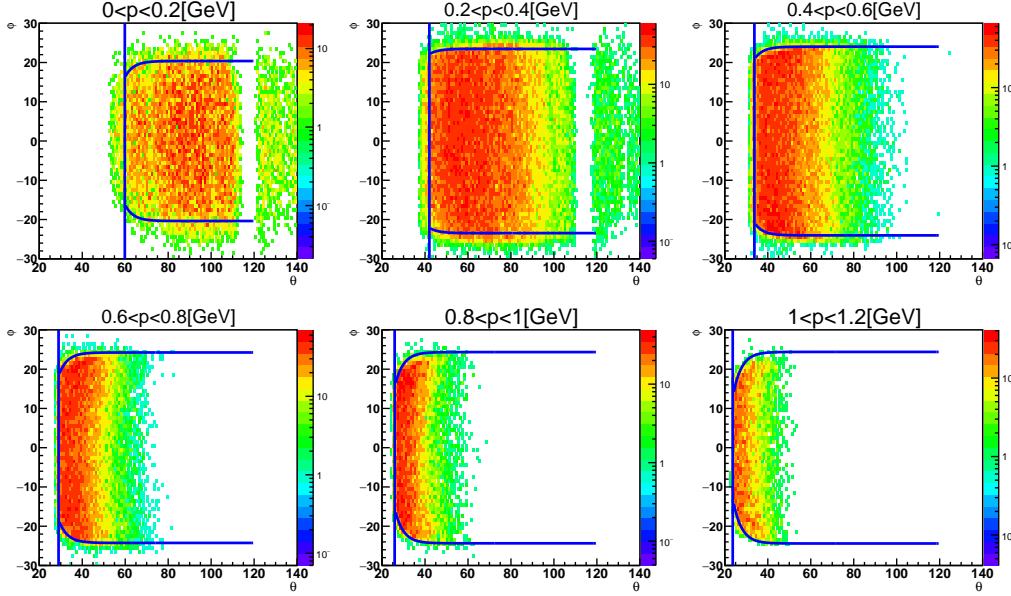


Figure 2.28: Example  $\phi$  versus  $\theta$  distributions of pions after event selection in sector 1 for  $0.2 \text{ GeV} < p_{\pi^-} < 1.2 \text{ GeV}$  within  $0.2 \text{ GeV}$  increasing steps, and the fiducial cuts (blue lines) are plotted here for sector 1.

979 to check if those fiducial cuts work properly for both experiment and simulation reconstructed  
 980 data, they are plotted on example  $\phi$  versus  $\theta$  distributions side by side for sector 1 in Fig. 2.29.  
 981 Besides applying  $\phi_{\pi^-}^{min} < \phi_{\pi^-} < \phi_{\pi^-}^{max}$  on experiment and simulation reconstructed data,  
 982  $\theta > \theta_{min}^{\pi^-}$  cuts are also applied.  $\theta_{min}^{\pi^-}$  is found empirically from  $\theta$  versus  $p$  distributions in Fig. 2.30 by  
 983

$$\theta_{min}^{\pi^-} = 11.09 + \frac{8.0}{0.472p_{\pi^-} + 0.117}, \quad (2.25)$$

984 which is represented by the black vertical lines in Fig. 2.29.

## 985 2.9.2 The Pion Polar Angle ( $\theta$ ) versus Momentum ( $p$ ) Cut

986 Like in case of electrons, we have to remove low-efficient regions of the detector for pions by  
 987 applying cuts on  $\theta$  versus  $p$  distributions, which are shown in Fig. 2.30 by paired black lines  
 988 for both experiment and simulation reconstructed data. For pions, the low efficient regions for  
 989 all sectors only show up in experiment reconstructed data rather than in the simulation recon-  
 990 structed data, nevertheless they are cut out for both experiment and simulation reconstructed  
 991 data. The cut functions are found empirically by

$$\theta = \begin{cases} C_0 + \frac{C_1}{C_2(p+C_3)+C_4} & , \text{ sector 1, 3, 4, 5, and 6} \\ C_0 + \frac{C_1}{C_2p+C_3} & , \text{ sector 2,} \end{cases} \quad (2.26)$$

992 where all parameters are listed in Tab. A.1 of the Appendix A.

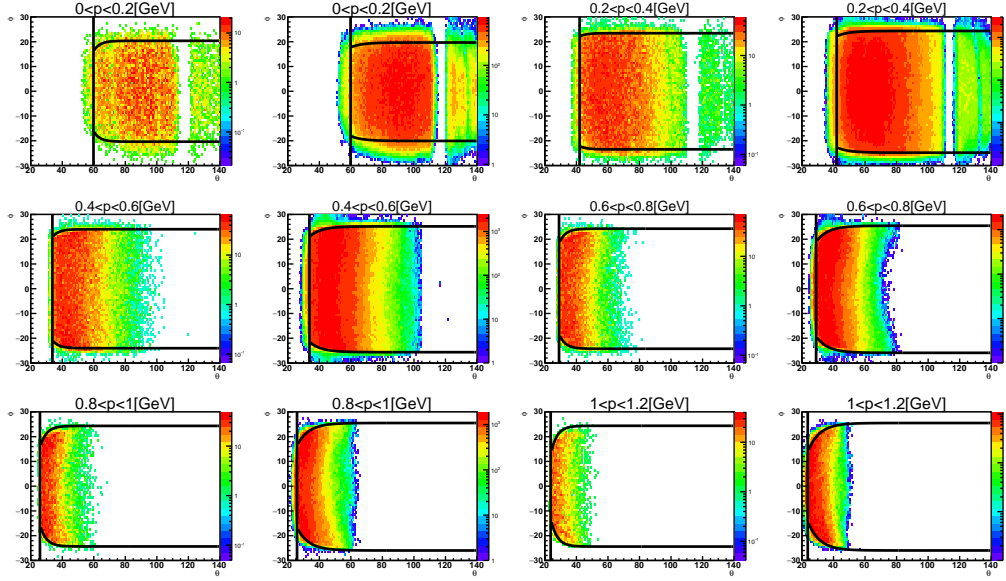


Figure 2.29:  $\phi$  versus  $\theta$  distributions of pions in different  $p_{\pi^-}$  bins after event selection are plotted for sector 1 for experiment (left) and simulation (right) reconstructed data each side by side. The black lines represent the fiducial-cut boundaries.

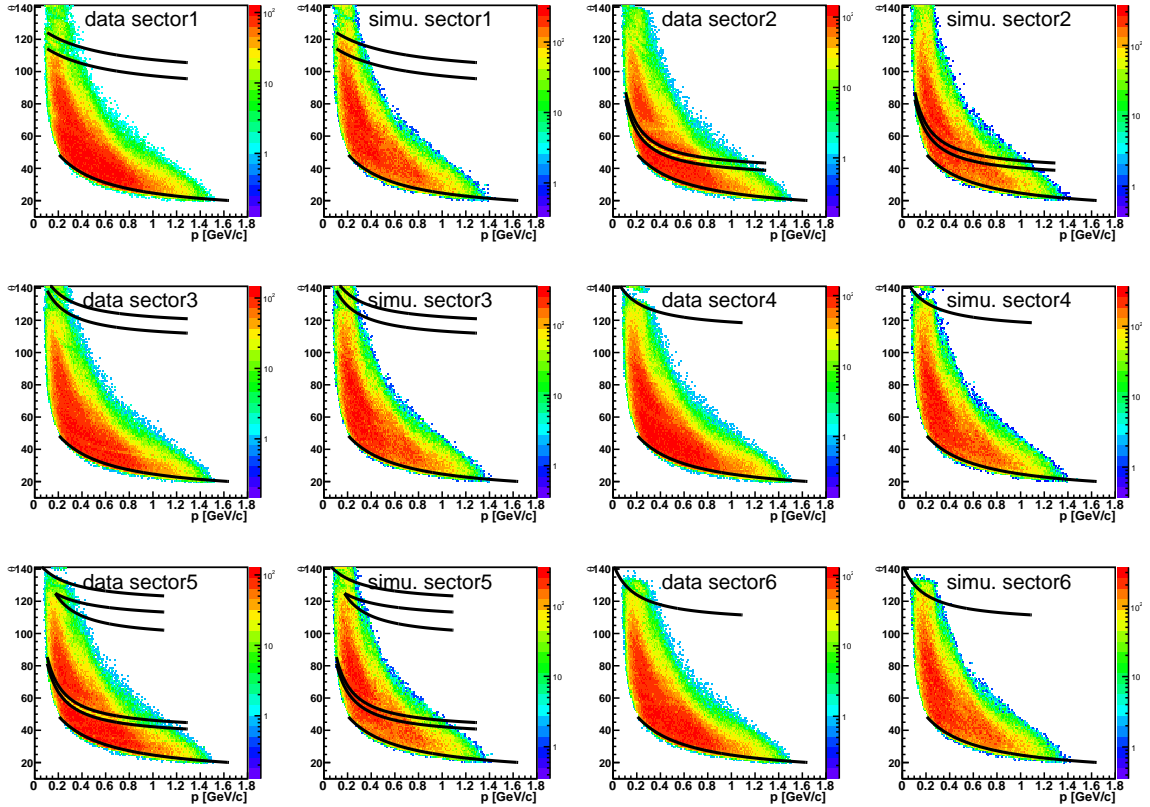


Figure 2.30:  $\theta$  versus  $p$  distributions of pions in six sectors are compared for experiment (left) and simulation (right) reconstructed data each side by side. The middle paired black lines show the removed regions, which are reflected in Fig. 2.29 by the vertical low event-rate bands, and the bottom black lines represent  $\theta > \theta_{min}^{\pi^-}$  cuts.

## 2.10 Proton Fiducial Cuts

For the proton fiducial cut, we follow the same procedure as for other particles to only accept stable efficiency regions of the detector. We apply the following cuts on both experimental data and simulation.

### 2.10.1 The Proton $\phi$ versus $\theta$ Cut

We plot the proton  $\phi$  versus  $\theta$  distributions in different momentum bins for each sector, see examples in Fig. 2.32. A typical projected  $\phi$  distribution for the  $28^\circ < \theta_{proton} < 30^\circ$  bin is shown in Fig. 2.31a, which is fit by the function Eq. (2.22) to get the corresponding fit parameters  $P_0$  and  $P_1$ . They are marked as stars in Fig. 2.31b and are fit by the functions  $\phi_{proton}^{max}$  and  $\phi_{proton}^{min}$  given by Eq. (2.27) to establish the fiducial-cut boundaries for protons. The fit parameters are momentum independent but different for different sectors (see this behavior in Fig. 2.32). All parameters are listed in Tab. A.7 in the Appendix A.

$$\begin{aligned}\phi_{proton}^{max} &= P_0(1 - e^{-P_1(\theta+P_2)}) + (\text{sector} - 1) * 60 \\ \phi_{proton}^{min} &= P_0(1 + e^{-P_1(\theta+P_2)}) + (\text{sector} - 1) * 60\end{aligned}\quad (2.27)$$

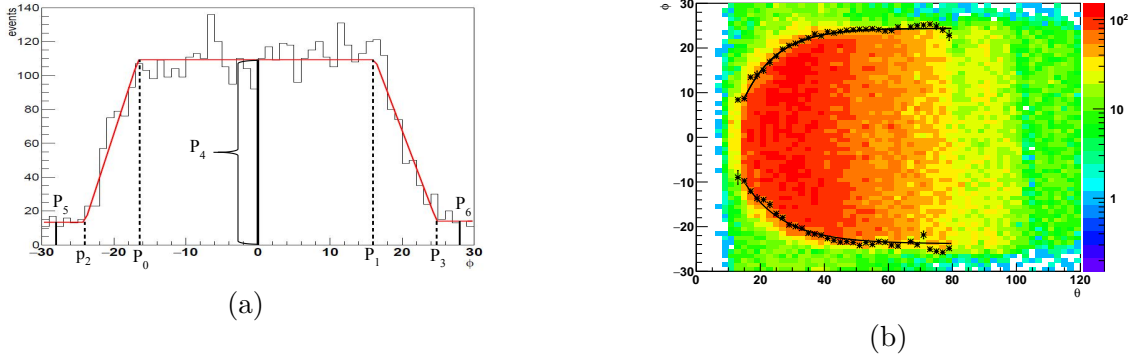


Figure 2.31: (a) Typical example for a  $\phi$  distribution of protons from the  $0.2 \text{ GeV} < |\vec{p}_{proton}| < 0.4 \text{ GeV}$  and  $28^\circ < \theta_{proton} < 30^\circ$  intervals in sector 1, which is fit by the function Eq. (2.22) and plotted as the red line. The corresponding fit parameters  $P_4$ ,  $P_5$ , and  $P_6$  are heights of the corresponding plateau regions of the trapezoid function, and  $P_0$ ,  $P_1$ ,  $P_2$ , and  $P_3$  are the corresponding  $\phi$  values of the inflection points. (b) The  $\phi$  versus  $\theta$  distribution of protons for sector 1 within the same momentum interval. Corresponding fit parameters  $P_0$  and  $P_1$  of each  $\theta$  bin are marked as stars, fit by the function Eq. (2.23), and shown by the black lines.

In Fig. 2.33, the proton fiducial-cut boundaries  $\phi_{proton}^{max}$  and  $\phi_{proton}^{min}$  are plotted as  $\phi$  versus  $\theta$  distributions for experiment and simulation reconstructed data to conclude that they include all the stable efficiency regions for both.

### 2.10.2 The Proton Polar Angle ( $\theta$ ) versus Momentum ( $p$ ) Cut

For protons, we only cut out the low efficient regions of sector 2 and 5, which are visible in Fig. 2.34, where the cut functions are found empirically by

$$\theta = \begin{cases} C_0 p^3 + C_1 p^2 + C_2 p + C_3 & , \text{sector 2} \\ C_0(p + C_1)C_2 + C_3 & , \text{sector5 - 1} \\ C_0(p + C_4)^3 + C_1(p + C_4)^2 + C_2 * (p + C_4) + C_3 & , \text{sector5 - 2,} \end{cases}\quad (2.28)$$

and for which all fit parameters are listed in Tab. A.2 in the Appendix A.

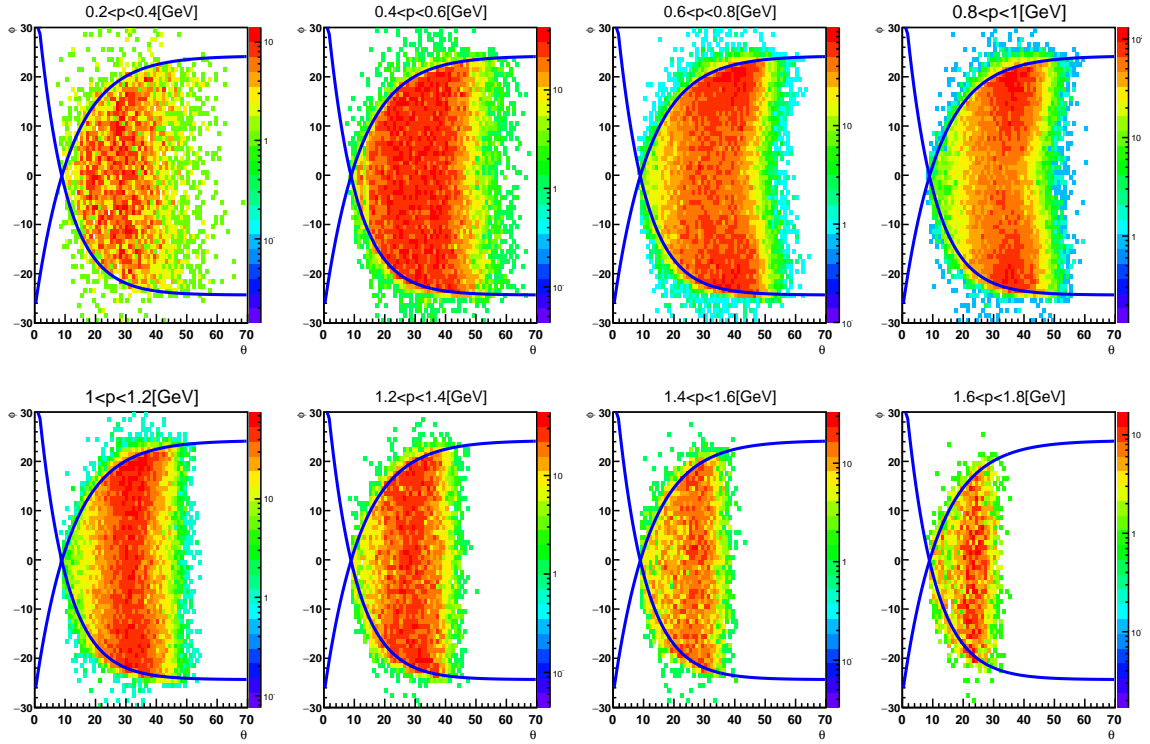


Figure 2.32: Example  $\phi$  versus  $\theta$  distributions for protons in sector 1 for  $0.2 \text{ GeV} < p_{\text{proton}} < 1.8 \text{ GeV}$  within  $0.2 \text{ GeV}$  increasing steps and the fiducial cuts (blue lines) for sector 1.

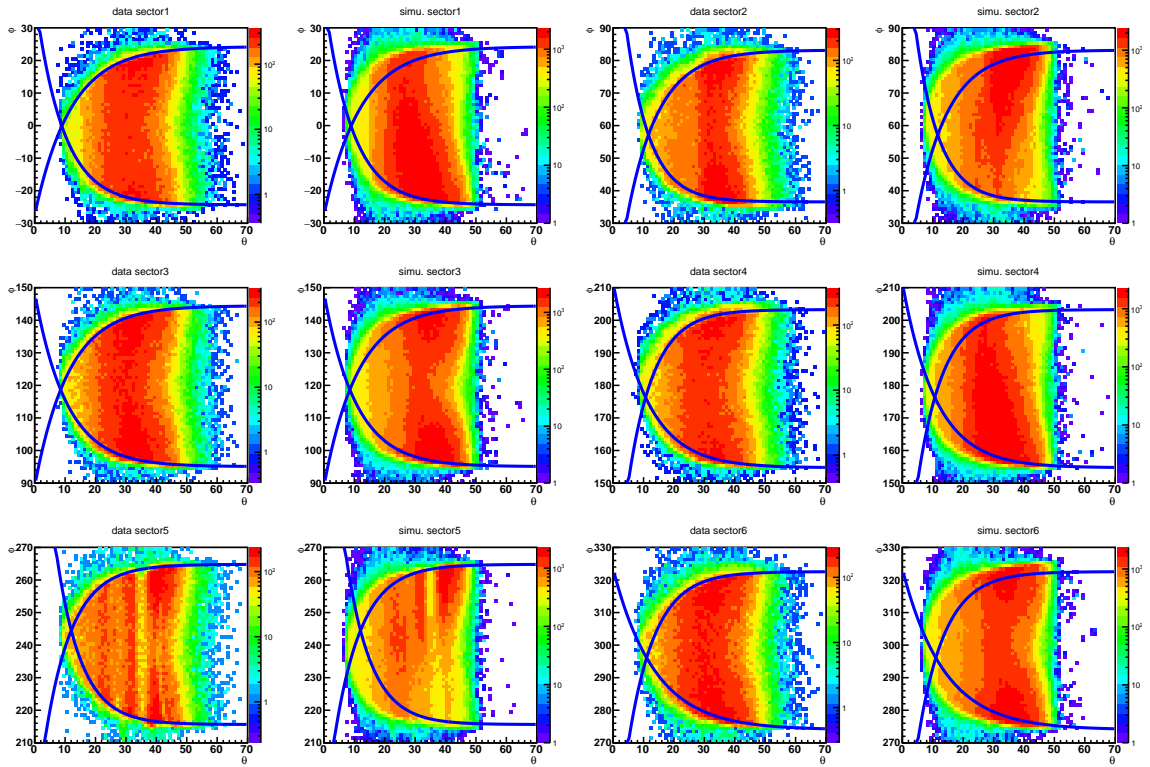


Figure 2.33:  $\phi$  versus  $\theta$  distributions of protons plotted for six sectors for experimental experiment (left) and simulation (right) reconstructed data each side by side. The blue lines represent fiducial-cut boundaries.

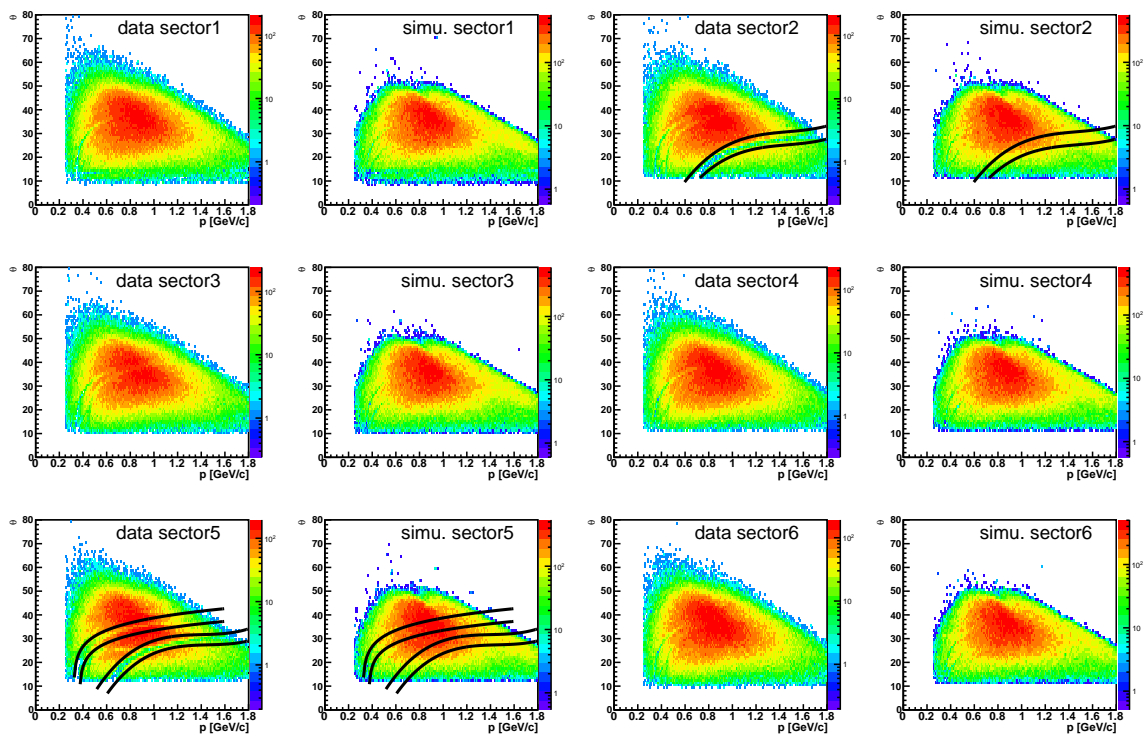


Figure 2.34:  $\theta$  versus  $p$  distributions of protons in all six sectors are compared for experimental (left) and simulation (right) reconstructed data each side by side. The middle paired black lines show the removed regions, which are reflected in Fig. 2.33 by the vertical low event-rate bands.

## 1012 2.11 Event Selection

1013 With the saved information of all but one final state particles ( $e'$ ,  $\pi^-$ , and  $p$ ) and the deuteron  
 1014 (D) at rest in the lab frame, we finally select and analyze events for the reaction  $\gamma^*n(p) \rightarrow$   
 1015  $p\pi^-(p)$  by applying the following cuts.

### 1016 2.11.1 Exclusive Events Selection

1017 For events that have reconstructed four momenta for  $e'$ ,  $\pi^-$ , and  $p$ , we calculate the missing  
 1018 “spectator” mass squared  $M_s^2$ , which is determined by

$$M_s^2 = (P_e^\mu - P_{e'}^\mu + P_D^\mu - P_{\pi^-}^\mu - P_p^\mu)^2, \quad (2.29)$$

1019 where  $P_e^\mu$ ,  $P_{e'}^\mu$ ,  $P_D^\mu$ ,  $P_{\pi^-}^\mu$ , and  $P_p^\mu$  are the four momenta of the corresponding particles. In order  
 1020 to select the exclusive process  $\gamma^*n(p) \rightarrow p\pi^-(p)$ , we apply the  $0.811 \text{ GeV}^2 < M_s^2 < 0.955 \text{ GeV}^2$   
 1021 missing mass cut to isolate the “spectator” proton peak (see Fig. 2.35), which should be around  
 1022 the proton rest mass squared ( $\sim 0.88 \text{ GeV}^2$ ).

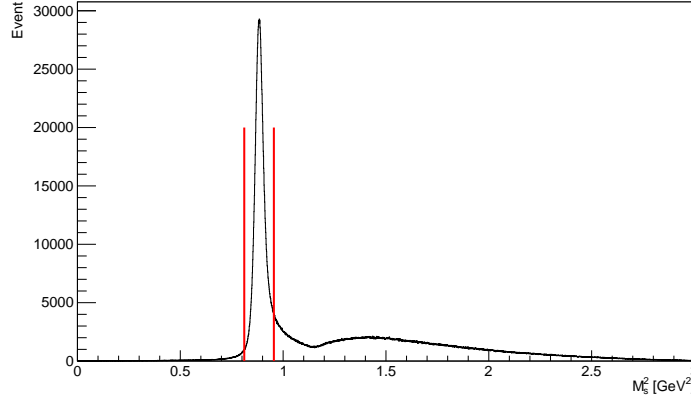


Figure 2.35: The  $M_s^2$  distribution with the two cut limits represented by the red lines illustrates the exclusive event selection process.

### 1023 2.11.2 Quasi-free Exclusive Events Selection

1024 Based on the exclusive events, we apply an additional cut on the missing momentum of the  
 1025 “spectator” ( $|\vec{p}_s|$ ) for both experiment and simulation reconstructed data, which is shown in  
 1026 Fig. 2.37a.  $|\vec{p}_s|$  is calculated by

$$|\vec{p}_s| = |\vec{p}_e - \vec{p}_{e'} - \vec{p}_{\pi^-} - \vec{p}_p|. \quad (2.30)$$

1027 The zoomed in Fig. 2.37b focuses on the low “spectator” momentum distribution (black line) for  
 1028 experimental data and the detector-reconstructed Monte Carlo (MC) simulated proton Fermi  
 1029 momentum distribution with the CD-Bonn potential (blue line) [20]. The comparison between  
 1030 the two curves reveals that the quasi-free process is absolutely dominant in the  $|\vec{p}_s| < 200 \text{ MeV}$   
 1031 region. When  $|\vec{p}_s| > 200 \text{ MeV}$ , the final state interaction becomes first measurable and then even  
 1032 dominant. Since the  $|\vec{p}_s|$  distribution of experimental data is right underneath the simulated  
 1033 Fermi momentum distribution (blue line) up to 200 MeV, we can successfully isolate the quasi-  
 1034 free process by applying this cut, and the assumed “spectator” becomes a true spectator  
 1035 proton. Meanwhile, we also cut away some good quasi-free events with this cut. Here “ $r$ ”

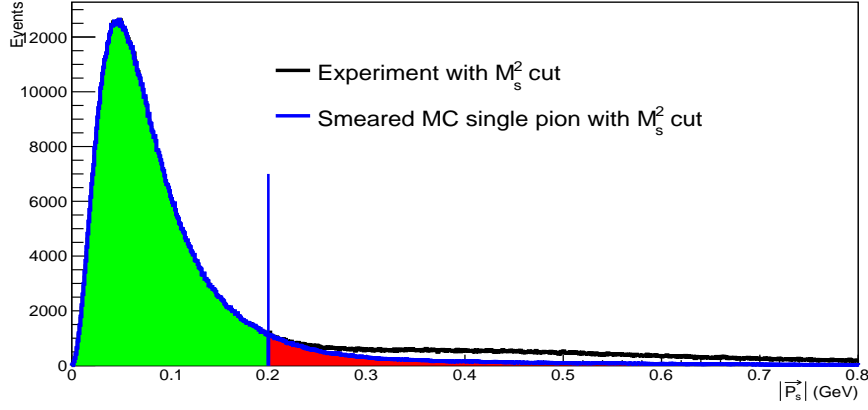


Figure 2.36: (Color online) The  $|\vec{p}_s|$  distribution of experimental data (black line) and simulation (blue line) where “green” and “red” filled areas represent the integral of the blue distribution from 0 MeV to 200 MeV and above 200 MeV, respectively.

1036 denotes the factor to correct good quasi-free events outside the  $|\vec{p}_s| < 200$  MeV cut. In order to  
 1037 calculate “ $r$ ”, the  $|\vec{p}_s| < 200$  MeV cut is applied to simulated events to get the  $|\vec{p}_s|$   
 1038 distribution for each kinematic bin. Then the factor  $r$  is calculated from the simulation reconstructed data  
 1039 by

$$r(W, Q^2, \cos \theta_{\pi^-}^*, \phi_{\pi^-}^*) = \frac{N^{simu-|\vec{p}_s| < 200 \text{ MeV}}(W, Q^2, \cos \theta_{\pi^-}^*, \phi_{\pi^-}^*)}{N^{simu-xf}(W, Q^2, \cos \theta_{\pi^-}^*, \phi_{\pi^-}^*)} = \frac{\text{green}}{\text{green} + \text{red}}, \quad (2.31)$$

1040 where  $N^{simu-xf}$  represents simulated exclusive quasi-free yields in each kinematic bin and  
 1041  $N^{simu-|\vec{p}_s| < 200 \text{ MeV}}$  corresponds to the simulation yields in each kinematic bin after applying  
 1042  $|\vec{p}_s| < 200$  MeV cut. The green and red areas are shown in the Fig 2.36 to represent the integral  
 1043 of  $|\vec{p}_s|$  distribution below and above the 200 MeV cut individually.

1044 The quasi-free process strongly dominates in  $|\vec{p}_s| < 200$  MeV region. Fig. 2.37a shows the  
 1045 missing momentum of spectator proton for black experimental data, red simulated data, and  
 1046 blue simulated data that is smeared due to the experimental resolution for the reconstructed  
 1047 measured missing momentum. This experiment is shown in Fig. 2.38. Since there is a clear  
 1048 difference between the simulated red and measured black missing momentum distribution, any  
 1049 final state interaction with a momentum transfer between spectator proton and any other  
 1050 hadron that is on average larger than 10 MeV (corresponding to an energy transfer larger than  
 1051 50 KeV) would cause a comparable additional smearing of the measured distribution beyond  
 1052 the smearing due to experimental resolution. Whereas no statistically significant difference  
 1053 between the smeared simulated (blue) and measured (black) missing momentum distributions  
 1054 is visible in Fig. 2.37b.

1055 Based on the good agreement of the  $|\vec{p}_s|$  distribution below 200 MeV between the experi-  
 1056 mental data (black line) and simulation (blue line) in Fig. 2.36, the  $r(W, Q^2, \cos \theta_{\pi^-}^*, \phi_{\pi^-}^*)$  should  
 1057 be the best estimated correction factor for those good quasi-free events lost by the cut.



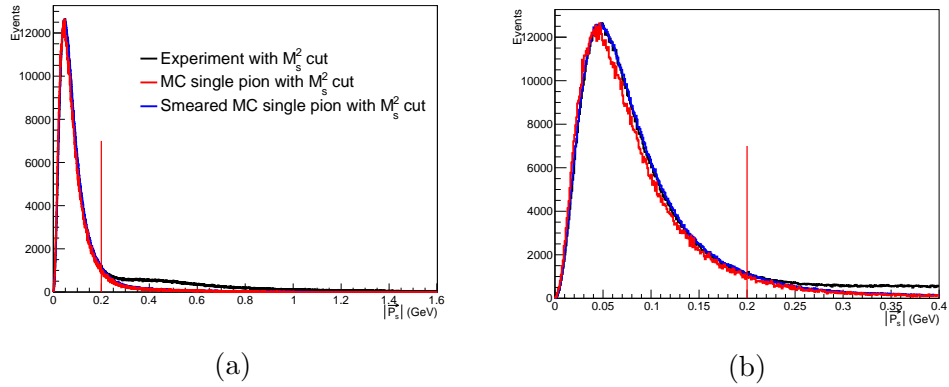


Figure 2.37: (a)(Color online) The black line represents the missing momentum distribution ( $|\vec{p}_s|$ ) of the unmeasured proton from experimental data. Based on the CD-Bonn potential [20], the Monte Carlo simulated scaled proton momentum distribution leads to the red line and the detector-smeared simulated scaled distribution to the blue line.(b) The zoomed plot of (a) to investigates this comparison clearly.

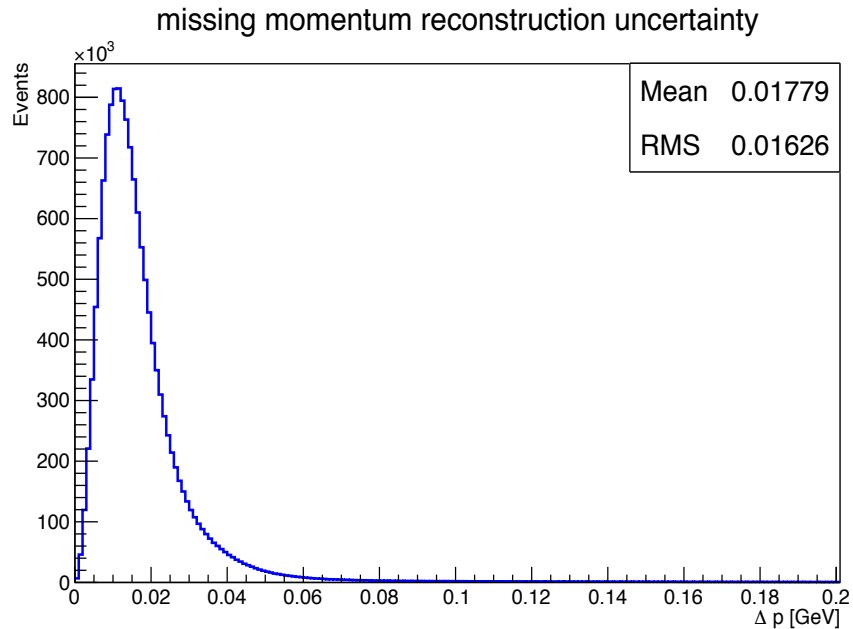


Figure 2.38: momentum resolution

# Chapter 3

## Simulation

In order to extract the cross sections for the reaction of interest, we need to have a good understanding of the detector behavior to get precision and accurate estimate of detector efficiency and acceptance. In this way, by correcting the obtained yield for the detector acceptance we can estimate the truly produced reaction yield. So, to obtain the detector acceptance we have to utilize a simulation process as laid out in the flowchart of Fig. 3.1. The details of each simulation step will be discussed in the following sections.

### 3.1 Event Generator

In this analysis, the electromagnetic multipole table [8] of the MAID2000 model [17] is used as an input for the event generator.  $en \rightarrow e'p\pi^-$  events with radiative effects, according to the prescription of Mo and Tsai [27], are generated by a modified version of the available “*ao\_rad*” software package (*cvs co ao\_rad* [9]). Based on the original “*ao\_rad*” package, for each generated  $en \rightarrow e'p\pi^-$  event, the initial neutron mass is set to the neutron rest mass and an additional proton is added as the output particle. This proton is generated based on the Fermi momentum from the CD-Bonn potential [20] and the rest proton mass. In this way, the generated proton is not change kinematics in the scattering process and behaves like a spectator ( $p_s$ ). It is, along with  $e'$ ,  $p$ , and  $\pi^-$ , reconstructed through the full simulation procedure, which is the same as the reconstruction procedure applied to the experimental data. After adding the “spectator” proton in the event generator, the simulated physics process is the same as the exclusive quasi-free process of the experimental data.

Besides the MAID2000 version, there are MAID98, MAID2003, and MAID2007 versions [18] also available in the “*ao\_rad*” package. In order to determine which version describes the experimental data best, we compare the  $W$  ( $W = W_f$ ) and  $Q^2$  distributions of the quasi-free exclusive events between different MAID versions and the data, as shown in Fig. 3.2a and Fig. 3.2b. The comparison of these  $W$  distributions shows that the MAID2000 version yields resonance peak positions that are closest to the data. The MAID2007 is the latest version, but the second resonance peak of that version is shifted relative to the experimental data. About 8 billion events were generated to cover the entire kinematic range listed in the Tab. 4.1 and a little bit beyond the range to account for resolution and bin migration effects for a total of 7830 kinematic bins.

### 3.2 GSIM

After generating the physics events of interest, the propagation of the final state particles through the CLAS detector is simulated. The available simulation package based on GEANT

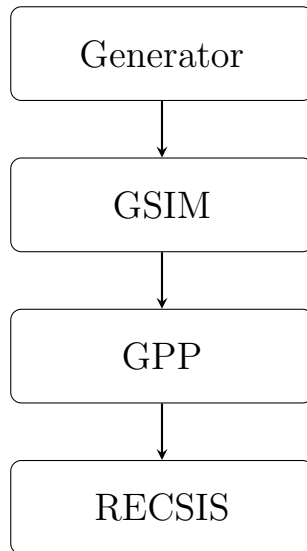


Figure 3.1: Flowchart showing the main steps of the detector and reaction simulation process.  $\gamma^*n(p) \rightarrow p\pi^-(p)$  events are generated by a realistic event generator, passed through GSIM [1] and GPP [2], and cooked by RECSIS [3].

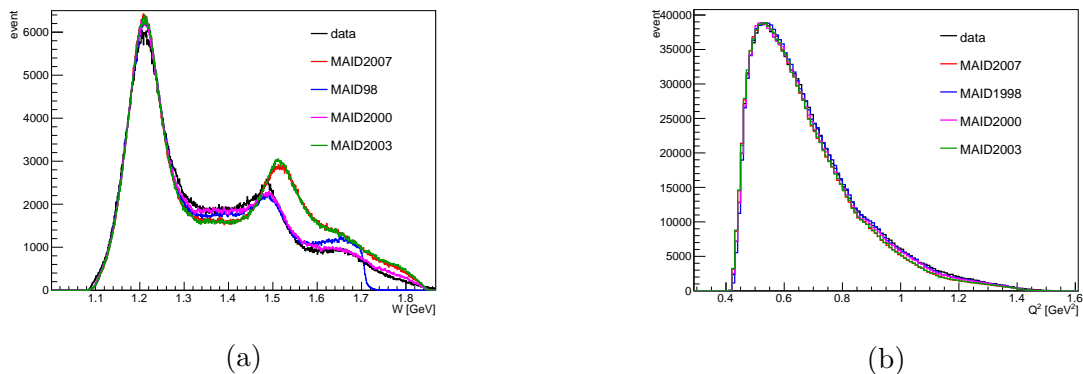


Figure 3.2: (a)  $W$  distributions of exclusive quasi-free events of experimental data (black) and the corresponding simulated distribution for the MAID98 (blue), MAID2000 (magenta), MAID2003 (green), and MAID2007 (red) versions. (b)  $Q^2$  distributions for the experimental events and the corresponding simulated events of (a).

1092 3 libraries (developed at CERN) of the CLAS collaboration, GSIM [1], propagates each of  
 1093 the particles through all CLAS detector components from the vertex produced by the event  
 1094 generator and provides the detector response in terms of raw signals (TDC and ADC) as does  
 1095 the actual CLAS detector. The GSIM-specific format-free read (“ffread card” [10]) is used as  
 1096 the configuration file of GSIM to configure which modules will be used in the simulation, which  
 1097 includes the following information for its command line option [5]:

- 1098 • energy cut-off in GEANT for various particles in various parts of the detector,
- 1099 • geometry of the detector,
- 1100 • magnetic field of the detector,
- 1101 • target material and geometry, and
- 1102 • beam position.

1103 The configuration file of GSIM listed in the reference [5] is used and adapted for this work only.

### 1104 3.3 GPP

1105 Although the GSIM simulation package includes all of the detector geometry and properties,  
 1106 it still overestimates the resolution of the drift chambers and SC system. So the GSIM Post  
 1107 Processor (GPP [2]) program is used to better match the resolution between experimental and  
 1108 simulation data, i.e. better agreement on the  $\Delta T$ ,  $M_s^2$ , and  $|\vec{P}_s|$  distributions of experimental  
 1109 and simulation data, which influence the results on the event selection level. There are two  
 1110 quantities to be adjusted in the GPP process. One is the DC smearing factor, which influences  
 1111 the tracking resolution, and the other is the SC smearing factor that adjusts timing resolution.  
 1112 Since experimental conditions may change by run, for the “ele” run, we have to find a new set  
 1113 of corresponding GPP smearing constants. For GPP parameter setting, we need to determine  
 1114 the run number (R), the DC smearing scale factor for regions 1, 2, and 3 ( $a$ ,  $b$ , and  $c$ ), and  
 1115 the SC smearing scale factor ( $f$ ). R should be set to any run number belonging to the “ele”  
 1116 run experimental data set in order to access the correct calibration constants in the calibration  
 1117 database. Assuming DC regions 1, 2, and 3 had identical resolutions, the same value is set for  
 1118  $a$ ,  $b$ , and  $c$ . We generated about 2 million electron-neutron exclusive quasi-free  $p\pi$  interaction  
 1119 events for each  $a = b = c$  and  $f$  combination to pass through the flowchart in Fig. 3.1. The  
 1120 quantity  $t_0$  (Eq. (2.9)) is measured to set the start time of each reconstructed event, which is  
 1121 used to calculate  $\Delta T$  for the hadron identification. So we can use it to determine the right  
 1122 value of  $f$ . For the simulation events, we set  $a = b = c = 2.5$  initially, which is consistent  
 1123 with the “ele” hydrogen target analysis [2]. Then by gradually changing the “f” values one  
 1124 obtains the Gaussian fitted  $\sigma$  values of the corresponding  $t_0$  distributions. In Fig. 3.4, these  
 1125  $\sigma$  values are presented by black points, which are fit by a linear function. In this way, we get  
 1126  $f = 0.9$  to match best the fitted  $\sigma$  value of the experimental data. In Fig. 3.3, the Gaussian  
 1127 fitted parameters  $\sigma$  show that the  $t_0$  distribution of experimental data and simulation have the  
 1128 same timing resolution by setting GPP parameters  $a = b = c = 2.5$  and  $f = 0.9$ .

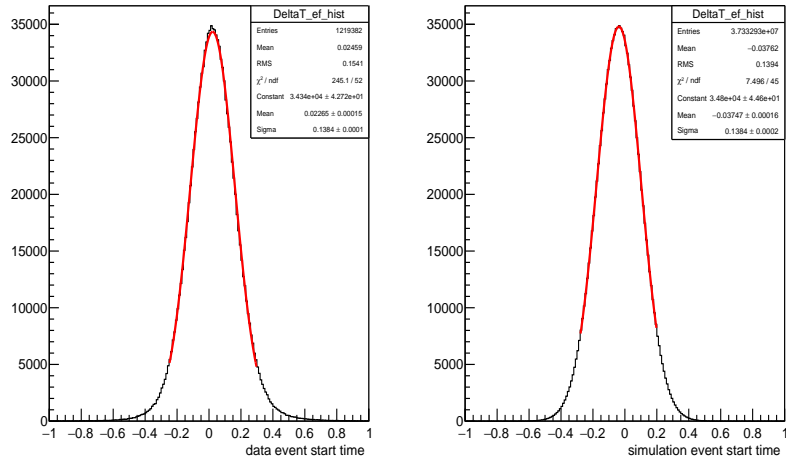


Figure 3.3: Event start time ( $t_0$ ) distributions of the exclusive quasi-free events for experimental data (left) and simulation with smearing factor  $f=0.9$  (right) are fit by Gaussian functions (red curves). The corresponding fit parameters are listed in the statistic boxes, respectively.

1129 The discrepancy between experiment and simulation reconstructed data of the “spectator”  
 1130 missing mass ( $M_s^2$ ) distribution, which can later influence our results, reflects the difference in  
 1131 the drift chamber resolution between experiment and simulation reconstructed data. Similar to  
 1132 the SC smearing factor determination, we fixed the parameter  $f = 0.9$  and changed  $a = b = c$   
 1133 parameters gradually for the simulation events. In Fig. 3.5, the Gaussian fitted  $\sigma$  values of  $M_s^2$

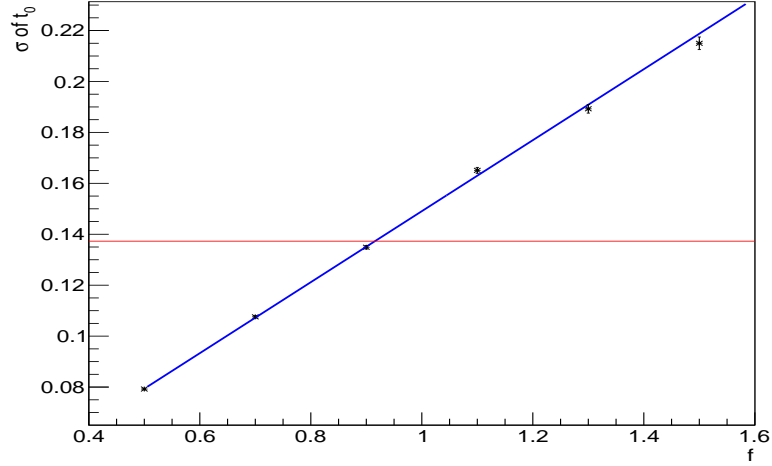


Figure 3.4: The  $\sigma$  of  $t_0$  versus  $f$  from the simulation events are fit by a linear function (blue), and the red line corresponds to the the  $\sigma$  of  $t_0$  from the measured exclusive quasi-free events. The  $f$  value corresponding to the cross point is used to smear the simulated detector SC resolution.

1134 distributions corresponding to different  $a = b = c$  values are plotted as black points and are  
 1135 fit by a linear function. From the fitted linear function, we finally set the smearing parameters  
 1136  $a = b = c = 2.5$  for the simulation events, which smear the drift chambers resolution of the  
 1137 simulation in the same way as the experiment does. We plot the  $M_s^2$  distributions of the  
 1138 simulation reconstructed events with GPP parameters  $f = 0.9$  and  $a = b = c = 2.5$  and the  
 1139 experimental reconstructed events in Fig. 5.7, and their Gaussian fitted parameters  $\sigma$  are equal  
 1140 to each other at  $\sigma = 0.01978$ , which shows the GPP parameters are under control for this  
 analysis.

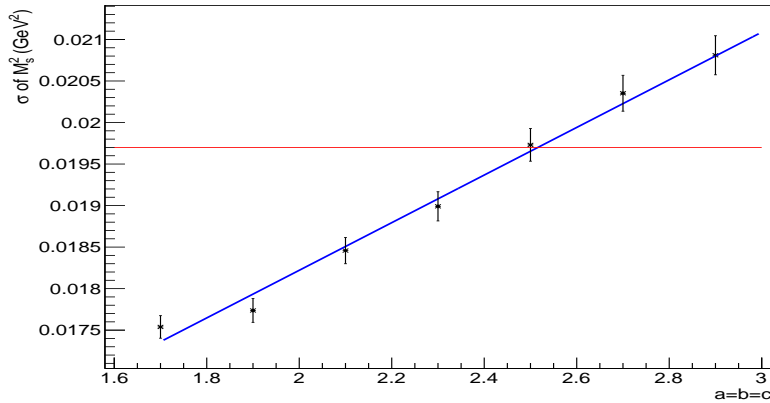


Figure 3.5: The fitted  $\sigma$  values of  $M_s^2$  distributions depending on different  $a = b = c$  values are plotted as black points. These are fit by a linear function (blue). The red horizontal line represents the fitted  $\sigma$  values of  $M_s^2$  distributions from the experimental reconstructed events. The value of  $a = b = c$  corresponding to the cross point is used to smear the simulated detector DC resolution.

1141

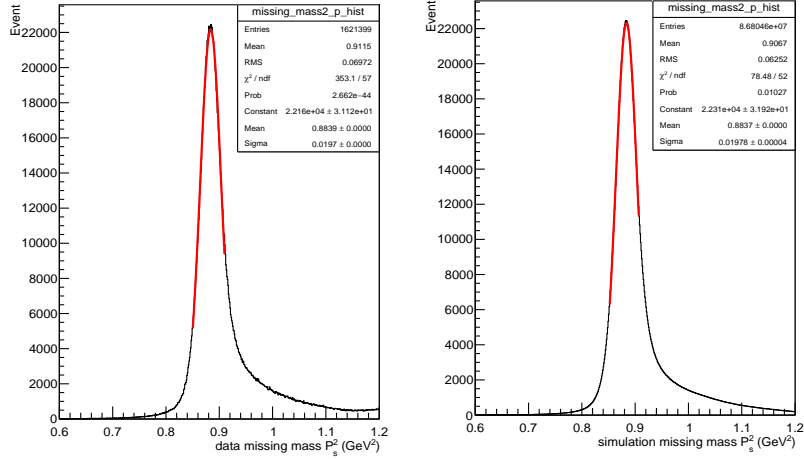


Figure 3.6: The  $M_s^2$  distributions of the exclusive quasi-free events for experimental data (left) and simulation with smearing factors  $f = 0.9$  and  $a = b = c = 2.5$  (right) are fit by Gaussian functions (red). The corresponding fit parameters are shown in their statistics legend boxes.

### 1142 3.4 RECSIS

1143 After the generated physics events are processed through GSIM and GPP, the outputs of GPP  
 1144 still contain ADC and TDC hit information for each detector component. Then the output  
 1145 files must be processed with the same reconstruction software (RECSIS) that is used for the  
 1146 experimental raw data. Certain modifications however were implemented in the processing of  
 1147 simulated data [3]. After the processing, the simulated events are analyzed similarly to the  
 1148 experimental events and are used to obtain the acceptance corrections, which are then applied  
 1149 to the experimental yield to extract the  $\gamma^*n(p) \rightarrow p\pi^-(p)$  cross sections. All the details are  
 1150 discussed in the following chapters.

# Chapter 4

## Corrections and Normalization

The simulated events are used to obtain the acceptance corrections, and the cross section function of the MAID model is used to calculate the bin centering corrections, both of which are applied to the final cross sections calculation. The incoming and outgoing scattered electrons can change their energy (emit photons) due to the radiative effects. Although those effects don't influence the kinematic variable  $W_f$  ( $W_f = \sqrt{(p^\mu + (\pi^-)^\mu)^2}$ ), but they can influence the variable  $Q^2$ . And we present the final cross sections in the kinematic variable  $W_f$ . As a cross check, in Fig. 1.3 of Chapter 1, the radiative corrected  $W_i$  distribution, where  $W_i$  is calculated by setting  $M_n$  by Eq. (1.15) of  $n^\mu$ , is consistent with the  $W_f$  distribution. For this work, the radiative effects are marginal compared to the systematic uncertainties. In addition to these corrections, we also check for consistency of the experimental data with other known cross sections, such as inclusive cross section of the process  $eD \rightarrow eX$ . All details of those procedures will be discussed in the following sections.

### 4.1 Kinematic Binning

In Chapter 1, we introduced the kinematic variables  $W = W_f$ ,  $Q^2$ ,  $\cos\theta_\pi^*$ , and  $\phi_\pi^*$  in which we present the final cross sections. The range of each kinematic variable is determined by the kinematic nature of the data, and the bin size is needed to be chosen as fine as possible to address the structure of the cross section; meanwhile we also need to minimize the statistical uncertainties to guarantee enough statistics in each kinematic bin. One possible binning solution is listed in Table 4.1 and is illustrated in Fig. 4.1 for  $W$  range covering the  $\Delta$  resonance, the second resonance, and the third resonance regions.  $W$  coverage is narrower at higher  $Q^2$  due to the kinematic limitations.

Table 4.1:  $W$  and  $Q^2$  binning of the analysis.

Variable	Lower limit	Upper limit	Number of bins	Bin size
$W$ , GeV	1.1	1.825	29	0.025 GeV
$Q^2$ , GeV <sup>2</sup>	0.4	1.0	3	0.2 GeV <sup>2</sup>

We observe the highest statistics in  $1.2 \text{ GeV} < W < 1.225 \text{ GeV}$  and  $0.4 \text{ GeV}^2 < Q^2 < 0.6 \text{ GeV}^2$  bin in Fig. 4.1. We show an example distribution corresponding to  $\cos\theta_\pi^*$  versus  $\phi_\pi^*$  distribution with  $\phi_\pi^*$  binned in 9 bins in Fig. 4.2. Due to the low  $\pi^-$  detector acceptance, even in this highest statistics  $W$  and  $Q^2$  bin, there are empty kinematic phase space cells in the very forward and the very backward  $\phi_{\pi^-}^*$  angles. We tried to enlarge the bin width of the variable  $\phi_{\pi^-}^*$ , different choices are presented in the Table 4.2. However, this method does not solve the empty cells problem except by increasing the number data points to help the cross

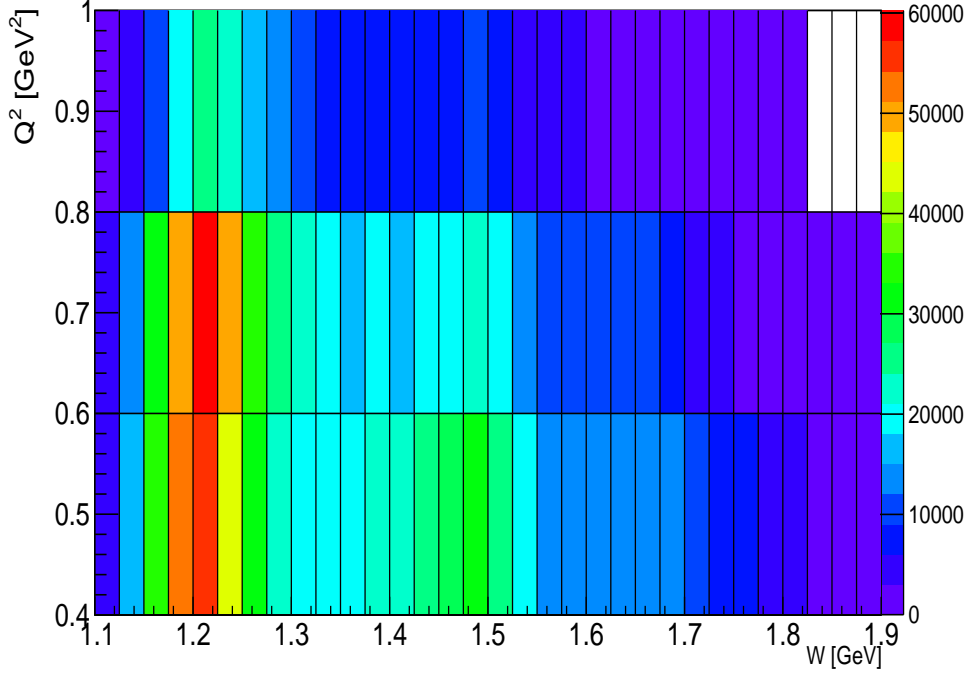


Figure 4.1:  $W$  and  $Q^2$  binning for the  $\pi^-$  electroproduction events, where vertical and horizontal lines are shown as the lower and upper corresponding bin limits.

1181 section process and serve as consistency check. In order to study the consistency of and to get  
 1182 the proper cross sections  $\phi^*$  dependence behavior, three sets of  $\phi^*$  bins have been chosen and  
 1183 combined to extract the cross section fit parameters by normalizing to the corresponding bin  
 size. These are listed in Tab. 4.2.

Table 4.2:  $\cos \theta_{\pi^-}^*$  and  $\phi_{\pi^-}^*$  binning of the analysis.

Variable	Lower limit	Upper limit	Number of bins	Bin size
$\cos \theta_{\pi^-}^*$	-1	1	10	0.2
$\phi_{\pi^-}^*$	$0^\circ$	$360^\circ$	9	$40^\circ$
$\phi_{\pi^-}^*$	$0^\circ$	$360^\circ$	8	$45^\circ$
$\phi_{\pi^-}^*$	$0^\circ$	$360^\circ$	6	$60^\circ$

1184

## 1185 4.2 Bin Centering Corrections

1186 The kinematic variables bin-size compromise with our bin-size setting discussed above reveals  
 1187 nicely that the cross section might vary significantly within each kinematic bin. In fact, the  
 1188 extracted cross section  $\frac{d\sigma}{d\Omega_{\pi^-}^*}$  is an average value for each 4 dimensional ( $W, Q^2, \cos \theta^*, \phi^*$ ) bin.  
 1189 Because of the possibly non-linear behavior of the cross section within a bin, the average cross-  
 1190 section value does not necessarily correspond to the center of the bin. So presenting the final  
 1191 cross section at the center of the bin may not be accurate. To account for such an error, a  
 1192 correction is applied to the cross sections for each 4 dimensional ( $W, Q^2, \cos \theta^*, \phi^*_{\pi^-}$ ) bin. This  
 1193 bin-centering correction ( $R_{BC}$ ) is calculated as

$$R_{BC}(W, Q^2, \cos \theta^*, \phi_{\pi^-}^*) = \frac{\sigma_{center}^{model}}{\sigma_{average}^{model}}, \quad (4.1)$$



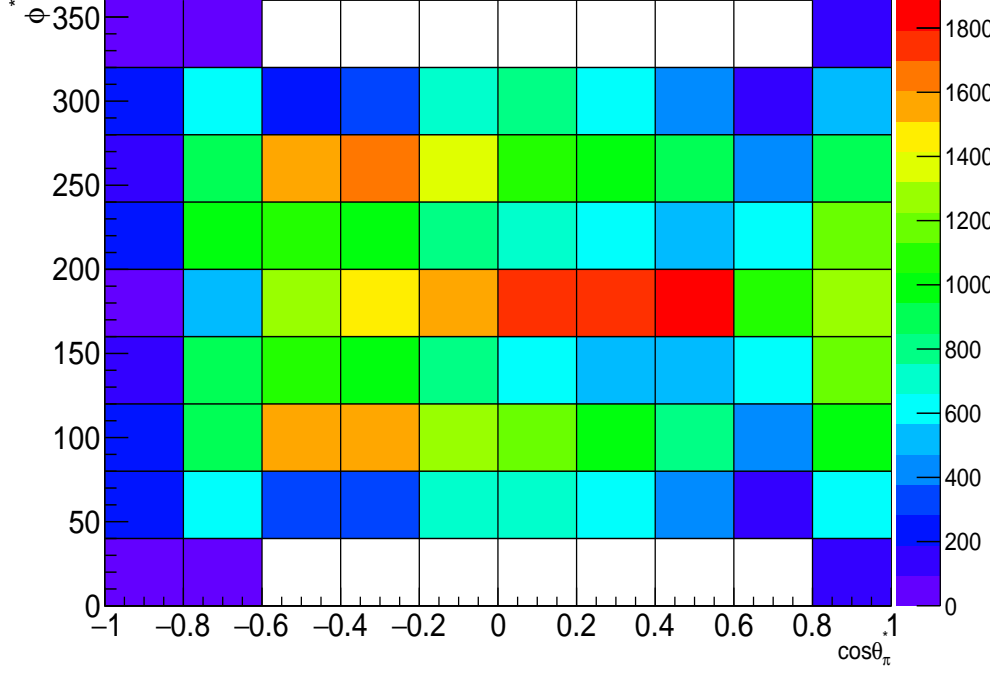


Figure 4.2: Example  $\cos \theta^*$  and  $\phi^*$  binning for the  $\pi^-$  electroproduction events in  $1.2 \text{ GeV} < W < 1.225 \text{ GeV}$  and  $0.4 \text{ GeV}^2 < Q^2 < 0.6 \text{ GeV}^2$  bin, where vertical and horizontal lines show the lower and the upper bin limits.

1194 where  $\sigma_{center}^{model}$  is the cross section calculated by using the parameterization function of MAID2000  
 1195 model at the numerical center of each kinematic bin, and  $\sigma_{average}^{model}$  is

$$\sigma_{average}^{model} = \frac{\int_{x_1}^{x_2} \sigma(x) dx}{\Delta W \Delta Q^2 \Delta \cos \theta^* \Delta \phi^*}, \quad (4.2)$$

1196 where  $x$  presents the kinematic bin  $(W, Q^2, \cos \theta^*, \phi^*)$ ,  $x_1$  and  $x_2$  are the limits of the bin, and  
 1197  $\sigma(x)$  is the MAID2000 model cross-section function. Figure 4.3 shows  $R_{BC}$  as a function of  
 1198  $\cos \theta^*$  and  $\phi^*$  for the example bin at  $W = 1.2125 \text{ GeV}$  and  $Q^2 = 0.5 \text{ GeV}^2$ .

### 1199 4.3 Luminosity

1200 The integrated luminosity ( $\mathcal{L}_{int}$ ) of “e1e” run is calculated as

$$\mathcal{L}_{int} = N_e N_d = \left( \frac{Q_{tot}}{e} \right) \times \left( \frac{N_A d_T l_T}{M_d} \right) = 2.6788 \times 10^{39} \text{ cm}^{-2}, \quad (4.3)$$

1201 where  $Q_{tot}$  is the total live time accumulated Faraday cup charge (4.420 mC), which is collected  
 1202 during the entire experiment production period. Furthermore,  $e$  is the elementary charge  
 1203 ( $1.6 \times 10^{-19} \text{ C}$ ),  $d_T$  is the density of the liquid deuterium target ( $0.1624 \text{ g/cm}^3$ , ignoring the  
 1204 temperature and pressure fluctuation of the target system),  $l_T$  is the target length (2 cm),  $N_A$  is  
 1205 Avogadro’s number ( $6.02 \times 10^{23} \text{ mol}^{-1}$ ), and  $M_d$  is the molar density of deuterium ( $2.014 \text{ g/mol}$ ).  
 1206 This value of  $\mathcal{L}_{int}$  is used in the Eq. (5.1) to calculate the cross section.

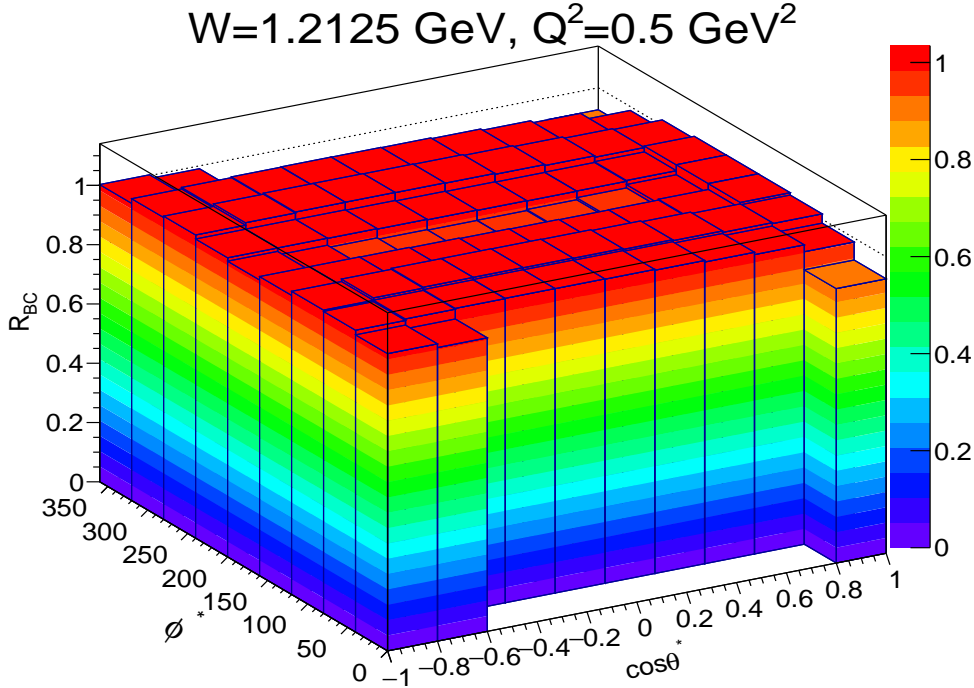


Figure 4.3: Bin centering corrections  $R_{BC}$  as a function of  $\cos\theta^*$  and  $\phi^*$  in the  $W = 1.2125 \text{ GeV}$  and  $Q^2 = 0.5 \text{ GeV}^2$  bin.

## 1207 4.4 Empty-Target Background Subtraction

1208 The “ele” empty-target run numbers are 36597, 36617, 36618, and 36619. These are used to  
 1209 estimate the background originating from the  $50 \mu\text{m}$ -thick Kapton target walls and subtract  
 1210 it from the full-target run data. The liquid Deuterium target in those runs was emptied. In  
 1211 order to quantify this background, all events from all empty-target runs are collected, then  
 1212 the same data analysis procedure is applied to those events. Then, the electron z-vertex ( $Z_e$ )  
 1213 distributions for full-target and empty-target events are compared as shown in Fig. 4.4a. There  
 1214 is a small peak at 2.58 cm due to the forward foil window, which should be exactly at the  
 1215 same position for both full-target and empty-target events. This peak can be used to judge the  
 1216 quality of the empty-target background subtraction. We calculate the integrated Faraday cup  
 1217 charge ratio by

$$S_{ratio} = \frac{Q_{total}}{Q_{empty}} = \frac{4.420 \text{ mC}}{0.467 \text{ mC}} = 9.465, \quad (4.4)$$

1218 where  $Q_{empty}$  is the total live time accumulated Faraday cup charge for all empty-target runs.  
 1219 Therefore, the empty-target  $Z_e$  distribution must be multiplied by  $S_{ratio}$  to be compared with  
 1220 the corresponding distribution of the full-target run events. The scaled  $Z_e$  distribution of the  
 1221 empty-target (red) in Fig. 4.4a has two peaks for the Kapton cell wall, and one peak at 2.73 cm  
 1222 related to the forward foil, which is slightly shifted from the corresponding peak in the full-  
 1223 target event distribution. The corresponding shift-corrected  $Z_e$  distribution of the empty-target  
 1224 (red) is plotted in Fig. 4.4b, where the forward foil peak is now consistent with that of the full-  
 1225 target  $Z_e$  distribution. We then subtract the  $S_{ratio}$  corrected empty-target  $Z_e$  distributions  
 1226 from the full-target  $Z_e$  distribution sector by sector. This procedure allows us to check that  
 1227 the 2.73 cm peak is vanished properly after subtracting the empty-target  $Z_e$  distribution from  
 1228 that of the full-target, examples are shown in Fig. 4.5. It turns out that the  $S_{ratio}$  has been  
 1229 determined correctly and that we can safely use it to subtract the  $S_{ratio}$  scaled empty-target  
 1230 from the full-target events in each kinematic bin and to extracted the final cross sections with

1231 Eq. (5.1). The absolute amount of this background due to cell walls is less than 1%, and the  
 1232 error of this background correction is absolutely negligible.

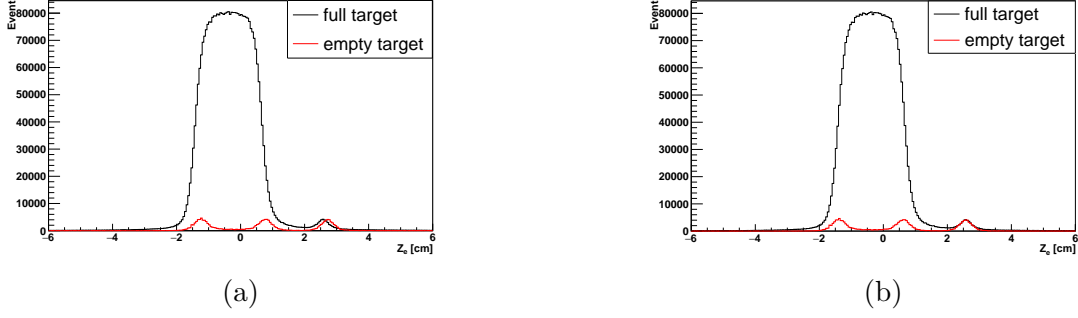


Figure 4.4: (a) Measured electron vertex ( $Z_e$ ) distributions for full target events (black) and scaled empty target events (red). (b) The black distribution is kept the same as (a), and the vertex distribution for scaled empty target events is shifted to ( $Z_e - 1.5$  mm) (red).

1232

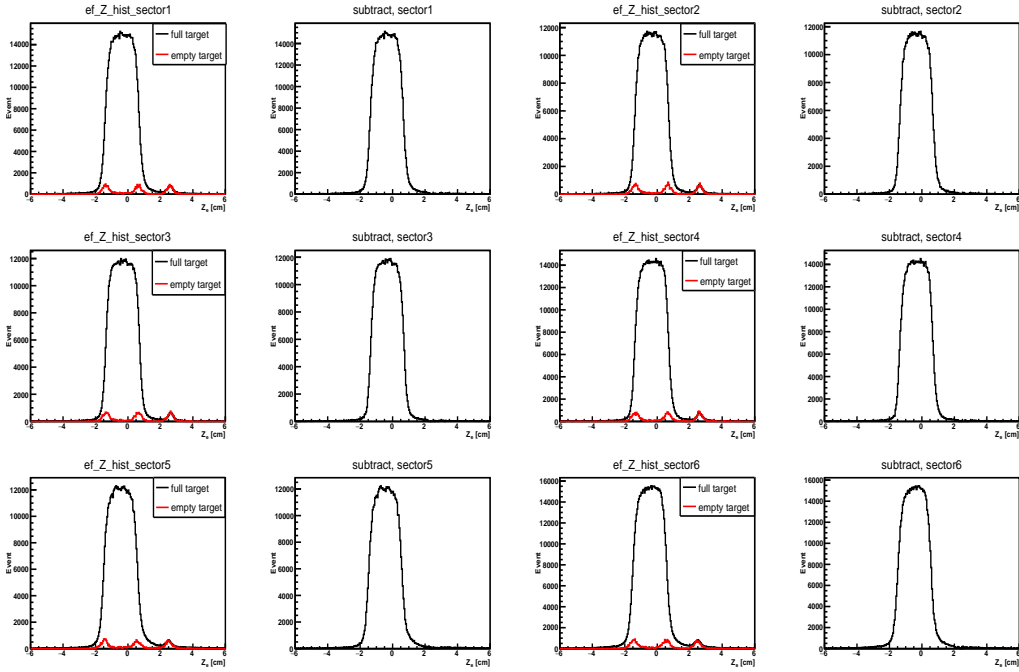


Figure 4.5:  $Z_e$  distributions for full- $LD_2$ -target (black) and scaled empty-target events (red) are plotted together in one canvas and compared with these of the empty target subtracted full  $LD_2$  target events sector by sector.

## 1233 4.5 Acceptance Corrections

1234 Acceptance correction factors ( $A^{Rad}$ ) are calculated using the Monte Carlo simulated events  
 1235 (total  $8 \times 10^9$  events to avoid statistics bias) for each 4-dimensional bin as

$$A^{Rad}(W, Q^2, \cos \theta^*, \phi^*) = \frac{N_{rec}^{Rad}(W, Q^2, \cos \theta^*, \phi^*)}{N_{thrown}^{Rad}(W, Q^2, \cos \theta^*, \phi^*)}, \quad (4.5)$$

1236 where  $N_{thrown}^{Rad}(W, Q^2, \cos \theta^*, \phi^*)$ , known as “thrown events”, represents the number of events  
 1237 that are generated by the physics event generator “*aao\_rad*” with the MAID2000 model in

1238 each kinematic bin radiative effects included.  $N_{rec}^{Rad}$  denotes the number of events in the same  
 1239 kinematic bin that have gone through the entire simulation process as shown in Fig. 3.1 and  
 1240 passed all analysis cuts, which are shown in the Tab. 5.1. Those acceptance corrections are  
 1241 applied to obtain the cross sections bin by bin later.

Table 4.3: Event Selection.

cuts	data	simulation
Electron $\theta_{CC}$ cut	yes	yes
Electron SF cut	yes	yes
Electron fiducial cut	yes	yes
Proton $\Delta T$ cut	yes	yes
Proton fiducial cut	yes	yes
Pion $\Delta T$ cut	yes	yes
Pion fiducial cut	yes	yes
Electron momentum correction	yes	no
Proton energy loss correction	yes	yes
$M_s^2$ cut	yes	yes
$p_s$ cut	yes	ye

## 1242 4.6 Radiative Corrections

1243 For this analysis, the approach developed by Mo and Tsai [27] is used for correcting the final  
 1244 results. The same amount of  $en \rightarrow e' p \pi^-$  events with and without radiative effects are generated  
 1245 by the available “*ao\_rad*” and “*ao\_norad*” software packages [9], respectively, by applying  
 1246 the same electromagnetic multipole table from the MAID2000 model. The radiative correction  
 1247 factor  $RC$  is calculated by

$$RC(W, Q^2, \cos \theta^*, \phi^*) = \frac{N_{thrown}^{Rad}(W, Q^2, \cos \theta^*, \phi^*)}{N_{thrown}^{noRad}(W, Q^2, \cos \theta^*, \phi^*)}, \quad (4.6)$$

1248 where  $N_{thrown}^{noRad}(W, Q^2, \cos \theta^*, \phi^*)$  are “thrown events” without radiative effects that are generated  
 1249 by the physics event generator “*ao\_norad*” in each kinematic bin.  $N_{thrown}^{Rad}(W, Q^2, \cos \theta^*, \phi^*)$   
 1250 corresponds to the same quantity used in Eq. (4.5). Finally the  $RC$  will be combined with the  
 1251 acceptance corrections factor  $A^{Rad}$  (Eq. (4.5)) to calculate the radiative corrected acceptance  
 1252  $A_{RC}$ , which is represented by

$$\begin{aligned} A_{RC}(W, Q^2, \cos \theta^*, \phi^*) &= A^{Rad}(W, Q^2, \cos \theta^*, \phi^*) RC_{correct}(W, Q^2, \cos \theta^*, \phi^*) \\ &= \frac{N_{rec}^{Rad}(W, Q^2, \cos \theta^*, \phi^*)}{N_{thrown}^{Rad}(W, Q^2, \cos \theta^*, \phi^*)} \frac{N_{thrown}^{Rad}(W, Q^2, \cos \theta^*, \phi^*)}{N_{thrown}^{noRad}(W, Q^2, \cos \theta^*, \phi^*)} \\ &= \frac{N_{rec}^{Rad}(W, Q^2, \cos \theta^*, \phi^*)}{N_{thrown}^{noRad}(W, Q^2, \cos \theta^*, \phi^*)}. \end{aligned} \quad (4.7)$$

1253 This factor is applied to the calculation of the cross sections in the Chapter 5, the example is  
 1254 shown in Eq. (5.1).

## 1255 4.7 Background Subtraction

1256 In order to obtain the right number of exclusive events for the process  $\gamma^* n(p) \rightarrow p \pi^- (p)$  from  
 1257 deuterium target data, we need to remove all possible backgrounds within the  $M_s^2$  cut region.

1258 For this reason, the events of the  $\gamma^*p \rightarrow p\pi^-\pi^+$  process, considered to be the main source  
1259 of possible physics background, are simulated by the double-pion scattering event generator  
1260 (“genev” [11]) under the same experimental condition as the “e1e” run. Then, we applied  
1261 the same data analysis procedure to these simulated events, and compared their  $M_s^2$  (calcu-  
1262 lated from Eq. (2.29)) distributions with that of the “e1e” run experimental data and the  
1263  $\gamma^*n(p) \rightarrow p\pi^-(p)$  simulation events to check the background contributions. The compared  
1264 results are shown in Fig. 4.6. Inside the  $0.811 \text{ GeV}^2 < M_s^2 < 0.955 \text{ GeV}^2$  cut region, there is no  
1265  $\gamma^*p \rightarrow p\pi^-\pi^+$  background contribution below  $1.1 \text{ GeV}^2$ . Furthermore, in order to check the ar-  
1266 bitrary background contribution, we compare the  $M_s^2$  distributions for experimental events with  
1267 simulated  $\gamma^*n(p) \rightarrow p\pi^-(p)$  events bin by bin. Typical example plots are shown in Fig. 4.7.  
1268 The  $M_s^2$  distributions of simulated events (red points) are normalized to the data distribution  
1269 by the integral of their  $M_s^2$  cut areas. In summary, from these above comparisons, there is no  
1270 need to do any background subtraction for the exclusive  $\gamma^*n(p) \rightarrow p\pi^-(p)$  process in the “e1e”  
1271 run.

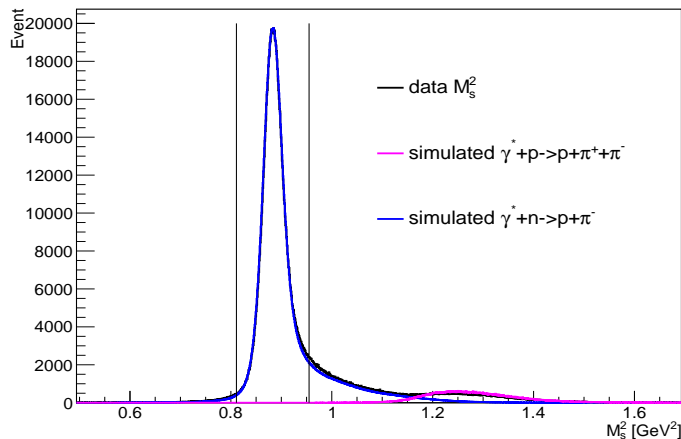


Figure 4.6:  $M_s^2$  distributions for measured (black) and simulated  $\gamma^*n(p) \rightarrow p\pi^-(p)$  (blue), as well as simulated  $\gamma^*p \rightarrow p\pi^-\pi^+$  events are plotted with the  $M_s^2$  cut limits.

## 1272 4.8 Inclusive Cross Section

1273 In order to cross check the determined luminosity in the deuteron-target measurement, we ex-  
1274 tract and compare the cross section of the inclusive scattering  $eD \rightarrow e'X$  process to Osipenko’s  
1275 world-data parameterization results [31]. In addition to this, we need to check if the problem of  
1276 the Cherenkov counter not working properly during the hydrogen target period [21] is presented  
1277 also in the deuteron target data.

1278 For inclusive scattering, since the cross section only depends on two kinematical variables,  
1279 it is convenient to choose  $W$  and  $Q^2$  as binning variables. Then, the inclusive cross section is  
1280 calculated by

$$\frac{d\sigma^2(W, Q^2)}{dWdQ^2} = \frac{N_{full}(W, Q^2) - S_{ratio}N_{empty}(W, Q^2)}{\mathcal{L}_{int}\Delta W\Delta Q^2\varepsilon_{eff}(W, Q^2)}, \quad (4.8)$$

1281 where  $N_{full}(W, Q^2)$  and  $N_{empty}(W, Q^2)$  correspond to the full-and the empty-target event yields  
1282 in each  $(W, Q^2)$  bin. These are inclusive scattering events which passed the whole electron  
1283 identification procedure described in Chapter 2. Furthermore,  $S_{ratio}$  and  $\mathcal{L}_{int}$  are calculated by  
1284 Eq. (4.4) and Eq. (4.3), respectively.  $\Delta W$  and  $\Delta Q^2$  represent the corresponding bin widths.

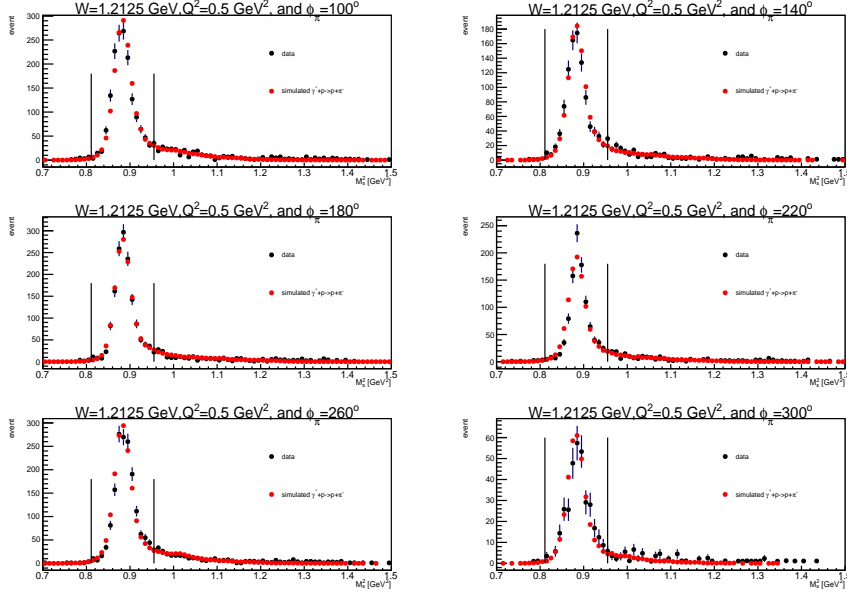


Figure 4.7:  $M_s^2$  distributions for measured (black) and simulated  $\gamma^*n(p) \rightarrow p\pi^-(p)$  (red) events are plotted with the  $M_s^2$  cut limits for  $W = 1.2125$  GeV,  $Q^2 = 0.5$  GeV<sup>2</sup>, and  $\cos\theta^* = -0.3$  in  $\phi_{\pi^-}^* = 100^\circ, 140^\circ, 180^\circ, 220^\circ, 260^\circ,$  and  $300^\circ$  bins individually.

1285 In addition,  $\varepsilon_{eff}(W, Q^2)$  is the acceptance correction for each  $(W, Q^2)$  bin calculated as

$$\varepsilon_{eff}(W, Q^2) = \frac{N_{rec}(W, Q^2)}{N_{thrown}(W, Q^2)}, \quad (4.9)$$

1286 where  $N_{rec}$  denotes to the number of events that passed through the entire simulation process  
 1287 as shown in Fig. 3.1, including the electron identification procedure,  $N_{thrown}$  represents those  
 1288 events that are generated by Osipenko's inclusive deuteron scattering event generator [12]. The  
 1289 generator is based on the world data cross section and includes radiative effects. In order to save  
 1290 simulation time, the thrown events are only generated in a looser fiducial-cut region compared  
 1291 to the data instead of in the complete  $4\pi$  phase space. In general, the inclusive cross section is  
 1292 calculated from the world data by

$$\frac{d\sigma^2(W, Q^2)}{dWdQ^2} = \frac{N_{thrown}(W, Q^2)}{N_{total}\Delta W\Delta Q^2}\sigma_{int}, \quad (4.10)$$

1293 where  $N_{total}$  is the total number of events generated in  $4\pi$  phase space,  $N_{thrown}(W, Q^2)$  corre-  
 1294 sponds to the yield in each  $(W, Q^2)$  bin, and  $\sigma_{int}$  is the integral cross section of the world data.  
 1295 In this way, we compare the inclusive  $eD \rightarrow e'X$  cross section calculated by Eq. (4.8) from the  
 1296 experimental data with that calculated by Eq. (4.10) from the world data parameterization.  
 1297 However, in this particular case, instead of comparing Eq. (4.8) with Eq. (4.10) results, one can  
 1298 compare  $\varepsilon_{eff}(W, Q^2) \times$  Eq. (4.8) with the  $\varepsilon_{eff}(W, Q^2) \times$  Eq. (4.10) results. For this particular  
 1299 event generator,  $\varepsilon_{eff}(W, Q^2)$  can also be written as

$$\varepsilon_{eff}(W, Q^2) = \frac{N_{rec}(W, Q^2)}{N_{thrown}(W, Q^2)} = \frac{N_{rec}(W, Q^2)\varepsilon_{fid}^{osi}(W, Q^2)}{N_{thrown}^{osi}(W, Q^2)}, \quad (4.11)$$

1300 where  $N_{thrown}^{osi}(W, Q^2)$  corresponds to the yield in each  $(W, Q^2)$  bin with  $\theta$  and  $\phi$  angles covered  
 1301 in Dr.Osipenko's fiducial-cut region [12] and  $\varepsilon_{fid}^{osi}(W, Q^2)$  is defined as  $\frac{N_{thrown}^{osi}(W, Q^2)}{N_{thrown}(W, Q^2)}$ .

1302 Multiplying Eq. (4.8) by  $\varepsilon_{eff}(W, Q^2)$ , the corresponding result is given by

$$\varepsilon_{eff}(W, Q^2) \times Eq. (4.8) = \frac{N_{full}(W, Q^2) - \frac{Q_{full}}{Q_{empty}}N_{empty}(W, Q^2)}{\mathcal{L}_{int}\Delta W\Delta Q^2}. \quad (4.12)$$

1303 Furthermore, we multiply Eq. (4.10) by  $\varepsilon_{eff}(W, Q^2)$ , which is calculated by Eq. (5.4) and leads  
 1304 to the whole expression

$$\begin{aligned}
 \varepsilon_{eff}(W, Q^2) \times Eq. (4.10) &= \frac{N_{rec}(W, Q^2)\varepsilon_{fid}^{osi}(W, Q^2)}{N_{thrown}^{osi}(W, Q^2)} \times \frac{N_{thrown}(W, Q^2)}{N_{total}\Delta W\Delta Q^2}\sigma_{int} \\
 &= \frac{N_{rec}(W, Q^2)\varepsilon_{fid}^{osi}(W, Q^2)}{N_{thrown}^{osi}(W, Q^2)} \times \frac{N_{thrown}^{osi}(W, Q^2)\varepsilon_{fid}^{osi}\sigma_{int}}{\varepsilon_{fid}^{osi}(W, Q^2)N_{total}\Delta W\Delta Q^2} \\
 &= \frac{N_{rec}(W, Q^2)}{N_{total}^{osi}\Delta W\Delta Q^2}\sigma_{int}^{osi},
 \end{aligned} \tag{4.13}$$

1305 where  $\varepsilon_{fid}^{osi}$  is the acceptance factor of Osipenko's event generator and  $\sigma_{int}^{osi}$  is the reduced inte-  
 1306 gral cross section corresponding to the Osipenko's fiducial-cut region. So finally, we compare  
 1307 Eq. (4.12) and Eq. (4.13) directly, and the corresponding comparison plots are shown in Fig. 4.8.  
 1308 Where the data normalized yields (black stars) extracted from Eq. (4.12) project on  $W$  vari-  
 1309 able in each individual  $Q^2$  bin are consistent with the model dependent Osipenko's world-data  
 1310 parameterization results calculated from Eq. (4.13) (magenta stars), which shows that overall  
 1311 luminosity and hence the corresponding normalization procedure is reliable within the esti-  
 1312 mated systematic error of 5% (see Chapter 5) and can therefore be applied to the exclusive  
 1313 scattering  $\gamma^*n(p) \rightarrow p\pi^-(p)$  process.

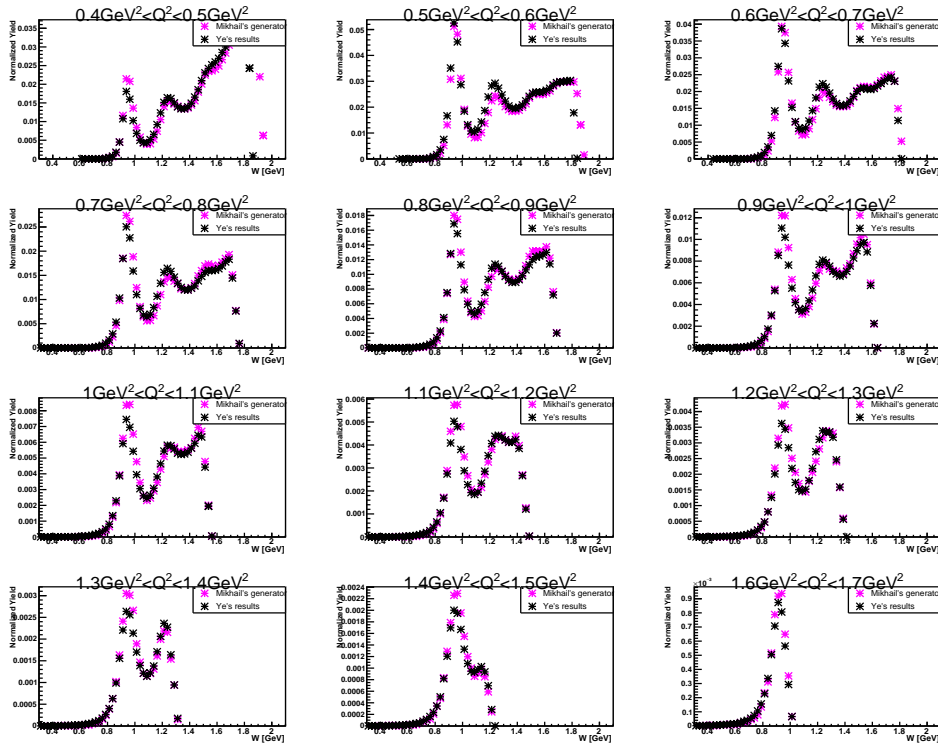


Figure 4.8:  $W$  dependent normalized yield distributions in the  $eD \rightarrow e'X$  process are presented for data with black stars and for Osipenko's world-data parameterization with magenta stars in individual  $Q^2$  bins from  $0.4 \text{ GeV}^2$  to  $1.7 \text{ GeV}^2$  in steps of  $\Delta Q^2 = 0.1 \text{ GeV}^2$ .

# Chapter 5

## Results

With all the information discussed in the previous chapters, the final cross sections will be calculated in this chapter.

### 5.1 Cross Sections

#### 5.1.1 The Exclusive Cross Section

The exclusive cross section of the  $\gamma^*n(p) \rightarrow p\pi^-(p)$  process can be calculated from the acceptance corrected yield of the exclusive events as

$$\begin{aligned} \frac{d\sigma^{ex}}{d\Omega_{\pi^-}^*} &= \frac{1}{\Gamma_v(W, Q^2)} \frac{d^4\sigma}{dW dQ^2 d\Omega_{\pi^-}^*} \\ &= \frac{(\Delta N_{full}(W, Q^2, \cos\theta_{\pi^-}^*, \phi_{\pi^-}^*) - S_{ratio}\Delta N_{empty}(W, Q^2, \cos\theta_{\pi^-}^*, \phi_{\pi^-}^*))R_{BC}}{\Gamma_v(W, Q^2) A_{RC}(W, Q^2, \cos\theta_{\pi^-}^*, \phi_{\pi^-}^*)\Delta W \Delta Q^2 \Delta \cos\theta_{\pi^-}^* \Delta \phi_{\pi^-}^* \mathcal{L}_{int}}, \end{aligned} \quad (5.1)$$

where  $\Delta N_{full}$  and  $\Delta N_{empty}$  represent the numbers of the exclusive events inside each 4-dimensional bin  $(W, Q^2, \cos\theta_{\pi^-}^*, \phi_{\pi^-}^*)$  for the target with and without  $LD_2$ , respectively.  $A_{RC}(W, Q^2, \cos\theta_{\pi^-}^*, \phi_{\pi^-}^*)$  is the radiative corrected acceptance-correction factor calculated from Eq. (4.7), and  $S_{ratio}$  is the integrated Faraday Cup ratio, which is calculated from Eq. (4.4). In addition,  $R_{BC}$  is the bin-centering correction factor, which is calculated from Eq. (4.1).  $\Gamma_v(W, Q^2)$  represents the virtual photon flux that is obtained from Eq. (1.25).  $\Delta W$ ,  $\Delta Q^2$ ,  $\Delta \cos\theta_{\pi^-}^*$  and  $\Delta \phi_{\pi^-}^*$  are the bin widths of the corresponding kinematic variables.  $\mathcal{L}_{int}$  is the luminosity calculated by Eq. (4.3).

#### 5.1.2 The Exclusive Quasi-free Cross Section

As described in Chapter 2, we extract the exclusive quasi-free events successfully by applying a  $|\vec{p}_s| < 200$  MeV cut on the exclusive events. The exclusive quasi-free cross section is then calculated by

$$\frac{d\sigma^{qf}}{d\Omega_{\pi^-}^*} = \frac{d\sigma^{cut}}{d\Omega_{\pi^-}^*} \frac{1}{r(W, Q^2, \cos\theta^*, \phi^*)}, \quad (5.2)$$

where  $\frac{d\sigma^{cut}}{d\Omega_{\pi^-}^*}$  is the cross section calculated after applying the  $|\vec{p}_s| < 200$  MeV cut and  $r(W, Q^2, \cos\theta^*, \phi^*)$  obtained from Eq. (2.31) denotes the factor to correct good quasi-free events outside the  $|\vec{p}_s| < 200$  MeV cut. Based on the yield of the cut-surviving events, the cross section is extracted as

$$\frac{d\sigma^{cut}}{d\Omega_{\pi^-}^*} = \frac{(\Delta N_{full}^{cut}(W, Q^2, \cos\theta^*, \phi^*) - S_{ratio}\Delta N_{empty}^{cut}(W, Q^2, \cos\theta^*, \phi^*))R_{BC}}{\Gamma_v(W, Q^2) A_{RC}^{cut}(W, Q^2, \cos\theta^*, \phi^*)\Delta W \Delta Q^2 \Delta \cos\theta^* \Delta \phi^* \mathcal{L}_{int}}, \quad (5.3)$$



1337 where “cut” presents the corresponding quantities that are calculated within the  $|\vec{p}_s| < 200$  MeV  
 1338 cut condition. For the quasi-free events, the radiative corrected acceptance  $A_{RC}^{cut}(W, Q^2, \cos\theta^*, \phi^*)$   
 1339 is calculated as:

$$A_{RC}^{cut}(W, Q^2, \cos\theta^*, \phi^*) = \frac{N_{rec}^{(|\vec{p}_s| < 200 \text{ MeV})Rad}(W, Q^2, \cos\theta^*, \pi^-)}{N_{thrown}^{(|\vec{p}_s| < 200 \text{ MeV})noRad}(W, Q^2, \cos\theta^*, \pi^-)}, \quad (5.4)$$

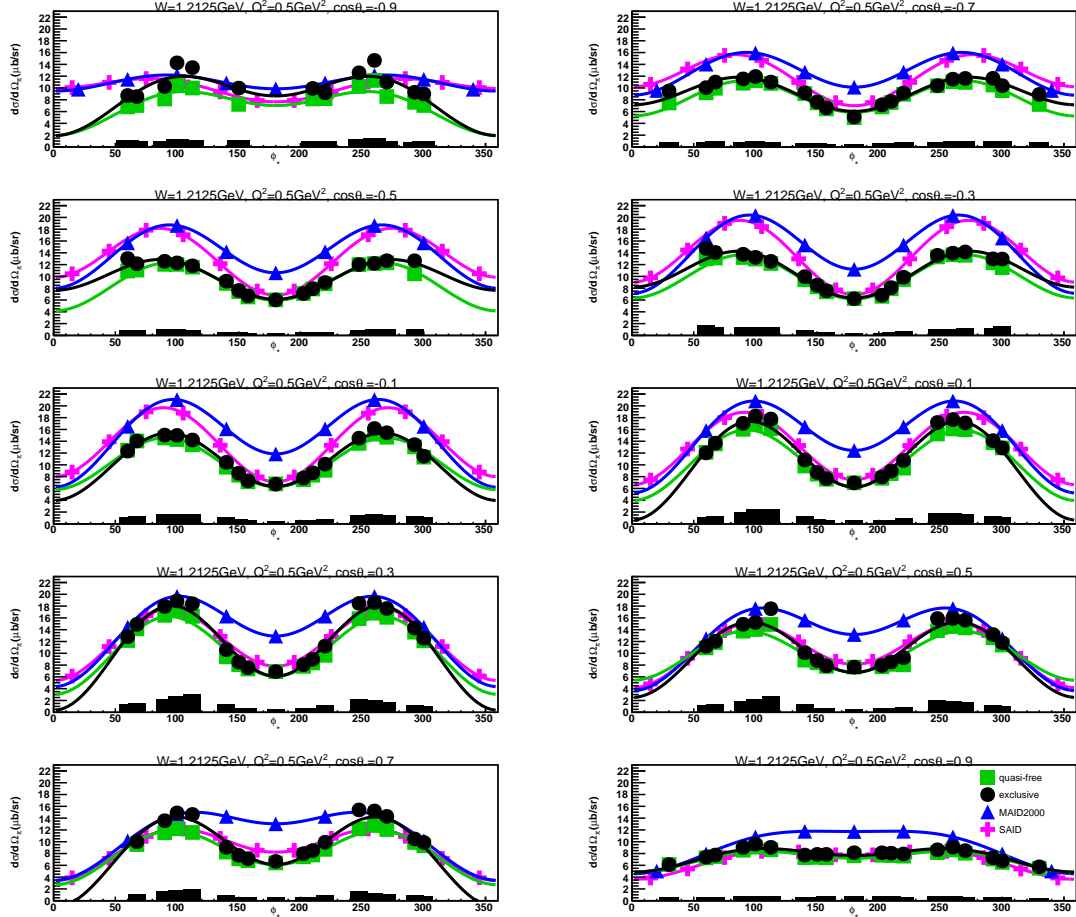


Figure 5.1: Exclusive (black points) and quasi-free (green squares) cross sections in  $\mu\text{b}/\text{sr}$  are represented for  $W = 1.2125$  GeV and  $Q^2 = 0.5$  GeV<sup>2</sup>. The  $\phi_{\pi^-}^*$  dependent cross sections are illustrated in each  $\cos\theta_{\pi^-}^*$  bin. The magenta crosses and blue triangles show SAID and MAID2000 model predictions. The color lines show fits to the cross sections by the function “ $a + b \cos 2\phi_{\pi^-}^* + c \cos \phi_{\pi^-}^*$ ”. The black bars at the bottom of each subplot represent the systematic uncertainty for each cross section points.

1340 From the above information, the full exclusive and quasi-free cross sections are calculated in  
 1341 dependence on the azimuthal angle  $\phi_{\pi^-}^*$ , which are plotted in the Appendix B for all available  
 1342 kinematic bins. In this way, the physics information is extracted conveniently by the angular  
 1343 dependencies of the cross sections. In the  $\Delta$  resonance region, the example  $\phi_{\pi^-}^*$  dependent cross  
 1344 sections with high statistics at  $W = 1.2125$  GeV for different  $Q^2$  bins are shown in Figs. 5.1,  
 1345 5.2, and 5.3. In these figures, the full exclusive and quasi-free cross sections are represented  
 1346 by the black points and green squares, respectively, as well as the corresponding systematic  
 1347 uncertainties (see Chapter 5.5) by the black bars in the bottom of each plot. These cross-  
 1348 section points are distributed symmetrically around  $\phi_{\pi^-}^* = 180^\circ$ ; this demonstrates the good  
 1349 quality of the measured cross sections. In addition, these  $\phi_{\pi^-}^*$  dependent cross sections are fit  
 1350 by the function “ $a + b \cos 2\phi_{\pi^-}^* + c \cos \phi_{\pi^-}^*$ ”, which is presented by the corresponding color line,

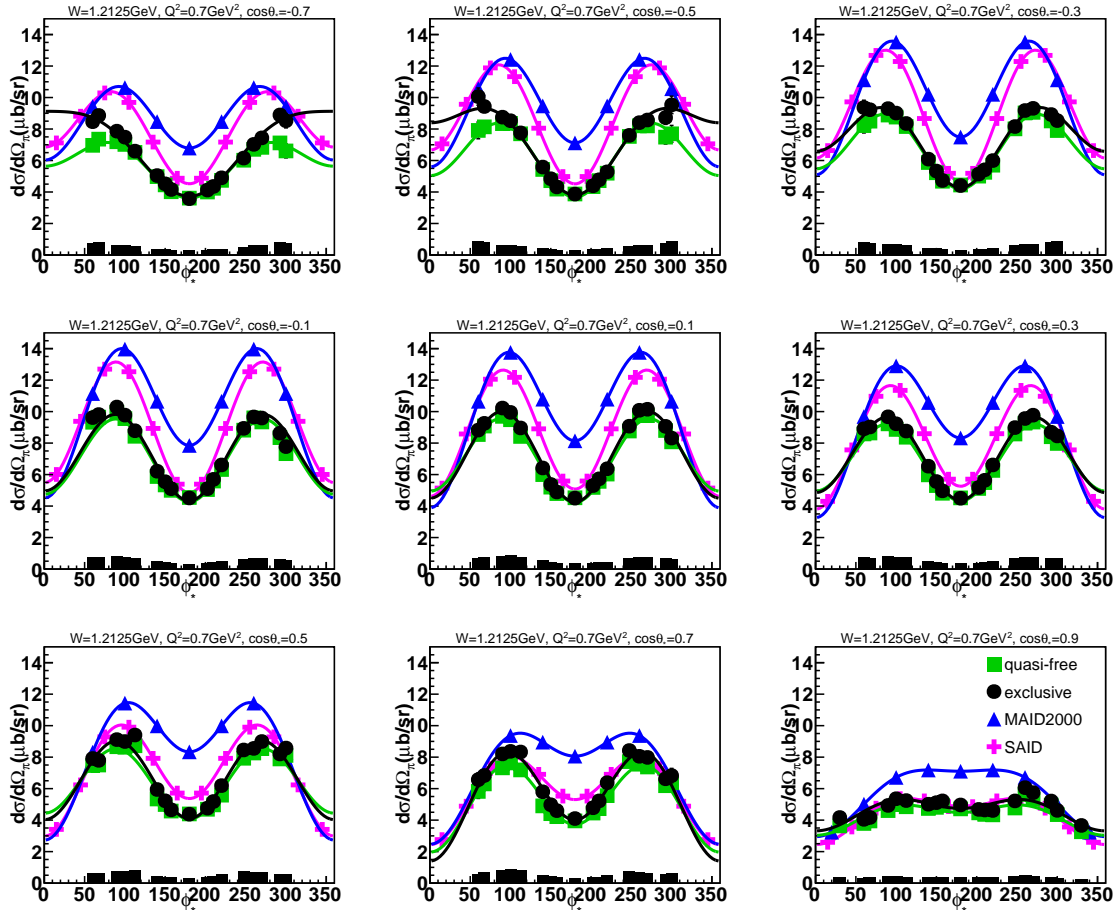


Figure 5.2: Exclusive (black points) and quasi-free (green squares) cross sections in  $\mu\text{b}/\text{sr}$  are represented for  $W = 1.2125$  GeV and  $Q^2 = 0.7$  GeV $^2$ . The  $\phi_{\pi^-}^*$  dependent cross sections are illustrated in each  $\cos \theta_{\pi^-}^*$  bin. The magenta crosses and blue triangles show SAID and MAID2000 model predictions. The color lines show fits to the cross sections by the function “ $a + b \cos 2\phi_{\pi^-}^* + c \cos \phi_{\pi^-}^*$ ”. The black bars at the bottom of each subplot represent the systematic uncertainty for each cross section points.

1351 to extract the physics quantities for the amplitude analysis. In Figs. 5.1, 5.2, and 5.3, these  
 1352 cross sections are presented at the same  $W = 1.2125$  GeV bin but with gradually increasing  
 1353  $Q^2$ . The comparison shows that these cross sections decrease with increasing  $Q^2$ . Furthermore,  
 1354 in each  $(W, Q^2, \cos \theta_{\pi^-}^*)$  bin, there is not enough data to provide statistically trustworthy cross  
 1355 sections at the very forward and backward  $\phi_{\pi^-}^*$  angles.

1356 In the second and the third resonance regions, examples of these cross sections are shown  
 1357 at  $W = 1.4875$  GeV and  $W = 1.6625$  GeV for the same  $Q^2 = 0.5$  GeV $^2$  bin in Figs. 5.4 and  
 1358 5.5, respectively. In the higher resonance region, we have even less statistics, leading to  $\phi_{\pi^-}^*$ -  
 1359 dependent cross sections with typically less data points at all  $\theta_{\pi^-}^*$  angles. As it can be seen in  
 1360 Figs. 5.1, 5.2, 5.3, 5.4, and 5.5, in each  $(W, Q^2, \cos \theta_{\pi^-}^*)$  bin, the exclusive cross section is  
 1361 always larger than the quasi-free cross section due to additional contributions from final state  
 1362 interactions.

1363 Furthermore, the measured cross sections are compared with the predictions of two models,  
 1364 SAID [4] and MAID2000 [8], which describe successfully the cross sections of the single pion  
 1365 production off the free proton in the low-lying resonance region. Examples of this comparison  
 1366 are shown in Figs. 5.1, 5.2, 5.3, 5.4, and 5.5. The magenta crosses and blue triangles represent  
 1367 the model predictions of SAID and MAID2000 individually. In the  $\Delta$  resonance region, these  
 1368 cross sections are in reasonable agreement with the predictions of the SAID model at forward

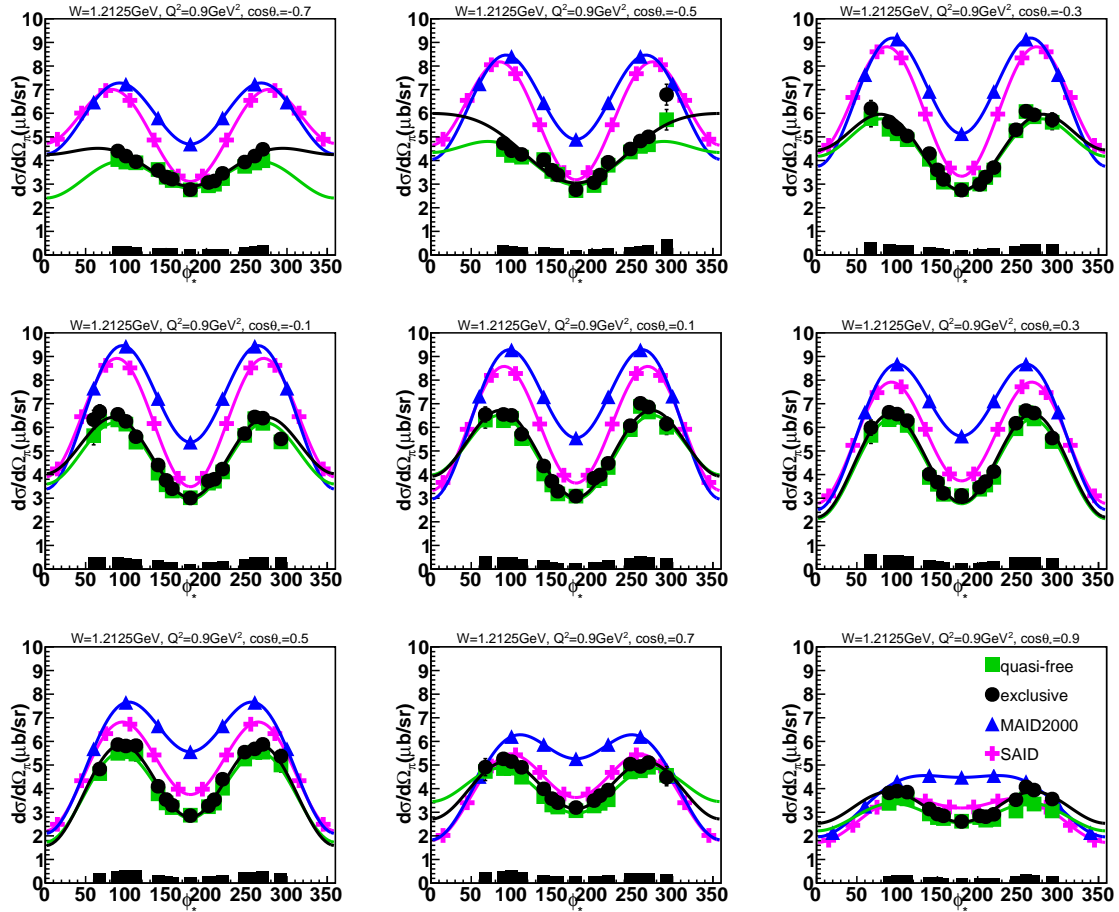


Figure 5.3: Exclusive (black points) and quasi-free (green squares) cross sections in  $\mu\text{b}/\text{sr}$  are represented for  $W = 1.2125$  GeV and  $Q^2 = 0.9$  GeV<sup>2</sup>. The  $\phi_{\pi^-}^*$  dependent cross sections are illustrated in each  $\cos \theta_{\pi^-}^*$  bin. The magenta crosses and blue triangles show SAID and MAID2000 model predictions. The color lines show fits to the cross sections by the function “ $a + b \cos 2\phi_{\pi^-}^* + c \cos \phi_{\pi^-}^*$ ”. The black bars at the bottom of each subplot represent the systematic uncertainty for each cross section points.

1369  $\theta_{\pi^-}^*$  angles. However, at the backward  $\theta_{\pi^-}^*$  angles, the measured cross sections are smaller than  
 1370 the prediction of both models. Due to the lack of experimental data for the  $\gamma^*n(p) \rightarrow p\pi^-(p)$   
 1371 process, the discrepancy between the model predictions and the measured cross-section results  
 1372 is not surprising. The models need neutron data to improve their predictions.

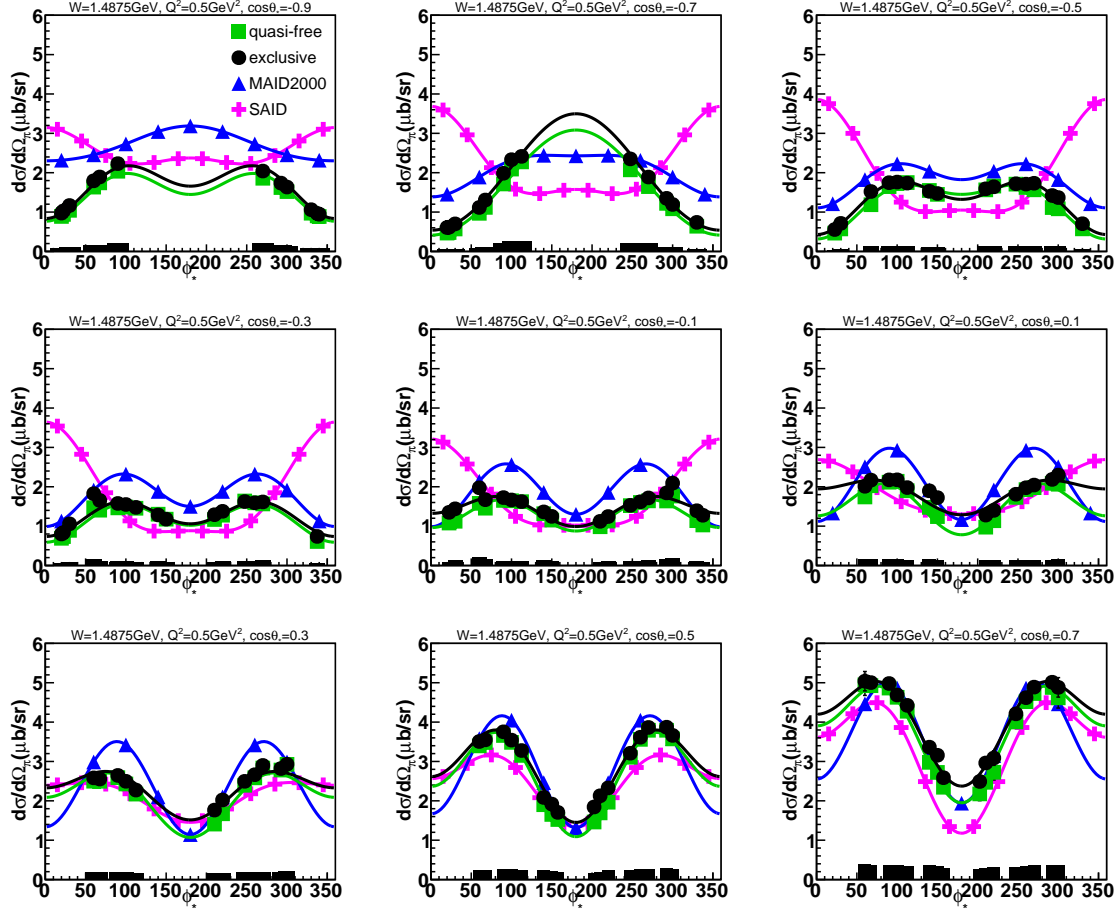


Figure 5.4: Exclusive (black points) and quasi-free (green squares) cross sections in  $\mu\text{b}/\text{sr}$  are represented for  $W = 1.4875$  GeV and  $Q^2 = 0.5$  GeV<sup>2</sup>. The  $\phi_{\pi^-}^*$  dependent cross sections are illustrated in each  $\cos\theta_{\pi^-}^*$  bin. The magenta crosses and blue triangles show SAID and MAID2000 model predictions. The color lines show fits to the cross sections by the function “ $a + b \cos 2\phi_{\pi^-}^* + c \cos \phi_{\pi^-}^*$ ”. The black bars at the bottom of each subplot represent the systematic uncertainty for each cross section points.

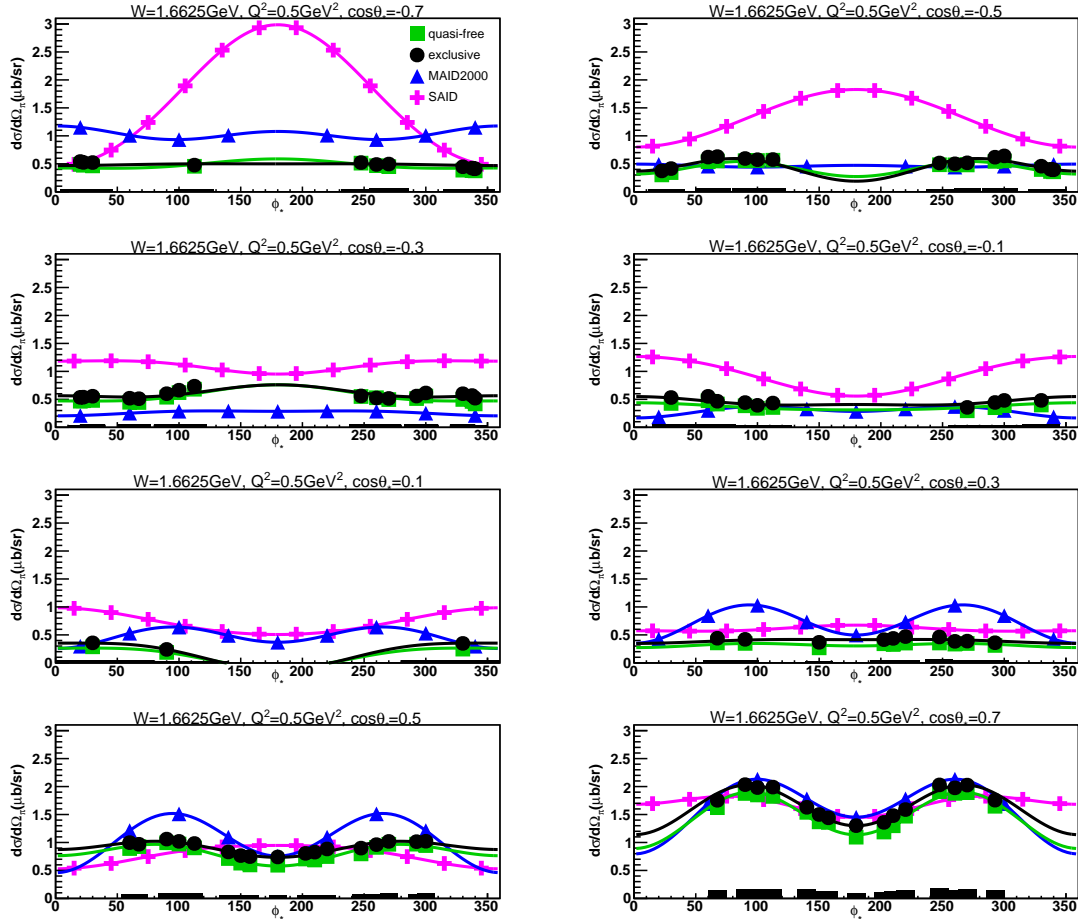


Figure 5.5: Exclusive (black points) and quasi-free (green squares) cross sections in  $\mu\text{b}/\text{sr}$  are represented for  $W = 1.6625 \text{ GeV}$  and  $Q^2 = 0.5 \text{ GeV}^2$ . The  $\phi_{\pi^*}$ -dependent cross sections are illustrated in each  $\cos\theta_{\pi^*}$  bin. The magenta crosses and blue triangles show SAID and MAID2000 model predictions. The color lines show fits to the cross sections by the function “ $a + b \cos 2\phi_{\pi^*} + c \cos \phi_{\pi^*}$ ”. The black bars at the bottom of each subplot represent the systematic uncertainty for each cross section points.

## 1373 5.2 Kinematically Defined Quasi-Free Contribution

1374 Figure 2.36 shows the spectator proton missing momentum distribution  $|\vec{P}_s|$ . The comparison  
 1375 of the kinematically determined  $|\vec{P}_s|$  distributions of the experimental and simulated data shows  
 1376 that the kinematically defined quasi-free process is absolutely dominant in the  $|\vec{P}_s| < 0.2$  GeV  
 1377 region, where as for  $|\vec{P}_s| > 0.2$  GeV FSI contributions appear and become increasingly larger.  
 1378 Beyond the extraction of the fully exclusive and quasi-free differential cross sections, this compar-  
 1379 ison allows us to calculate the final-state-interaction contribution factor  $R_{FSI}$  for each 4  
 1380 dimensional bin  $(W, Q^2, \cos \theta_{\pi^-}^*, \phi_{\pi^-}^*)$  kinematically. This factor hence provide information on  
 1381 the fraction of final state interactions in the fully exclusive process and is defined by

$$R_{FSI}(W, Q^2, \cos \theta_{\pi^-}^*, \phi_{\pi^-}^*) = \frac{\frac{d\sigma^{qf}}{d\Omega_{\pi^-}^*}}{\frac{d\sigma^{ex}}{d\Omega_{\pi^-}^*}}. \quad (5.5)$$

1382 The ratio between the final state interaction contribution factors  $R_{FSI}(W, Q^2, \cos \theta_{\pi^-}^*, \phi_{\pi^-}^*)$  and  
 1383  $R_{FSI}(W, Q^2, \cos \theta_{\pi^-}^*)$  (i.e.  $R_{FSI}(W, Q^2, \cos \theta_{\pi^-}^*, \phi_{\pi^-}^*)$  integrated over  $\phi_{\pi^-}^*$ ) are plotted against  
 1384  $\phi_{\pi^-}^*$ , and distribution examples for  $1.2 \text{ GeV} < W < 1.225 \text{ GeV}$  and  $0.6 \text{ GeV}^2 < Q^2 < 0.8 \text{ GeV}^2$   
 1385 are shown in Fig. 5.6 for  $W_f$  binning. Each individual plot represents the ratios for different  
 1386  $\cos \theta_{\pi^-}^*$  bins. For quasi-free events, binning data in  $W_f$  is the best choice from what we have  
 1387 observed, see Chapter 1. In order to present meaningful values of  $R_{FSI}$ , we have to bin exclusive  
 1388 events in  $W_f = \sqrt{(p^\mu + \pi^\mu)^2}$  to be consistent with the binning of quasi-free events, even though,  
 1389  $W_f$  for exclusive events with final state interaction is less than the true  $W = W_i$ , since the  
 1390 undetected outgoing proton is carrying away additional momentum.

1391 In order to quantify the dependence of kinematically defined final-state-interaction contri-  
 1392 bution factors  $R_{FSI}$  on the polar angle  $\theta_{\pi^-}^*$ , the  $\phi_{\pi^-}^*$  integrated  $R_{FSI}$  versus  $\theta_{\pi^-}^*$  distributions  
 1393 are plotted for different  $W$  and  $Q^2$  bins, which are shown in the Figs. 5.7, 5.8, and 5.9, re-  
 1394 spectively. From Figs. 5.7, 5.8, and 5.9, it turns out that the kinematically defined final state  
 1395 interaction contribution for the reaction  $\gamma^* n(p) \rightarrow p\pi^-(p)$  with the “e1e” run data kinematic  
 1396 coverage is on average about 10% – 20%.

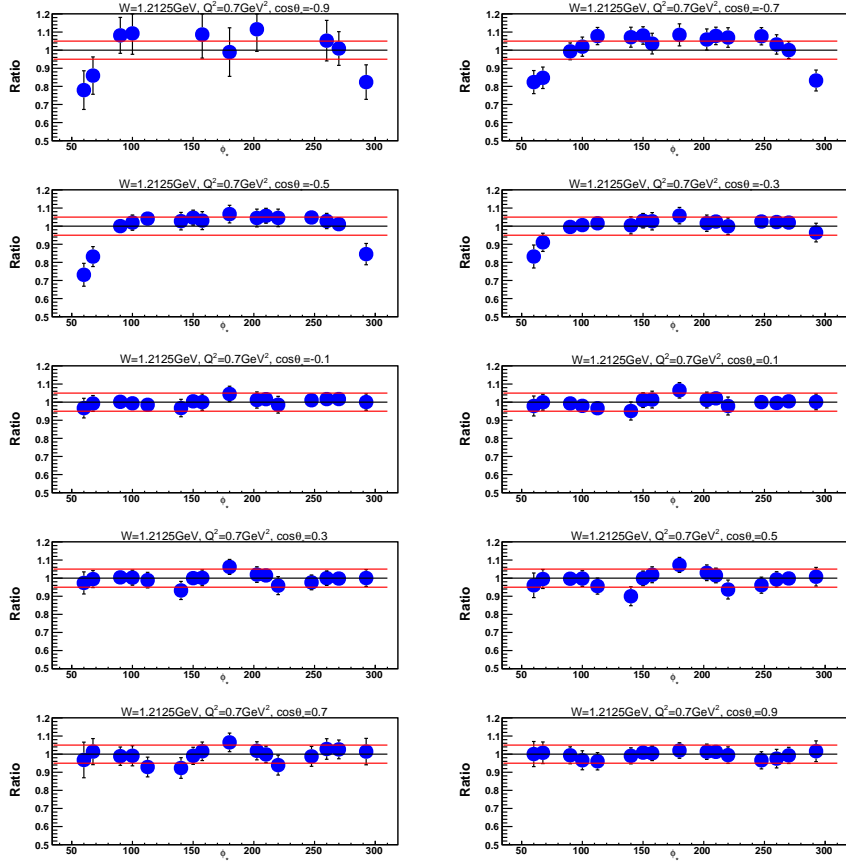


Figure 5.6: The ratios of  $R_{FSI}(W_i, Q^2, \cos \theta_{\pi^-}^*, \phi_{\pi^-}^*)$  over  $R_{FSI}(W_i, Q^2, \cos \theta_{\pi^-}^*)$  are represented by Blue points for different  $\phi_{\pi^-}^*$  at  $1.2 \text{ GeV} < W < 1.225 \text{ GeV}$  and  $0.6 \text{ GeV}^2 < Q^2 < 0.8 \text{ GeV}^2$ . The individual plot shows the ratios for different  $\cos \theta_{\pi^-}^*$  bins. The three lines from bottom to top correspond to 0.95, 1, and 1.05, respectively.

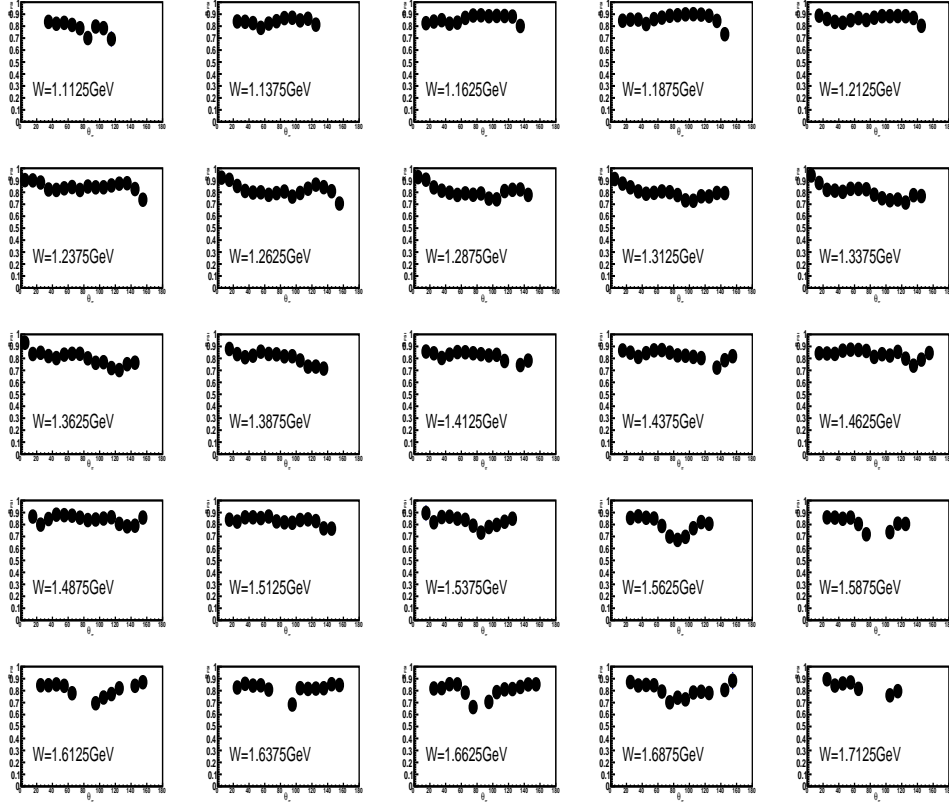


Figure 5.7:  $R_{FSI}$  versus  $\theta_{\pi^-}^*$  distribution example for individual  $W_f$  bins, which are increasing by 0.025 GeV in the range of  $1.1 \text{ GeV} < W < 1.725 \text{ GeV}$  for  $0.4 \text{ GeV}^2 < Q^2 < 0.6 \text{ GeV}^2$ .

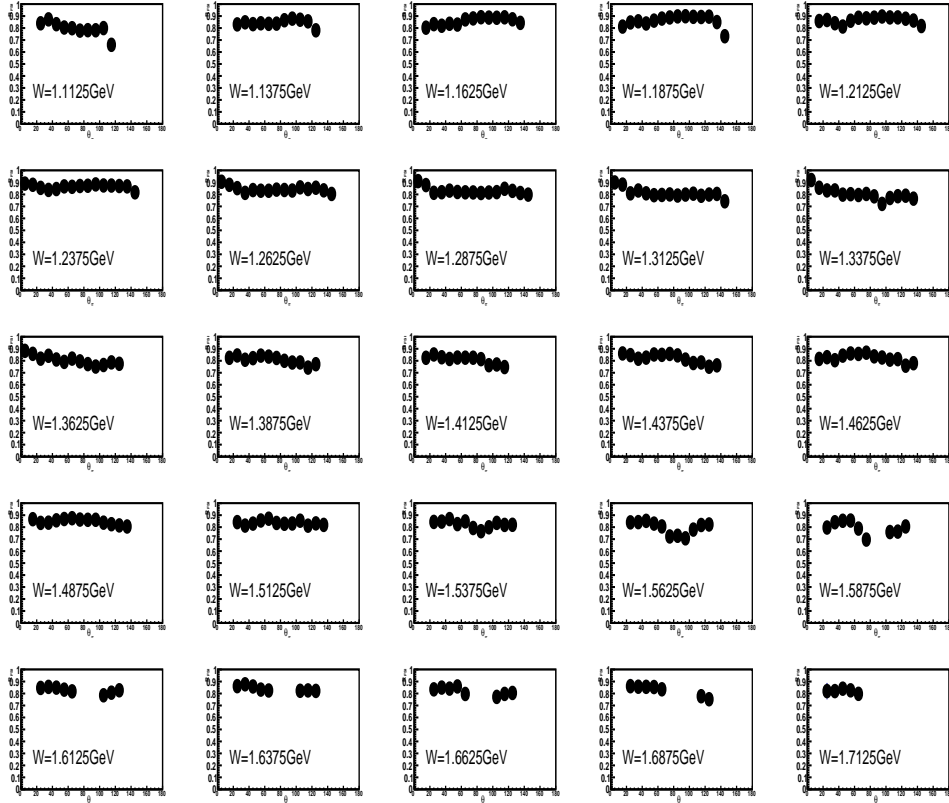


Figure 5.8:  $R_{FSI}$  versus  $\theta_{\pi^-}^*$  distributions example for individual  $W_f$  bins, which are increasing by 0.025 GeV in the range of  $1.1 \text{ GeV} < W < 1.725 \text{ GeV}$  for  $0.6 \text{ GeV}^2 < Q^2 < 0.8 \text{ GeV}^2$ .



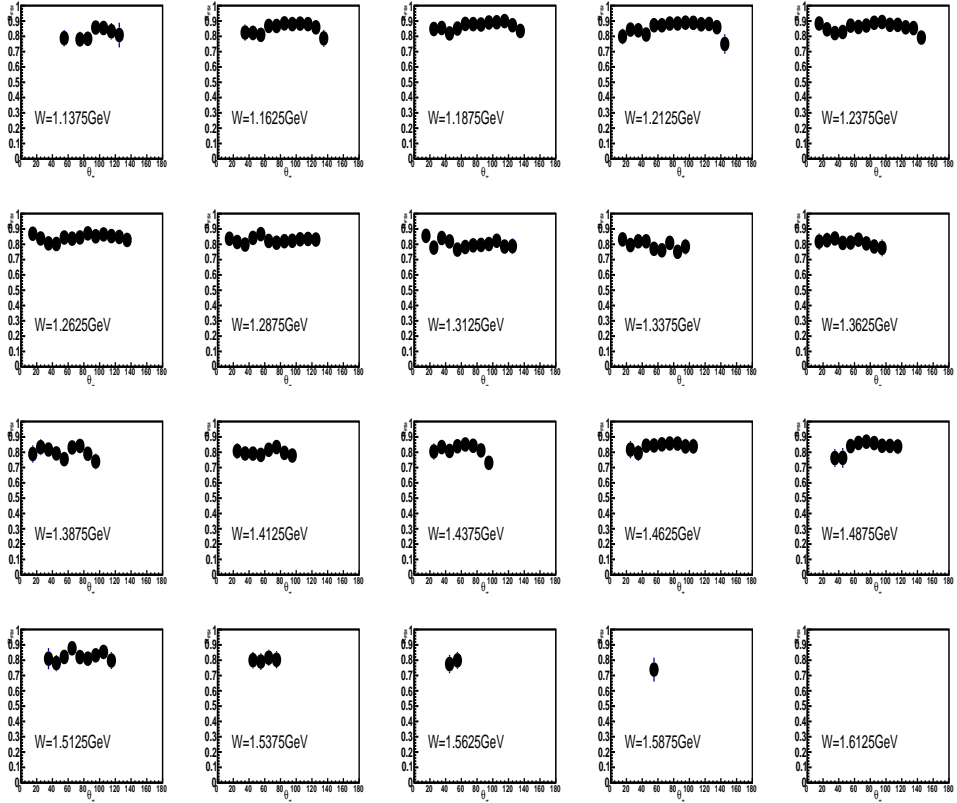


Figure 5.9:  $R_{FSI}$  versus  $\theta_{\pi^-}^*$  distributions example for individual  $W_f$  bins, which are increasing by  $0.025 \text{ GeV}$  in the range of  $1.125 \text{ GeV} < W < 1.6 \text{ GeV}$  for  $0.8 \text{ GeV}^2 < Q^2 < 1.0 \text{ GeV}^2$ .

## 5.3 Structure Functions

1398 The above hadronic cross sections are fit in terms of  $\cos \phi_{\pi^-}^*$  and  $\cos 2\phi_{\pi^-}^*$  (Eq. (5.6)) to ex-  
 1399 tract the structure functions. Each fitted function has three fit parameters  $a$ ,  $b$ , and  $c$ , which  
 1400 correspond to the structure functions  $\sigma_T + \epsilon\sigma_L$ ,  $\sigma_{TT}$ , and  $\sigma_{TL}$ , respectively,

$$\frac{d\sigma}{d\Omega_{\pi^-}^*} = a + b \cos 2\phi_{\pi^-}^* + c \cos \phi_{\pi^-}^*, \quad a = \sigma_T + \epsilon\sigma_L, \quad b = \epsilon\sigma_{TT}, \quad \text{and} \quad c = \sqrt{2\epsilon(1+\epsilon)}\sigma_{TL}, \quad (5.6)$$

1401 where  $\epsilon$  is the transverse polarization of the virtual photon, “T” and “L” represent transverse  
 1402 and longitudinal components, as well as “TT” and “TL” the interference terms. The exclusive  
 1403 and quasi-free cross sections from Eq. (5.1) and Eq. (5.2), respectively, are fit to extract the  
 1404 corresponding structure functions. Examples at  $W = 1.2125$  GeV with  $Q^2 = 0.5$  GeV<sup>2</sup>,  
 1405  $Q^2 = 0.7$  GeV<sup>2</sup>, and  $Q^2 = 0.9$  GeV<sup>2</sup> are shown in Fig. 5.1. In addition, these structure functions  
 1406 are also compared with the predictions of the SAID and MAID2000 models. The solid black  
 1407 bars show the systematic errors that are calculated through error propagation procedure, see  
 1408 Chapter 5.5. The color lines represent the corresponding Legendre polynomial expansions for  
 $\pi^-$  angular momenta up to  $l = 2$ . These fits are discussed in the following section.

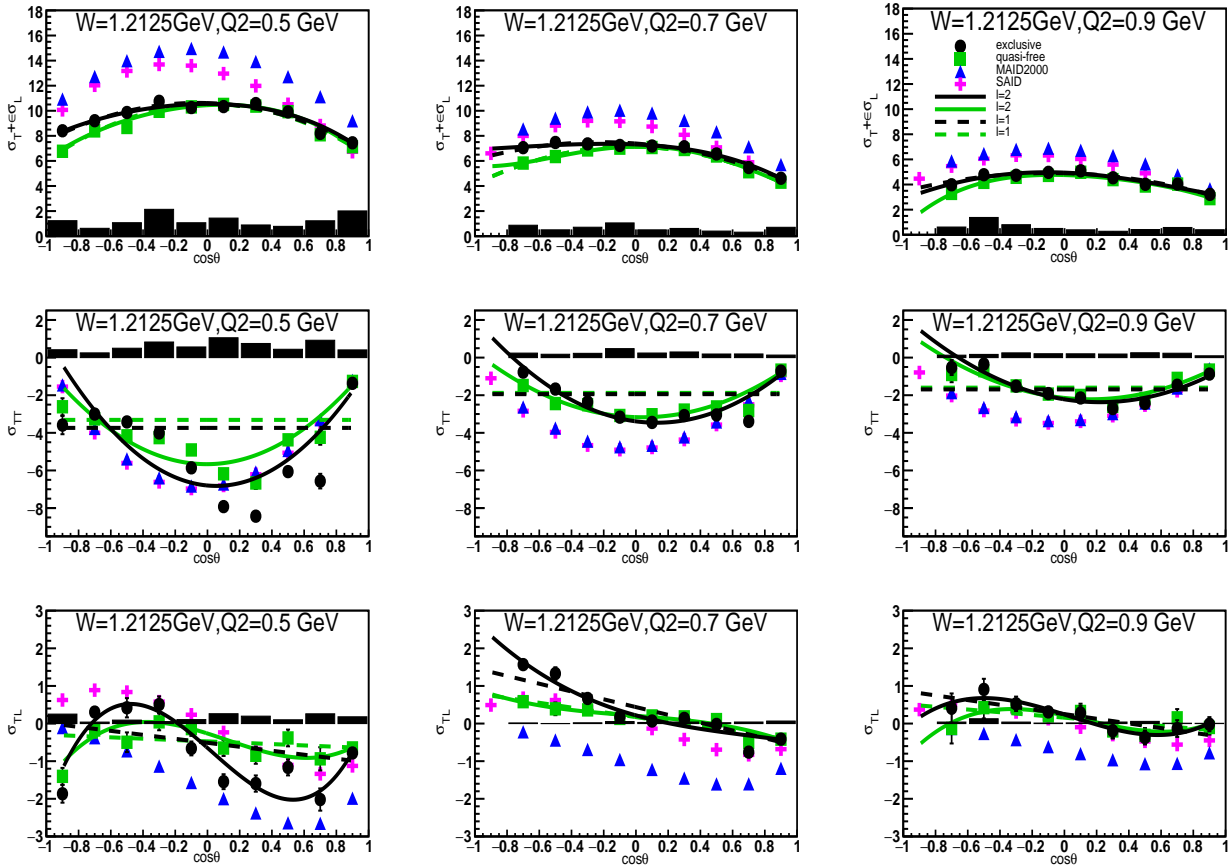


Figure 5.10: Example of the  $\cos \theta_{\pi^-}^*$  dependent structure functions  $\sigma_T + \epsilon\sigma_L$  (top row),  $\sigma_{TT}$  (middle row), and  $\sigma_{TL}$  (bottom row) for  $W = 1.2125$  GeV at  $Q^2 = 0.5$  GeV<sup>2</sup> (left column),  $Q^2 = 0.7$  GeV<sup>2</sup> (middle column), and  $Q^2 = 0.9$  GeV<sup>2</sup> (right column) that are extracted for the exclusive (black points) and quasi-free (green squares) cross sections and compared with the predictions of the SAID (magenta points) and MAID2000 (blue points) models. The solid black bars represent the corresponding systematic uncertainties. The Legendre polynomial expansions are fitted to the corresponding structure function data for  $\pi^-$  angular momenta up to  $l = 1$  by dash lines, and up to  $l = 2$  by solid lines.

## 1410 5.4 Legendre Polynomials Expansion

1411 For each  $(W, Q^2)$  bin, the extracted structure functions are functions of  $\cos\theta_{\pi^-}^*$  and can be  
 1412 expressed in terms of Legendre polynomials. In this way, we can get insight on the dominant  
 1413 wave contribution in a particular resonance region. The Legendre polynomial expansion of the  
 1414 structure functions for  $\pi^-$  angular momentum up to  $l = 1$  ( $p$ -wave) can be expressed by

$$\sigma_T + \epsilon\sigma_L = A_0P_0(\cos\theta_{\pi^-}^*) + A_1P_1(\cos\theta_{\pi^-}^*) + A_2P_2(\cos\theta_{\pi^-}^*), \quad (5.7)$$

$$\sigma_{TT} = B_0P_0(\cos\theta_{\pi^-}^*), \quad (5.8)$$

$$\sigma_{TL} = C_0P_0(\cos\theta_{\pi^-}^*) + C_1P_1(\cos\theta_{\pi^-}^*), \quad (5.9)$$

1417 and up to  $l = 2$  ( $d$ -wave) by

$$\begin{aligned} \sigma_T + \epsilon\sigma_L = & A_0P_0(\cos\theta_{\pi^-}^*) + A_1P_1(\cos\theta_{\pi^-}^*) + A_2P_2(\cos\theta_{\pi^-}^*) + A_3P_3(\cos\theta_{\pi^-}^*) \\ & + A_4P_4(\cos\theta_{\pi^-}^*), \end{aligned} \quad (5.10)$$

$$\sigma_{TT} = B_0P_0(\cos\theta_{\pi^-}^*) + B_1P_1(\cos\theta_{\pi^-}^*) + B_2P_2(\cos\theta_{\pi^-}^*), \quad \text{and} \quad (5.11)$$

$$\sigma_{TL} = C_0P_0(\cos\theta_{\pi^-}^*) + C_1P_1(\cos\theta_{\pi^-}^*) + C_2P_2(\cos\theta_{\pi^-}^*) + C_3P_3(\cos\theta_{\pi^-}^*), \quad (5.12)$$

1420 where  $P_l(\cos\theta_{\pi^-}^*)$  corresponds to the  $l$ th-order Legendre polynomial, and the coefficients  $A_l$ ,  
 1421  $B_l$ , and  $C_l$  represent the Legendre moments, which can be associated with the magnetic ( $M_{l\pm}$ ),  
 1422 electric ( $E_{l\pm}$ ), and scalar ( $S_{l\pm}$ )  $\pi N$  multipoles [33]. In Fig. 5.10, the dashed lines show that  
 1423 the Legendre polynomial expansion of the structure functions up to  $l = 1$  fails to provide an  
 1424 adequate description of the interference structure functions  $\sigma_{TL}$  and  $\sigma_{TT}$  extracted from the  
 1425 data, but up to  $l = 2$  (solid lines) leads already to a reasonable description.

## 1426 5.5 Systematic Uncertainty

1427 The first source of systematic uncertainties are the cuts used for particle identification and  
 1428 event selection. It is not feasible to determine the ideal cut positions, so we estimate how the  
 1429 final results depend on the shape and the position of a particular cut.

1430 Since the cross sections are presented in the CM frame, all measured particle momenta from  
 1431 the lab frame have to be boosted to the CM frame through with the boost vector  $\vec{\beta}$ , which can  
 1432 be calculated either from the initial particle ( $n^\mu$  and  $q^\mu$ ) or final particles ( $\pi^{-\mu}$  and  $p^\mu$ ) four  
 1433 momenta. Even though we finally use  $\vec{\beta}_f$ , which is calculated from the final state particles,  
 1434 the influence on the final cross sections by using different  $\vec{\beta}$ s contributes to the systematic  
 1435 uncertainty. Hence, the second source of systematic uncertainty is determined by estimating  
 1436 how much the final results are influenced by the choice of different boost vectors.

1437 In order to isolate the exclusive quasi-free process  $\gamma^*n(p_s) \rightarrow p\pi^-(p_s)$ , the missing momen-  
 1438 tum  $P_s$  distribution needs to be compared with the simulated Fermi momentum of the spectator.  
 1439 The Fermi momentum distribution of the independent ‘‘spectator’’ proton is generated by the  
 1440 CD-Bonn potential [20] in the event generator. The CD-Bonn potential is considered to be  
 1441 more accurate than other models, such as the Pairs [26] and Hulthen [16] potentials, but for  
 1442 the purpose of the systematic uncertainty study, all three deuteron potential distributions are  
 1443 compared to determine the third source of the systematic uncertainty.

1444 The bin centering correction factor is calculated from the cross-section function of a reaction  
 1445 model, so the influence of applying  $R_{BC}$ , as it is calculated from different models, on the cross  
 1446 sections is the fourth source of the systematic uncertainty.

1447 Last but not least, the normalization uncertainty extracted from the comparison of our  
 1448 measured inclusive cross sections with the world data parameterization results accounts for the  
 1449 last source of the systematic uncertainty.

1450 To study how cut are influencing the results, we typically vary the chosen cuts by making  
 1451 them tighter or looser for both data and simulation. So the final results for the systematic  
 1452 uncertainty found due to variation of cuts is determined as the RMS of the deviations of the  
 1453 varied cross section from the original one by

$$\Delta_{cut^i}^{RMS} = \sqrt{\frac{\Delta_{tight}^2 + \Delta_{loose}^2}{2}}, \quad (5.13)$$

1454 where  $\Delta_{tight}$  and  $\Delta_{loose}$  correspond to the difference between the cross sections with the chosen  
 1455 cut and the varied one.

1456 The following cuts are studied to determine the final systematic uncertainty.

### 1457 5.5.1 Electron ID cuts

- 1458 •  $\theta_{CC}$  cut

1459 We vary the  $\theta_{CC}$  cut within

$$\begin{aligned} \theta_{CC\mu} - 3\sigma < \theta_{CC} < \theta_{CC\mu} + 2\sigma \text{ (tight) and} \\ \theta_{CC\mu} - 5\sigma < \theta_{CC} < \theta_{CC\mu} + 4\sigma \text{ (loose),} \end{aligned} \quad (5.14)$$

1460 where  $\mu$  ( $\theta_{CC\mu}$ ) and  $\sigma$  are the original cut parameters, which are introduced in the electron  
 1461 identification section of Chapter 2. The same procedure is applied to the simulation. With  
 1462 the tight or loose cut conditions, the cross sections are calculated exactly in the same way  
 1463 as the above reported final cross section. The systematic uncertainty is determined for  
 1464 each 4-dimensional variable bin, and the average systematic uncertainty over all bins due  
 1465 to the  $\theta_{CC}$  cut is 0.78%.

- 1466 • Electron sampling fraction cut

1467 Similar to the  $\theta_{CC}$  cut, variations of the sampling fraction cut are represented by

$$\begin{aligned} \left(\frac{E_{total}}{p_e}\right)_\mu - 2\sigma < \frac{E_{total}}{p_e} < \left(\frac{E_{total}}{p_e}\right)_\mu + 2\sigma \text{ (tight) and} \\ \left(\frac{E_{total}}{p_e}\right)_\mu - 4\sigma < \frac{E_{total}}{p_e} < \left(\frac{E_{total}}{p_e}\right)_\mu + 4\sigma \text{ (loose),} \end{aligned} \quad (5.15)$$

1468 where  $\mu$  and  $\sigma$  are the original sampling fraction cut parameters. The average systematic  
 1469 uncertainty over all bins due to this cut is 1.26%.

- 1470 • Electron fiducial cut

1471 Electron fiducial tight and loose cut definitions are

$$\begin{aligned} (sector - 1) * 60^\circ - \Delta\phi_e + 1^\circ < \phi_e^{sector} < (sector - 1) * 60^\circ + \Delta\phi_e - 1^\circ \text{ (tight) ;} \\ (sector - 1) * 60^\circ - \Delta\phi_e - 1^\circ < \phi_e^{sector} < (sector - 1) * 60^\circ + \Delta\phi_e + 1^\circ \text{ (loose) ,} \end{aligned} \quad (5.16)$$

1472 where  $\Delta\phi_e$  is defined by Eq. (2.20). The electron fiducial cuts contribute 2.10% on average  
 1473 to the final systematic uncertainties.

### 1474 5.5.2 $\pi^-$ ID cuts

- 1475 •  $\pi^- \Delta T$  cut

1476 The pion identification is based on the timing  $\Delta T$  cut, and the chosen cuts are listed in

1477  
1478

Eq. (2.10). In order to determine the influence of the  $\Delta T$  cut variation on the final cross sections, we tighten or loosen the chosen cut as

$$\begin{aligned} (\Delta T_{\pi^-})_{\mu} - 2\sigma < \Delta T_{\pi^-} < (\Delta T_{\pi^-})_{\mu} + 2\sigma \text{ (tight) and} \\ (\Delta T_{\pi^-})_{\mu} - 4\sigma < \Delta T_{\pi^-} < (\Delta T_{\pi^-})_{\mu} + 4\sigma \text{ (loose),} \end{aligned} \quad (5.17)$$

1479  
1480

where  $\mu$  and  $\sigma$  are the originally chosen cut parameters. Figure 5.11 shows tight, chosen, and loose cuts together on the  $\pi^-$   $\Delta T$  distributions for all sectors. The average systematic uncertainty over all bins due to this cut is 1.78%.

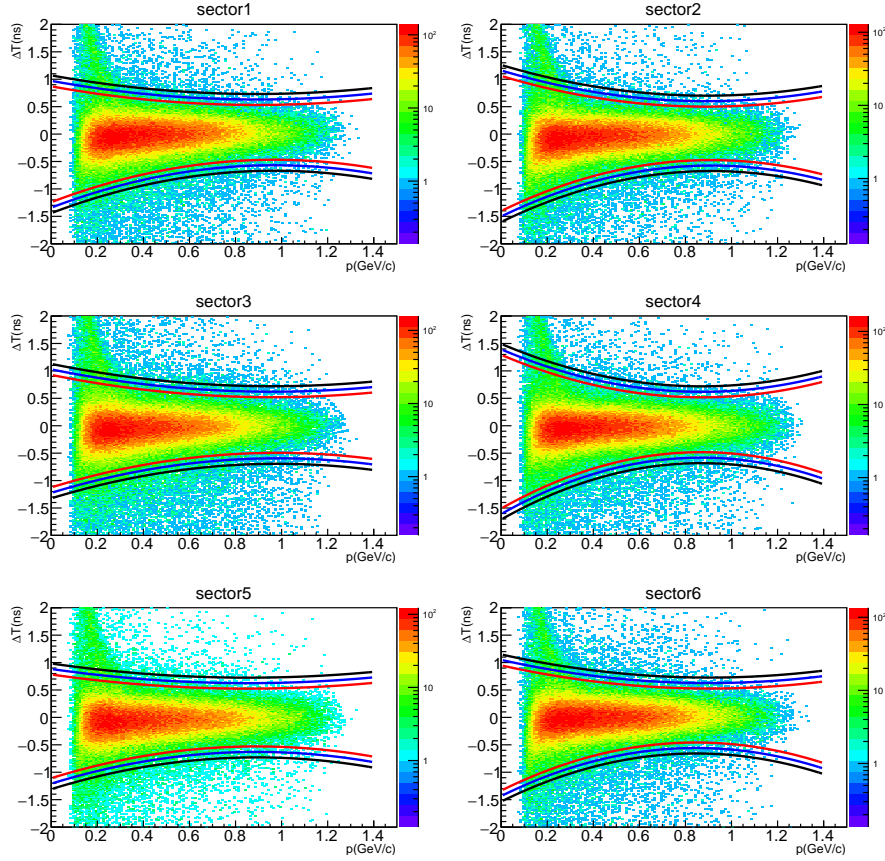


Figure 5.11: The  $\Delta T$  distribution of pions in six sectors. The black, blue, and red lines represent the  $4\sigma$ ,  $3\sigma$ , and  $2\sigma$  cut boundaries, respectively.

1481

1482 •  $\pi^-$  fiducial cut

1483 We vary the  $\pi^-$  fiducial cut within

$$\begin{aligned} \phi_{\pi^-}^{\min} + 1^\circ < \phi_{\pi^-} < \phi_{\pi^-}^{\max} - 1^\circ \text{ (tight) and} \\ \phi_{\pi^-}^{\min} - 1^\circ < \phi_{\pi^-} < \phi_{\pi^-}^{\max} + 1^\circ \text{ (loose) ,} \end{aligned} \quad (5.18)$$

1484  
1485

where  $\phi_{\pi^-}^{\min}$  and  $\phi_{\pi^-}^{\max}$  are described in Eq. (2.23). The average systematic uncertainty over all bins generated by this source is 1.73%.

1486 **5.5.3 Proton ID cuts**

1487 • Proton  $\Delta T$  cut

1488 Similar to the pion  $\Delta T$  cut procedure, we tighten or loosen the chosen proton  $\Delta T$  cut

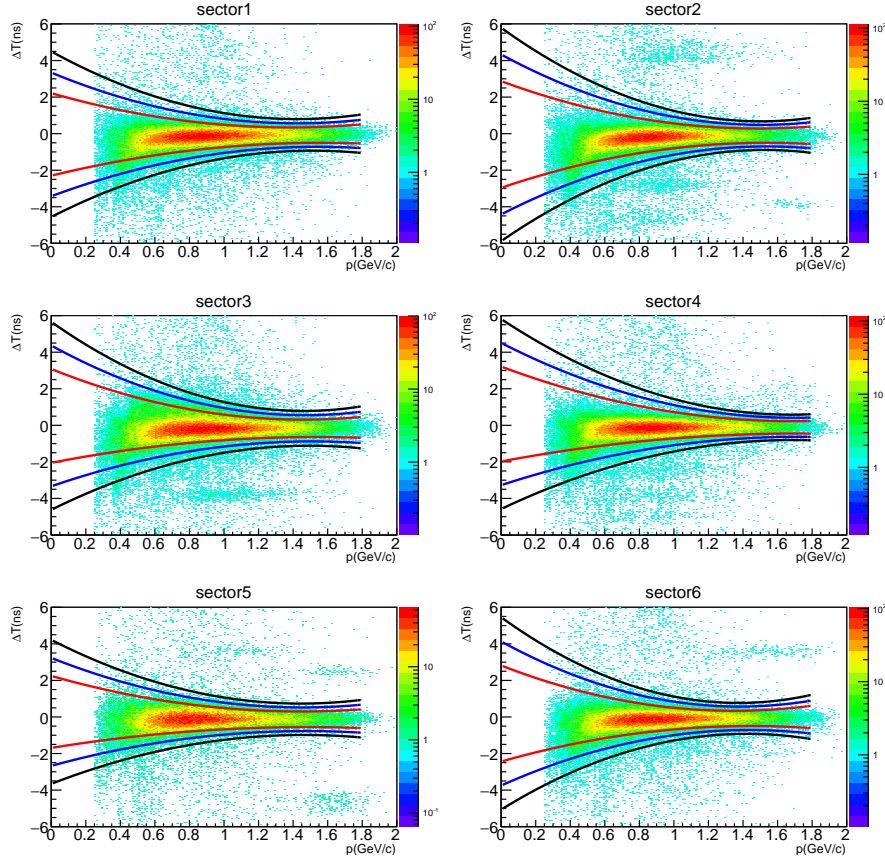


Figure 5.12: The  $\Delta T$  distribution of protons in six sectors. The black, blue, and red lines represent the  $4\sigma$ ,  $3\sigma$ , and  $2\sigma$  cut boundaries, respectively.

1489 described in Eq. (2.11) within

$$\begin{aligned} (\Delta T_{proton})_{\mu} - 2\sigma < \Delta T_{proton} < (\Delta T_{proton})_{\mu} + 2\sigma \text{ (tight); and} \\ (\Delta T_{proton})_{\mu} - 4\sigma < \Delta T_{proton} < (\Delta T_{proton})_{\mu} + 4\sigma \text{ (loose),} \end{aligned} \quad (5.19)$$

1490 where  $\mu$  and  $\sigma$  are the originally chosen cuts parameters. All cuts are shown in Fig. 5.12.  
1491 The average systematic uncertainty over all bins contributed due to this cut is 1.39%.

1492 • Proton fiducial cut

1493 We tighten or loosen the chosen proton fiducial cuts presented in Eq. (2.27) within

$$\begin{aligned} \phi_{proton}^{min} + 1^{\circ} < \phi_{proton} < \phi_{proton}^{max} - 1^{\circ} \text{ (tight) and} \\ \phi_{proton}^{min} - 1^{\circ} < \phi_{proton} < \phi_{proton}^{max} + 1^{\circ} \text{ (loose) ,} \end{aligned} \quad (5.20)$$

1494 which are shown in Fig. 5.13 as black and magenta lines individually for all sectors. The  
1495 average systematical error over all bins due to the proton fiducial cut is 2.39%.

## 1496 5.5.4 Event Selection

1497 •  $M_s^2$  cut

1498 We varied the chosen  $M_s^2$  cut limits within

$$\begin{aligned} 0.840 \text{ GeV} < M_s^2 < 0.919 \text{ GeV} \text{ (tight); and} \\ 0.811 \text{ GeV} < M_s^2 < 0.955 \text{ GeV} \text{ (loose),} \end{aligned} \quad (5.21)$$

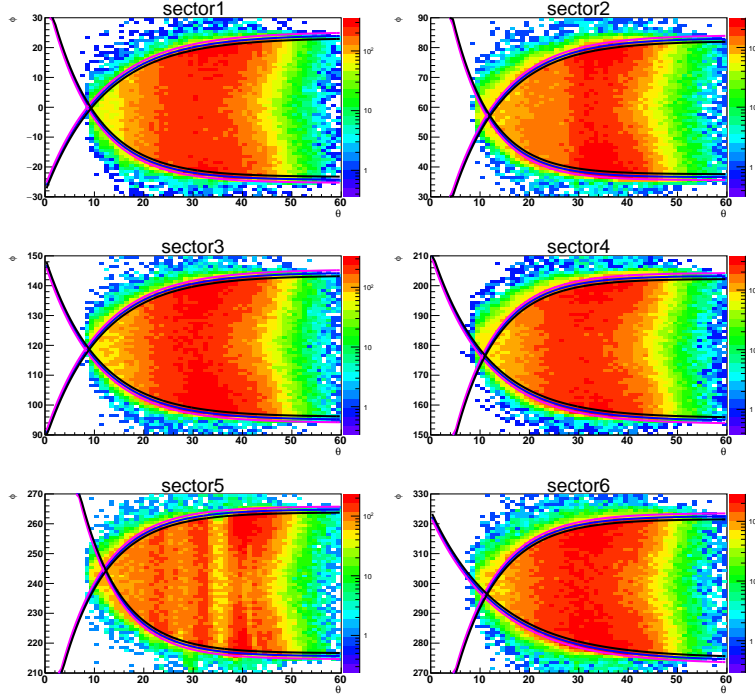


Figure 5.13: (Color online) The  $\phi_p$  versus  $\theta_p$  distributions for six sectors without proton fiducial cuts. The magenta, blue, and black lines represent loose, chosen, and tight proton fiducial cuts, respectively.

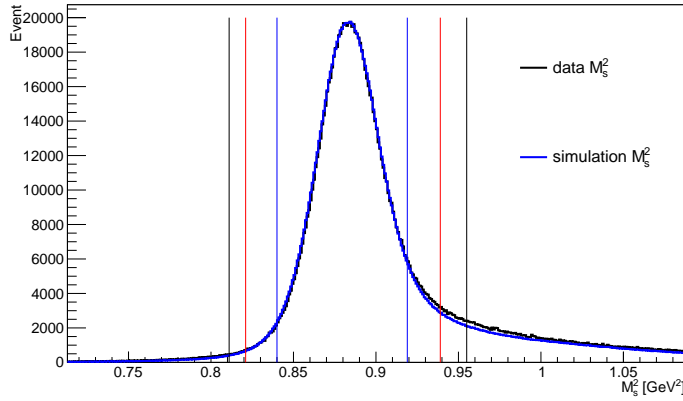


Figure 5.14: (Color online) The spectator missing mass squared  $M_s^2$  distributions for data (black curve) and simulation (blue curve). The black, red, and blue vertical lines represent loose, chosen, and tight  $M_s^2$  cuts, respectively.

1499 which are all shown in Fig. 5.14. The average systematic uncertainty over all bins due to  
 1500 this cut is 2.29%.

1501 •  $|\vec{P}_s|$  cut

1502 We modified the tight and loose  $|\vec{P}_s|$  cuts within

$$\begin{aligned}
 &0.18 \text{ GeV} < |\vec{P}_s| \text{ (tight); and} \\
 &0.22 \text{ GeV} < |\vec{P}_s| \text{ (loose),}
 \end{aligned}
 \tag{5.22}$$

1503 which are all shown with the chosen  $|\vec{P}_s| > 0.2 \text{ GeV}$  cut in Fig. 5.15. The  $|\vec{P}_s|$  cut is on  
 1504 average responsible for 2.21% of the final systematic uncertainty.

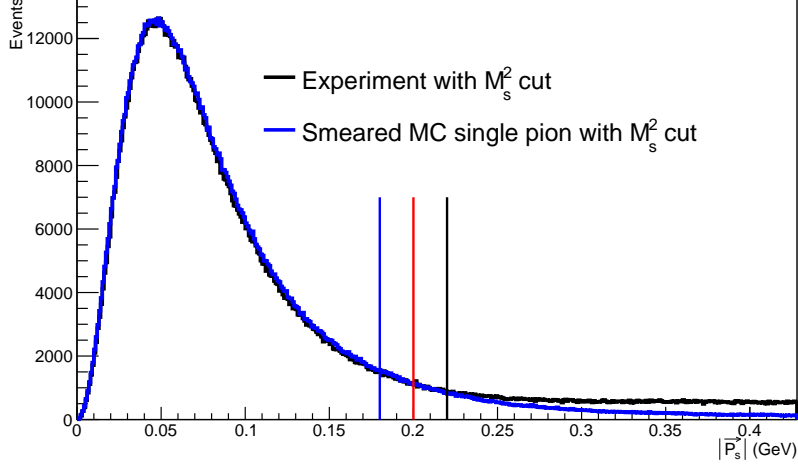


Figure 5.15: (Color online) The spectator missing momentum  $|\vec{P}_s|$  distributions for data (black curve) and simulation (blue curve). The black, red, and blue vertical lines represent loose, chosen, and tight  $|\vec{P}_s|$  cuts, respectively.

### 1505 5.5.5 Boost

1506 In the “Boost the Kinematic variables” section of Chapter 1, we introduce the boost method.  
 1507 Firstly, we boost all particles’ momenta measured in the lab frame into the neutron rest frame  
 1508 with the boost vector  $\vec{\beta}_1$  (Eq. (5.24)), and then we directly boost all particles’ momenta from  
 1509 the lab frame to the CM frame, where the net momentum of the final proton and  $\pi^-$  is zero.  
 1510 The second boost vector  $\vec{\beta}_f$  is calculated from the final particles (proton and  $\pi^-$ ) as

$$\vec{\beta}_f = \frac{\vec{p} + \vec{\pi}^-}{E_p + E_{\pi^-}}, \quad (5.23)$$

1511 where  $E_p$  and  $E_{\pi^-}$  are the energies of the proton and  $\pi^-$ , respectively. Hence the boost vector  
 1512  $\vec{\beta}_f$  is well-defined. Furthermore, since the initial neutron is bound in the deuteron, the boost  
 1513 vector  $\vec{\beta}_1$  needs to be studied due to the off-shell effects, and it can be calculated by

$$\begin{aligned} \vec{\beta}_1 &= -\vec{n}/E_n \text{ with} \\ \vec{n} &= -\vec{p}_s \text{ and} \\ E_n &= \sqrt{(-\vec{p}_s)^2 + (M_n)^2}, \end{aligned} \quad (5.24)$$

1514 where  $E_n$  is the energy and  $M_n$  is the mass of the initial off-shell neutron, but the neutron mass  
 1515 ( $M_n$ ) is not well-defined and can be varied empirically as follows

$$M_n = m_n, \quad (5.25)$$

$$1516 \quad M_n = m_n - 2K - 2MeV, \quad (5.26)$$

$$1517 \quad M_n = m_n - K - 1MeV, \quad (5.27)$$

$$1518 \quad M_n = m_n + K + 1MeV, \text{ and} \quad (5.28)$$

$$1519 \quad M_n = m_n + 2K + 2MeV, \quad (5.29)$$

1520 where  $K = \frac{(|\vec{p}_s|)^2}{2m_n}$  and  $m_n$  is neutron rest mass. Here, the Eq. (5.26) and Eq. (5.29) show two  
 1521 extreme cases of distributing the off-shellness. In order to choose the most reasonable  $M_n$ , the



1522 quasi-free events ( $|\vec{p}_s| < 200$  MeV) have been studied. Since the condition of  $W_i = W_f$  should  
 1523 be satisfied by the quasi-free events, the  $W_f$  and  $W_i$  with different  $M_n$  settings (Eqs. (5.25) to  
 1524 (5.29)) are plotted in Fig. 1.3 (section 1.4), which shows that the red solid line ( $W_i$  by setting  
 1525  $M_n = m_n - 2\frac{k_n^2}{2m_n} - 2\text{MeV}$ ) and black solid line ( $W_f$ ) agree best with each other over the covered  
 1526  $W$  region for the quasi-free events. The comparison hence reveals that Eq. (5.26) is the best  
 1527 choice to set boost vector  $\vec{\beta}_1$ . We calculate the RMS of the deviations of the cross sections that  
 1528 are calculated with  $\vec{\beta}_1$  by setting  $M_n$  to the different values according to Eqs. (5.25) to (5.29).  
 1529 The systematic uncertainty averaged over all bins due to the different boosts is 2.12%.

### 1530 5.5.6 Deuteron Potential

1531 We generate the spectator momentum distribution with the CD-Bonn deuteron potential, which  
 1532 allows us to isolate the exclusive quasi-free process and to calculate the kinematically defined  
 1533 final-state-interaction contribution factor  $R_{FSI}$ . There are also other popular deuteron potential  
 1534 models available, as for example the Paris and Hulthen potentials. So we plot the normalized  
 1535 cumulative “spectator” proton momentum distributions based on the deuteron potentials of  
 1536 these three models in Fig. 5.16, and compare the ratios corresponding to the integrals of these  
 1537 distributions from  $|\vec{p}| = 0$  GeV/c to  $|\vec{p}| = 0.2$  GeV/c and from  $|\vec{p}| = 0$  GeV/c to  $|\vec{p}| = 1$  GeV/c  
 1538 to get the RMS of the deviations impacted by the CD-Bonn potential from the other two  
 1539 potentials. The systematic uncertainty due to these different deuteron potential models is 3.2%  
 when averaged over all every 4-dimensional bins.

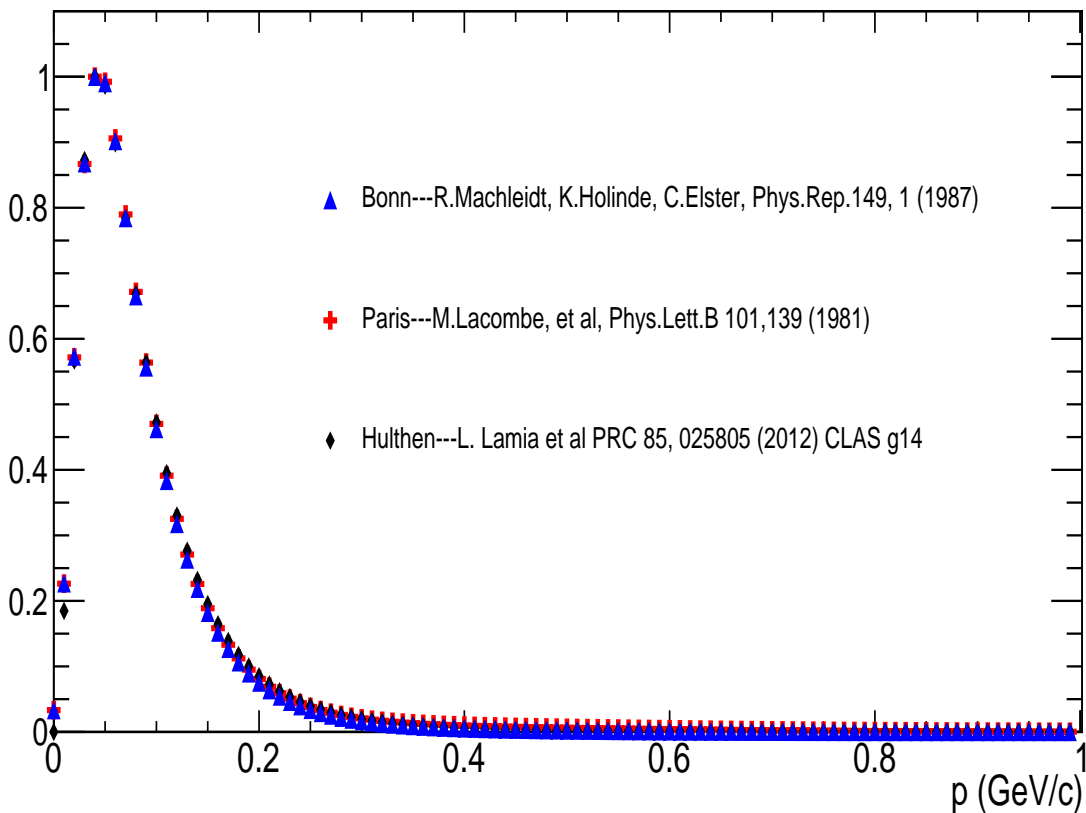


Figure 5.16: The normalized cumulative “spectator” proton momentum distributions from different deuteron potentials. The black, blue, and red points represent the CD-Bonn, Paris, and Hulthen potentials, respectively.

### 1541 5.5.7 Bin Centering Correction

1542 In the previous chapter, the MAID2000 model was selected to calculate the bin centering correc-  
1543 tion factor  $R_{BC}$ . In Fig. 3.2a it is shown that the MAID2000 model describes the experimental  
1544 data better than other MAID versions. However, for the systematic uncertainty study, the  
1545 factor  $R_{BC}$  is calculated with MAID98 and MAID2007 separately and applied to the uncor-  
1546 rected cross sections. The difference between these  $R_{BC}$  corrected cross section is then used to  
1547 quantify the systematic uncertainty due to  $R_{BC}$  being calculated from different versions of the  
1548 MAID model. The average systematic uncertainty found by the deviation of the cross sections  
1549 corrected by  $R_{BC}$  calculated by MAID2000 from these corrected by  $R_{BC}$  calculated by MAID98  
1550 is 0.55% on average. Even though the MAID2007 model does not describe the experimental  
1551 data well at all, the  $R_{BC}$  calculated by this version would still only contribute 1.39% to the  
1552 final systematic uncertainty.

### 1553 5.5.8 Radiative Correction

1554 The cross sections are represented by the variables  $W_f$ ,  $Q^2$ ,  $\cos \theta_{\pi^-}^*$ , and  $\phi_{\pi^-}^*$ . The radiative  
1555 correction applied by the Mo and Tsai [27] approach is carried out to mitigate the influence  
1556 on the  $Q^2$  distribution (since the radiative effects don't influence  $W_f$  variable). The example  
1557 plots of above quasi-free differential cross sections with and without radiative correction for  
1558  $W = 1.2125$  GeV and  $Q^2 = 0.7$  GeV<sup>2</sup> are shown in Fig. 5.17 as red points and black squares,  
1559 respectively. The difference between both cross sections in the covered  $W$  and  $Q^2$  region is  
1560 on average about  $\pm 2.0\%$ . Since there is no Exclurad code available for the exclusive radiative  
1561 correction for the single-pion electroproduction off the “bound” neutron, in order to estimate  
1562 the systematic uncertainty of radiative correction, we assume a 100% uncertainty of the Mo  
1563 and Tsai approach, but even then the average systematic uncertainty of the radiative correction  
1564 is 2.0% .

### 1565 5.5.9 Normalization

1566 In order to quantify the systematic uncertainty in the overall luminosity, usually a compar-  
1567 ison with previously existing experimental data (if there is an overlapping kinematic region)  
1568 or well-known theoretical parameterizations have commonly been used. In the latter case, for  
1569 the electroproductions off a free proton, the elastic cross section is usually used for the com-  
1570 parison. For this analysis (electroproduction off the bound neutron in a deuterium target) the  
1571 above methods are not suitable, so a comparison of the measured inclusive cross sections and  
1572 Osipenko's world-data parameterization is carried out. Since the overall luminosity is the same  
1573 for all  $(W, Q^2)$  bins and due to the relatively large uncertainty of Osipenko's model for different  
1574  $W$  and  $Q^2$  values, the  $W$  and  $Q^2$  weighted average ratios of the Osipenko world-data param-  
1575 eterization (Eq. (4.13)) and the measured inclusive cross sections (Eq. (4.12)) are calculated.  
1576 It turns out that these ratios deviate from “1” by no more than 5%. Due to the model depen-  
1577 dence of the Osipenko event generator, we also cross check against the systematic uncertainty  
1578 of quasi-elastic scattering cross section of nucleons in nuclei. Iuliia Skorodumina compared  
1579 the available world data in similar kinematic regions with the best available parametrizations  
1580 and normalizations and found that the world data as well as the normalized “e1e” data only  
1581 agree to the 5%-level with these parametrizations, Iu. A. Skorodumina's CLAS12 Note 2019-  
1582 003 [25], which is consistent with our Osipenko driven uncertainty. Hence 5% is used as the  
1583 overall normalization uncertainty, which includes target geometry, target density, and Faraday  
1584 cup uncertainties.

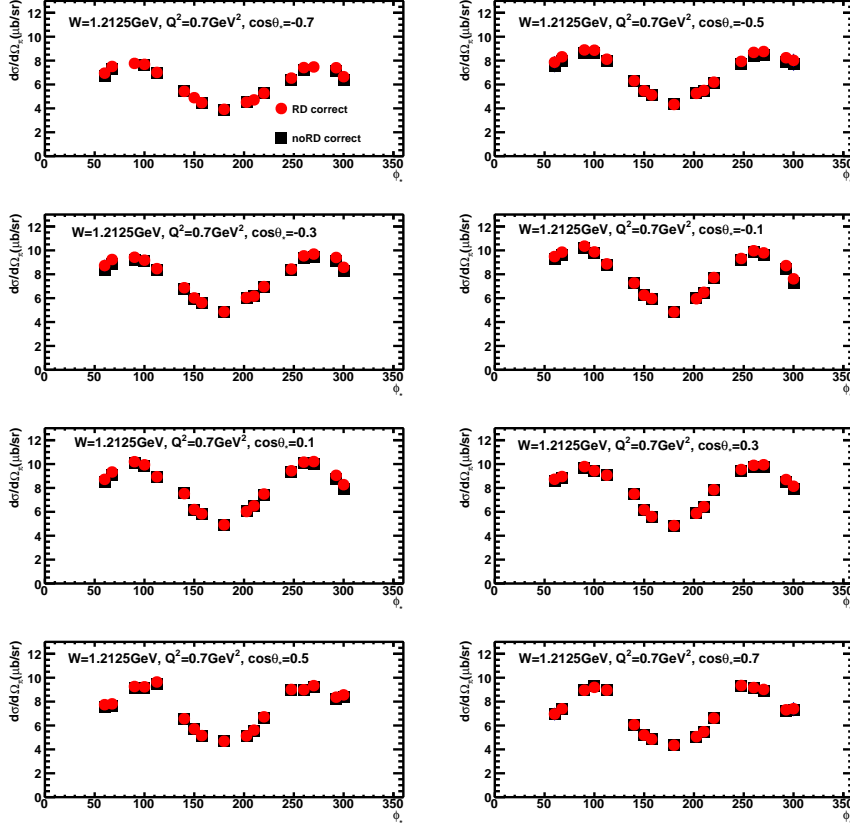


Figure 5.17: The  $\phi_{\pi^*}^-$  dependence of the exclusive cross sections with and without radiative correction are marked as red points and black squares, respectively for an example at  $W = 1.2125$  GeV and  $Q^2 = 0.7$  GeV<sup>2</sup>. The individual plots correspond to different  $\cos \theta_{\pi^*}^-$  bins.

### 1585 5.5.10 Summary

1586 Summing over all of the above systematic uncertainty sources listed in the Tab. 5.1, the total average systematic uncertainty is 8.26%. From the above discussion, the total systematic

Table 5.1: Summary of sources of the average systematical uncertainty.

Sources	Uncertainty (%)
Electron $\theta_{CC}$ cut	0.78
Electron SF cut	1.26
Electron fiducial cut	2.10
Proton $\Delta T$ cut	1.39
Proton fiducial cut	2.39
Pion $\Delta T$ cut	1.78
Pion fiducial cut	1.73
$M_s^2$ cut	2.29
$p_s$ cut	2.21
Boosts	2.12
Potential	3.2
Bin center correction	0.55
Radiative correction	2.0
Normalization	5.0
Total	8.6

1587 uncertainty can be calculated bin by bin

$$\Delta_{RMS} = \sqrt{\sum_i^9 (\Delta_{cut^i}^{RMS})^2 + (\Delta_{boost}^{RMS})^2 + \Delta_{potential}^2 + \Delta_{RBC}^2 + \Delta_{Rad}^2 + \Delta_{normalization}^2}, \quad (5.30)$$

1588 where for each variable bin  $\Delta_{cut^i}^{RMS}$  corresponds to the RMS of the cross-section deviations of  
 1589 the modified cut (tight or loose) from the chosen cut and  $\Delta_{boost}^{RMS}$  to the RMS of deviations  
 1590 of the cross sections between different boost vectors  $\vec{\beta}_i$  and  $\vec{\beta}_f$ .  $\Delta_{potential}$  corresponds to the  
 1591 deviations of the CD-Bonn potential from other potentials, which is 3.2% for every variable  
 1592 bin,  $\Delta_{Rad}$  to the radiative correction, and  $\Delta_{normalization}$  to the CLAS standard normalization  
 1593 uncertainty, which is 5% for every variable bin.  $\Delta_{RMS}$  is shown as back bars in the final  
 1594 hadronic differential cross section plots in Figs. 5.1, 5.2, 5.3, 5.4, and 5.5.

### 1595 5.5.11 Error Propagation

1596 The above systematic uncertainty is calculated for the cross section. In order to have the  
 1597 systematic uncertainty for the structure functions, we apply the same procedure to the  $\phi_{\pi^-}^*$ -  
 1598 dependent cross section fit ( $a + b \cos 2\phi_{\pi^-}^* + c \cos \phi_{\pi^-}^*$ ) for the chosen cross sections and all other  
 1599 cross-section variations, corresponding to the different cuts, boost, potential, bin centering  
 1600 corrections, and normalizations. Then the RMS of the structure functions is given by Eq. (5.30)  
 1601 bin by bin for three sets of  $\phi_{\pi^-}^*$  bins ( $\Delta\phi_{\pi^-}^* = 40^\circ$ ,  $\Delta\phi_{\pi^-}^* = 45^\circ$ , and  $\Delta\phi_{\pi^-}^* = 60^\circ$ ), respectively.  
 1602 The smallest RMS of the three sets of  $\phi_{\pi^-}^*$  bins, the RMS of  $\Delta\phi_{\pi^-}^* = 40^\circ$  bins, is set to the  
 1603 final systematic uncertainty of the structure functions, and is shown as black bar for each data  
 1604 point in Fig. 5.10. The average of systematic uncertainties over  $Q^2$  and  $\cos\theta_{\pi^-}^*$  for the structure  
 1605 functions that are shown in Fig. 5.10 is 11.17% in the  $W = 1.2125$  GeV bin.

# Chapter 6

## Summary and Conclusions

The JLab CLAS “e1e” experiment provides data to extract the differential cross sections of the process  $\gamma^*n(p) \rightarrow p\pi^-(p)$ , which is  $\pi^-$  electroproduction off the neutron in the deuterium, with in the corresponding kinematic coverage  $W = 1.1 - 1.825$  GeV and  $Q^2 = 0.4 - 1.0$  GeV<sup>2</sup>. The experimental data were analyzed in such a way that all stages of this analysis were processed through a series of data consistent tests and cross-checks to provide reliable measured results. The reliability of the absolute normalization was confirmed by the agreement between the measured inclusive cross sections and the available world-data’s parameterization results.

The existing  $\gamma^*n \rightarrow p\pi^-$  event generator was modified to include the spectator (proton) information based on the CD-Bonn potential [20] to simulate the real quasi-free process. With this method, the exclusive quasi-free process is isolated successfully as demonstrated by the comparison of the spectator momentum distribution of simulation with the measured data, and the kinematical final-state-interaction contribution factor  $R_{FSI}$  is extracted directly from the experimental data according to the ratio between the exclusive quasi-free and full cross sections. The kinematical final state interaction contributions in  $\pi^-$  electroproduction is on average about 10% – 20% for the above kinematic coverage. Furthermore, we quantify that the influence of off-shell effects on the final cross section is marginal.

These are the first results for the full exclusive and quasi-free electroproduction cross sections off the bound neutron in the above mentioned kinematic region. These cross sections provide input for a combined analysis of pion electroproduction off the free proton, the bound proton, and the bound neutron under the same experimental conditions, which is a unique way to extract in the experimentally best possible way information about the off-shell and final-state-interaction effects in deuterium that must be considered in order to extract the free neutron information. These cross sections enrich the database for further development of the reaction theory for exclusive reactions off nucleons bound in deuterium.

Additionally, the associated unpolarized structure functions  $\sigma_T + \epsilon\sigma_L$ ,  $\sigma_{TT}$ , and  $\sigma_{TL}$  have been extracted from the  $\phi_{\pi^-}^*$  dependence of the differential cross sections with appropriate systematic uncertainty estimates.

The statistics for the  $\gamma^*n(p) \rightarrow p\pi^-(p)$  channel is limited due to the short experiment time and the relatively low detector acceptance for the  $\pi^-$  particle. In order to get even better fit results in both the very forward and the very backward polar and azimuthal angles of  $\pi^-$ , particularly in the higher resonance region, it would be valuable to run further deuterium target experiments with the upgraded CLAS12 detector, at  $Q^2$  up to 11 GeV<sup>2</sup>. This would also allow us to improve our knowledge of the  $Q^2$  evolution of the transition form factors off the bound nucleon system, and would ultimately grant access to the isospin-dependent structure of baryons.

# 1643 References

- 1644 [1] GSIM, <http://nuclear.unh.edu/~maurik/Gsim/>.
- 1645 [2] “e1e” 2 GeV run analysis, <https://www.jlab.org/Hall-B/secure/e1/markov/2GeV/newDesign/simulation/simulation.html>.
- 1646
- 1647 [3] Simutcl, <https://userweb.jlab.org/~tianye/cook>.
- 1648 [4] SAID, <http://gwdac.phys.gwu.edu/>.
- 1649 [5] Datatcl, <https://userweb.jlab.org/~tianye/cook>.
- 1650 [6] CLAS Online BOS Bank Viewer, <http://clasweb.jlab.org/bos/browsebos.php>.
- 1651 [7] Golden Run List, [https://userweb.jlab.org/~tianye/e1e\\_analysis/good\\_file\\_list](https://userweb.jlab.org/~tianye/e1e_analysis/good_file_list).
- 1652
- 1653 [8] MAID, <http://portal.kph.uni-mainz.de/MAID//>.
- 1654 [9] CVS, [https://clasweb.jlab.org/wiki/index.php/Previous\\_Main\\_Page](https://clasweb.jlab.org/wiki/index.php/Previous_Main_Page).
- 1655 [10] FFREAD card definitions, [http://cnr2.kent.edu/e895/eosg/eosg\\_manual/node60.html](http://cnr2.kent.edu/e895/eosg/eosg_manual/node60.html).
- 1656
- 1657 [11] genev, [https://clasweb.jlab.org/wiki/index.php/CLAS\\_Offline](https://clasweb.jlab.org/wiki/index.php/CLAS_Offline).
- 1658 [12] M. Osipenko, personal communications.
- 1659 [13] CJ Bebek, CN Brown, M Herzlinger, Stephen D Holmes, CA Lichtenstein, FM Pipkin, S Raither, and LK Siefert. Determination of the pion form factor up to  $Q^2 = 4 \text{ GeV}^2$  from single-charged-pion electroproduction. *Physical Review D*, 13(1):25, 1976.
- 1660
- 1661
- 1662 [14] CJ Bebek, CN Brown, SD Holmes, RV Kline, FM Pipkin, S Raither, LK Siefert, A Browman, KM Hanson, D Larson, et al. Electroproduction of single pions at low  $\varepsilon$  and a measurement of the pion form factor up to  $Q^2 = 10 \text{ GeV}^2$ . *Physical Review D*, 17(7):1693, 1978.
- 1663
- 1664
- 1665
- 1666 [15] VD Burkert and T-SH Lee. Electromagnetic meson production in the nucleon resonance region. *International Journal of Modern Physics E*, 13(06):1035–1111, 2004.
- 1667
- 1668 [16] JB Cladis, WN Hess, and BJ Moyer. Nucleon momentum distributions in deuterium and carbon inferred from proton scattering. *Physical Review*, 87(3):425, 1952.
- 1669
- 1670 [17] D Drechsel, O Hanstein, SS Kamalov, and L Tiator. A unitary isobar model for pion photo- and electroproduction on the proton up to 1 GeV. *Nuclear Physics A*, 645(1):145–174, 1999.
- 1671
- 1672

- 1673 [18] D Drechsel, SS Kamalov, and L Tiator. Unitary isobar model—MAID2007. *The European*  
1674 *Physical Journal A*, 34(1):69–97, 2007.
- 1675 [19] K.S. Egiyan. Determination of electron energy cut due to the clas ec threshold. pages  
1676 CLAS Note 1999–007, Jefferson Laboratory.
- 1677 [20] DR Entem and R Machleidt. Accurate charge-dependent nucleon-nucleon potential at  
1678 fourth order of chiral perturbation theory. *Physical Review C*, 68(4):041001, 2003.
- 1679 [21] G. Fedotov. Personal communications.
- 1680 [22] David Gaskell, Abdellah Ahmidouch, Pawel Ambrozewicz, H Anklin, John Arrington,  
1681 K Assamagan, Steven Avery, Kevin Bailey, Oliver K Baker, Shelton Beedoe, et al. Longi-  
1682 tudinal Electroproduction of Charged Pions from  $H_1$ ,  $H_2$ , and  $He_3$ . *Physical review letters*,  
1683 87(20):202301, 2001.
- 1684 [23] R Gilman, M Bernheim, M Brussel, J Cheminaud, J-F Danel, J-P Didelez, M-A Duval,  
1685 G Fournier, R Frascaria, RJ Holt, et al. Forward-angle charged-pion electroproduction in  
1686 the deuteron. *Physical review letters*, 64(6):622, 1990.
- 1687 [24] GM Huber, HP Blok, Cornel Butuceanu, David Gaskell, Tanja Horn, DJ Mack, David  
1688 Abbott, Konrad Aniol, Heinz Anklin, Christopher Armstrong, et al. Separated Response  
1689 Function Ratios in Exclusive, Forward  $\pi^\pm$  Electroproduction. *Physical review letters*,  
1690 112(18):182501, 2014.
- 1691 [25] G.V. Fedotov Iu.A. Skorodumina and R.W. Gothe. Testing Parameterizations of the  
1692 Deuteron Quasi-Elastic Peak. pages CLAS Note 2019–003, Jefferson Laboratory.
- 1693 [26] M Lacombe, B Loiseau, R Vinh Mau, J Cote, P Pires, and R De Tournell. Parametrization  
1694 of the deuteron wave function of the paris nn potential. *Physics Letters B*, 101:139–140,  
1695 1981.
- 1696 [27] Luke W Mo and Yung-Su Tsai. Radiative Corrections to Elastic and Inelastic ep and up  
1697 Scattering. *Reviews of Modern Physics*, 41(1):205, 1969.
- 1698 [28] JV Morris, DC Darvill, M Davenport, F Foster, G Gughes, J Wright, J Allison, B Dickin-  
1699 son, S Hill, M Ibbotson, et al. Forward electroproduction of charged pions from deuterons  
1700 at  $Q^2 = 1.0(\text{GeV}/c)^2$ . *Physics Letters B*, 86(2):211–214, 1979.
- 1701 [29] R. Niyazov and L. B. Weinstein. Fiducial Cut For Positive Hadrons in CLAS/E2 data at  
1702 4.4 GeV. pages CLAS Note 2001–013, Jefferson Laboratory.
- 1703 [30] M. Osipenko. Matching between the electron candidate track and the cherenkov counter  
1704 hit. pages CLAS Note 2004–020, Jefferson Laboratory.
- 1705 [31] M Osipenko, G Ricco, S Simula, M Battaglieri, M Ripani, G Adams, P Ambrozewicz,  
1706 M Anghinolfi, B Asavapibhop, G Asryan, et al. Measurement of the deuteron structure  
1707 function  $f_2$  in the resonance region and evaluation of its moments. *Physical Review C*,  
1708 73(4):045205, 2006.
- 1709 [32] K. Park. Kinematics corrections for clas. pages CLAS Note 2003–012, Jefferson Laboratory.
- 1710 [33] Alan Steven Raskin and T William Donnelly. Polarization in coincidence electron scatter-  
1711 ing from nuclei. *Annals of Physics*, 191(1):78–142, 1989.

- 1712 [34] J Wright, DC Darvill, M Davenport, F Foster, G Hughes, JV Morris, J Allison, B Dickin-  
1713 son, S Hill, M Ibbotson, et al. Electroproduction of single charged pions from deuterons  
1714 at  $Q^2 \sim 0.5(\text{GeV}/c)^2$ . *Nuclear Physics B*, 181(3):403–420, 1981.



# 1715 Appendix A

## 1716 Parameter Tables

Table A.1: Parameters of pion  $\theta$  versus  $p$  cut functions.

Sector	Position	$C_0$	$C_1$	$C_2$	$C_3$	$C_4$
1	upper	96.090	8.000	0.472	0.250	0.117
	lower	86.090	8.000	0.472	0.250	0.117
2	upper	38.152	$3.699 \times 10^{-5}$	$5.408 \times 10^{-6}$	$1.812 \times 10^{-7}$	
	lower	33.652	$3.699 \times 10^{-5}$	$5.408 \times 10^{-6}$	$1.812 \times 10^{-7}$	
3	upper	116.152	$3.699 \times 10^{-5}$	$5.408 \times 10^{-6}$	0.1	$1.812 \times 10^{-7}$
	lower	107.152	$3.699 \times 10^{-5}$	$5.408 \times 10^{-6}$	0.08	$1.812 \times 10^{-7}$
4	upper	113.152	$3.699 \times 10^{-5}$	$5.408 \times 10^{-6}$	0.15	$1.812 \times 10^{-7}$
5-1	upper	118.152	$6.699 \times 10^{-5}$	$5.408 \times 10^{-6}$	0.2	$1.812 \times 10^{-7}$
5-2	upper	108.152	$3.699 \times 10^{-5}$	$5.408 \times 10^{-6}$	0.2	$1.812 \times 10^{-7}$
	lower	96.152	$3.699 \times 10^{-5}$	$5.408 \times 10^{-6}$	0.03	$1.812 \times 10^{-7}$
5-3	upper	39.652	$3.699 \times 10^{-5}$	$5.408 \times 10^{-6}$	0.01	$1.812 \times 10^{-7}$
	lower	35.652	$3.699 \times 10^{-5}$	$5.408 \times 10^{-6}$	0.01	$1.812 \times 10^{-7}$
6	upper	106.152	$3.699 \times 10^{-5}$	$5.408 \times 10^{-6}$	0.15	$1.812 \times 10^{-7}$

Table A.2: Parameters of proton  $\theta$  versus  $p$  cut functions.

Sector	Position	$C_0$	$C_1$	$C_2$	$C_3$	$C_4$
2	upper	26.509	-116.557	175.167	-64.472	
	lower	26.509	-116.557	175.167	-64.572	
5-1	upper	88.042	-0.321	0.070	-46.934	
	lower	87.094	-0.371	0.065	-50.990	
5-2	upper	31.248	-135.817	198.038	-65.168	0.045
	lower	31.248	-135.817	198.038	-69.468	-0.010

Table A.3:  $\Delta T$  shift parameters.

Sector	Counter	$\Delta t_1$ (ns)	$\Delta t_2$ (ns)	$\Delta t_3$ (ns)	$\Delta t_4$ (ns)	$\Delta t_5$ (ns)
1	25	0.34				
	36	-0.36				
	43	-0.04				
	41	3.63	0.18	-2.96		
	42	-0.08	-2.14			
	45	4.72	3.16	0.32	-3.04	
	46	-0.03	-1.02	-2.15	-5.82	
	47	5.97	5.00	0.22		
2	24	1.18				
	22	0.09				
	27	-0.46				
	29	-0.37				
	36	-0.46				
	37	0.25				
	40	2.90	-0.10	-2.74	-7.17	
	41	8.40	7.34	4.10	3.05	-1.80
	42	4.78	0.45			
	43	10.81	8.22	6.94		
	44	6.69	3.93			
	45	5.30	0.25			
	46	8.05	0.85			
	47	0.11	-1.66			
3	11	0.34				
	23	0.21				
	24	-0.33				
	25	3.42				
	30	-0.16				
	35	-0.40				
	38	-0.53				
	36	-0.18				
	40	-0.10	-3.95			
	41	-0.05	-0.86			
	42	-2.03	-5.50			
	43	-0.50	-3.60			
	44	-8.19	-10.52			
	46	-0.60	-1.44	-3.35		
	47	4.62	2.00	-0.61		

Table A.4:  $\Delta T$  shift parameters continued.

Sector	Counter	$\Delta t_1$ (ns)	$\Delta t_2$ (ns)	$\Delta t_3$ (ns)	$\Delta t_4$ (ns)
4	22	0.08			
	23	-0.35			
	25	-0.37			
	26	-0.27			
	27	-0.48			
	37	-0.42			
	38	-0.53			
	39	4.24			
	40	-0.21			
	41	0.59			
	42	2.95	0.04		
	43	2.99	1.29	-0.99	
	44	-0.12			
	45	0.07			
	46	1.19	0.17		
47	0.04				
5	22	0.14			
	24	0.01			
	25	0.08			
	37	0.43			
	40	4.65	1.44		
	41	-0.44			
	42	4.23	1.17	0.28	-1.86
	43	2.37	0.46		
	44	0.76	-0.73		
	45	0.08			
	46	-2.11			
47	-2.06	-4.10			
6	25	-2.11			
	31	1.55			
	40	3.90	0.05		
	43	-1.77			
	44	1.37	-0.06		
	45	3.69	0.10		
	47	5.26	2.63	0.85	

Table A.5: Parameters of the proton momentum correction function.

parameter	value
$C_0$	$-2.01369 \times 10^{-2}$
$C_1$	$2.36456 \times 10^{-4}$
$C_2$	$2.18450 \times 10^{-6}$
$C_3$	$1.29756 \times 10^{-2}$
$C_4$	$-2.00838 \times 10^{-4}$
$C_5$	$1.88744 \times 10^{-6}$
$C_6$	$1.03155 \times 10^{-2}$
$C_7$	$-7.19808 \times 10^{-5}$
$C_8$	$6.11292 \times 10^{-7}$

Table A.6: Parameters of pion  $\theta$  versus  $\phi$  cut functions.

	parameter	$P_0$	$P_1$	$P_2$
data	$C_{0max}$	25.1028	-0.248504	-0.470204
	$C_{0min}$	-25.1039	0.249551	0.470333
	$C_2$	20.4540	2.52675	3.34473
	$C_1$	0.255487		
simulation	$C_{0max}$	27.0012	-0.741629	-0.723387
	$C_{0min}$	-27.5001	0.777486	0.734897
	$C_2$	14.1899	0.999445	2.84491
	$C_1$	0.135487		

Table A.7: Parameters of proton  $\theta$  versus  $\phi$  cut functions.

sector	function	$P_0$	$P_1$	$P_2$
1	$\phi_{max}$	24.2559	0.0840516	-9.00173
	$\phi_{min}$	-24.3303	0.1096713	-8.85532
2	$\phi_{max}$	83.1846	0.0967659	0.376712
	$\phi_{min}$	36.5613	0.129967	-7.20855
3	$\phi_{max}$	144.4382	0.0895825	10.7034
	$\phi_{min}$	95.0490	0.0955602	6.03828
4	$\phi_{max}$	203.271	0.11877	6.32992
	$\phi_{min}$	155.694	0.090633	11.05086
5	$\phi_{max}$	264.817	0.112822	10.7241
	$\phi_{min}$	215.618	0.122742	4.34678
6	$\phi_{max}$	323.471	0.113954	10.9227
	$\phi_{min}$	275.005	0.0729742	24.2907

Table A.8:  $\theta_e$  correction function parameters.

Para	$\theta_e$	ind	sec1	sec 2	sec3	sec 4	sec 5	sec 6
$\alpha$	[16,32.5]	A	0.20E-01	-0.13	0.57	1.76	0.63E-01	0.28E-01
		B	-0.25E-02	-0.16E-02	0.77E-02	-0.18E-01	0.34E-02	0.42E-02
		C	0.15E-03	0.27E-03	0.58E-03	0.49E-03	0.39E-03	0.27E-03
	[32.5,44]	A	6.25	5.22	0.57	1.76	24.81	8.53
		B	-0.27	-0.65	0.77E-02	-0.18E-01	17.04	-0.10E-02
		C	-0.32E-03	-0.35E-01	0.58E-03	0.49E-03	0.21E-02	0.12E-02
$\beta$	[16,32.5]	A	-0.50E-03	0.10E-01	-0.99E-01	-0.25	-0.48E-03	-0.42E-04
		B	0.97E-04	0.95E-04	-0.17E-03	0.37E-02	-0.84E-04	-0.76E-04
		C	0.45E-05	0.75E-07	-0.11E-04	-0.89E-05	-0.49E-05	0.60E-06
	[32.5,44]	A	-0.47	-0.40	-0.99E-01	-0.25	-1.91	-0.62
		B	0.21E-01	0.51E-01	-0.17E-03	0.37E-02	-1.34	0.61E-04
		C	0.11E-04	0.13E-02	-0.11E-04	-0.89E-05	-0.53E-04	-0.28E-04
$\gamma$	[16,32.5]	A		-0.17E-03	0.59E-02	0.12E-01		
		B				-0.22E-03		
		C	0.11E-03	-0.10E-03	-0.12E-03	0.12E-03	-0.96E-04	0.73E-04
	[32.5,44]	A	0.11E-01	0.10E-01	0.59E-02	0.12E-01	0.49E-01	0.15E-01
		B	-0.55E-03	-0.13E-02		-0.22E-03	0.24E-01	0.81E-06
		C	-0.22E-03	0.24E-04	-0.12E-03	0.12E-03	-0.21E-03	-0.13E-03
$\xi$	[16,32.5]	A			-0.14E-03	-0.14E-03		
		B				0.52E-05		
		C	449	449	449	449	449	449
	[32.5,44]	A	-0.98E-04	-0.87E-04	-0.14E-03	-0.14E-03	-0.41E-03	-0.12E-03
		B	0.47E-05	0.11E-04		0.52E-05	0.53E-03	0.14E-07
		C	449	-0.70E-06	449	449	449	449
$\eta$	[16,32.5]	A			0.12E-05	-0.62E-05		
		B				-0.43E-07		
		C	8.05	-1.25	-1.53	1.44	-1.26	8.13
	[32.5,44]	A			0.12E-05	-0.62E-05		
		B				-0.43E-07	-0.21E-04	0.23E-09
		C	-8.18		-1.53	1.44	-0.16	-0.90
$\kappa$	[16,32.5]	A				0.19E-06		
		B						
		C						
	[32.5,44]	A				0.19E-06		
		B					0.18E-06	-0.21E-10
		C		-0.23E-07				
$\varepsilon$	[16,32.5]	A				-0.15E-08		
		B						
		C						
	[32.5,44]	A				-0.15E-08		
		B						
		C		0.47E-09				

Table A.9:  $p_e$  correction function parameters.

Para	$\theta_e$	ind	sec1	sec 2	sec3	sec 4	sec 5	sec 6
$\alpha$	[16,52]	$A'$	1.01	1.0	1.01	1.01	0.99	1.01
		$B'$	-0.10E-02	-0.16E-02	-0.27E-02	-0.30E-02	-0.18E-02	-0.78E-03
		$C'$	-0.90E-04	-0.48E-04	-0.85E-04	-0.42E-04	-0.53E-04	0.35E-05
		$D'$					-0.22E-07	
		$E'$					0.50E-08	
$\beta$	[16,52]	$A'$	-0.34E-03	0.58E-04	-0.25E-02	-0.74E-03	0.19E-02	-0.28E-03
		$B'$	0.85E-05	0.92E-04	0.28E-03	0.40E-03	0.15E-03	0.90E-04
		$C'$	0.87E-05	0.52E-05	0.82E-05	0.42E-05	0.56E-05	-0.15E-06
		$D'$					-0.69E-09	
		$E'$					0.11E-09	
$\gamma$	[16,52]	$A'$	-0.69E-06	-0.29E-05	0.10E-03	0.85E-05	-0.71E-04	0.39E-05
		$B'$	0.12E-05	-0.17E-05	-0.65E-05	-0.18E-04	-0.48E-05	-0.27E-05
		$C'$	-0.26E-06	-0.16E-06	-0.24E-06	-0.12E-06	-0.19E-06	
$\xi$	[16,52]	$A'$	0.81E-07	0.48E-07	-0.11E-05		0.80E-06	
		$B'$	-0.21E-07	0.89E-08	-0.54E-07	0.34E-06	0.47E-07	0.22E-07
		$C'$	0.24E-08	0.15E-08	0.23E-08	0.12E-08	0.19E-08	
$\eta$	[16,52]	$A'$		-0.14E-07				
		$B'$			0.32E-08	-0.23E-08		
		$C'$						
$\kappa$	[16,52]	$A'$			0.22E-09			
		$B'$			-0.27E-10			
		$C'$						

1717 **Appendix B**

1718 **Differential Cross Sections**

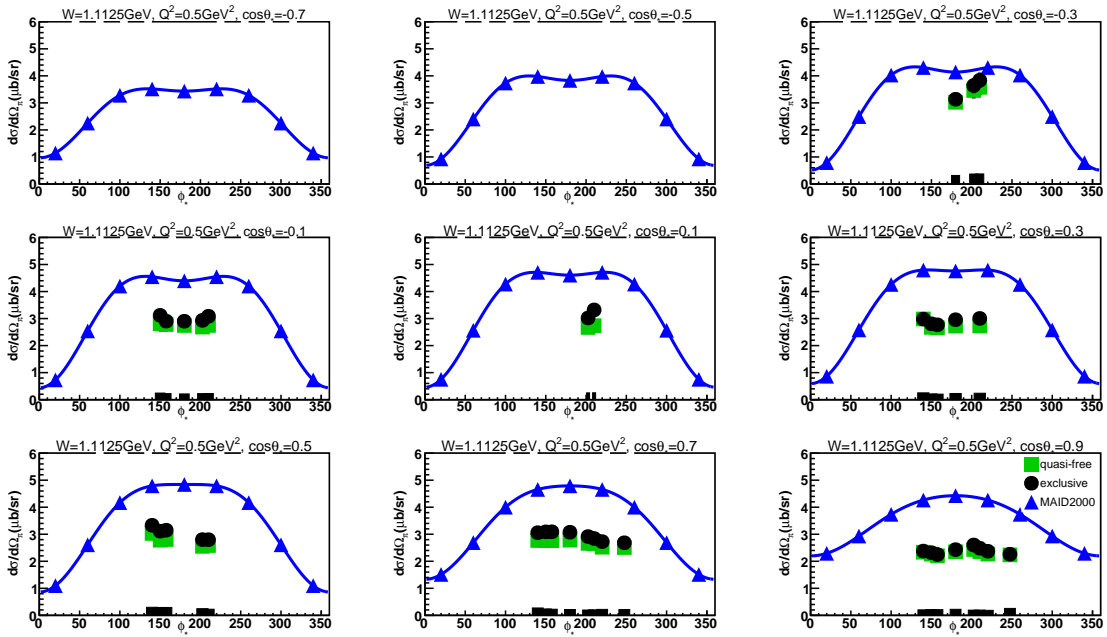


Figure B.1: Exclusive (black points) and quasi-free (green squares) cross sections in  $\mu\text{b}/\text{sr}$  are represented for  $W = 1.1125 \text{ GeV}$  and  $Q^2 = 0.5 \text{ GeV}^2$ . The  $\phi_{\pi^-}^*$  dependent cross sections are illustrated in each  $\cos \theta_{\pi^-}^*$  bin. The blue triangles show MAID2000 model predictions. The blue lines show fits to the model predictions by the function “ $a + b \cos 2\phi_{\pi^-}^* + c \cos \phi_{\pi^-}^*$ ”. The black bars at the bottom of each subplot represent the systematic uncertainty for each cross section points.

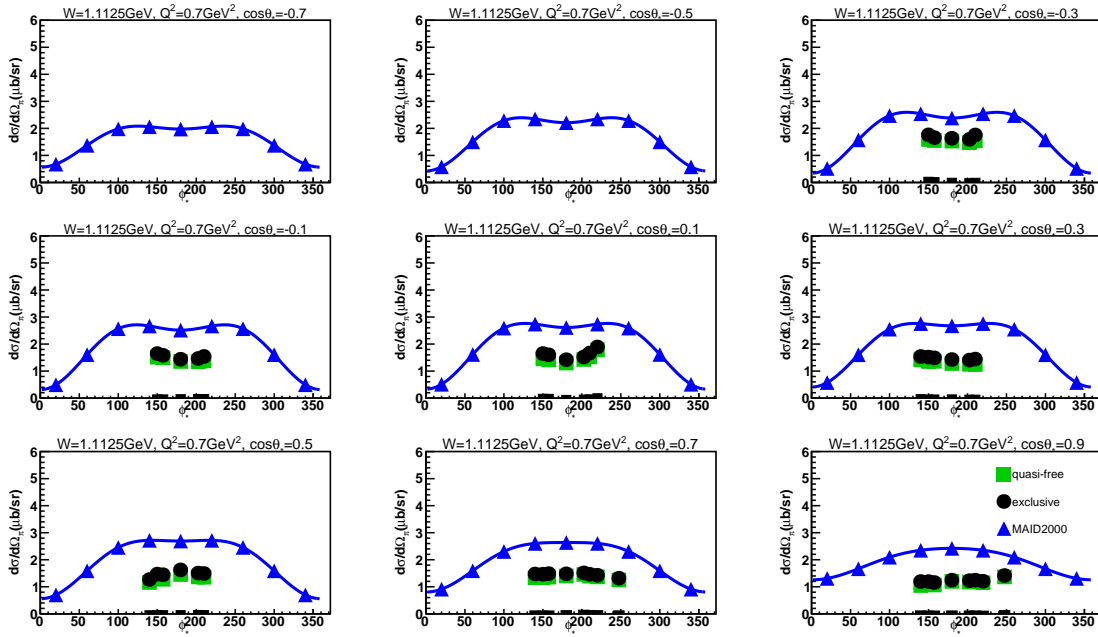


Figure B.2: Exclusive (black points) and quasi-free (green squares) cross sections in  $\mu\text{b}/\text{sr}$  are represented for  $W = 1.1125 \text{ GeV}$  and  $Q^2 = 0.7 \text{ GeV}^2$ . The  $\phi_{\pi^-}^*$  dependent cross sections are illustrated in each  $\cos \theta_{\pi^-}^*$  bin. The blue triangles show MAID2000 model predictions. The blue lines show fits to the model predictions by the function “ $a + b \cos 2\phi_{\pi^-}^* + c \cos \phi_{\pi^-}^*$ ”. The black bars at the bottom of each subplot represent the systematic uncertainty for each cross section points.



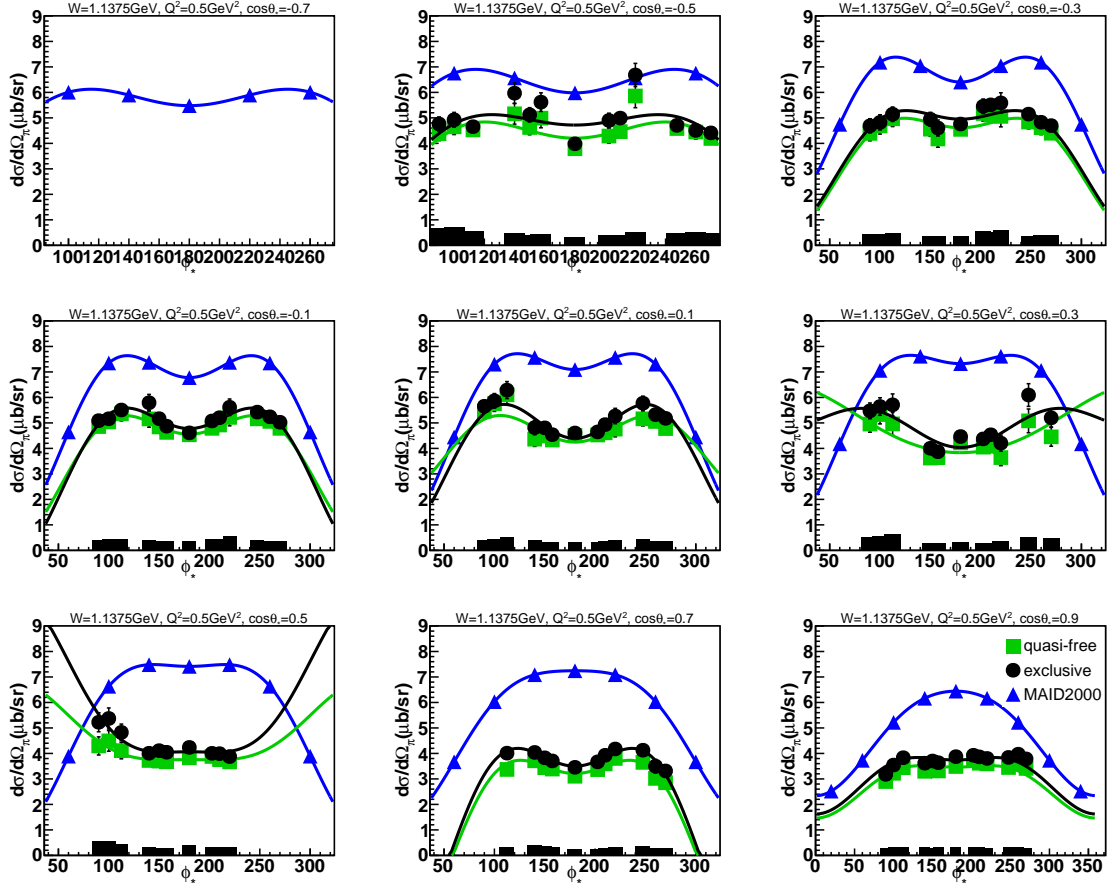


Figure B.3: Exclusive (black points) and quasi-free (green squares) cross sections in  $\mu\text{b}/\text{sr}$  are represented for  $W = 1.1375 \text{ GeV}$  and  $Q^2 = 0.5 \text{ GeV}^2$ . The  $\phi_{\pi^-}^*$  dependent cross sections are illustrated in each  $\cos \theta_{\pi^-}^*$  bin. The blue triangles show MAID2000 model predictions. The blue lines show fits to the model predictions by the function “ $a + b \cos 2\phi_{\pi^-}^* + c \cos \phi_{\pi^-}^*$ ”. The black bars at the bottom of each subplot represent the systematic uncertainty for each cross section points.

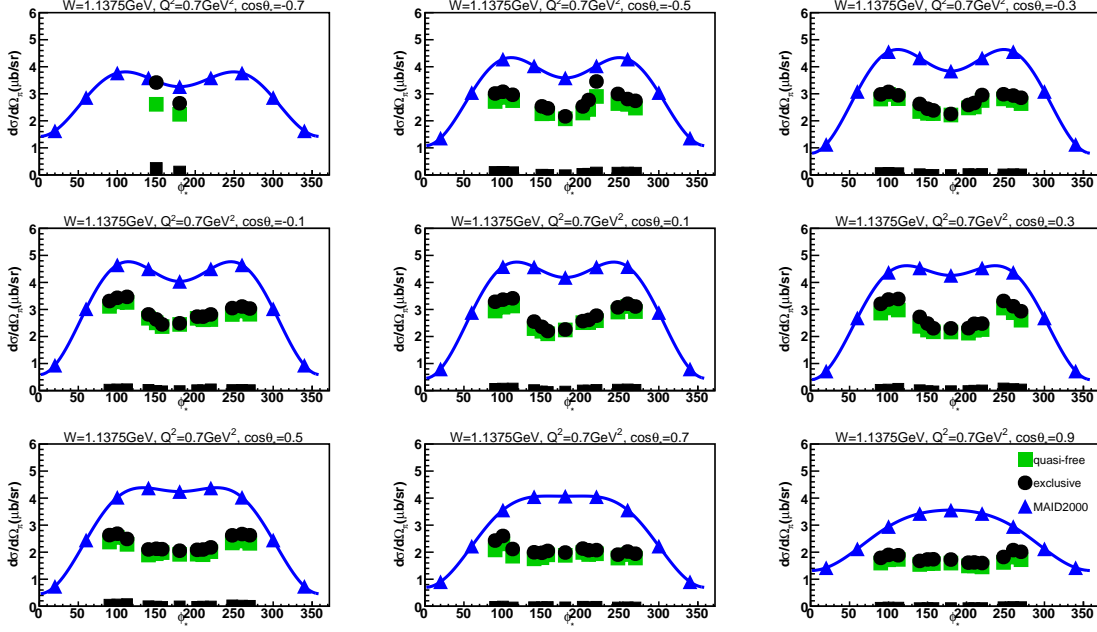


Figure B.4: Exclusive (black points) and quasi-free (green squares) cross sections in  $\mu\text{b}/\text{sr}$  are represented for  $W = 1.1375 \text{ GeV}$  and  $Q^2 = 0.7 \text{ GeV}^2$ . The  $\phi_{\pi^-}^*$  dependent cross sections are illustrated in each  $\cos \theta_{\pi^-}^*$  bin. The blue triangles show MAID2000 model predictions. The blue lines show fits to the model predictions by the function “ $a + b \cos 2\phi_{\pi^-}^* + c \cos \phi_{\pi^-}^*$ ”. The black bars at the bottom of each subplot represent the systematic uncertainty for each cross section points.

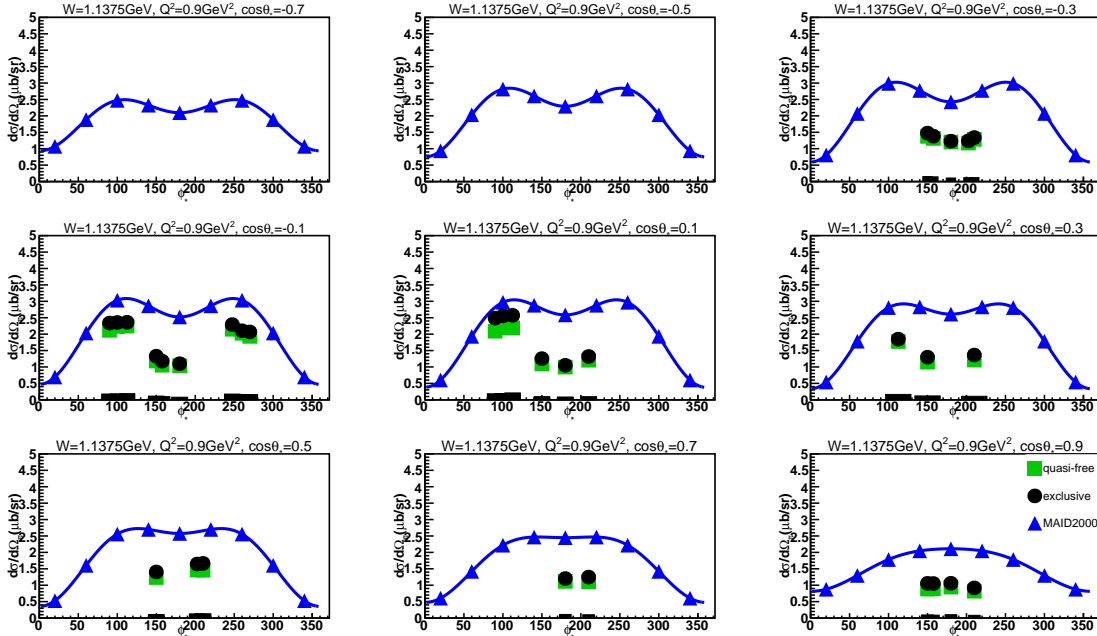


Figure B.5: Exclusive (black points) and quasi-free (green squares) cross sections in  $\mu\text{b}/\text{sr}$  are represented for  $W = 1.1375 \text{ GeV}$  and  $Q^2 = 0.9 \text{ GeV}^2$ . The  $\phi_{\pi^-}^*$  dependent cross sections are illustrated in each  $\cos \theta_{\pi^-}^*$  bin. The blue triangles show MAID2000 model predictions. The blue lines show fits to the model predictions by the function “ $a + b \cos 2\phi_{\pi^-}^* + c \cos \phi_{\pi^-}^*$ ”. The black bars at the bottom of each subplot represent the systematic uncertainty for each cross section points.

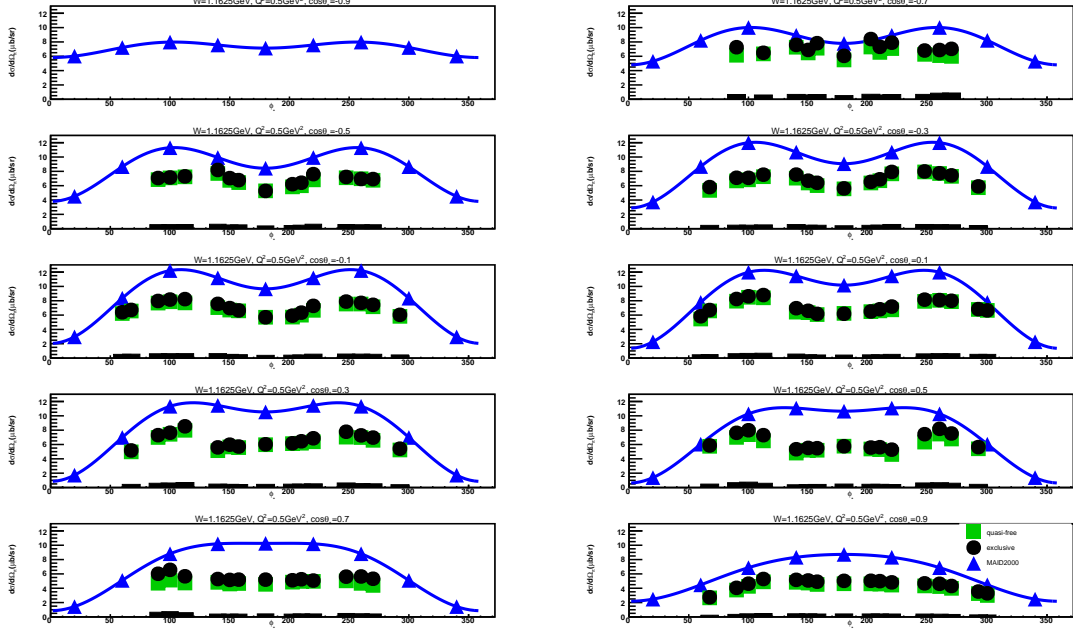


Figure B.6: Exclusive (black points) and quasi-free (green squares) cross sections in  $\mu\text{b}/\text{sr}$  are represented for  $W = 1.1625$  GeV and  $Q^2 = 0.5$  GeV<sup>2</sup>. The  $\phi_{\pi^-}^*$  dependent cross sections are illustrated in each  $\cos \theta_{\pi^-}^*$  bin. The blue triangles show MAID2000 model predictions. The blue lines show fits to the model predictions by the function “ $a + b \cos 2\phi_{\pi^-}^* + c \cos \phi_{\pi^-}^*$ ”. The black bars at the bottom of each subplot represent the systematic uncertainty for each cross section points.

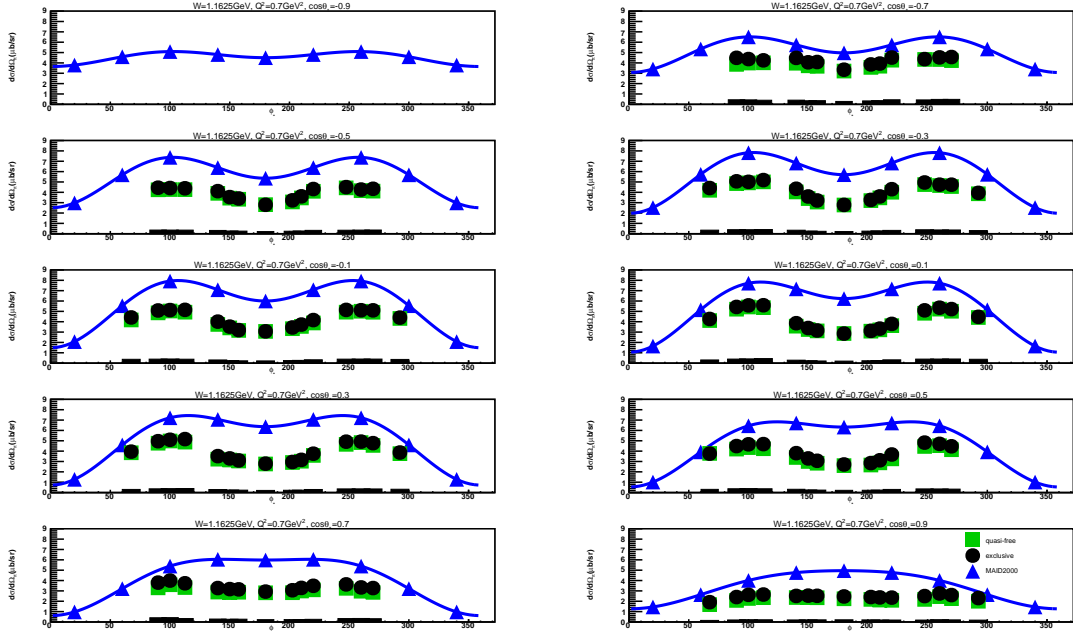


Figure B.7: Exclusive (black points) and quasi-free (green squares) cross sections in  $\mu\text{b}/\text{sr}$  are represented for  $W = 1.1625$  GeV and  $Q^2 = 0.7$  GeV<sup>2</sup>. The  $\phi_{\pi^-}^*$  dependent cross sections are illustrated in each  $\cos \theta_{\pi^-}^*$  bin. The blue triangles show MAID2000 model predictions. The blue lines show fits to the model predictions by the function “ $a + b \cos 2\phi_{\pi^-}^* + c \cos \phi_{\pi^-}^*$ ”. The black bars at the bottom of each subplot represent the systematic uncertainty for each cross section points.

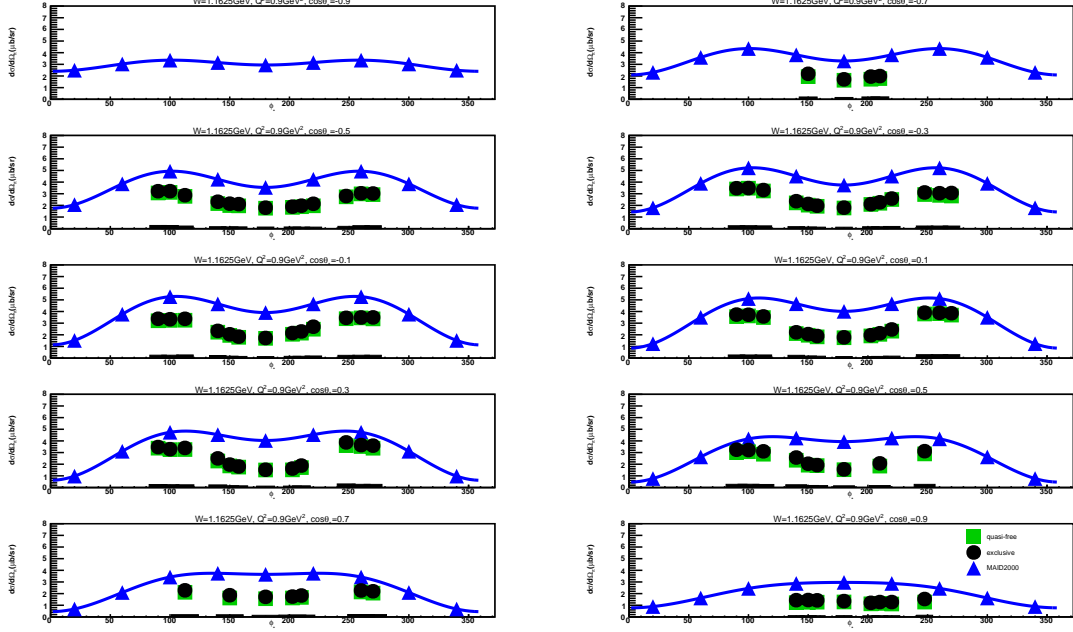


Figure B.8: Exclusive (black points) and quasi-free (green squares) cross sections in  $\mu\text{b}/\text{sr}$  are represented for  $W = 1.1625$  GeV and  $Q^2 = 0.9$  GeV<sup>2</sup>. The  $\phi_{\pi^-}^*$  dependent cross sections are illustrated in each  $\cos \theta_{\pi^-}^*$  bin. The blue triangles show MAID2000 model predictions. The blue lines show fits to the model predictions by the function “ $a + b \cos 2\phi_{\pi^-}^* + c \cos \phi_{\pi^-}^*$ ”. The black bars at the bottom of each subplot represent the systematic uncertainty for each cross section points.

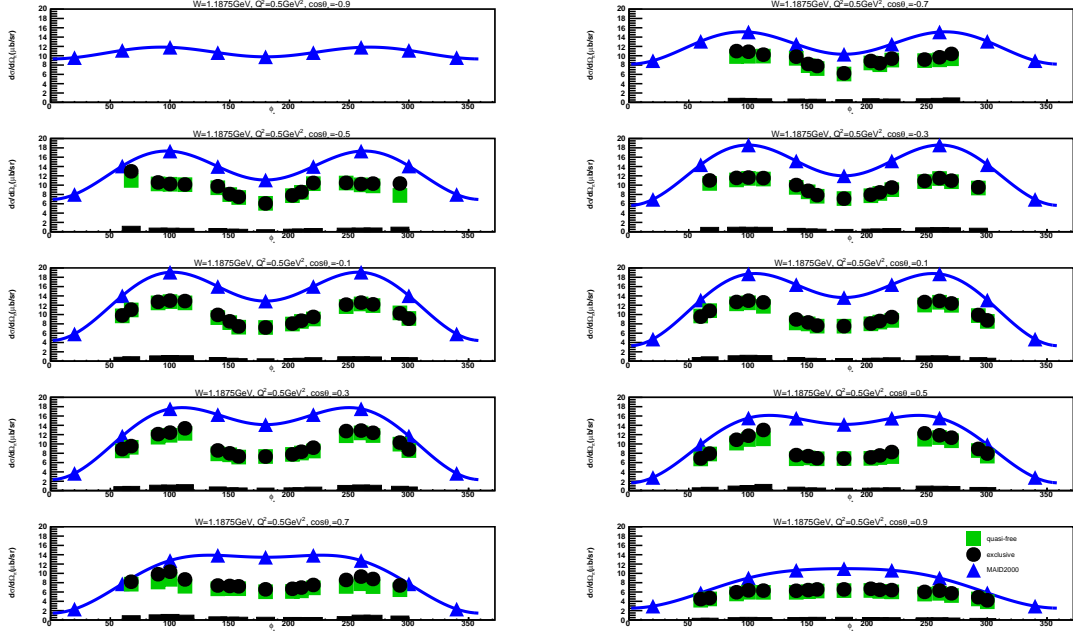


Figure B.9: Exclusive (black points) and quasi-free (green squares) cross sections in  $\mu\text{b}/\text{sr}$  are represented for  $W = 1.1875$  GeV and  $Q^2 = 0.5$  GeV<sup>2</sup>. The  $\phi_{\pi^-}^*$  dependent cross sections are illustrated in each  $\cos \theta_{\pi^-}^*$  bin. The blue triangles show MAID2000 model predictions. The blue lines show fits to the model predictions by the function “ $a + b \cos 2\phi_{\pi^-}^* + c \cos \phi_{\pi^-}^*$ ”. The black bars at the bottom of each subplot represent the systematic uncertainty for each cross section points.

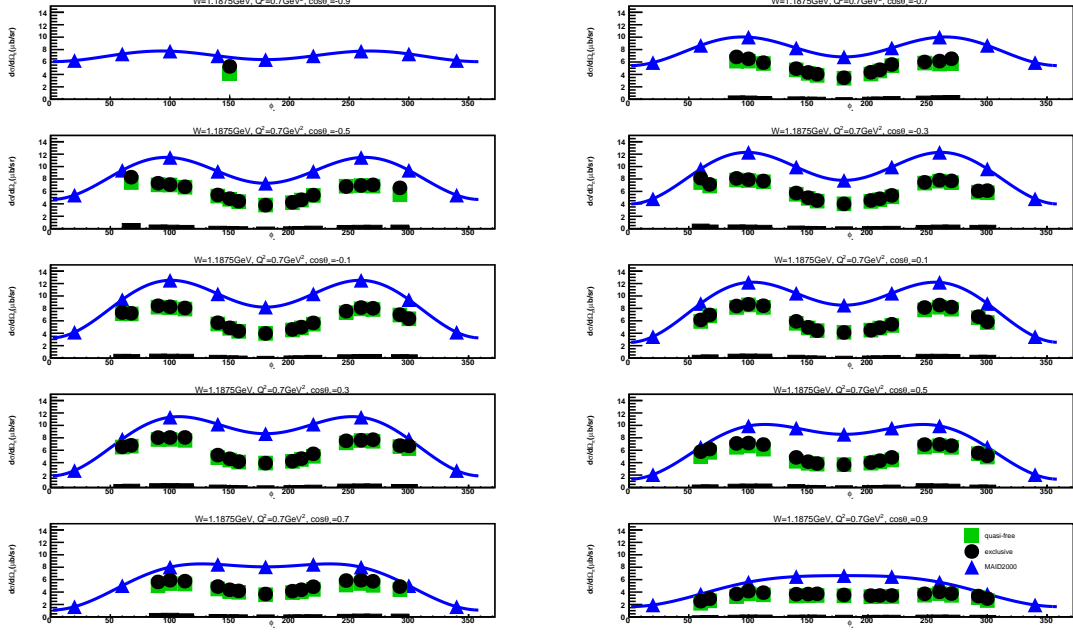


Figure B.10: Exclusive (black points) and quasi-free (green squares) cross sections in  $\mu\text{b}/\text{sr}$  are represented for  $W = 1.1875$  GeV and  $Q^2 = 0.7$  GeV<sup>2</sup>. The  $\phi_{\pi^-}^*$  dependent cross sections are illustrated in each  $\cos \theta_{\pi^-}^*$  bin. The blue triangles show MAID2000 model predictions. The blue lines show fits to the model predictions by the function “ $a + b \cos 2\phi_{\pi^-}^* + c \cos \phi_{\pi^-}^*$ ”. The black bars at the bottom of each subplot represent the systematic uncertainty for each cross section points.

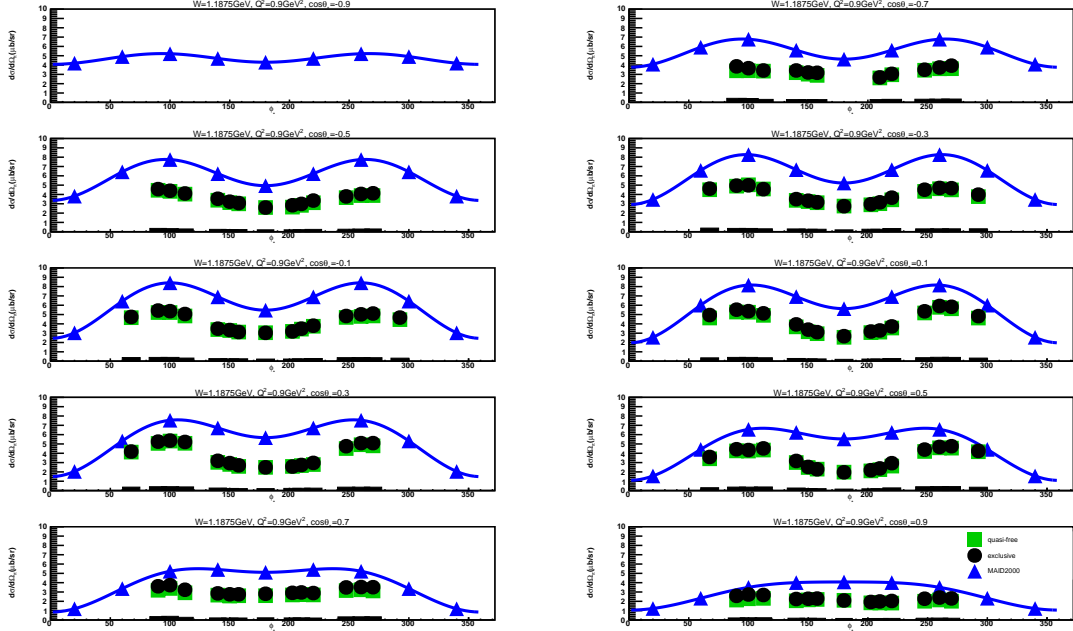


Figure B.11: Exclusive (black points) and quasi-free (green squares) cross sections in  $\mu\text{b}/\text{sr}$  are represented for  $W = 1.1875$  GeV and  $Q^2 = 0.9$  GeV<sup>2</sup>. The  $\phi_{\pi^-}^*$  dependent cross sections are illustrated in each  $\cos \theta_{\pi^-}^*$  bin. The blue triangles show MAID2000 model predictions. The blue lines show fits to the model predictions by the function “ $a + b \cos 2\phi_{\pi^-}^* + c \cos \phi_{\pi^-}^*$ ”. The black bars at the bottom of each subplot represent the systematic uncertainty for each cross section points.

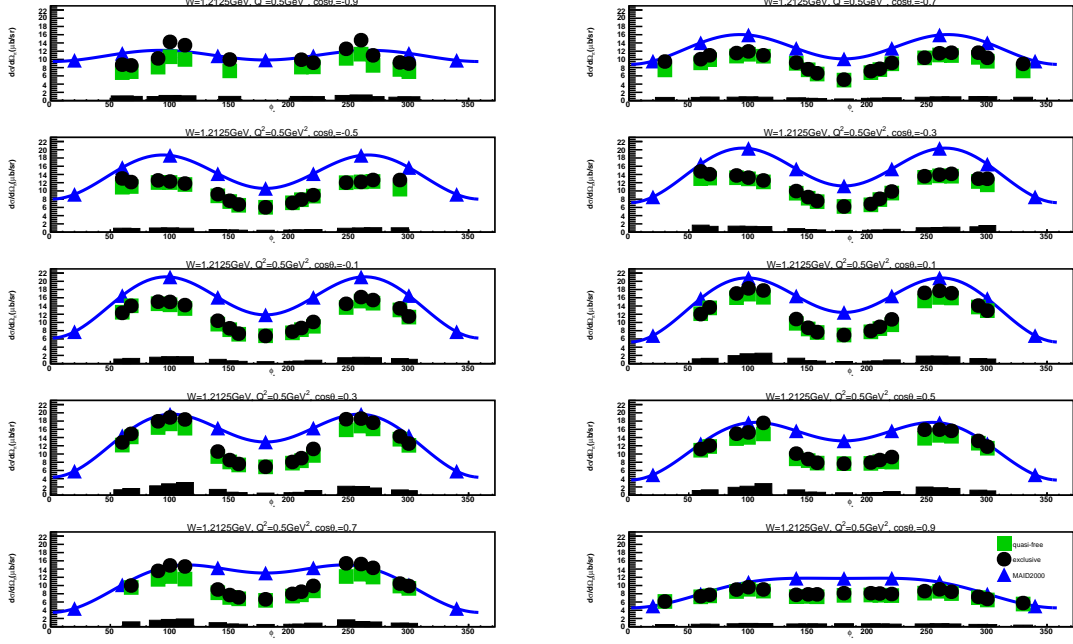


Figure B.12: Exclusive (black points) and quasi-free (green squares) cross sections in  $\mu\text{b}/\text{sr}$  are represented for  $W = 1.2125$  GeV and  $Q^2 = 0.5$  GeV<sup>2</sup>. The  $\phi_{\pi^*}^*$  dependent cross sections are illustrated in each  $\cos \theta_{\pi^*}^*$  bin. The blue triangles show MAID2000 model predictions. The blue lines show fits to the model predictions by the function “ $a + b \cos 2\phi_{\pi^*}^* + c \cos \phi_{\pi^*}^*$ ”. The black bars at the bottom of each subplot represent the systematic uncertainty for each cross section points.

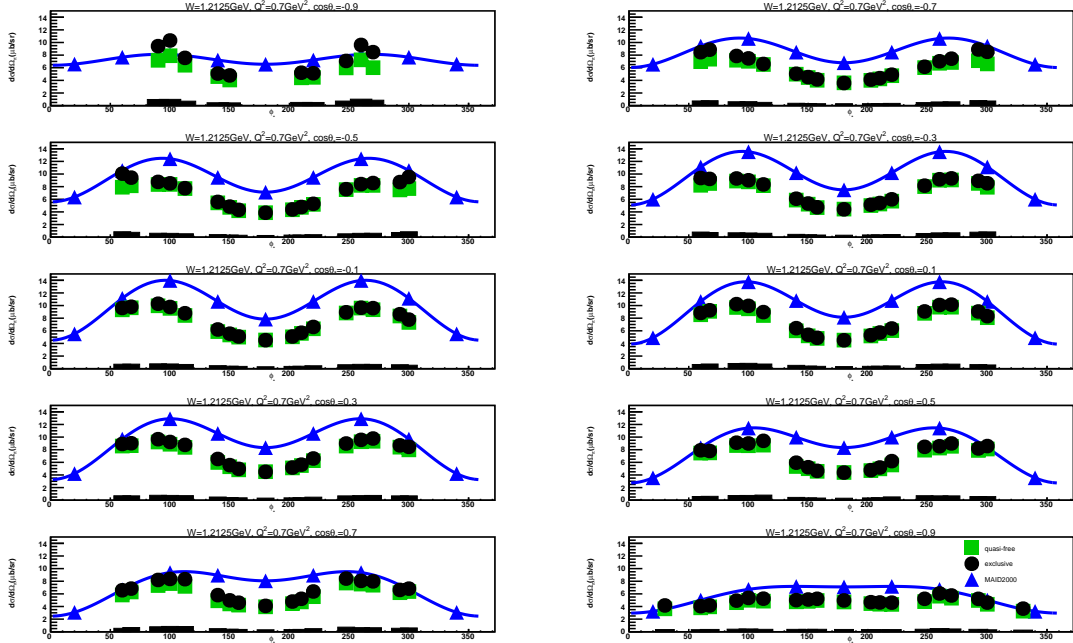


Figure B.13: Exclusive (black points) and quasi-free (green squares) cross sections in  $\mu\text{b}/\text{sr}$  are represented for  $W = 1.2125$  GeV and  $Q^2 = 0.7$  GeV<sup>2</sup>. The  $\phi_{\pi^*}^*$  dependent cross sections are illustrated in each  $\cos \theta_{\pi^*}^*$  bin. The blue triangles show MAID2000 model predictions. The blue lines show fits to the model predictions by the function “ $a + b \cos 2\phi_{\pi^*}^* + c \cos \phi_{\pi^*}^*$ ”. The black bars at the bottom of each subplot represent the systematic uncertainty for each cross section points.

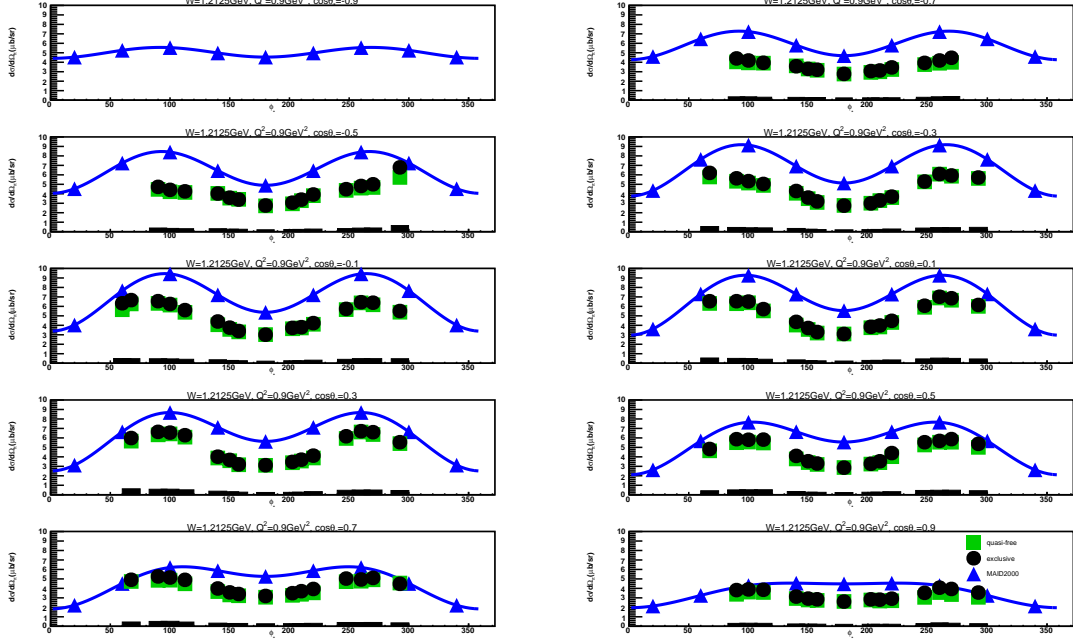


Figure B.14: Exclusive (black points) and quasi-free (green squares) cross sections in  $\mu\text{b}/\text{sr}$  are represented for  $W = 1.2125$  GeV and  $Q^2 = 0.9$  GeV<sup>2</sup>. The  $\phi_{\pi^-}^*$  dependent cross sections are illustrated in each  $\cos\theta_{\pi^-}^*$  bin. The blue triangles show MAID2000 model predictions. The blue lines show fits to the model predictions by the function “ $a + b \cos 2\phi_{\pi^-}^* + c \cos \phi_{\pi^-}^*$ ”. The black bars at the bottom of each subplot represent the systematic uncertainty for each cross section points.

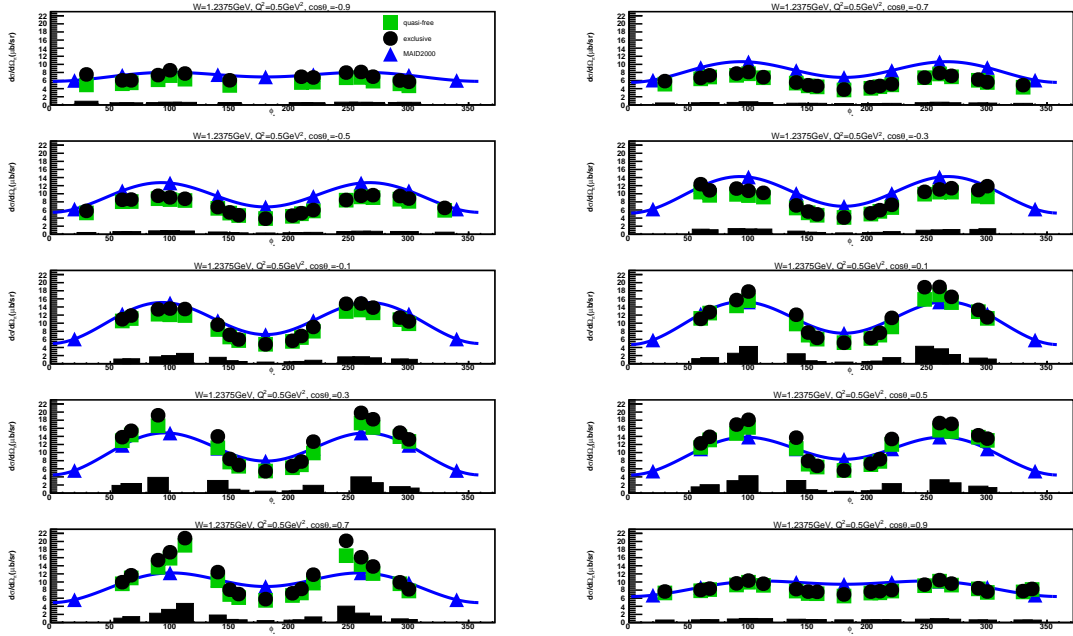


Figure B.15: Exclusive (black points) and quasi-free (green squares) cross sections in  $\mu\text{b}/\text{sr}$  are represented for  $W = 1.2375$  GeV and  $Q^2 = 0.5$  GeV<sup>2</sup>. The  $\phi_{\pi^-}^*$  dependent cross sections are illustrated in each  $\cos\theta_{\pi^-}^*$  bin. The blue triangles show MAID2000 model predictions. The blue lines show fits to the model predictions by the function “ $a + b \cos 2\phi_{\pi^-}^* + c \cos \phi_{\pi^-}^*$ ”. The black bars at the bottom of each subplot represent the systematic uncertainty for each cross section points.

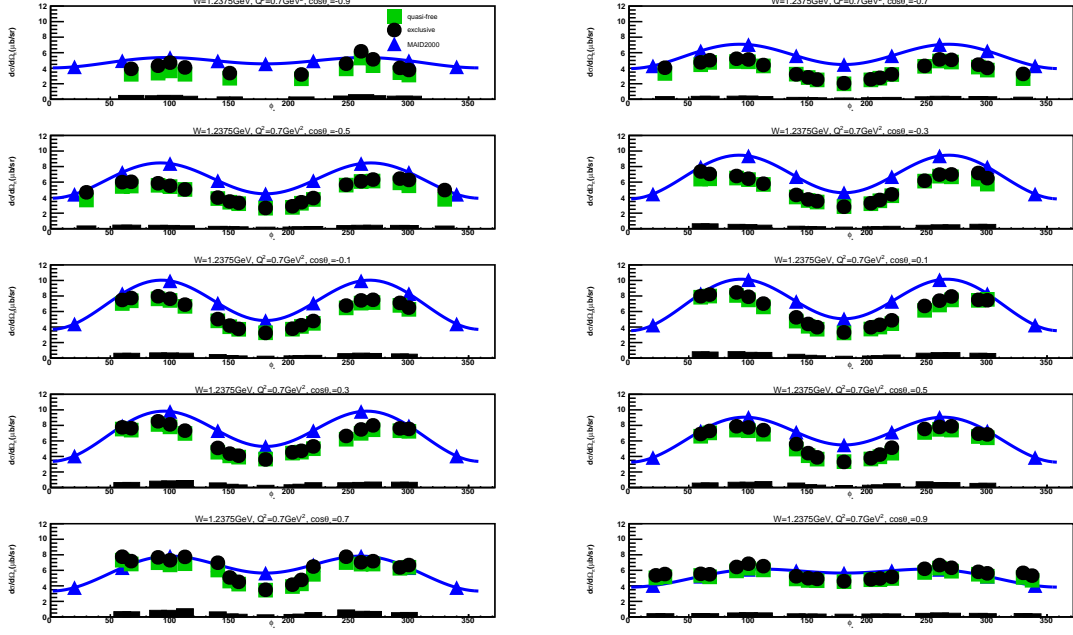


Figure B.16: Exclusive (black points) and quasi-free (green squares) cross sections in  $\mu\text{b}/\text{sr}$  are represented for  $W = 1.2375$  GeV and  $Q^2 = 0.7$  GeV<sup>2</sup>. The  $\phi_{\pi^-}^*$  dependent cross sections are illustrated in each  $\cos \theta_{\pi^-}^*$  bin. The blue triangles show MAID2000 model predictions. The blue lines show fits to the model predictions by the function “ $a + b \cos 2\phi_{\pi^-}^* + c \cos \phi_{\pi^-}^*$ ”. The black bars at the bottom of each subplot represent the systematic uncertainty for each cross section points.

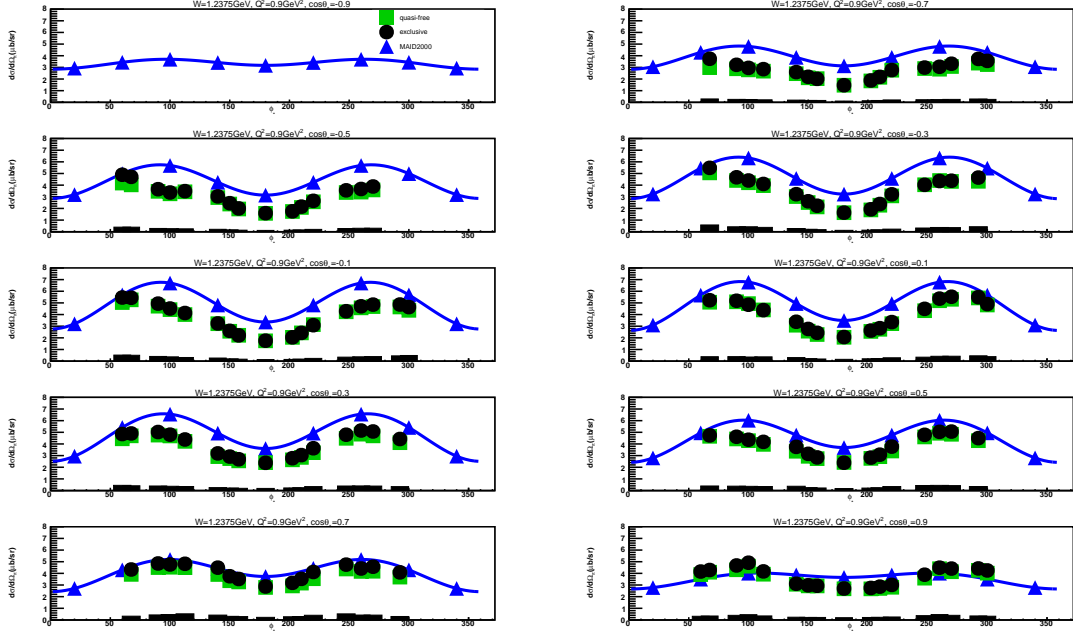


Figure B.17: Exclusive (black points) and quasi-free (green squares) cross sections in  $\mu\text{b}/\text{sr}$  are represented for  $W = 1.2375$  GeV and  $Q^2 = 0.9$  GeV<sup>2</sup>. The  $\phi_{\pi^-}^*$  dependent cross sections are illustrated in each  $\cos \theta_{\pi^-}^*$  bin. The blue triangles show MAID2000 model predictions. The blue lines show fits to the model predictions by the function “ $a + b \cos 2\phi_{\pi^-}^* + c \cos \phi_{\pi^-}^*$ ”. The black bars at the bottom of each subplot represent the systematic uncertainty for each cross section points.



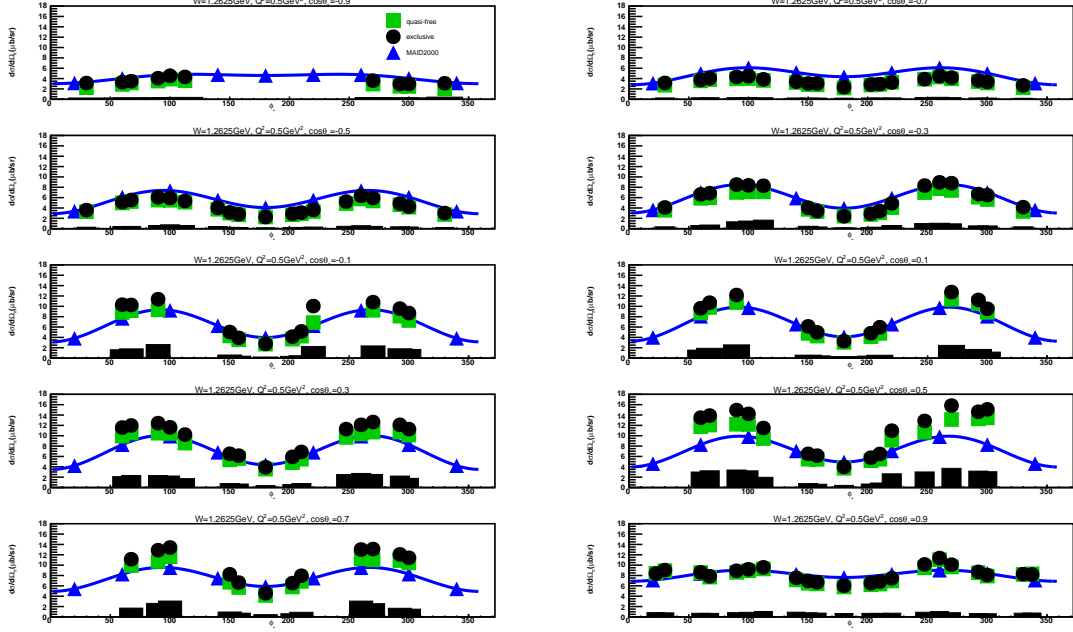


Figure B.18: Exclusive (black points) and quasi-free (green squares) cross sections in  $\mu\text{b}/\text{sr}$  are represented for  $W = 1.2625$  GeV and  $Q^2 = 0.5$  GeV<sup>2</sup>. The  $\phi_{\pi^-}^*$  dependent cross sections are illustrated in each  $\cos \theta_{\pi^-}^*$  bin. The blue triangles show MAID2000 model predictions. The blue lines show fits to the model predictions by the function “ $a + b \cos 2\phi_{\pi^-}^* + c \cos \phi_{\pi^-}^*$ ”. The black bars at the bottom of each subplot represent the systematic uncertainty for each cross section points.

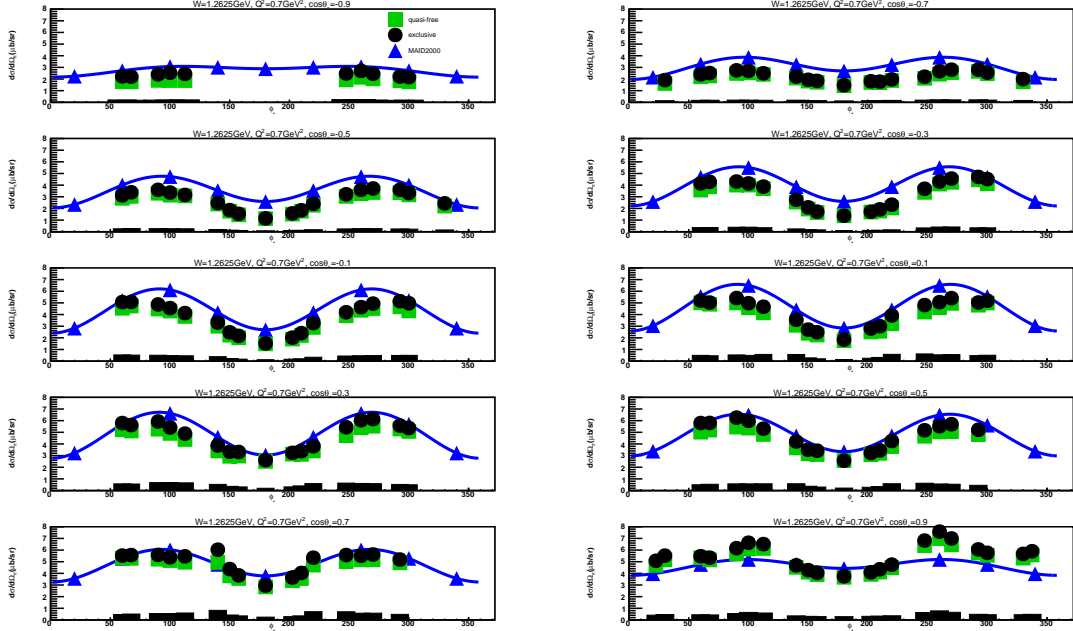


Figure B.19: Exclusive (black points) and quasi-free (green squares) cross sections in  $\mu\text{b}/\text{sr}$  are represented for  $W = 1.2625$  GeV and  $Q^2 = 0.7$  GeV<sup>2</sup>. The  $\phi_{\pi^-}^*$  dependent cross sections are illustrated in each  $\cos \theta_{\pi^-}^*$  bin. The blue triangles show MAID2000 model predictions. The blue lines show fits to the model predictions by the function “ $a + b \cos 2\phi_{\pi^-}^* + c \cos \phi_{\pi^-}^*$ ”. The black bars at the bottom of each subplot represent the systematic uncertainty for each cross section points.

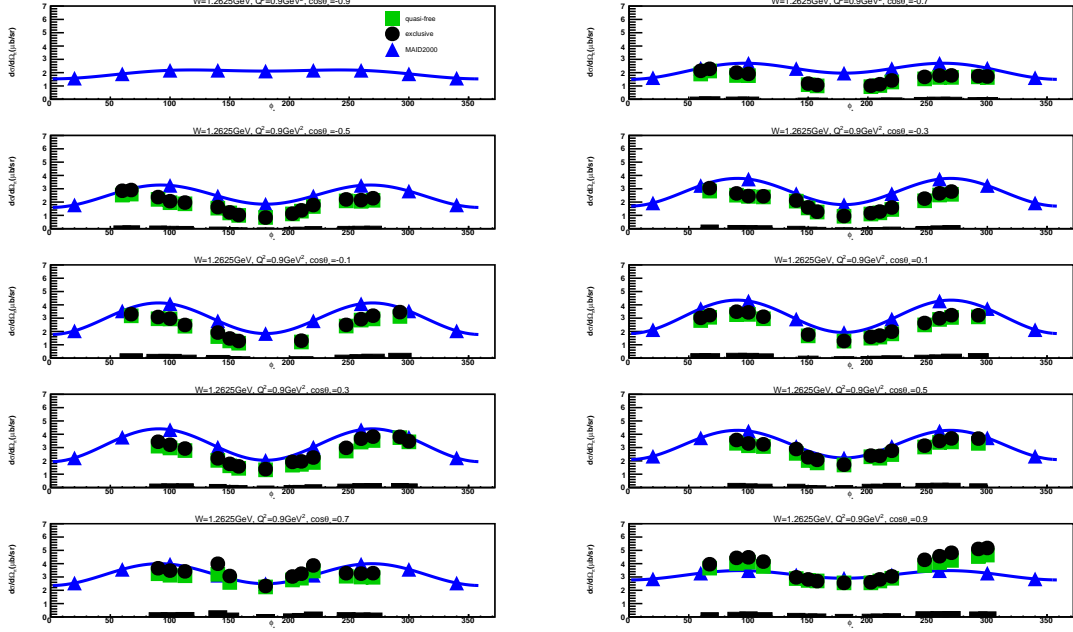


Figure B.20: Exclusive (black points) and quasi-free (green squares) cross sections in  $\mu\text{b}/\text{sr}$  are represented for  $W = 1.2625$  GeV and  $Q^2 = 0.9$  GeV<sup>2</sup>. The  $\phi_{\pi^-}^*$  dependent cross sections are illustrated in each  $\cos \theta_{\pi^-}^*$  bin. The blue triangles show MAID2000 model predictions. The blue lines show fits to the model predictions by the function “ $a + b \cos 2\phi_{\pi^-}^* + c \cos \phi_{\pi^-}^*$ ”. The black bars at the bottom of each subplot represent the systematic uncertainty for each cross section points.

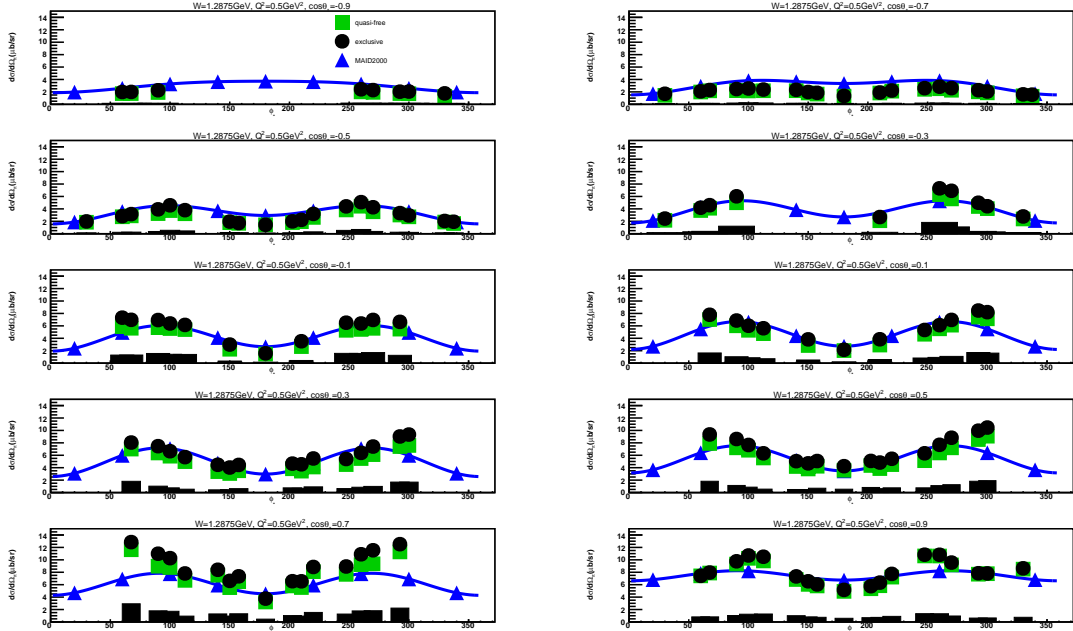


Figure B.21: Exclusive (black points) and quasi-free (green squares) cross sections in  $\mu\text{b}/\text{sr}$  are represented for  $W = 1.2875$  GeV and  $Q^2 = 0.5$  GeV<sup>2</sup>. The  $\phi_{\pi^-}^*$  dependent cross sections are illustrated in each  $\cos \theta_{\pi^-}^*$  bin. The blue triangles show MAID2000 model predictions. The blue lines show fits to the model predictions by the function “ $a + b \cos 2\phi_{\pi^-}^* + c \cos \phi_{\pi^-}^*$ ”. The black bars at the bottom of each subplot represent the systematic uncertainty for each cross section points.

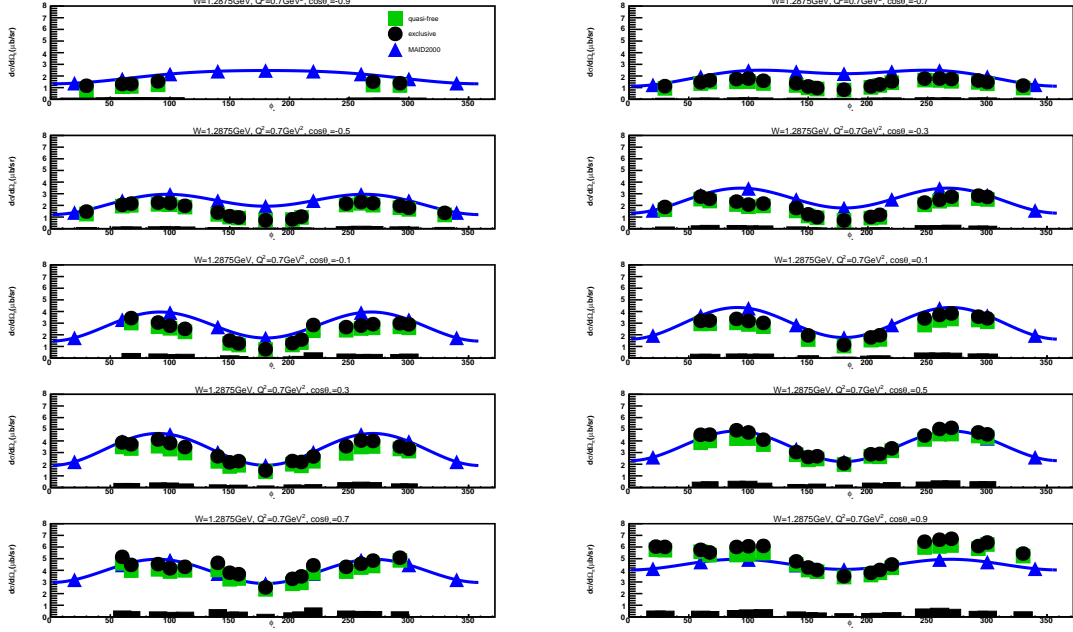


Figure B.22: Exclusive (black points) and quasi-free (green squares) cross sections in  $\mu\text{b}/\text{sr}$  are represented for  $W = 1.2875$  GeV and  $Q^2 = 0.5$  GeV<sup>2</sup>. The  $\phi_{\pi^-}^*$  dependent cross sections are illustrated in each  $\cos \theta_{\pi^-}^*$  bin. The blue triangles show MAID2000 model predictions. The blue lines show fits to the model predictions by the function “ $a + b \cos 2\phi_{\pi^-}^* + c \cos \phi_{\pi^-}^*$ ”. The black bars at the bottom of each subplot represent the systematic uncertainty for each cross section points.

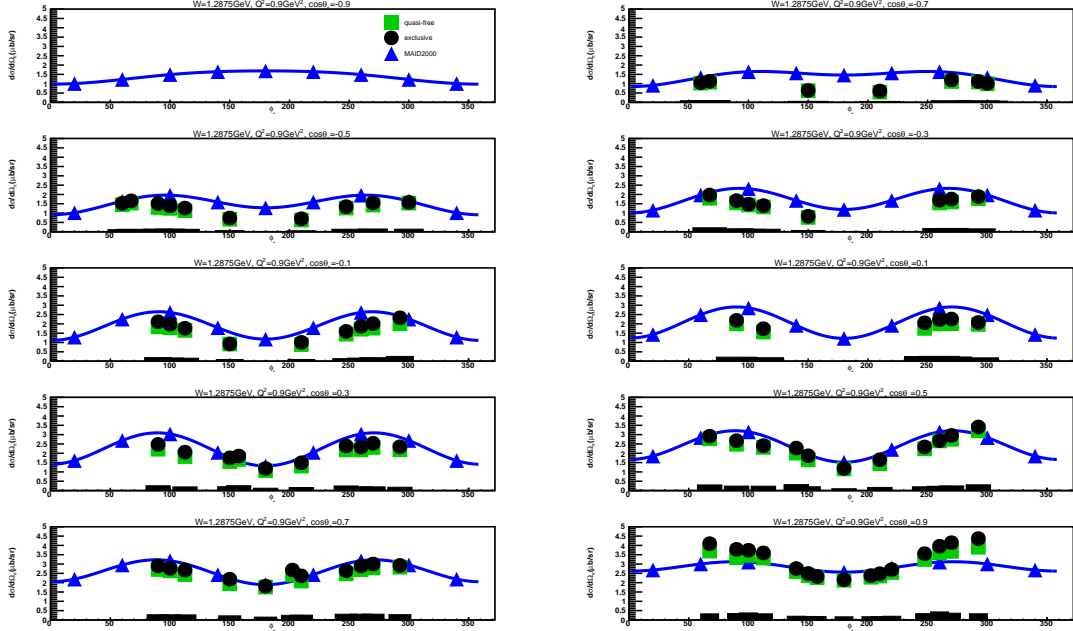


Figure B.23: Exclusive (black points) and quasi-free (green squares) cross sections in  $\mu\text{b}/\text{sr}$  are represented for  $W = 1.2875$  GeV and  $Q^2 = 0.9$  GeV<sup>2</sup>. The  $\phi_{\pi^-}^*$  dependent cross sections are illustrated in each  $\cos \theta_{\pi^-}^*$  bin. The blue triangles show MAID2000 model predictions. The blue lines show fits to the model predictions by the function “ $a + b \cos 2\phi_{\pi^-}^* + c \cos \phi_{\pi^-}^*$ ”. The black bars at the bottom of each subplot represent the systematic uncertainty for each cross section points.

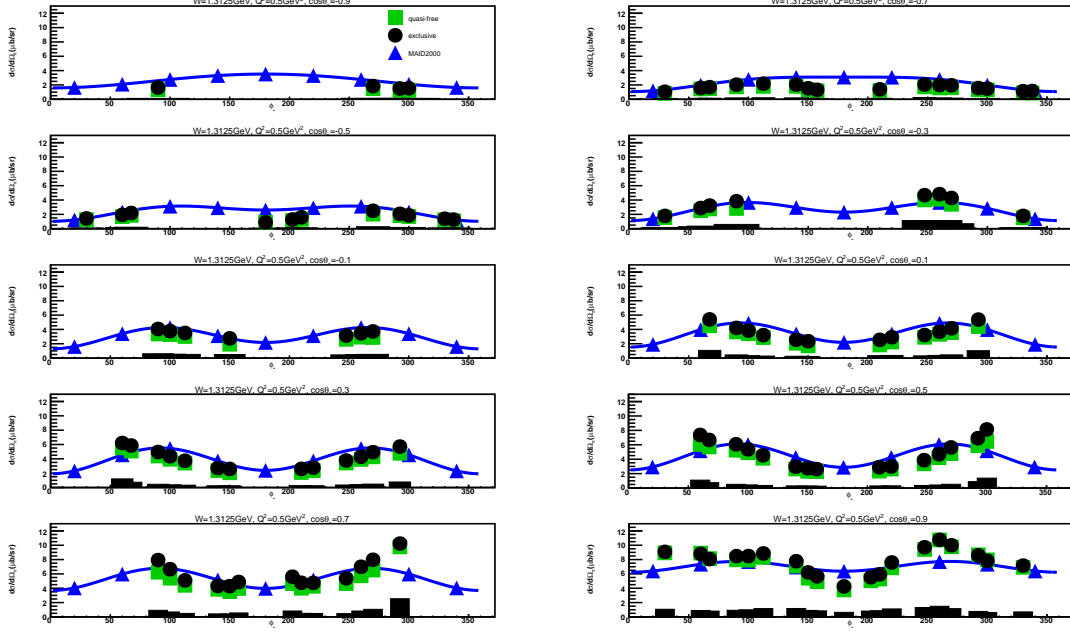


Figure B.24: Exclusive (black points) and quasi-free (green squares) cross sections in  $\mu\text{b}/\text{sr}$  are represented for  $W = 1.3125$  GeV and  $Q^2 = 0.5$  GeV<sup>2</sup>. The  $\phi_{\pi^-}^*$  dependent cross sections are illustrated in each  $\cos \theta_{\pi^-}^*$  bin. The blue triangles show MAID2000 model predictions. The blue lines show fits to the model predictions by the function “ $a + b \cos 2\phi_{\pi^-}^* + c \cos \phi_{\pi^-}^*$ ”. The black bars at the bottom of each subplot represent the systematic uncertainty for each cross section points.

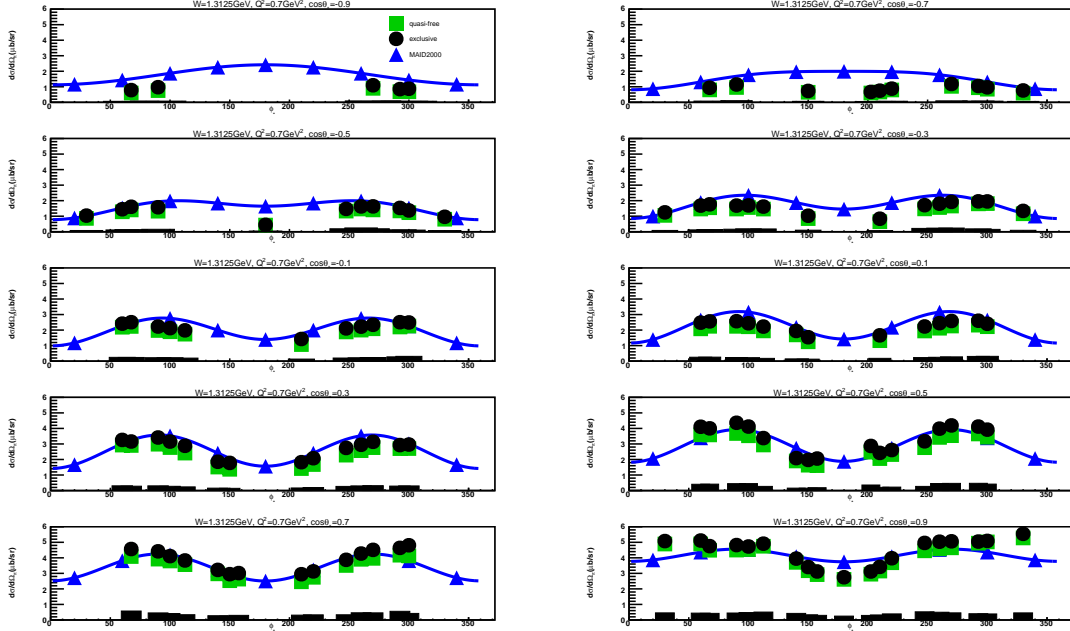


Figure B.25: Exclusive (black points) and quasi-free (green squares) cross sections in  $\mu\text{b}/\text{sr}$  are represented for  $W = 1.3125$  GeV and  $Q^2 = 0.7$  GeV<sup>2</sup>. The  $\phi_{\pi^-}^*$  dependent cross sections are illustrated in each  $\cos \theta_{\pi^-}^*$  bin. The blue triangles show MAID2000 model predictions. The blue lines show fits to the model predictions by the function “ $a + b \cos 2\phi_{\pi^-}^* + c \cos \phi_{\pi^-}^*$ ”. The black bars at the bottom of each subplot represent the systematic uncertainty for each cross section points.

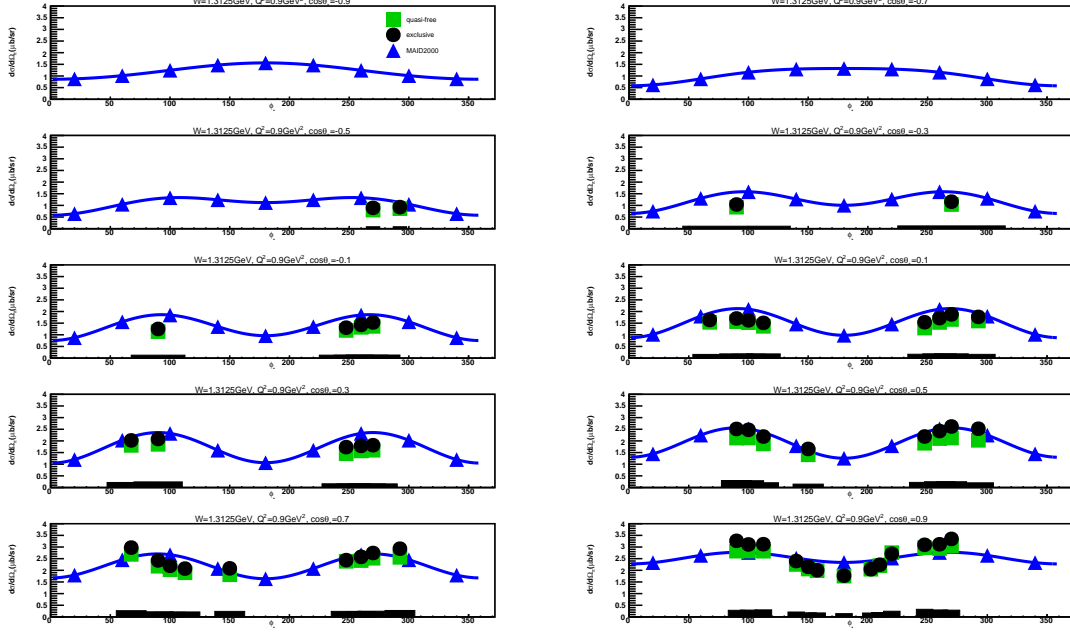


Figure B.26: Exclusive (black points) and quasi-free (green squares) cross sections in  $\mu\text{b}/\text{sr}$  are represented for  $W = 1.3125$  GeV and  $Q^2 = 0.9$  GeV<sup>2</sup>. The  $\phi_{\pi^-}^*$  dependent cross sections are illustrated in each  $\cos \theta_{\pi^-}^*$  bin. The blue triangles show MAID2000 model predictions. The blue lines show fits to the model predictions by the function “ $a + b \cos 2\phi_{\pi^-}^* + c \cos \phi_{\pi^-}^*$ ”. The black bars at the bottom of each subplot represent the systematic uncertainty for each cross section points.

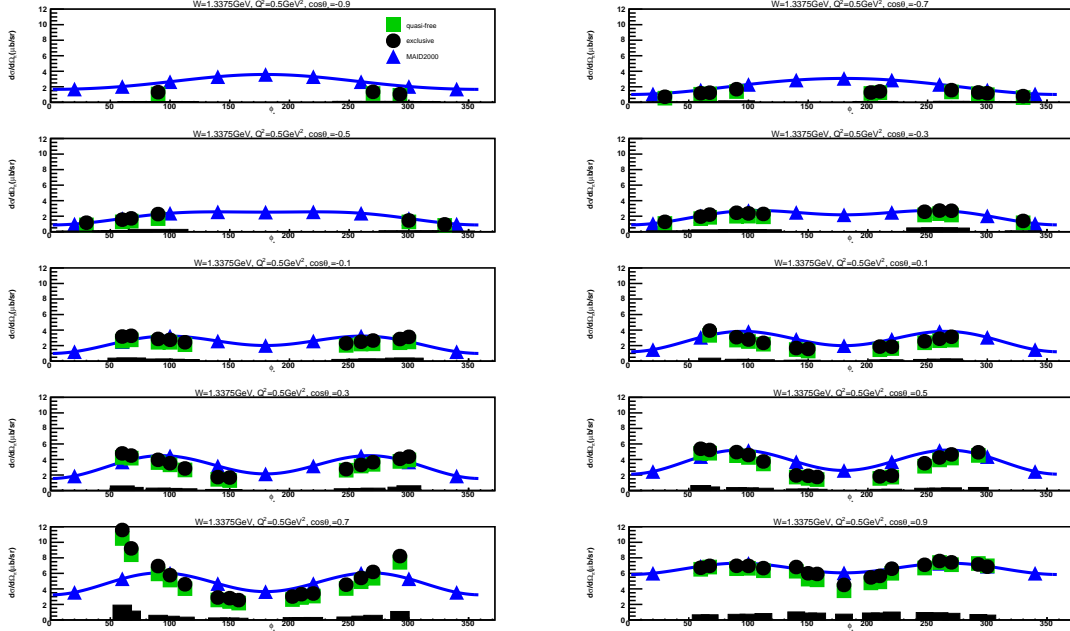


Figure B.27: Exclusive (black points) and quasi-free (green squares) cross sections in  $\mu\text{b}/\text{sr}$  are represented for  $W = 1.3375$  GeV and  $Q^2 = 0.5$  GeV<sup>2</sup>. The  $\phi_{\pi^-}^*$  dependent cross sections are illustrated in each  $\cos \theta_{\pi^-}^*$  bin. The blue triangles show MAID2000 model predictions. The blue lines show fits to the model predictions by the function “ $a + b \cos 2\phi_{\pi^-}^* + c \cos \phi_{\pi^-}^*$ ”. The black bars at the bottom of each subplot represent the systematic uncertainty for each cross section points.

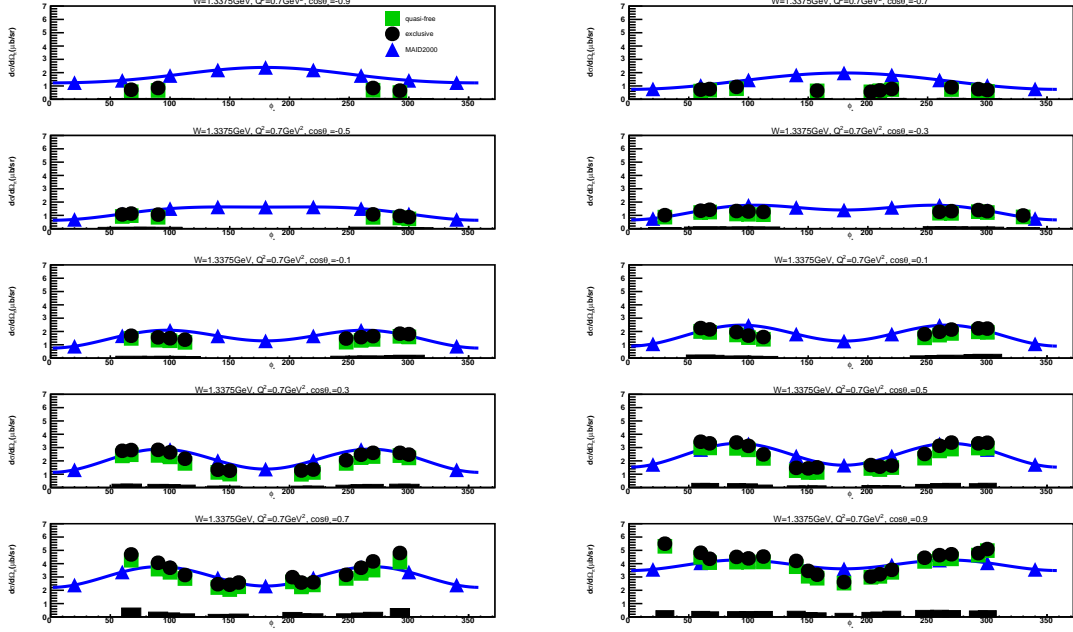


Figure B.28: Exclusive (black points) and quasi-free (green squares) cross sections in  $\mu\text{b}/\text{sr}$  are represented for  $W = 1.2125$  GeV and  $Q^2 = 0.5$  GeV<sup>2</sup>. The  $\phi_{\pi^-}^*$  dependent cross sections are illustrated in each  $\cos \theta_{\pi^-}^*$  bin. The blue triangles show MAID2000 model predictions. The blue lines show fits to the model predictions by the function “ $a + b \cos 2\phi_{\pi^-}^* + c \cos \phi_{\pi^-}^*$ ”. The black bars at the bottom of each subplot represent the systematic uncertainty for each cross section points.

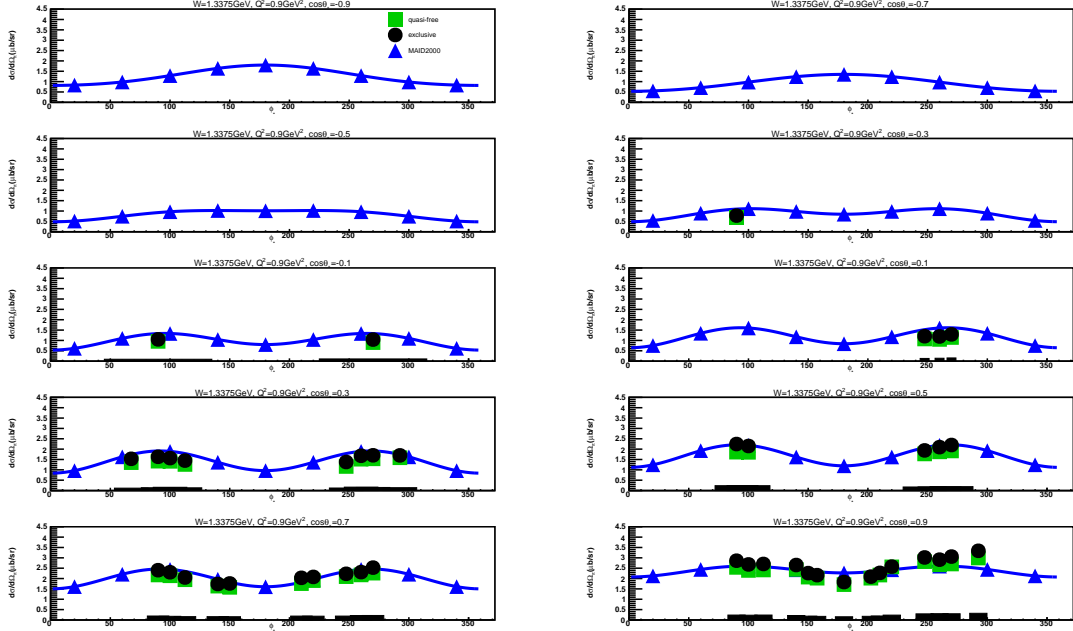


Figure B.29: Exclusive (black points) and quasi-free (green squares) cross sections in  $\mu\text{b}/\text{sr}$  are represented for  $W = 1.2125$  GeV and  $Q^2 = 0.5$  GeV<sup>2</sup>. The  $\phi_{\pi^-}^*$  dependent cross sections are illustrated in each  $\cos \theta_{\pi^-}^*$  bin. The blue triangles show MAID2000 model predictions. The blue lines show fits to the model predictions by the function “ $a + b \cos 2\phi_{\pi^-}^* + c \cos \phi_{\pi^-}^*$ ”. The black bars at the bottom of each subplot represent the systematic uncertainty for each cross section points.

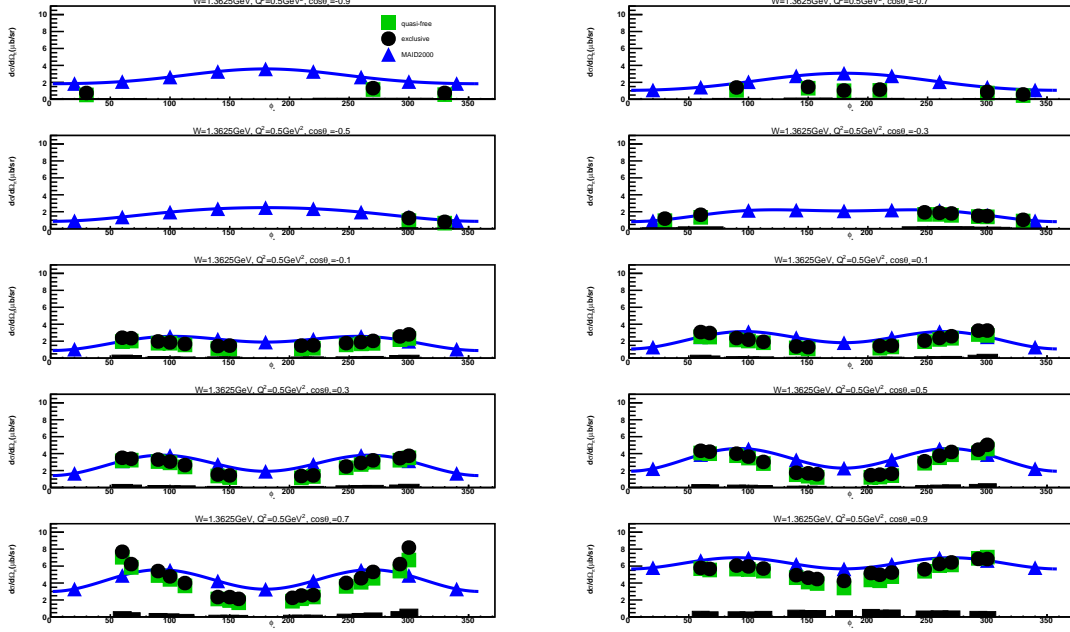


Figure B.30: Exclusive (black points) and quasi-free (green squares) cross sections in  $\mu\text{b}/\text{sr}$  are represented for  $W = 1.3625$  GeV and  $Q^2 = 0.5$  GeV<sup>2</sup>. The  $\phi_{\pi^-}^*$  dependent cross sections are illustrated in each  $\cos \theta_{\pi^-}^*$  bin. The blue triangles show MAID2000 model predictions. The blue lines show fits to the model predictions by the function “ $a + b \cos 2\phi_{\pi^-}^* + c \cos \phi_{\pi^-}^*$ ”. The black bars at the bottom of each subplot represent the systematic uncertainty for each cross section points.

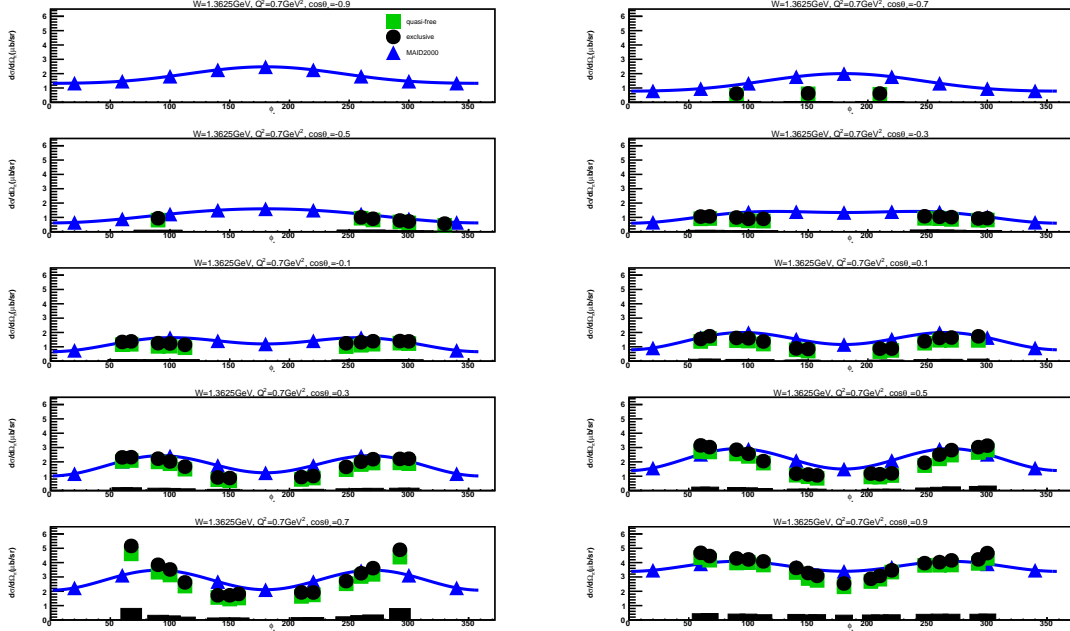


Figure B.31: Exclusive (black points) and quasi-free (green squares) cross sections in  $\mu\text{b}/\text{sr}$  are represented for  $W = 1.3625$  GeV and  $Q^2 = 0.7$  GeV<sup>2</sup>. The  $\phi_{\pi^-}^*$  dependent cross sections are illustrated in each  $\cos \theta_{\pi^-}^*$  bin. The blue triangles show MAID2000 model predictions. The blue lines show fits to the model predictions by the function “ $a + b \cos 2\phi_{\pi^-}^* + c \cos \phi_{\pi^-}^*$ ”. The black bars at the bottom of each subplot represent the systematic uncertainty for each cross section points.

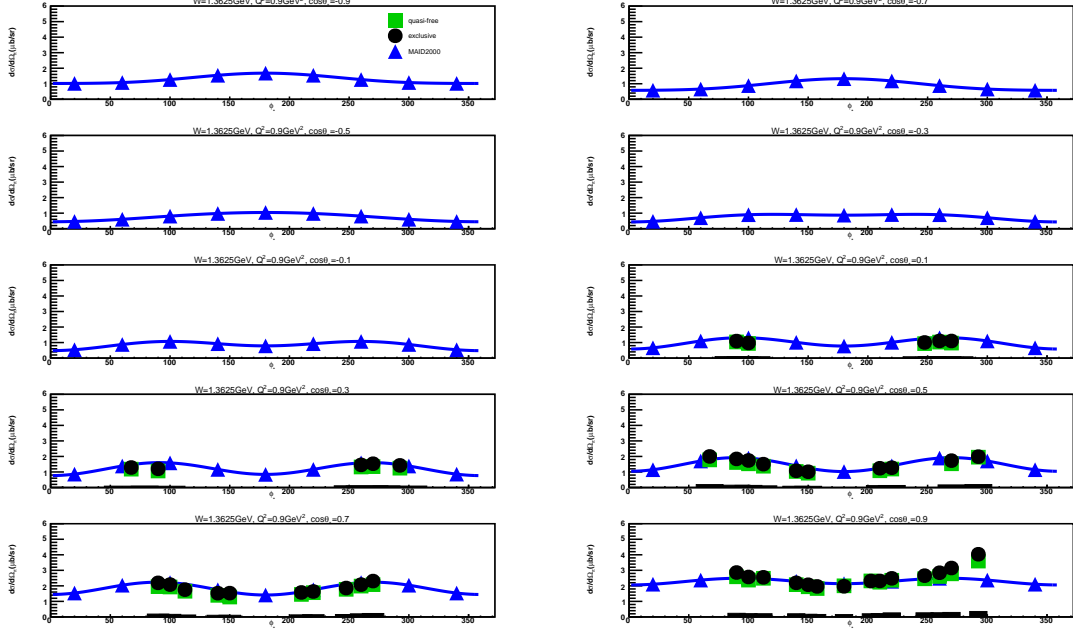


Figure B.32: Exclusive (black points) and quasi-free (green squares) cross sections in  $\mu\text{b}/\text{sr}$  are represented for  $W = 1.3625$  GeV and  $Q^2 = 0.9$  GeV<sup>2</sup>. The  $\phi_{\pi^-}^*$  dependent cross sections are illustrated in each  $\cos \theta_{\pi^-}^*$  bin. The blue triangles show MAID2000 model predictions. The blue lines show fits to the model predictions by the function “ $a + b \cos 2\phi_{\pi^-}^* + c \cos \phi_{\pi^-}^*$ ”. The black bars at the bottom of each subplot represent the systematic uncertainty for each cross section points.

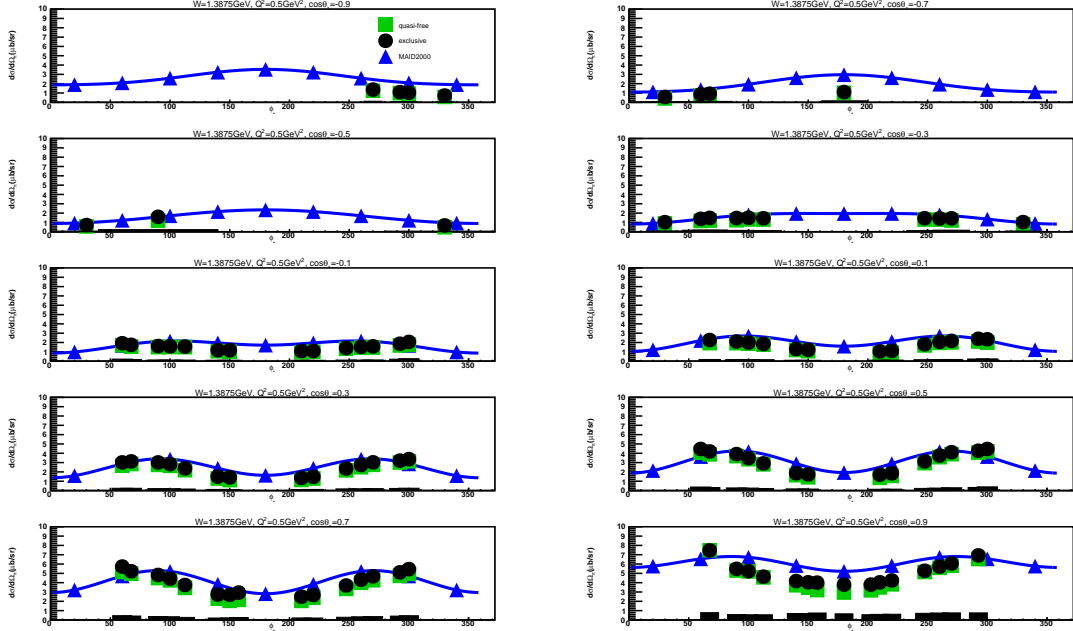


Figure B.33: Exclusive (black points) and quasi-free (green squares) cross sections in  $\mu\text{b}/\text{sr}$  are represented for  $W = 1.3875$  GeV and  $Q^2 = 0.5$  GeV<sup>2</sup>. The  $\phi_{\pi^-}^*$  dependent cross sections are illustrated in each  $\cos \theta_{\pi^-}^*$  bin. The blue triangles show MAID2000 model predictions. The blue lines show fits to the model predictions by the function “ $a + b \cos 2\phi_{\pi^-}^* + c \cos \phi_{\pi^-}^*$ ”. The black bars at the bottom of each subplot represent the systematic uncertainty for each cross section points.



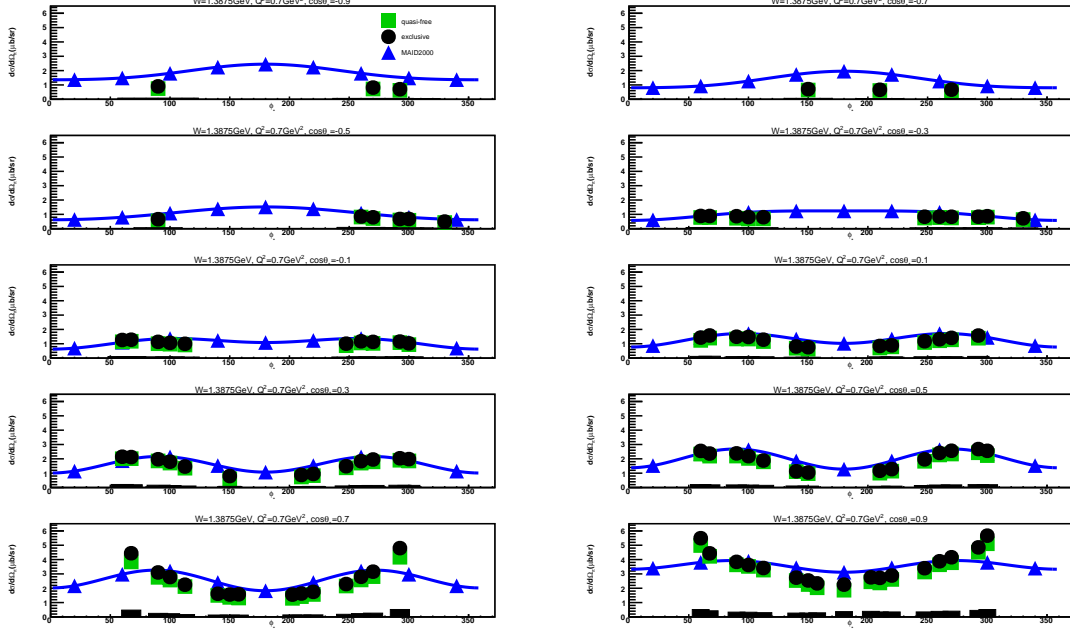


Figure B.34: Exclusive (black points) and quasi-free (green squares) cross sections in  $\mu\text{b}/\text{sr}$  are represented for  $W = 1.3875$  GeV and  $Q^2 = 0.7$  GeV<sup>2</sup>. The  $\phi_{\pi^-}^*$  dependent cross sections are illustrated in each  $\cos \theta_{\pi^-}^*$  bin. The blue triangles show MAID2000 model predictions. The blue lines show fits to the model predictions by the function “ $a + b \cos 2\phi_{\pi^-}^* + c \cos \phi_{\pi^-}^*$ ”. The black bars at the bottom of each subplot represent the systematic uncertainty for each cross section points.

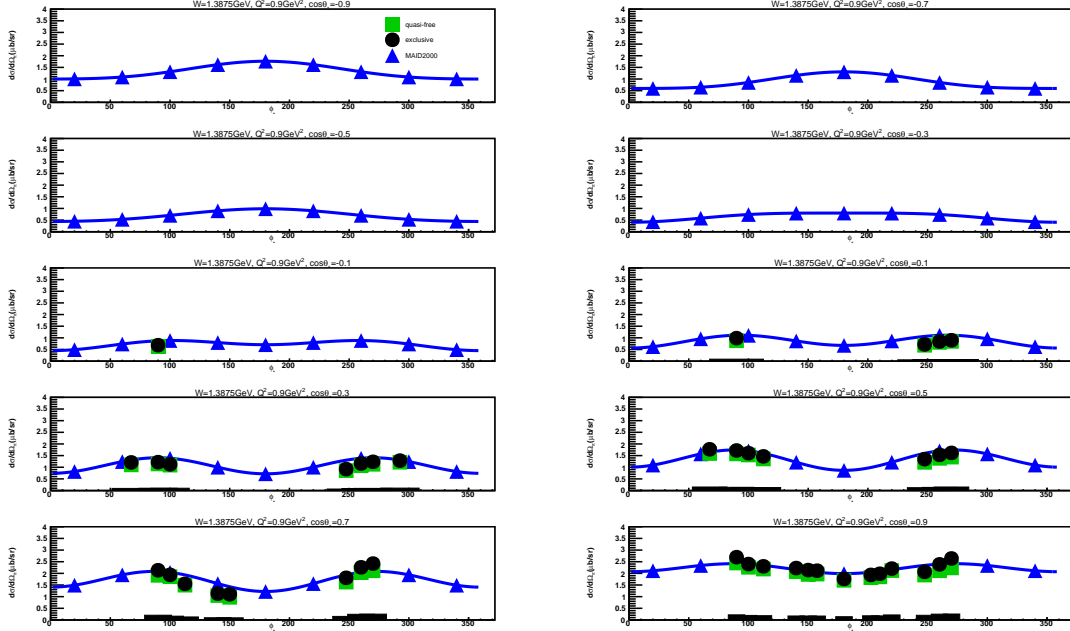


Figure B.35: Exclusive (black points) and quasi-free (green squares) cross sections in  $\mu\text{b}/\text{sr}$  are represented for  $W = 1.3875$  GeV and  $Q^2 = 0.9$  GeV<sup>2</sup>. The  $\phi_{\pi^-}^*$  dependent cross sections are illustrated in each  $\cos \theta_{\pi^-}^*$  bin. The blue triangles show MAID2000 model predictions. The blue lines show fits to the model predictions by the function “ $a + b \cos 2\phi_{\pi^-}^* + c \cos \phi_{\pi^-}^*$ ”. The black bars at the bottom of each subplot represent the systematic uncertainty for each cross section points.

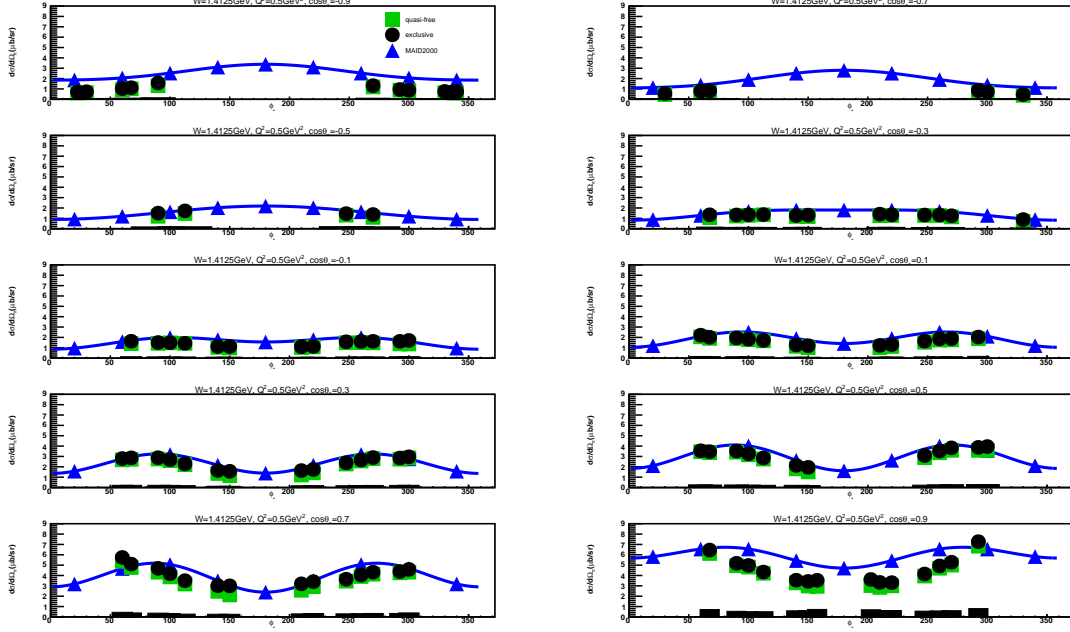


Figure B.36: Exclusive (black points) and quasi-free (green squares) cross sections in  $\mu\text{b}/\text{sr}$  are represented for  $W = 1.4125$  GeV and  $Q^2 = 0.5$  GeV<sup>2</sup>. The  $\phi_{\pi^-}^*$  dependent cross sections are illustrated in each  $\cos \theta_{\pi^-}^*$  bin. The blue triangles show MAID2000 model predictions. The blue lines show fits to the model predictions by the function “ $a + b \cos 2\phi_{\pi^-}^* + c \cos \phi_{\pi^-}^*$ ”. The black bars at the bottom of each subplot represent the systematic uncertainty for each cross section points.

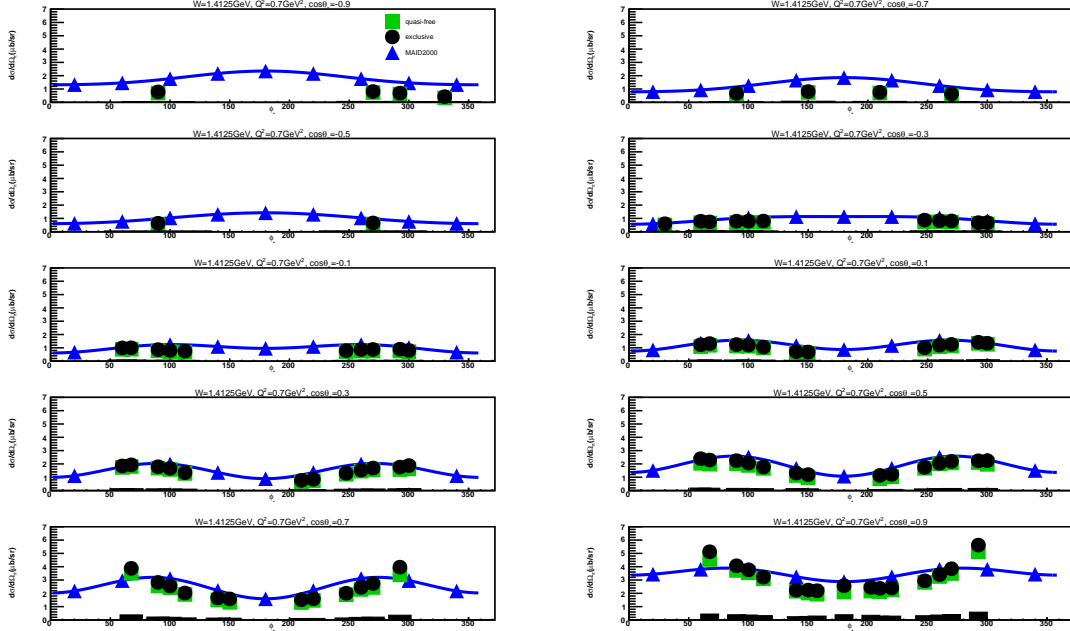


Figure B.37: Exclusive (black points) and quasi-free (green squares) cross sections in  $\mu\text{b}/\text{sr}$  are represented for  $W = 1.4125$  GeV and  $Q^2 = 0.7$  GeV<sup>2</sup>. The  $\phi_{\pi^-}^*$  dependent cross sections are illustrated in each  $\cos \theta_{\pi^-}^*$  bin. The blue triangles show MAID2000 model predictions. The blue lines show fits to the model predictions by the function “ $a + b \cos 2\phi_{\pi^-}^* + c \cos \phi_{\pi^-}^*$ ”. The black bars at the bottom of each subplot represent the systematic uncertainty for each cross section points.

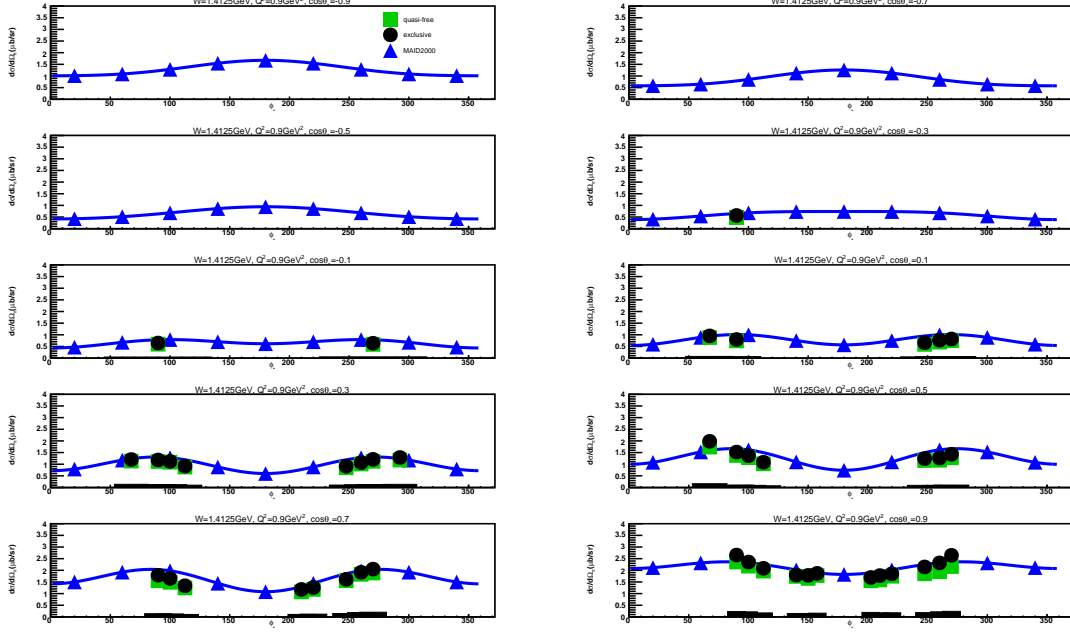


Figure B.38: Exclusive (black points) and quasi-free (green squares) cross sections in  $\mu\text{b}/\text{sr}$  are represented for  $W = 1.4125$  GeV and  $Q^2 = 0.9$  GeV<sup>2</sup>. The  $\phi_{\pi^-}^*$  dependent cross sections are illustrated in each  $\cos \theta_{\pi^-}^*$  bin. The blue triangles show MAID2000 model predictions. The blue lines show fits to the model predictions by the function “ $a + b \cos 2\phi_{\pi^-}^* + c \cos \phi_{\pi^-}^*$ ”. The black bars at the bottom of each subplot represent the systematic uncertainty for each cross section points.

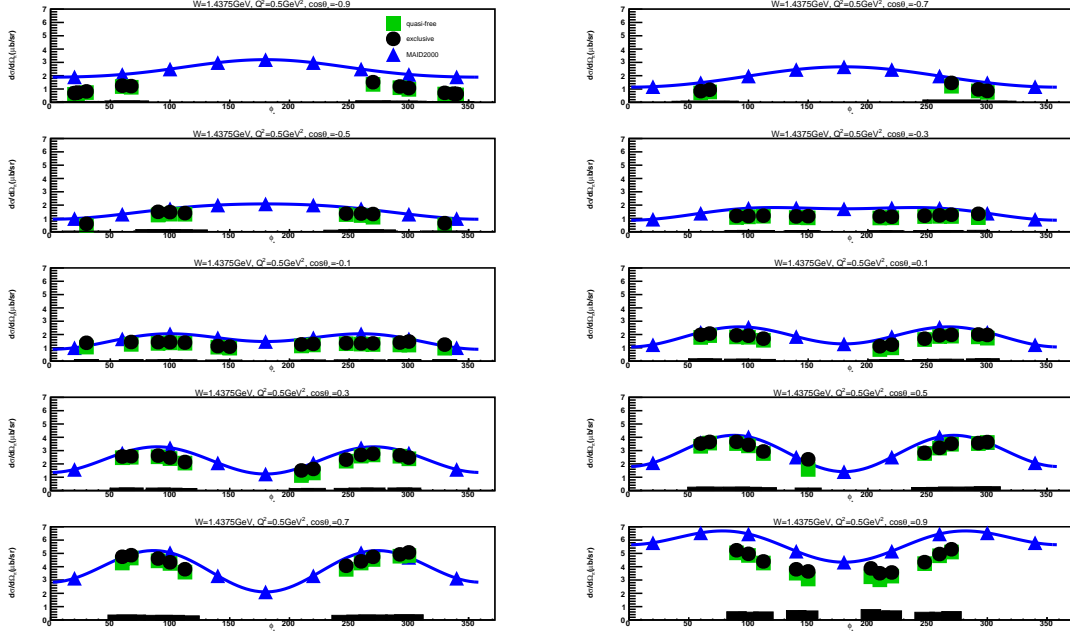


Figure B.39: Exclusive (black points) and quasi-free (green squares) cross sections in  $\mu\text{b}/\text{sr}$  are represented for  $W = 1.4375$  GeV and  $Q^2 = 0.5$  GeV<sup>2</sup>. The  $\phi_{\pi^-}^*$  dependent cross sections are illustrated in each  $\cos \theta_{\pi^-}^*$  bin. The blue triangles show MAID2000 model predictions. The blue lines show fits to the model predictions by the function “ $a + b \cos 2\phi_{\pi^-}^* + c \cos \phi_{\pi^-}^*$ ”. The black bars at the bottom of each subplot represent the systematic uncertainty for each cross section points.

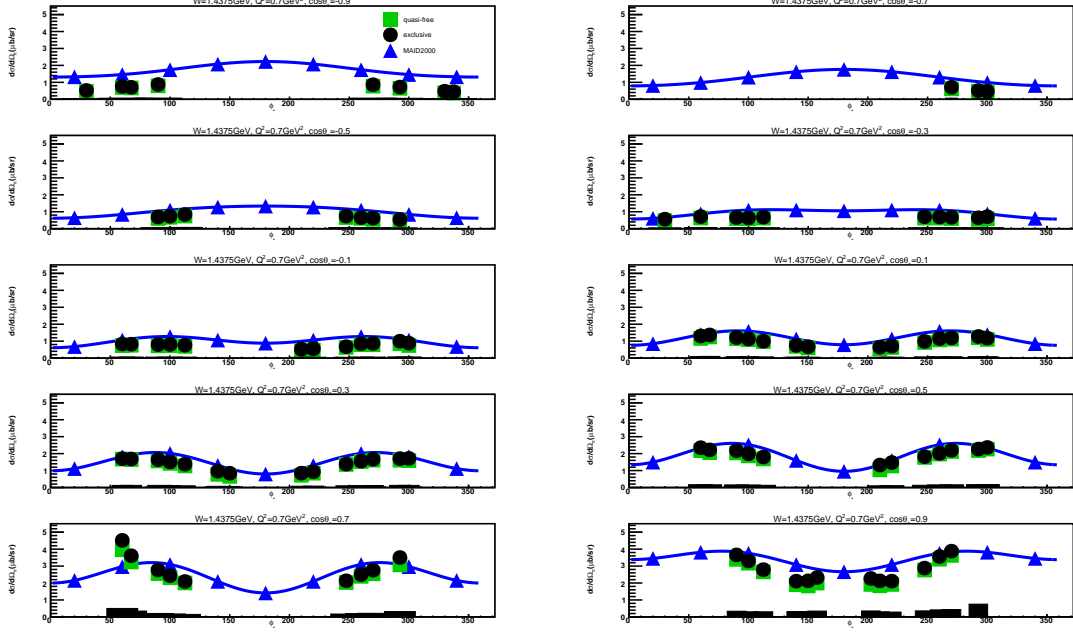


Figure B.40: Exclusive (black points) and quasi-free (green squares) cross sections in  $\mu\text{b}/\text{sr}$  are represented for  $W = 1.4375$  GeV and  $Q^2 = 0.7$  GeV<sup>2</sup>. The  $\phi_{\pi^-}^*$  dependent cross sections are illustrated in each  $\cos \theta_{\pi^-}^*$  bin. The blue triangles show MAID2000 model predictions. The blue lines show fits to the model predictions by the function “ $a + b \cos 2\phi_{\pi^-}^* + c \cos \phi_{\pi^-}^*$ ”. The black bars at the bottom of each subplot represent the systematic uncertainty for each cross section points.

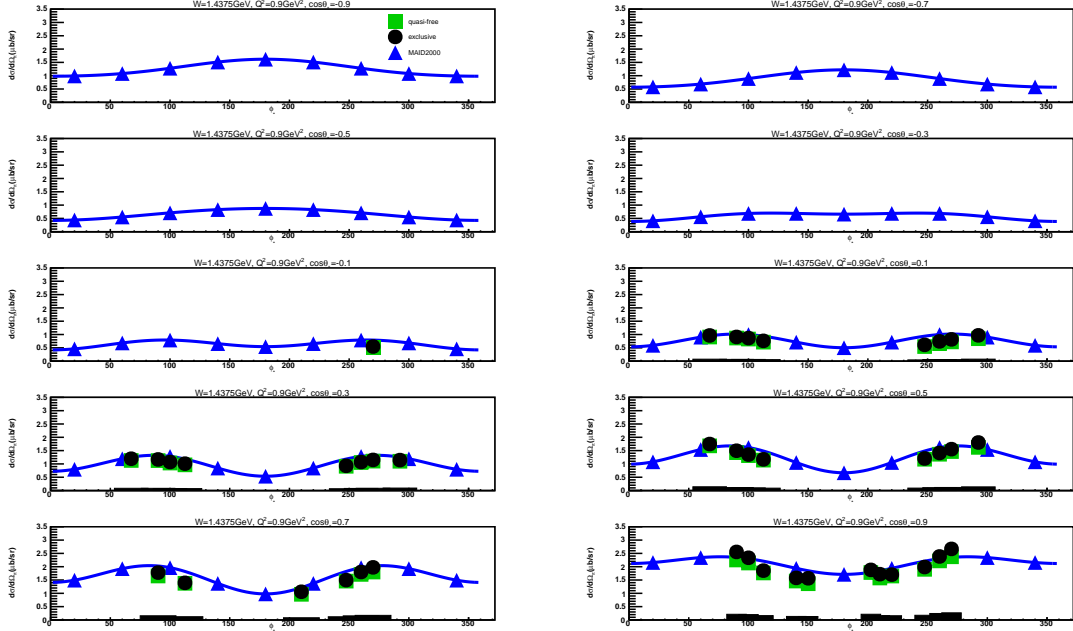


Figure B.41: Exclusive (black points) and quasi-free (green squares) cross sections in  $\mu\text{b}/\text{sr}$  are represented for  $W = 1.4375$  GeV and  $Q^2 = 0.9$  GeV<sup>2</sup>. The  $\phi_{\pi^-}^*$  dependent cross sections are illustrated in each  $\cos \theta_{\pi^-}^*$  bin. The blue triangles show MAID2000 model predictions. The blue lines show fits to the model predictions by the function “ $a + b \cos 2\phi_{\pi^-}^* + c \cos \phi_{\pi^-}^*$ ”. The black bars at the bottom of each subplot represent the systematic uncertainty for each cross section points.

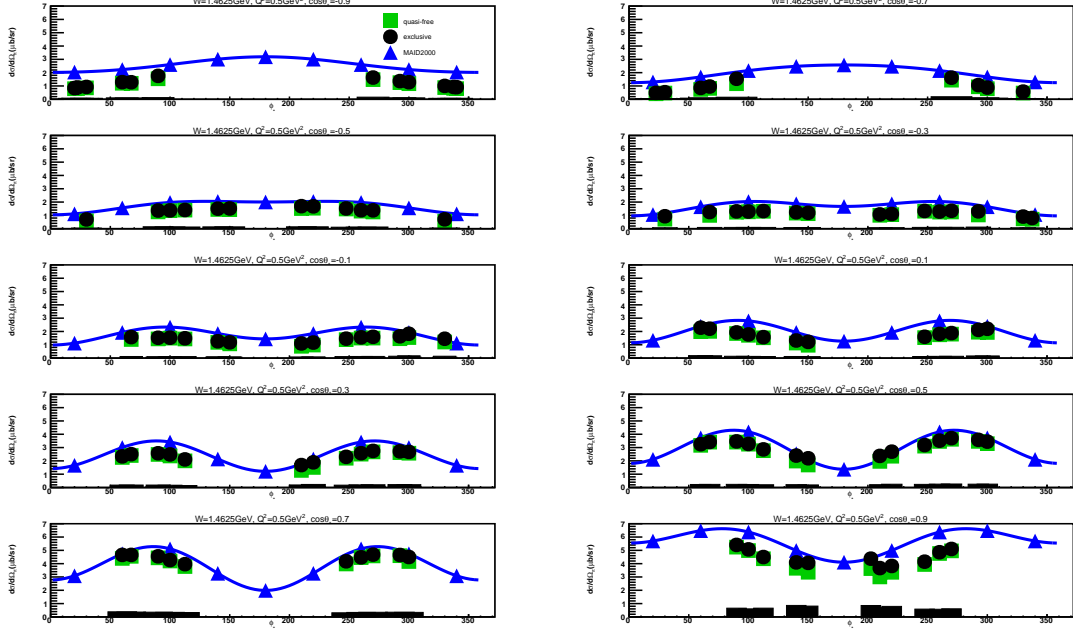


Figure B.42: Exclusive (black points) and quasi-free (green squares) cross sections in  $\mu\text{b}/\text{sr}$  are represented for  $W = 1.4625$  GeV and  $Q^2 = 0.5$  GeV<sup>2</sup>. The  $\phi_{\pi^-}^*$  dependent cross sections are illustrated in each  $\cos \theta_{\pi^-}^*$  bin. The blue triangles show MAID2000 model predictions. The blue lines show fits to the model predictions by the function “ $a + b \cos 2\phi_{\pi^-}^* + c \cos \phi_{\pi^-}^*$ ”. The black bars at the bottom of each subplot represent the systematic uncertainty for each cross section points.

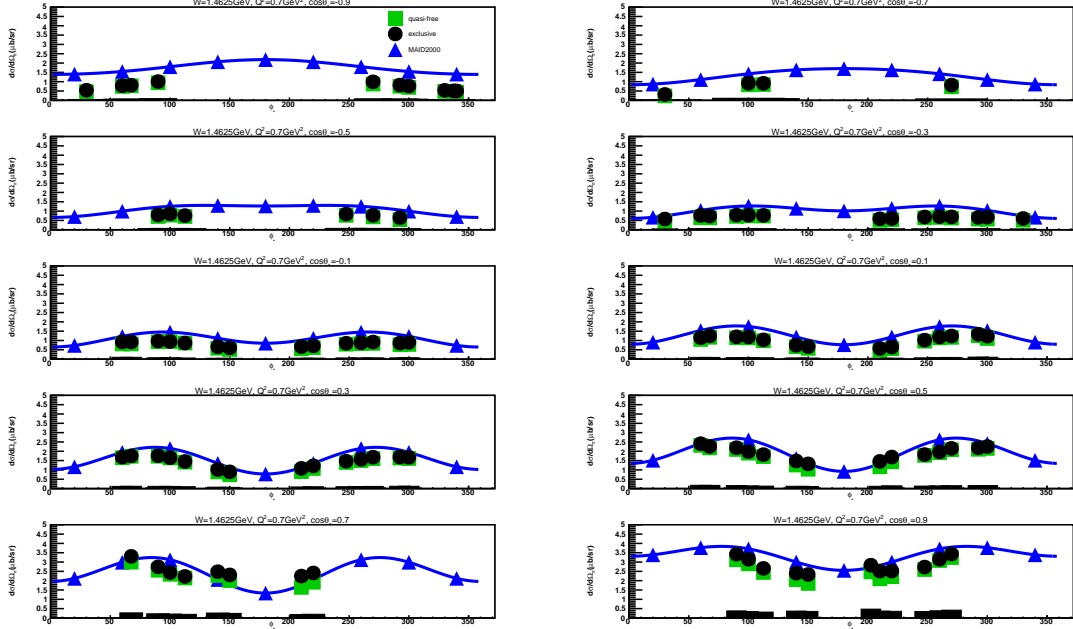


Figure B.43: Exclusive (black points) and quasi-free (green squares) cross sections in  $\mu\text{b}/\text{sr}$  are represented for  $W = 1.4625$  GeV and  $Q^2 = 0.7$  GeV<sup>2</sup>. The  $\phi_{\pi^-}^*$  dependent cross sections are illustrated in each  $\cos \theta_{\pi^-}^*$  bin. The blue triangles show MAID2000 model predictions. The blue lines show fits to the model predictions by the function “ $a + b \cos 2\phi_{\pi^-}^* + c \cos \phi_{\pi^-}^*$ ”. The black bars at the bottom of each subplot represent the systematic uncertainty for each cross section points.

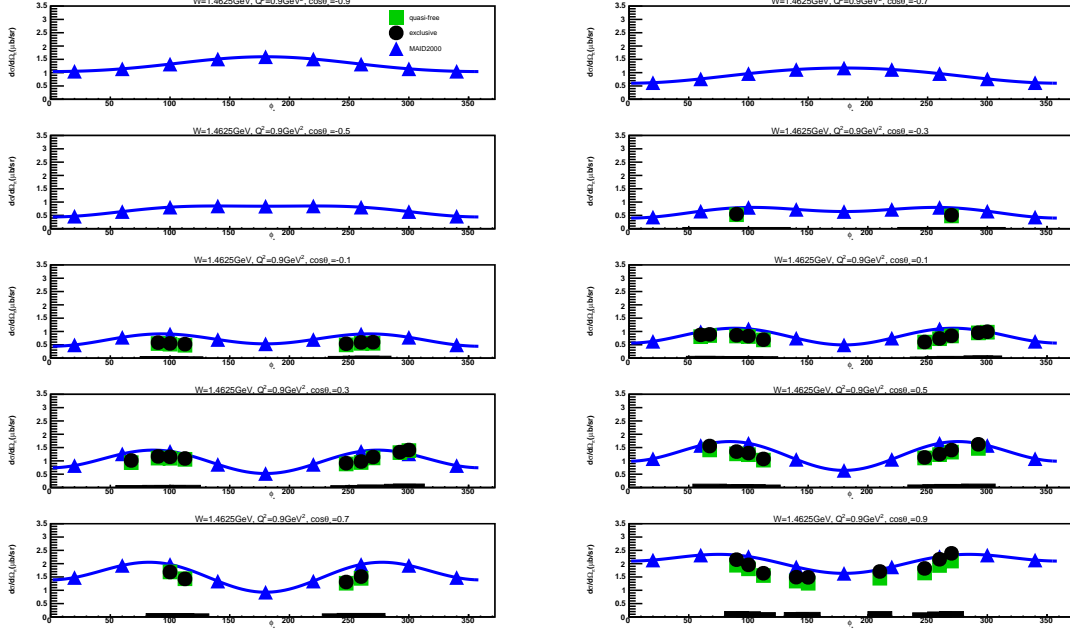


Figure B.44: Exclusive (black points) and quasi-free (green squares) cross sections in  $\mu\text{b}/\text{sr}$  are represented for  $W = 1.4625$  GeV and  $Q^2 = 0.9$  GeV<sup>2</sup>. The  $\phi_{\pi^-}^*$  dependent cross sections are illustrated in each  $\cos \theta_{\pi^-}^*$  bin. The blue triangles show MAID2000 model predictions. The blue lines show fits to the model predictions by the function “ $a + b \cos 2\phi_{\pi^-}^* + c \cos \phi_{\pi^-}^*$ ”. The black bars at the bottom of each subplot represent the systematic uncertainty for each cross section points.

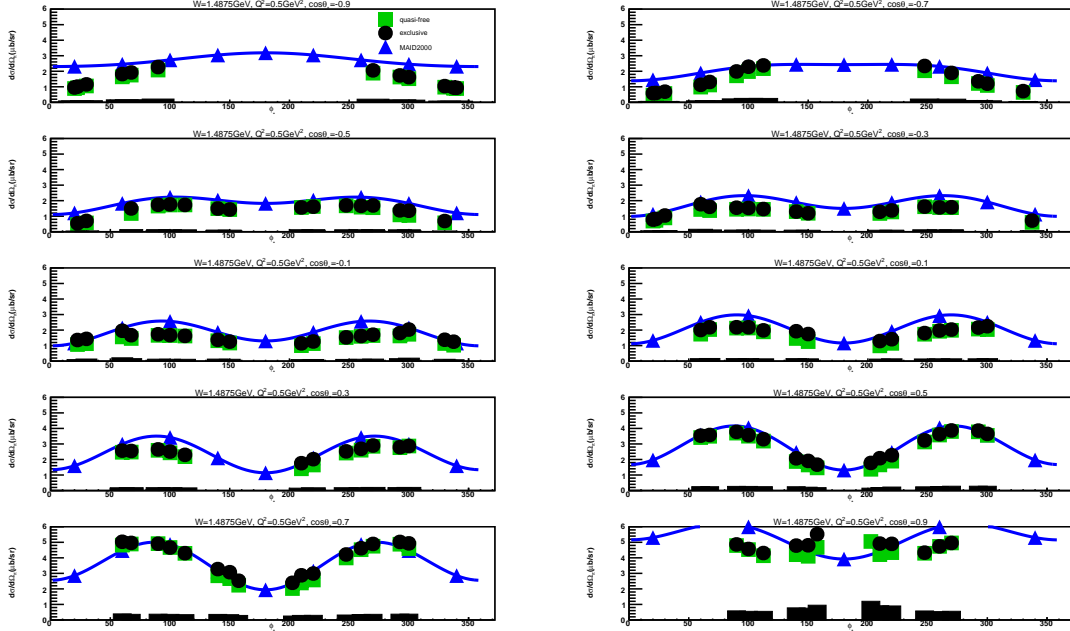


Figure B.45: Exclusive (black points) and quasi-free (green squares) cross sections in  $\mu\text{b}/\text{sr}$  are represented for  $W = 1.4875$  GeV and  $Q^2 = 0.5$  GeV<sup>2</sup>. The  $\phi_{\pi^-}^*$  dependent cross sections are illustrated in each  $\cos \theta_{\pi^-}^*$  bin. The blue triangles show MAID2000 model predictions. The blue lines show fits to the model predictions by the function “ $a + b \cos 2\phi_{\pi^-}^* + c \cos \phi_{\pi^-}^*$ ”. The black bars at the bottom of each subplot represent the systematic uncertainty for each cross section points.

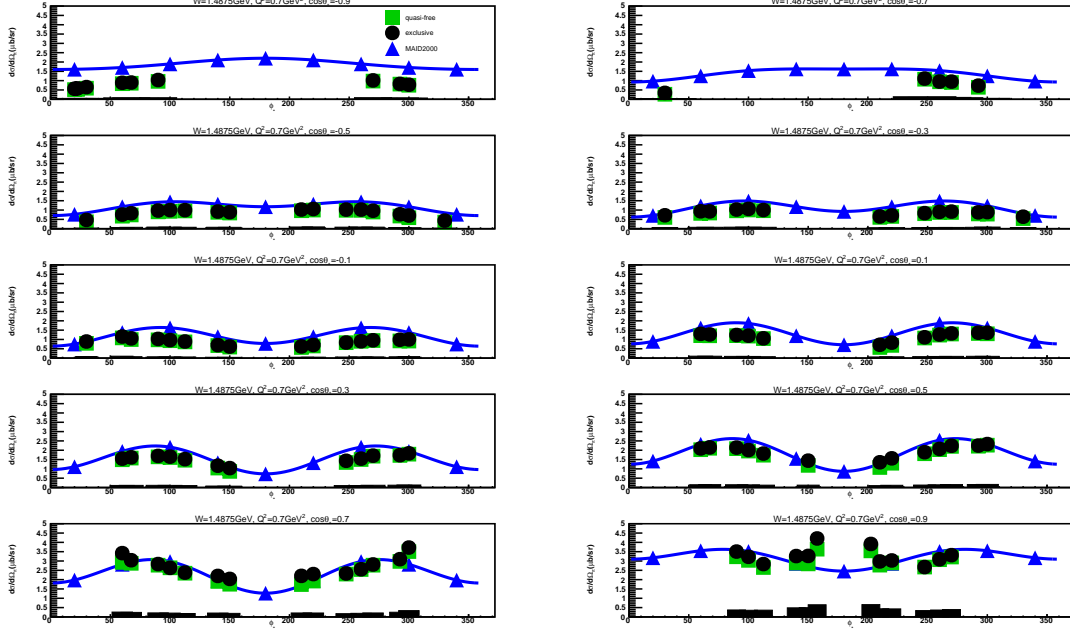


Figure B.46: Exclusive (black points) and quasi-free (green squares) cross sections in  $\mu\text{b}/\text{sr}$  are represented for  $W = 1.4875$  GeV and  $Q^2 = 0.7$  GeV<sup>2</sup>. The  $\phi_{\pi^-}^*$  dependent cross sections are illustrated in each  $\cos \theta_{\pi^-}^*$  bin. The blue triangles show MAID2000 model predictions. The blue lines show fits to the model predictions by the function “ $a + b \cos 2\phi_{\pi^-}^* + c \cos \phi_{\pi^-}^*$ ”. The black bars at the bottom of each subplot represent the systematic uncertainty for each cross section points.

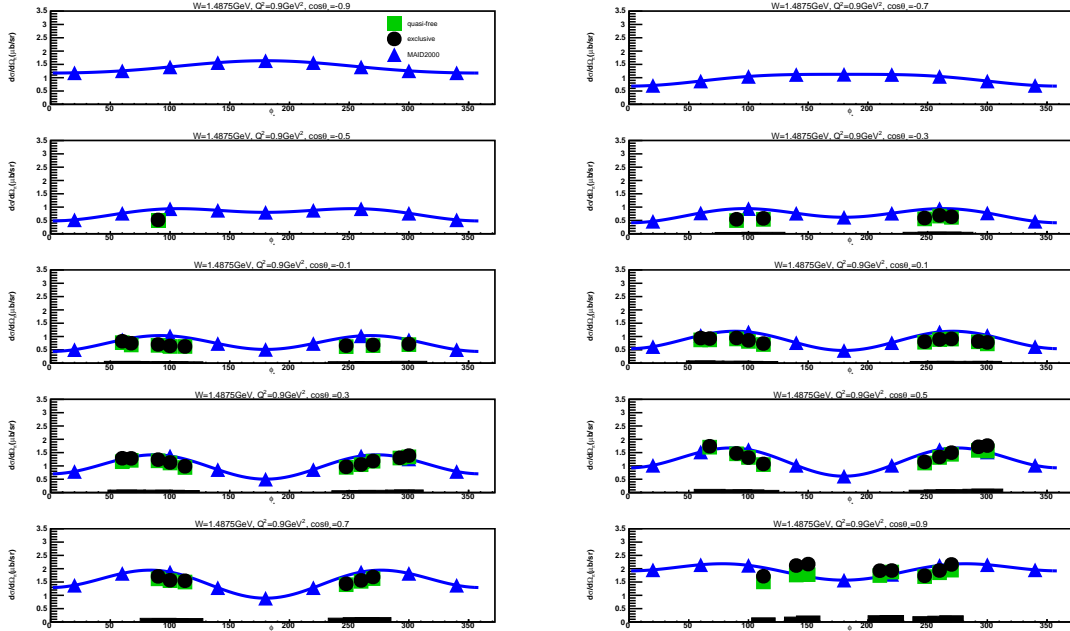


Figure B.47: Exclusive (black points) and quasi-free (green squares) cross sections in  $\mu\text{b}/\text{sr}$  are represented for  $W = 1.4875$  GeV and  $Q^2 = 0.9$  GeV<sup>2</sup>. The  $\phi_{\pi^-}^*$  dependent cross sections are illustrated in each  $\cos \theta_{\pi^-}^*$  bin. The blue triangles show MAID2000 model predictions. The blue lines show fits to the model predictions by the function “ $a + b \cos 2\phi_{\pi^-}^* + c \cos \phi_{\pi^-}^*$ ”. The black bars at the bottom of each subplot represent the systematic uncertainty for each cross section points.

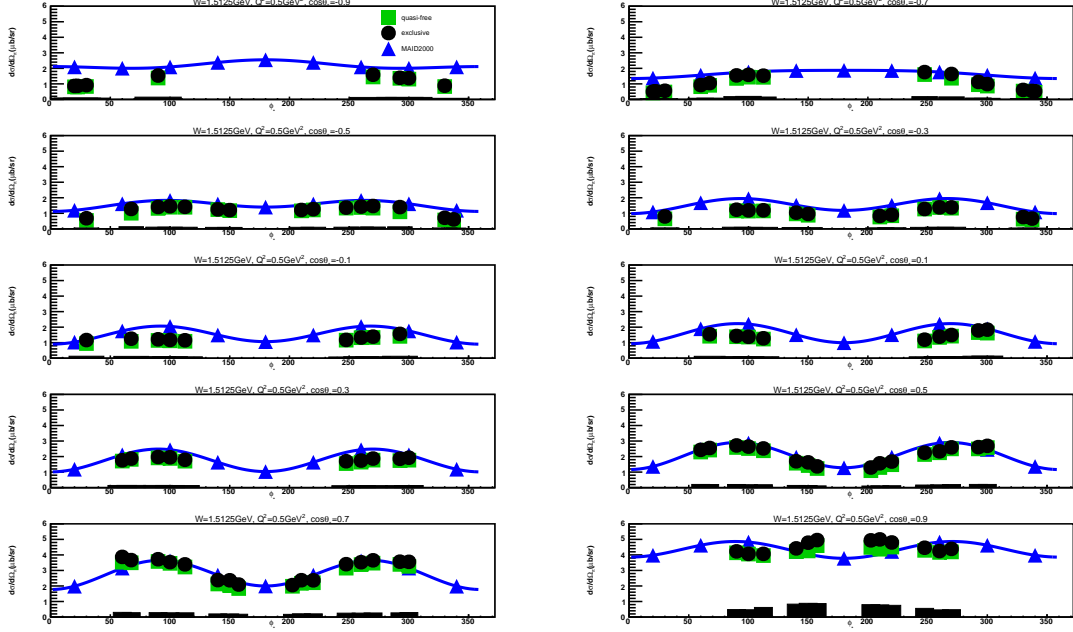


Figure B.48: Exclusive (black points) and quasi-free (green squares) cross sections in  $\mu\text{b}/\text{sr}$  are represented for  $W = 1.5125$  GeV and  $Q^2 = 0.5$  GeV<sup>2</sup>. The  $\phi_{\pi^-}^*$  dependent cross sections are illustrated in each  $\cos\theta_{\pi^-}^*$  bin. The blue triangles show MAID2000 model predictions. The blue lines show fits to the model predictions by the function “ $a + b \cos 2\phi_{\pi^-}^* + c \cos \phi_{\pi^-}^*$ ”. The black bars at the bottom of each subplot represent the systematic uncertainty for each cross section points.

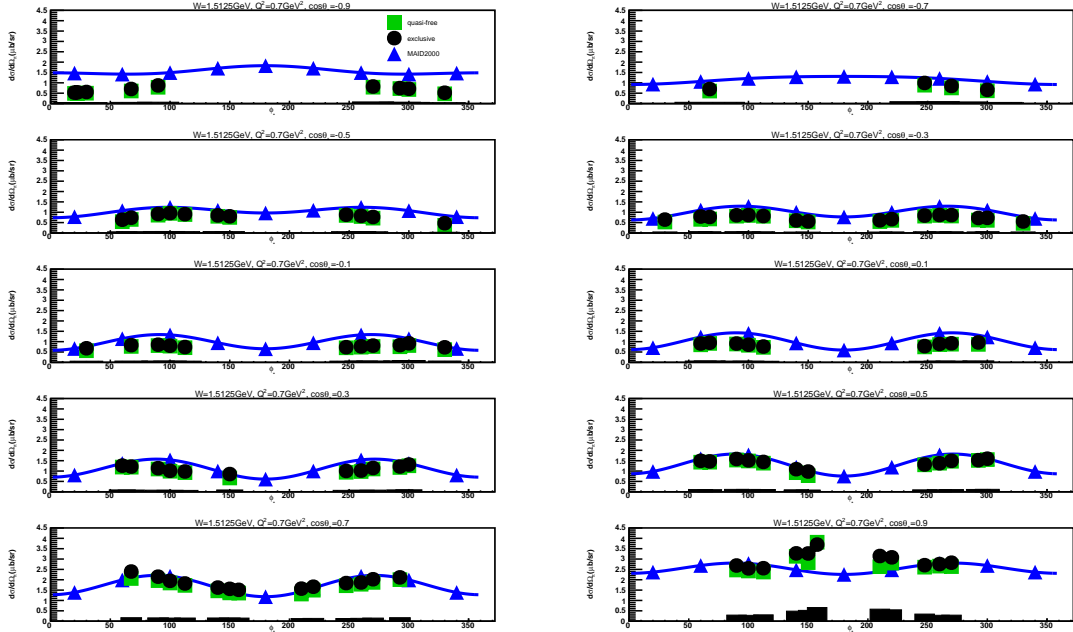


Figure B.49: Exclusive (black points) and quasi-free (green squares) cross sections in  $\mu\text{b}/\text{sr}$  are represented for  $W = 1.5125$  GeV and  $Q^2 = 0.7$  GeV<sup>2</sup>. The  $\phi_{\pi^-}^*$  dependent cross sections are illustrated in each  $\cos\theta_{\pi^-}^*$  bin. The blue triangles show MAID2000 model predictions. The blue lines show fits to the model predictions by the function “ $a + b \cos 2\phi_{\pi^-}^* + c \cos \phi_{\pi^-}^*$ ”. The black bars at the bottom of each subplot represent the systematic uncertainty for each cross section points.



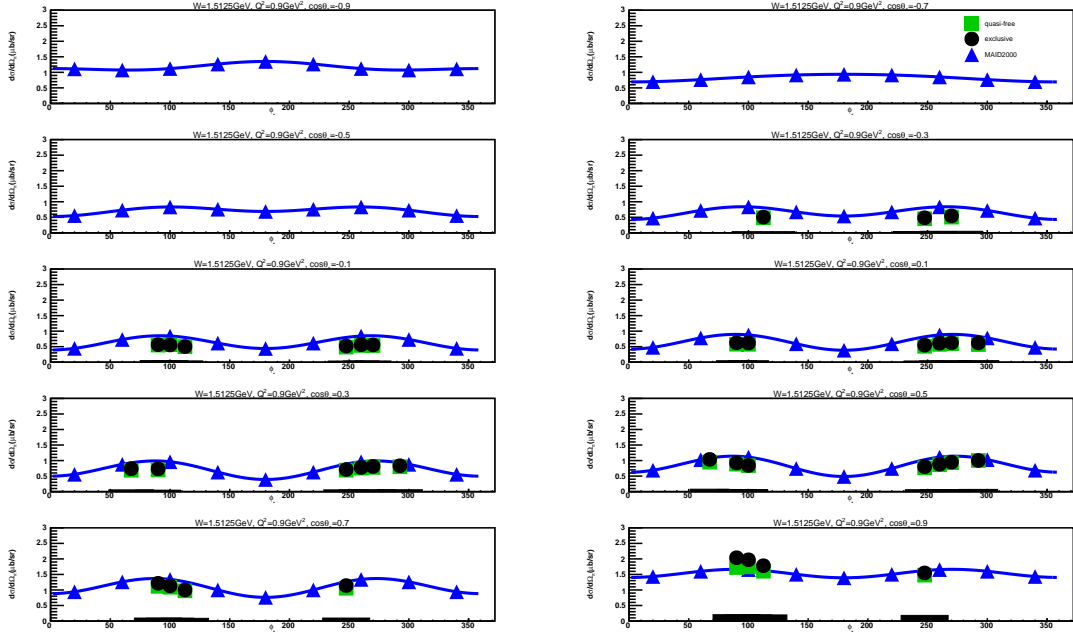


Figure B.50: Exclusive (black points) and quasi-free (green squares) cross sections in  $\mu\text{b}/\text{sr}$  are represented for  $W = 1.5125$  GeV and  $Q^2 = 0.9$  GeV<sup>2</sup>. The  $e\phi_{\pi^-}^*$  dependent cross sections are illustrated in each  $\cos\theta_{\pi^-}^*$  bin. The blue triangles show MAID2000 model predictions. The blue lines show fits to the model predictions by the function “ $a + b \cos 2\phi_{\pi^-}^* + c \cos \phi_{\pi^-}^*$ ”. The black bars at the bottom of each subplot represent the systematic uncertainty for each cross section points.

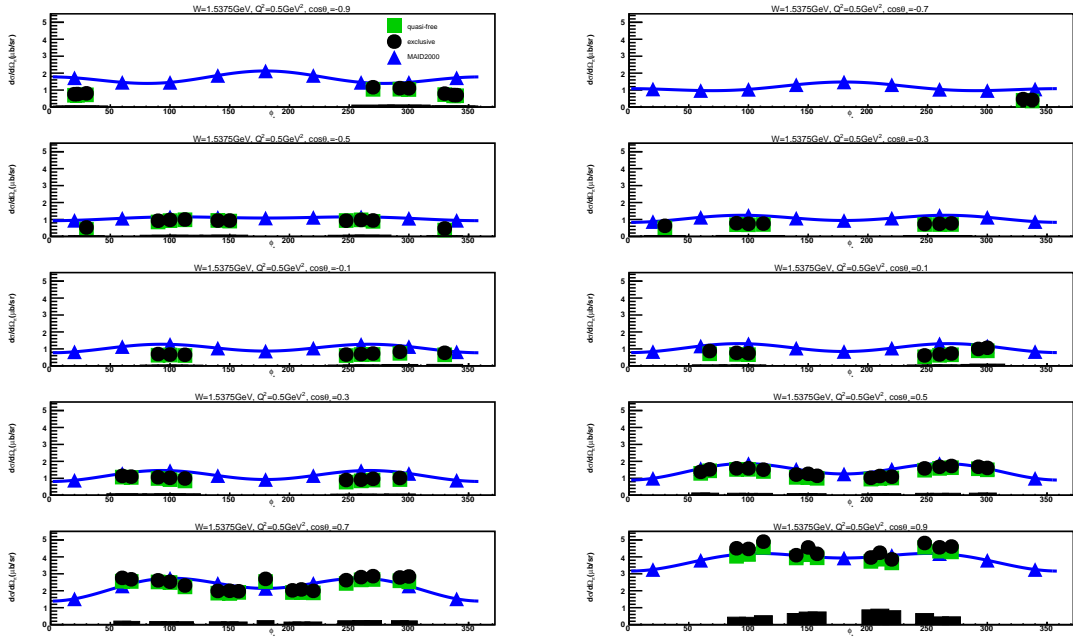


Figure B.51: Exclusive (black points) and quasi-free (green squares) cross sections in  $\mu\text{b}/\text{sr}$  are represented for  $W = 1.5375$  GeV and  $Q^2 = 0.5$  GeV<sup>2</sup>. The  $e\phi_{\pi^-}^*$  dependent cross sections are illustrated in each  $\cos\theta_{\pi^-}^*$  bin. The blue triangles show SAID and MAID2000 model predictions. The color lines show fits to the model predictions by the function “ $a + b \cos 2\phi_{\pi^-}^* + c \cos \phi_{\pi^-}^*$ ”. The black bars at the bottom of each subplot represent the systematic uncertainty for each cross section points.

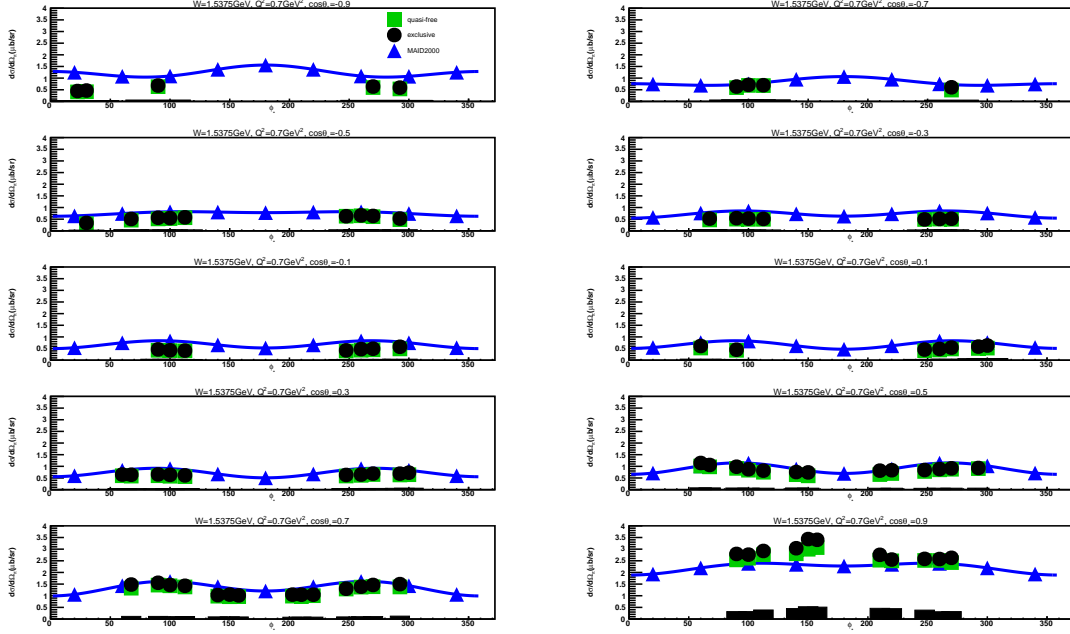


Figure B.52: Exclusive (black points) and quasi-free (green squares) cross sections in  $\mu\text{b}/\text{sr}$  are represented for  $W = 1.5375$  GeV and  $Q^2 = 0.7$  GeV<sup>2</sup>. The  $\phi_{\pi^-}^*$  dependent cross sections are illustrated in each  $\cos \theta_{\pi^-}^*$  bin. The blue triangles show SAID and MAID2000 model predictions. The color lines show fits to the model predictions by the function “ $a + b \cos 2\phi_{\pi^-}^* + c \cos \phi_{\pi^-}^*$ ”. The black bars at the bottom of each subplot represent the systematic uncertainty for each cross section points.

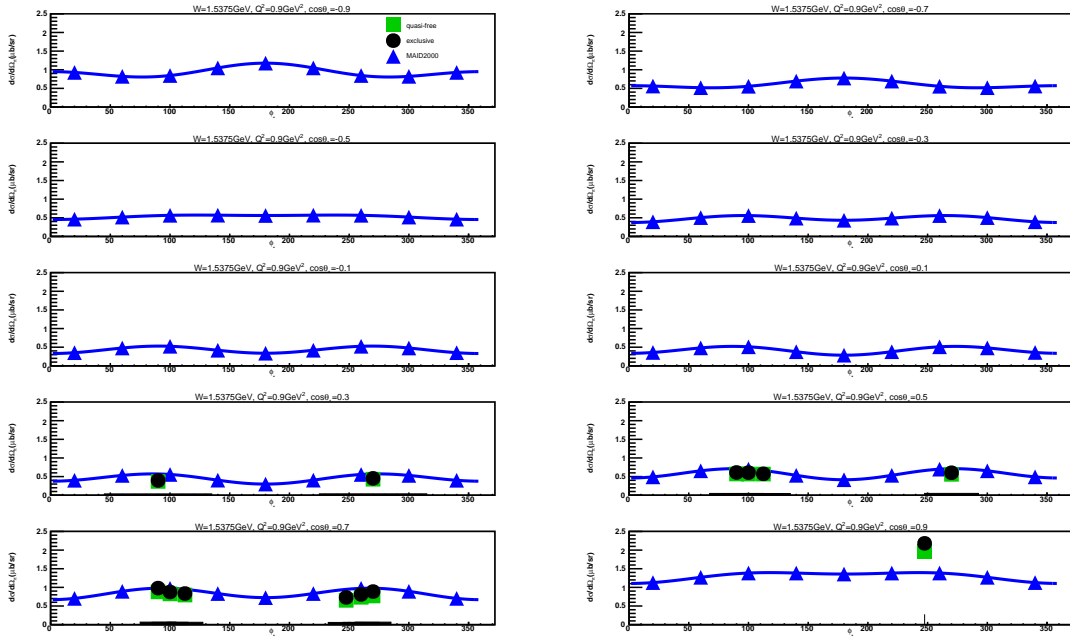


Figure B.53: Exclusive (black points) and quasi-free (green squares) cross sections in  $\mu\text{b}/\text{sr}$  are represented for  $W = 1.5375$  GeV and  $Q^2 = 0.9$  GeV<sup>2</sup>. The  $\phi_{\pi^-}^*$  dependent cross sections are illustrated in each  $\cos \theta_{\pi^-}^*$  bin. The blue triangles show SAID and MAID2000 model predictions. The color lines show fits to the model predictions by the function “ $a + b \cos 2\phi_{\pi^-}^* + c \cos \phi_{\pi^-}^*$ ”. The black bars at the bottom of each subplot represent the systematic uncertainty for each cross section points.

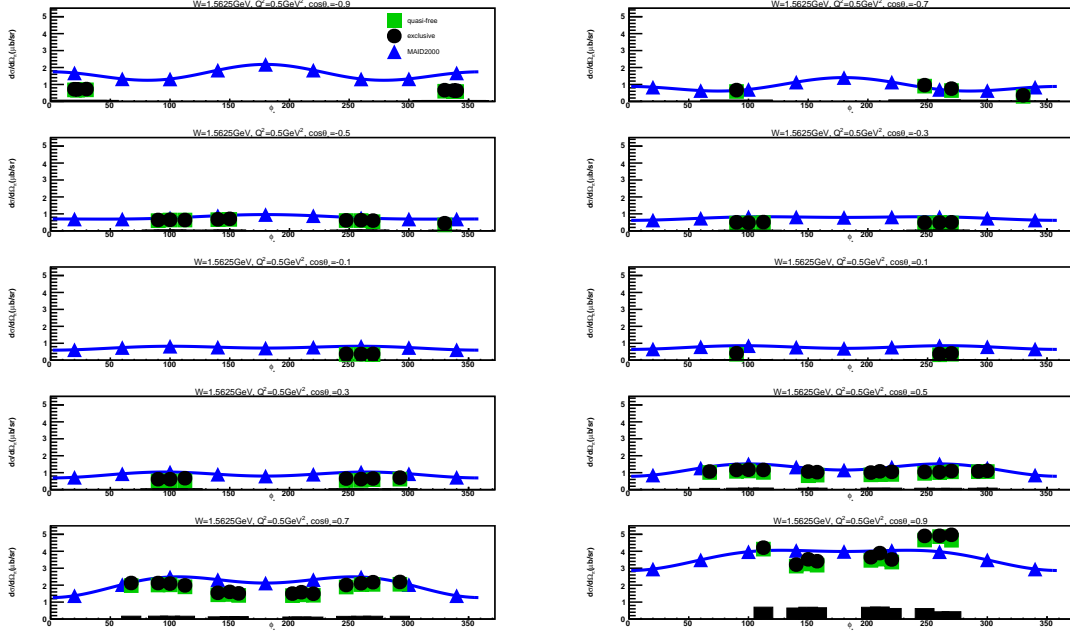


Figure B.54: Exclusive (black points) and quasi-free (green squares) cross sections in  $\mu\text{b}/\text{sr}$  are represented for  $W = 1.5625$  GeV and  $Q^2 = 0.5$  GeV<sup>2</sup>. The  $\phi_{\pi^-}^*$  dependent cross sections are illustrated in each  $\cos \theta_{\pi^-}^*$  bin. The blue triangles show SAID and MAID2000 model predictions. The color lines show fits to the model predictions by the function “ $a + b \cos 2\phi_{\pi^-}^* + c \cos \phi_{\pi^-}^*$ ”. The black bars at the bottom of each subplot represent the systematic uncertainty for each cross section points.

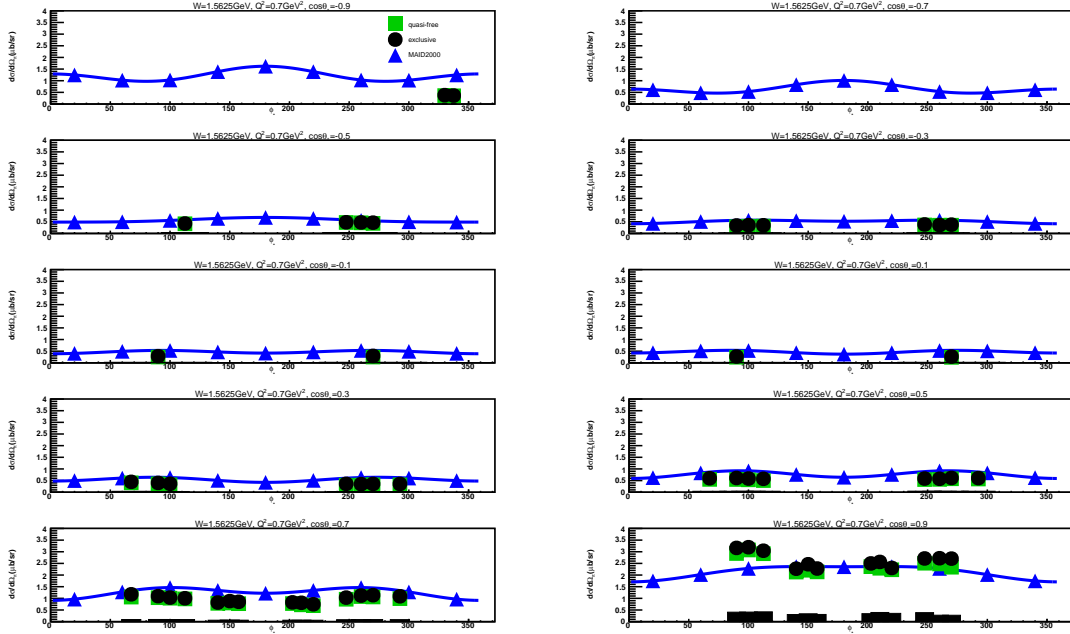


Figure B.55: Exclusive (black points) and quasi-free (green squares) cross sections in  $\mu\text{b}/\text{sr}$  are represented for  $W = 1.5625$  GeV and  $Q^2 = 0.7$  GeV<sup>2</sup>. The  $\phi_{\pi^-}^*$  dependent cross sections are illustrated in each  $\cos \theta_{\pi^-}^*$  bin. The blue triangles show SAID and MAID2000 model predictions. The color lines show fits to the model predictions by the function “ $a + b \cos 2\phi_{\pi^-}^* + c \cos \phi_{\pi^-}^*$ ”. The black bars at the bottom of each subplot represent the systematic uncertainty for each cross section points.

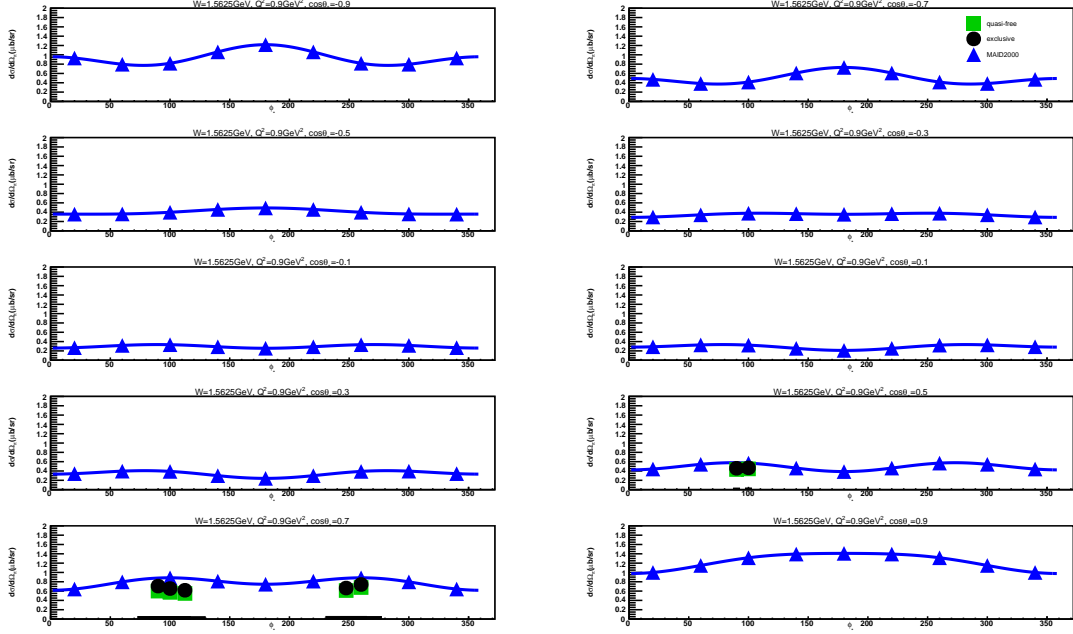


Figure B.56: Exclusive (black points) and quasi-free (green squares) cross sections in  $\mu\text{b}/\text{sr}$  are represented for  $W = 1.5625 \text{ GeV}$  and  $Q^2 = 0.9 \text{ GeV}^2$ . The  $\phi_{\pi^-}^*$  dependent cross sections are illustrated in each  $\cos \theta_{\pi^-}^*$  bin. The blue triangles show SAID and MAID2000 model predictions. The color lines show fits to the model predictions by the function “ $a + b \cos 2\phi_{\pi^-}^* + c \cos \phi_{\pi^-}^*$ ”. The black bars at the bottom of each subplot represent the systematic uncertainty for each cross section points.

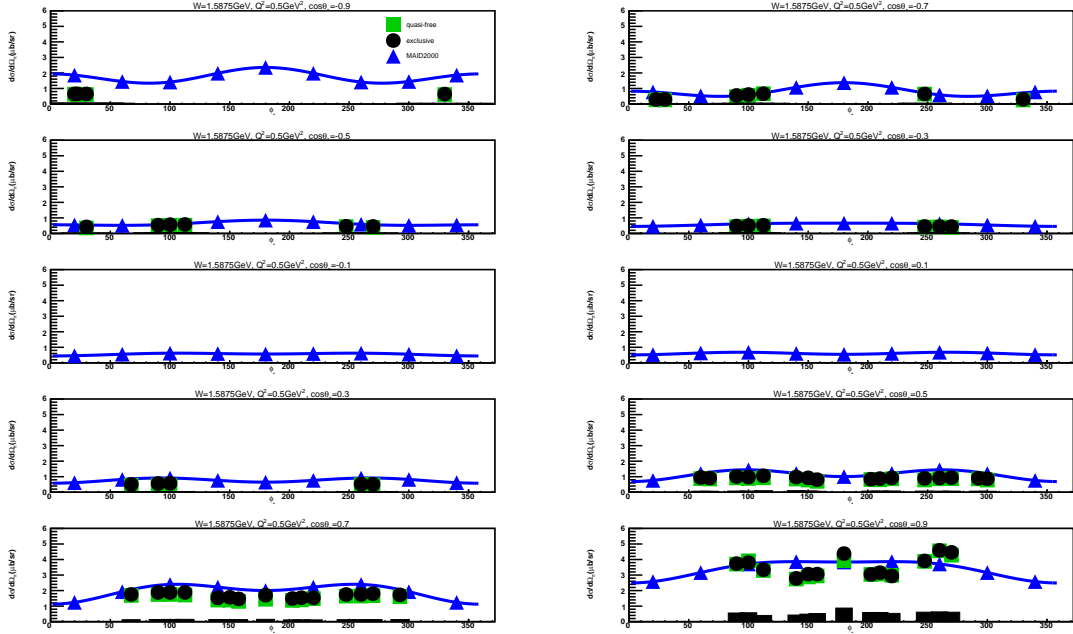


Figure B.57: Exclusive (black points) and quasi-free (green squares) cross sections in  $\mu\text{b}/\text{sr}$  are represented for  $W = 1.5875 \text{ GeV}$  and  $Q^2 = 0.5 \text{ GeV}^2$ . The  $\phi_{\pi^-}^*$  dependent cross sections are illustrated in each  $\cos \theta_{\pi^-}^*$  bin. The blue triangles show SAID and MAID2000 model predictions. The color lines show fits to the model predictions by the function “ $a + b \cos 2\phi_{\pi^-}^* + c \cos \phi_{\pi^-}^*$ ”. The black bars at the bottom of each subplot represent the systematic uncertainty for each cross section points.

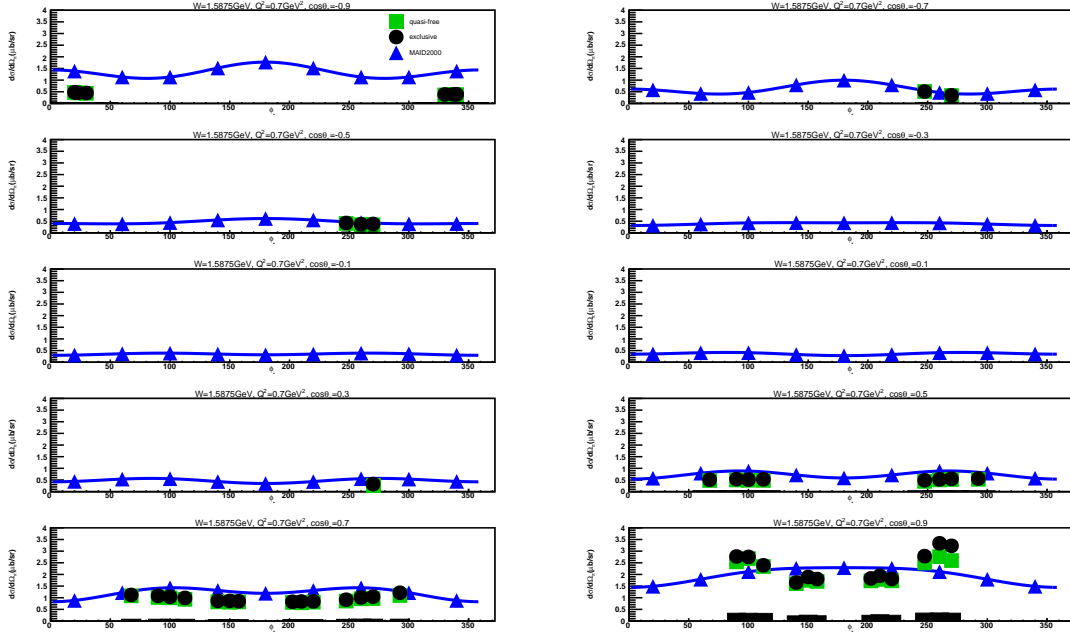


Figure B.58: Exclusive (black points) and quasi-free (green squares) cross sections in  $\mu\text{b}/\text{sr}$  are represented for  $W = 1.5875$  GeV and  $Q^2 = 0.7$  GeV $^2$ . The  $\phi_{\pi^-}^*$  dependent cross sections are illustrated in each  $\cos \theta_{\pi^-}^*$  bin. The blue triangles show SAID and MAID2000 model predictions. The color lines show fits to the model predictions by the function “ $a + b \cos 2\phi_{\pi^-}^* + c \cos \phi_{\pi^-}^*$ ”. The black bars at the bottom of each subplot represent the systematic uncertainty for each cross section points.

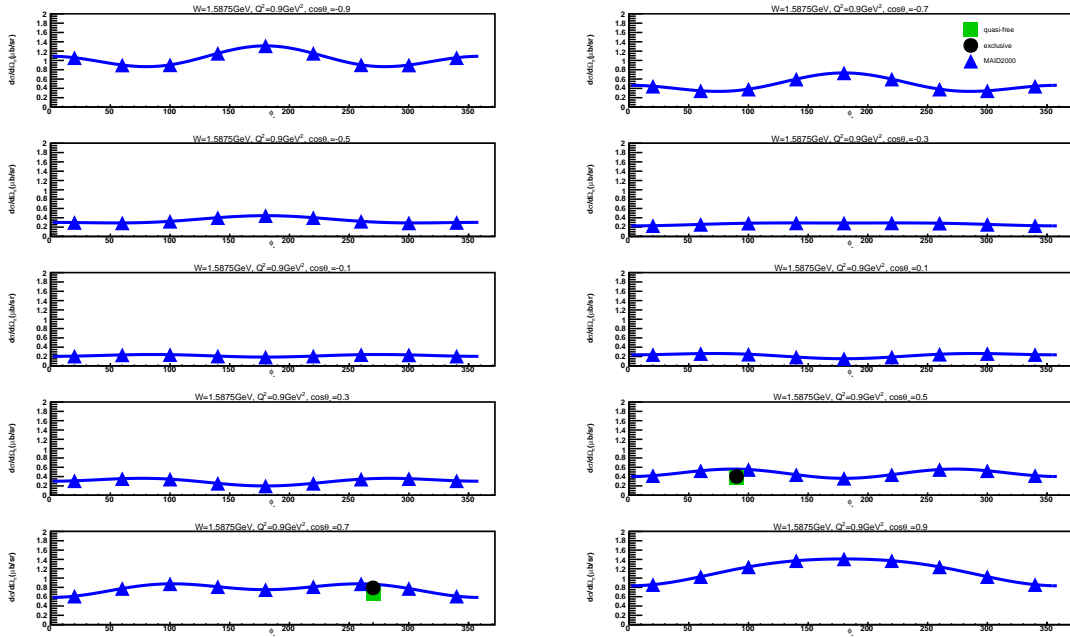


Figure B.59: Exclusive (black points) and quasi-free (green squares) cross sections in  $\mu\text{b}/\text{sr}$  are represented for  $W = 1.5875$  GeV and  $Q^2 = 0.9$  GeV $^2$ . The  $\phi_{\pi^-}^*$  dependent cross sections are illustrated in each  $\cos \theta_{\pi^-}^*$  bin. The blue triangles show SAID and MAID2000 model predictions. The color lines show fits to the model predictions by the function “ $a + b \cos 2\phi_{\pi^-}^* + c \cos \phi_{\pi^-}^*$ ”. The black bars at the bottom of each subplot represent the systematic uncertainty for each cross section points.

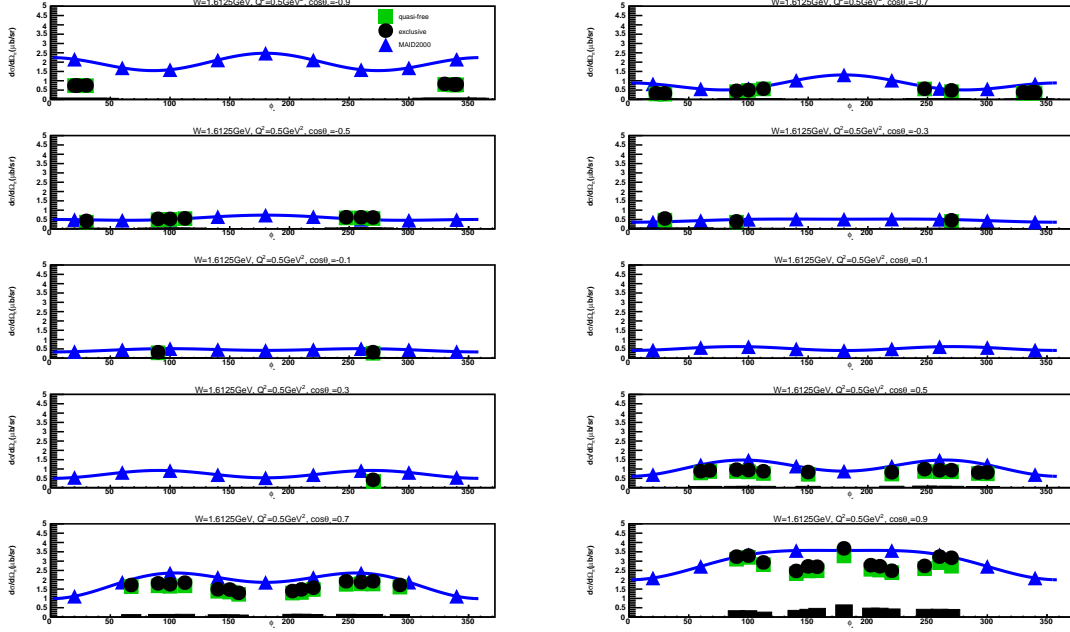


Figure B.60: Exclusive (black points) and quasi-free (green squares) cross sections in  $\mu\text{b}/\text{sr}$  are represented for  $W = 1.6125$  GeV and  $Q^2 = 0.5$  GeV<sup>2</sup>. The  $\phi_{\pi^-}^*$  dependent cross sections are illustrated in each  $\cos \theta_{\pi^-}^*$  bin. The blue triangles show SAID and MAID2000 model predictions. The color lines show fits to the model predictions by the function “ $a + b \cos 2\phi_{\pi^-}^* + c \cos \phi_{\pi^-}^*$ ”. The black bars at the bottom of each subplot represent the systematic uncertainty for each cross section points.

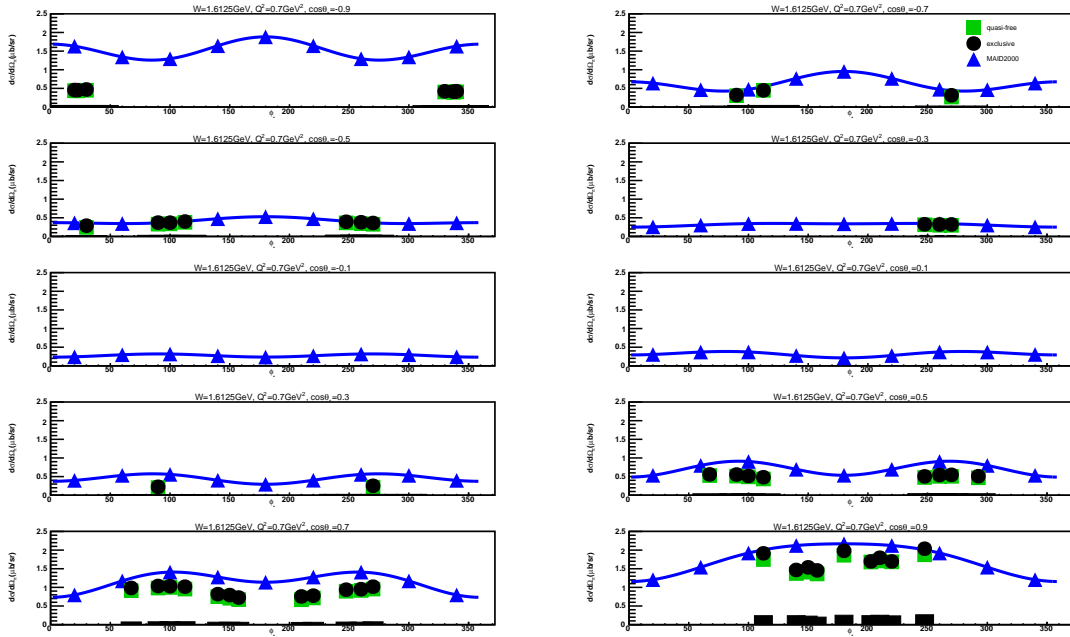


Figure B.61: Exclusive (black points) and quasi-free (green squares) cross sections in  $\mu\text{b}/\text{sr}$  are represented for  $W = 1.6125$  GeV and  $Q^2 = 0.7$  GeV<sup>2</sup>. The  $\phi_{\pi^-}^*$  dependent cross sections are illustrated in each  $\cos \theta_{\pi^-}^*$  bin. The blue triangles show SAID and MAID2000 model predictions. The color lines show fits to the model predictions by the function “ $a + b \cos 2\phi_{\pi^-}^* + c \cos \phi_{\pi^-}^*$ ”. The black bars at the bottom of each subplot represent the systematic uncertainty for each cross section points.

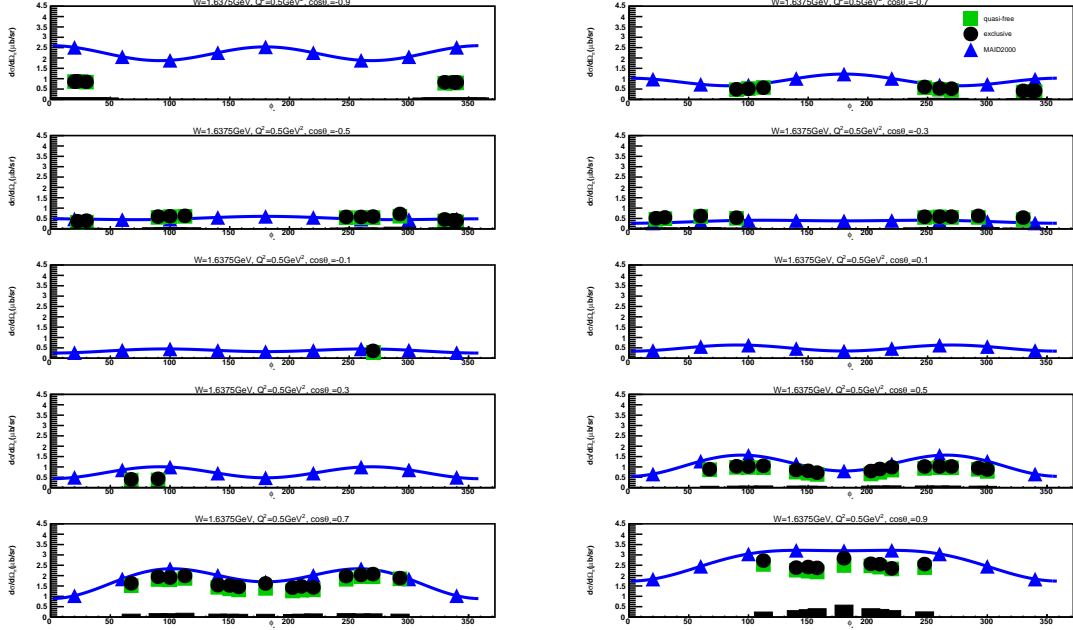


Figure B.62: Exclusive (black points) and quasi-free (green squares) cross sections in  $\mu\text{b}/\text{sr}$  are represented for  $W = 1.6375$  GeV and  $Q^2 = 0.5$  GeV<sup>2</sup>. The  $\phi_{\pi^-}^*$  dependent cross sections are illustrated in each  $\cos \theta_{\pi^-}^*$  bin. The blue triangles show SAID and MAID2000 model predictions. The color lines show fits to the model predictions by the function “ $a + b \cos 2\phi_{\pi^-}^* + c \cos \phi_{\pi^-}^*$ ”. The black bars at the bottom of each subplot represent the systematic uncertainty for each cross section points.

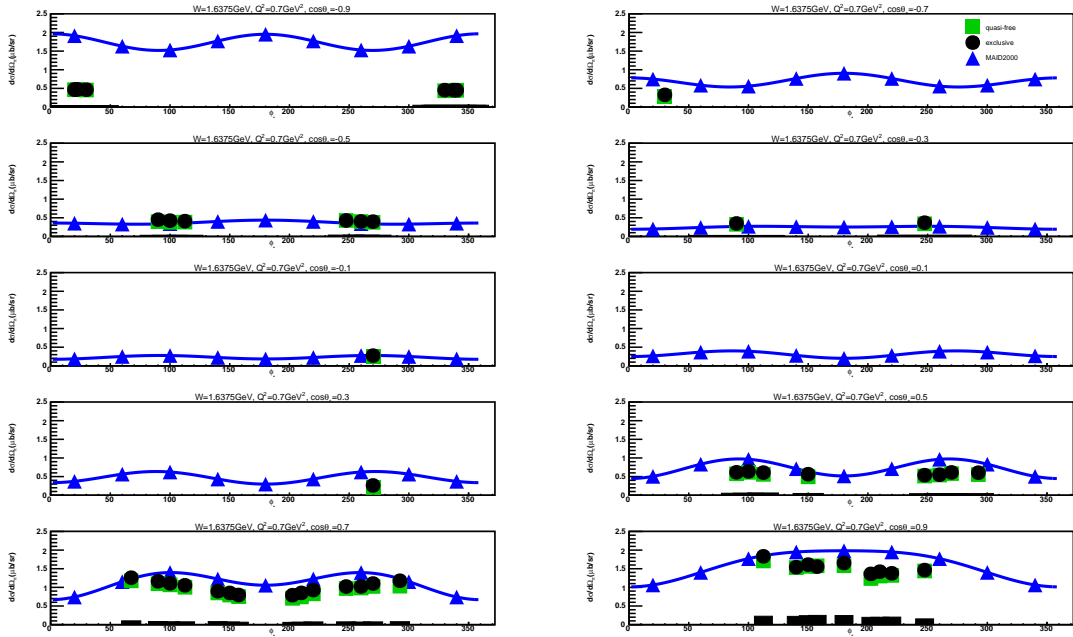


Figure B.63: Exclusive (black points) and quasi-free (green squares) cross sections in  $\mu\text{b}/\text{sr}$  are represented for  $W = 1.6375$  GeV and  $Q^2 = 0.7$  GeV<sup>2</sup>. The  $\phi_{\pi^-}^*$  dependent cross sections are illustrated in each  $\cos \theta_{\pi^-}^*$  bin. The blue triangles show SAID and MAID2000 model predictions. The color lines show fits to the model predictions by the function “ $a + b \cos 2\phi_{\pi^-}^* + c \cos \phi_{\pi^-}^*$ ”. The black bars at the bottom of each subplot represent the systematic uncertainty for each cross section points.

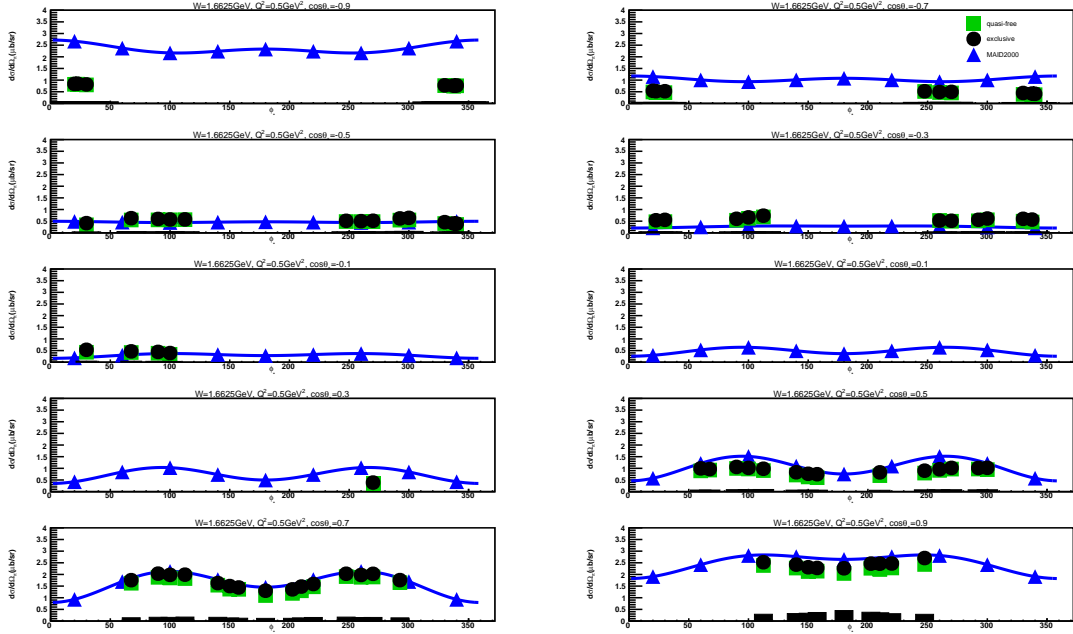


Figure B.64: Exclusive (black points) and quasi-free (green squares) cross sections in  $\mu\text{b}/\text{sr}$  are represented for  $W = 1.6625$  GeV and  $Q^2 = 0.5$  GeV<sup>2</sup>. The  $\phi_{\pi^*}^-$  dependent cross sections are illustrated in each  $\cos\theta_{\pi^*}^-$  bin. The blue triangles show SAID and MAID2000 model predictions. The color lines show fits to the model predictions by the function “ $a + b \cos 2\phi_{\pi^*}^- + c \cos \phi_{\pi^*}^-$ ”. The black bars at the bottom of each subplot represent the systematic uncertainty for each cross section points.

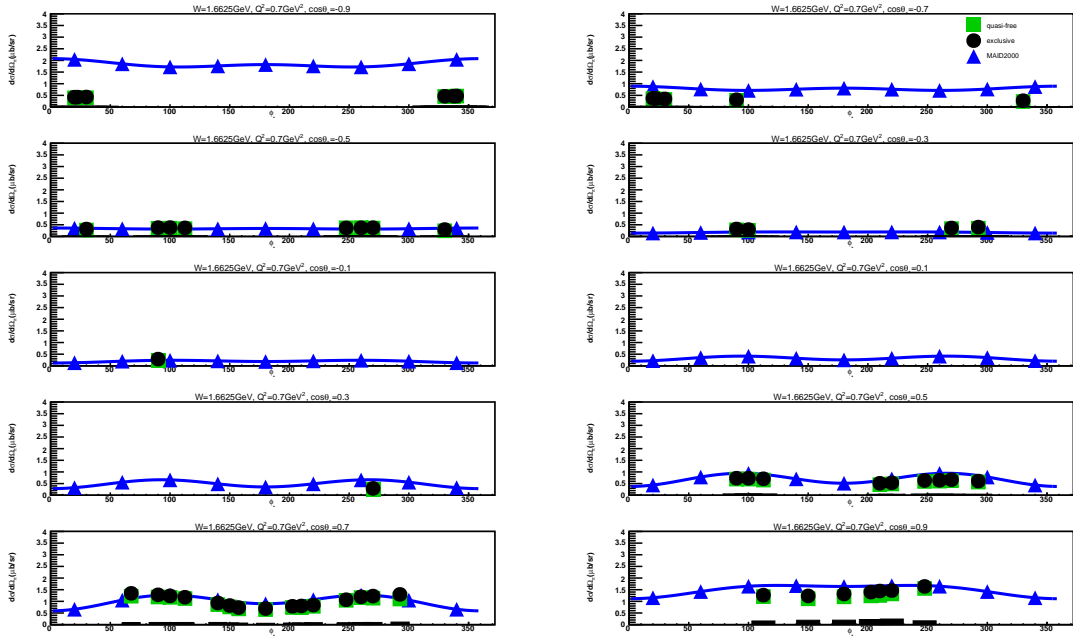


Figure B.65: Exclusive (black points) and quasi-free (green squares) cross sections in  $\mu\text{b}/\text{sr}$  are represented for  $W = 1.6625$  GeV and  $Q^2 = 0.7$  GeV<sup>2</sup>. The  $\phi_{\pi^*}^-$  dependent cross sections are illustrated in each  $\cos\theta_{\pi^*}^-$  bin. The blue triangles show SAID and MAID2000 model predictions. The color lines show fits to the model predictions by the function “ $a + b \cos 2\phi_{\pi^*}^- + c \cos \phi_{\pi^*}^-$ ”. The black bars at the bottom of each subplot represent the systematic uncertainty for each cross section points.



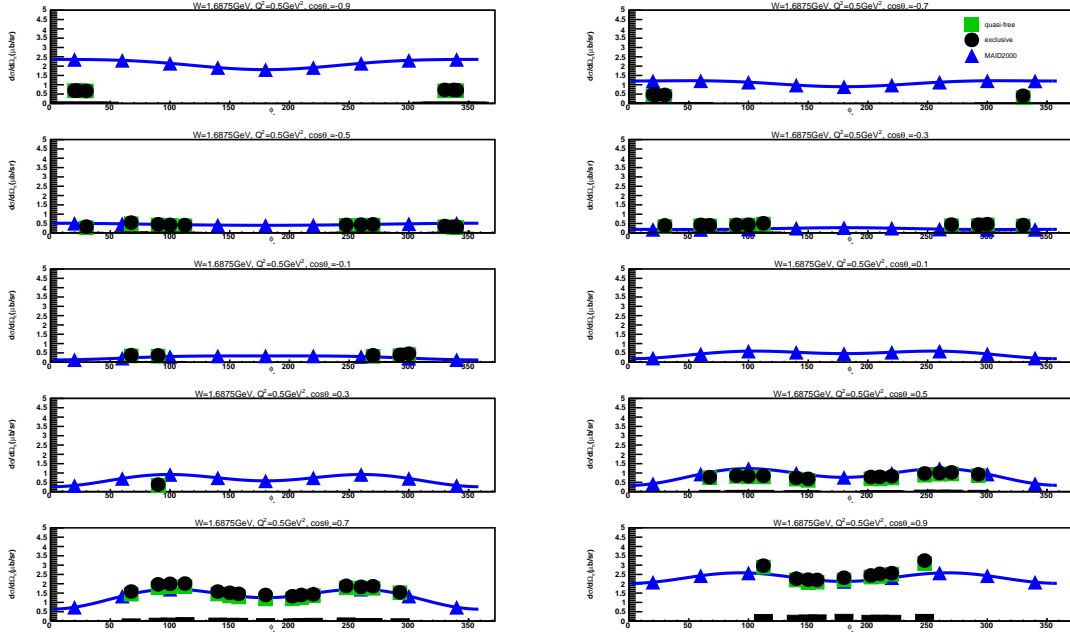


Figure B.66: Exclusive (black points) and quasi-free (green squares) cross sections in  $\mu\text{b}/\text{sr}$  are represented for  $W = 1.6875$  GeV and  $Q^2 = 0.5$  GeV<sup>2</sup>. The  $\phi_{\pi^-}^*$  dependent cross sections are illustrated in each  $\cos \theta_{\pi^-}^*$  bin. The blue triangles show SAID and MAID2000 model predictions. The color lines show fits to the model predictions by the function “ $a + b \cos 2\phi_{\pi^-}^* + c \cos \phi_{\pi^-}^*$ ”. The black bars at the bottom of each subplot represent the systematic uncertainty for each cross section points.

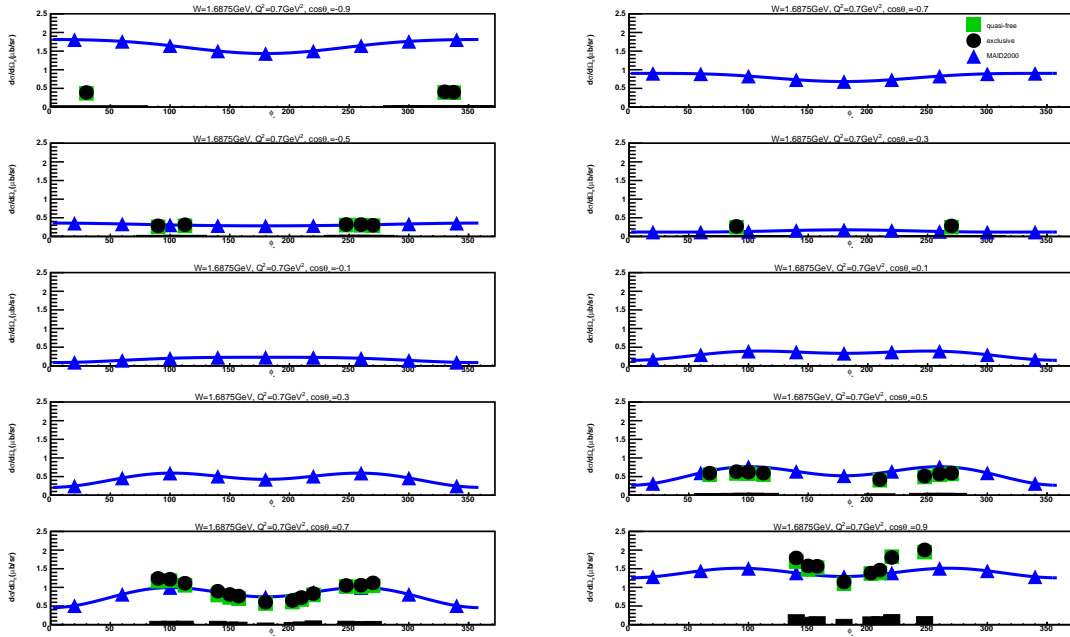


Figure B.67: Exclusive (black points) and quasi-free (green squares) cross sections in  $\mu\text{b}/\text{sr}$  are represented for  $W = 1.6875$  GeV and  $Q^2 = 0.7$  GeV<sup>2</sup>. The  $\phi_{\pi^-}^*$  dependent cross sections are illustrated in each  $\cos \theta_{\pi^-}^*$  bin. The blue triangles show SAID and MAID2000 model predictions. The color lines show fits to the model predictions by the function “ $a + b \cos 2\phi_{\pi^-}^* + c \cos \phi_{\pi^-}^*$ ”. The black bars at the bottom of each subplot represent the systematic uncertainty for each cross section points.

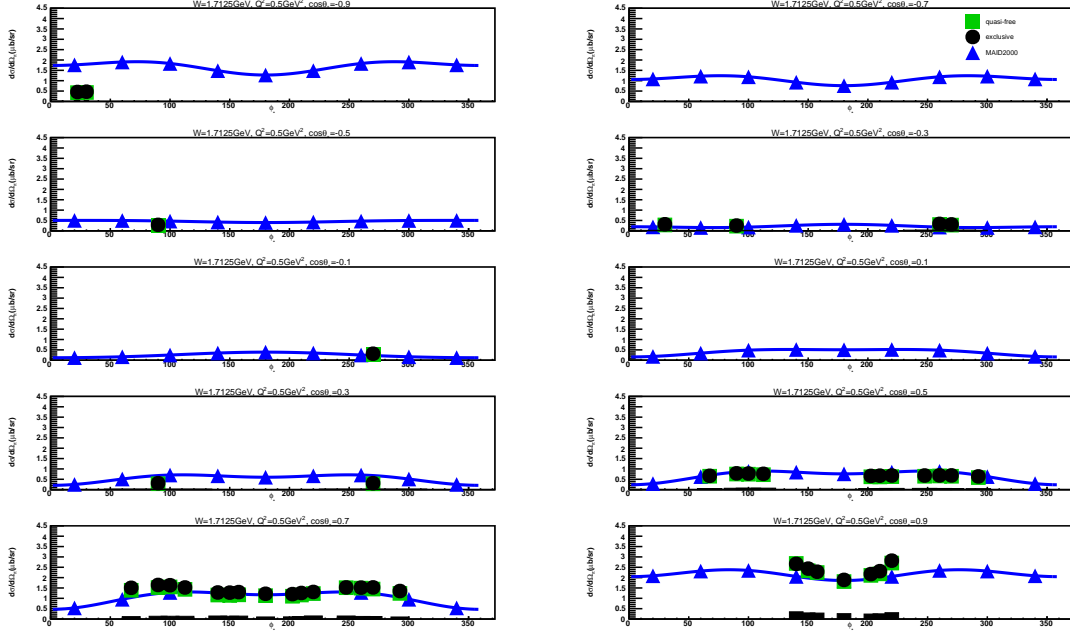


Figure B.68: Exclusive (black points) and quasi-free (green squares) cross sections in  $\mu\text{b}/\text{sr}$  are represented for  $W = 1.7125$  GeV and  $Q^2 = 0.5$  GeV<sup>2</sup>. The  $\phi_{\pi^-}^*$  dependent cross sections are illustrated in each  $\cos \theta_{\pi^-}^*$  bin. The blue triangles show SAID and MAID2000 model predictions. The color lines show fits to the model predictions by the function “ $a + b \cos 2\phi_{\pi^-}^* + c \cos \phi_{\pi^-}^*$ ”. The black bars at the bottom of each subplot represent the systematic uncertainty for each cross section points.

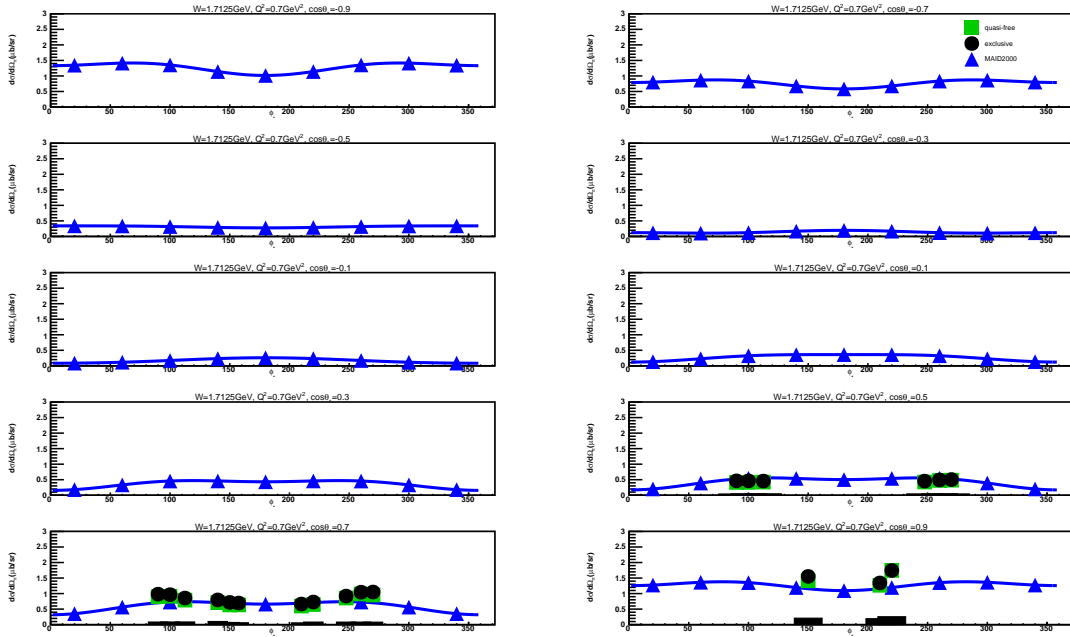


Figure B.69: Exclusive (black points) and quasi-free (green squares) cross sections in  $\mu\text{b}/\text{sr}$  are represented for  $W = 1.7125$  GeV and  $Q^2 = 0.7$  GeV<sup>2</sup>. The  $\phi_{\pi^-}^*$  dependent cross sections are illustrated in each  $\cos \theta_{\pi^-}^*$  bin. The blue triangles show SAID and MAID2000 model predictions. The color lines show fits to the model predictions by the function “ $a + b \cos 2\phi_{\pi^-}^* + c \cos \phi_{\pi^-}^*$ ”. The black bars at the bottom of each subplot represent the systematic uncertainty for each cross section points.

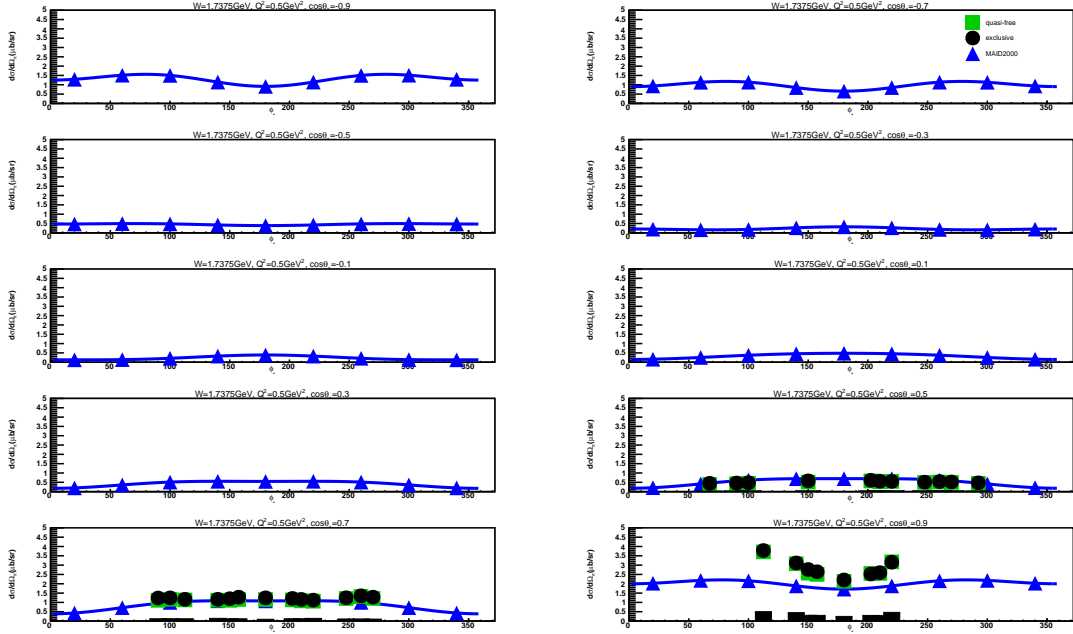


Figure B.70: Exclusive (black points) and quasi-free (green squares) cross sections in  $\mu\text{b}/\text{sr}$  are represented for  $W = 1.7375$  GeV and  $Q^2 = 0.5$  GeV<sup>2</sup>. The  $\phi_{\pi^-}^*$  dependent cross sections are illustrated in each  $\cos \theta_{\pi^-}^*$  bin. The blue triangles show SAID and MAID2000 model predictions. The color lines show fits to the model predictions by the function “ $a + b \cos 2\phi_{\pi^-}^* + c \cos \phi_{\pi^-}^*$ ”. The black bars at the bottom of each subplot represent the systematic uncertainty for each cross section points.

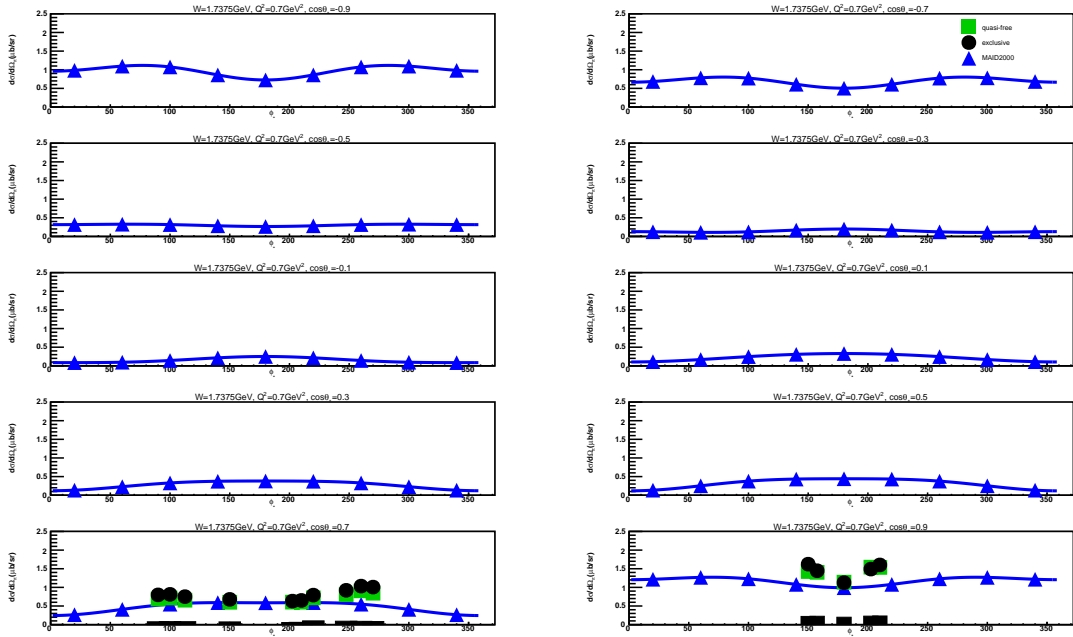


Figure B.71: Exclusive (black points) and quasi-free (green squares) cross sections in  $\mu\text{b}/\text{sr}$  are represented for  $W = 1.7375$  GeV and  $Q^2 = 0.7$  GeV<sup>2</sup>. The  $\phi_{\pi^-}^*$  dependent cross sections are illustrated in each  $\cos \theta_{\pi^-}^*$  bin. The blue triangles show SAID and MAID2000 model predictions. The color lines show fits to the model predictions by the function “ $a + b \cos 2\phi_{\pi^-}^* + c \cos \phi_{\pi^-}^*$ ”. The black bars at the bottom of each subplot represent the systematic uncertainty for each cross section points.

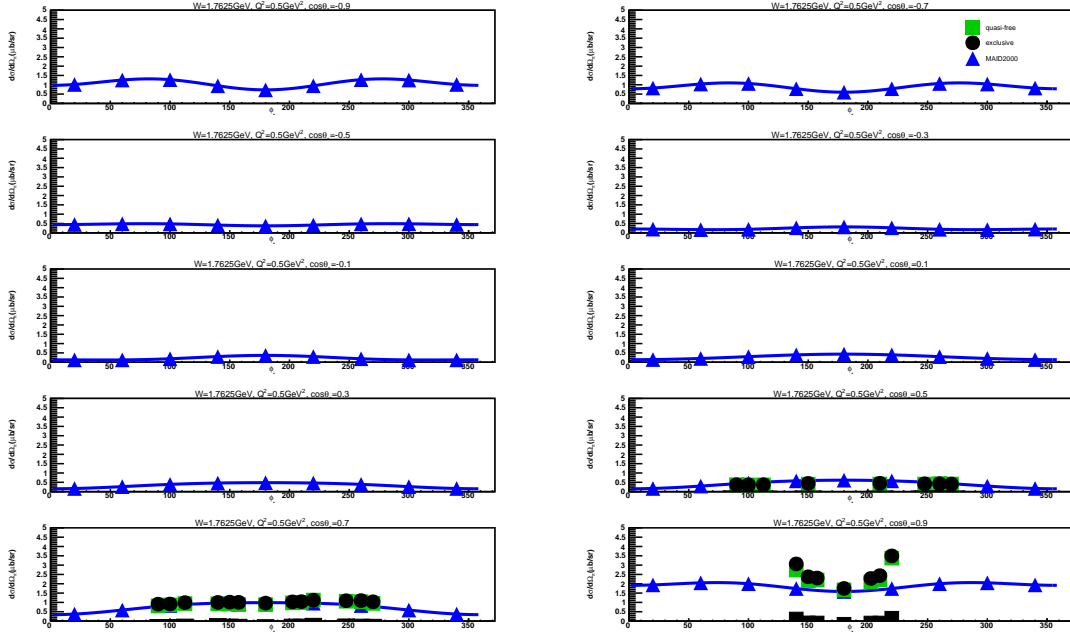


Figure B.72: Exclusive (black points) and quasi-free (green squares) cross sections in  $\mu\text{b}/\text{sr}$  are represented for  $W = 1.7625$  GeV and  $Q^2 = 0.5$  GeV<sup>2</sup>. The  $\phi_{\pi^-}^*$  dependent cross sections are illustrated in each  $\cos \theta_{\pi^-}^*$  bin. The blue triangles show SAID and MAID2000 model predictions. The color lines show fits to the model predictions by the function “ $a + b \cos 2\phi_{\pi^-}^* + c \cos \phi_{\pi^-}^*$ ”. The black bars at the bottom of each subplot represent the systematic uncertainty for each cross section points.

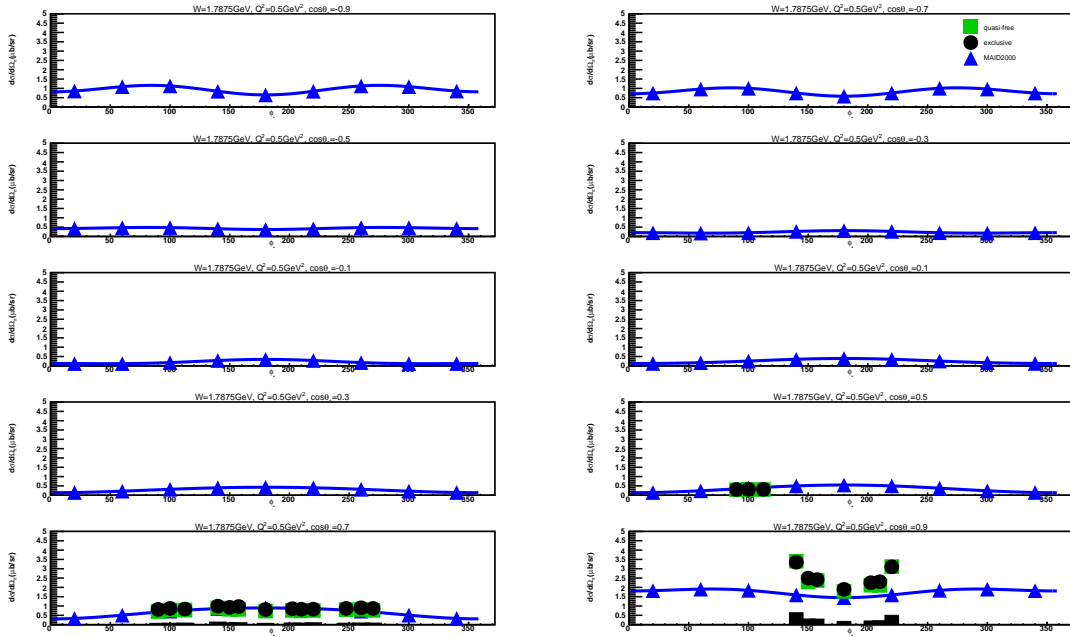


Figure B.73: Exclusive (black points) and quasi-free (green squares) cross sections in  $\mu\text{b}/\text{sr}$  are represented for  $W = 1.7875$  GeV and  $Q^2 = 0.5$  GeV<sup>2</sup>. The  $\phi_{\pi^-}^*$  dependent cross sections are illustrated in each  $\cos \theta_{\pi^-}^*$  bin. The blue triangles show SAID and MAID2000 model predictions. The color lines show fits to the model predictions by the function “ $a + b \cos 2\phi_{\pi^-}^* + c \cos \phi_{\pi^-}^*$ ”. The black bars at the bottom of each subplot represent the systematic uncertainty for each cross section points.

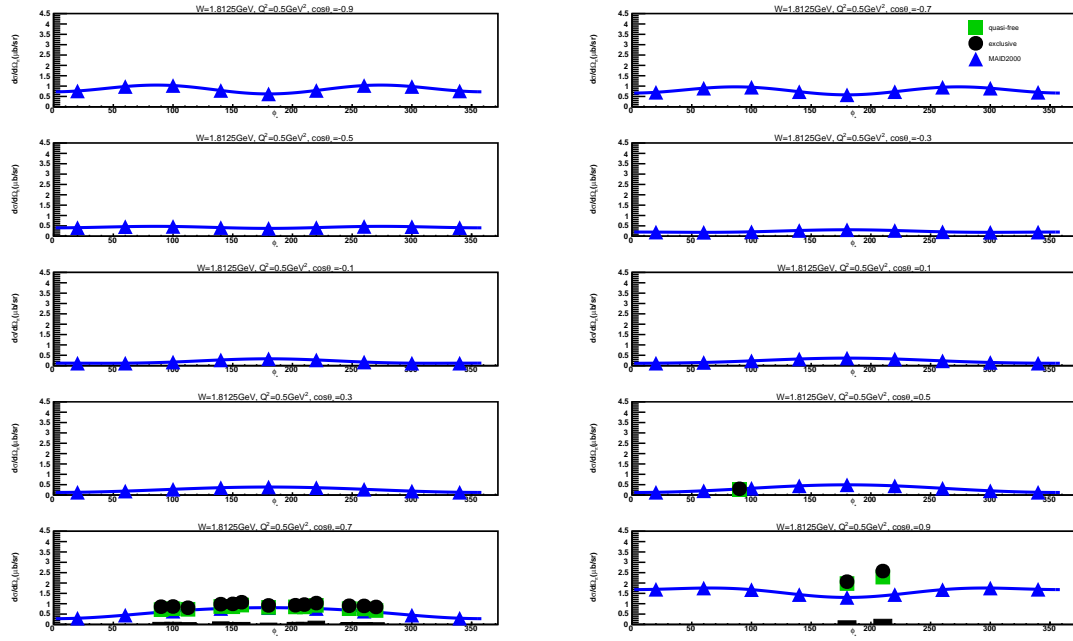


Figure B.74: Exclusive (black points) and quasi-free (green squares) cross sections in  $\mu\text{b}/\text{sr}$  are represented for  $W = 1.8125$  GeV and  $Q^2 = 0.5$  GeV<sup>2</sup>. The  $\phi_{\pi^-}^*$  dependent cross sections are illustrated in each  $\cos \theta_{\pi^-}^*$  bin. The blue triangles show SAID and MAID2000 model predictions. The color lines show fits to the model predictions by the function “ $a + b \cos 2\phi_{\pi^-}^* + c \cos \phi_{\pi^-}^*$ ”. The black bars at the bottom of each subplot represent the systematic uncertainty for each cross section points.